Bose-Einstein condensates with long-range dipolar interactions

van Bijnen, R.M.W.

Award date:
2008

Bose-Einstein condensates with long range dipolar interactions

R.M.W. van Bijnen

October 24, 2008

Abstract

Bose-Einstein condensation is a phase transition which atoms undergo when cooled near absolute zero temperature

Since the theoretical prediction in 1924, and the spectacular experimental confirmation of Bose-Einstein condensation in 1995, a rich new field in physics has emerged studying ultracold degenerate quantum gases. Although these ultracold gases are very dilute, their properties are nevertheless strongly influenced by interatomic interactions. Usually, these interactions are dominated by short range, isotropic contact interactions. In contrast, the recently realised Bose-Einstein Condensate (BEC) of Chromium atoms[1] contains long-range, anisotropic dipolar interactions leading to interesting new physics.

In this graduation project, stationary states of such dipolar BECs in harmonic traps are investigated for various experimentally relevant parameters. Furthermore, the elementary excitations of the BEC are calculated, as well as its response to a rotating perturbation. Finally, some more advanced topics such as vortex interactions and condensate response to impurities are investigated.

[1] A. Griesmaier *et al.*, "Bose-Einstein Condensation of Chromium", Phys. Rev. Lett. **94**, 160401 (2005)

Contents

1. Introduction

1.1. Bose Einstein Condensation

Consider a collection of N indistinguishable, non-interacting particles, trapped in some potential. When the temperature of this system is lowered, the articles will move to lower quantum states of the trap. When the particles are Fermions (half-integer spin), there cannot be more than two particles occupying the same state by the Pauli exclusion principle. At some temperature therefore all the N lowest quantum states will be occupied by precisely one particle, and nothing further will happen.

However, Bosons (particles with integer spin) do not have this restriction, and any arbitrary number of particles can occupy the same quantum state. Therefore, when the temperature is being lowered, more and more particles will fall into the ground state of the trap and the population of this state becomes macroscopic. This phenomenon is called *Bose-Einstein condensation*. It was predicted already in 1924 by Albert Einstein after expanding the work of Satyendra Bose, who had sent him a paper about the statistics of photons (which are Bosons) for comments.

Extending the massless photon statistics to massive Bosons, Einstein arrived at the following distribution function for the i^{th} state of the trapping potential,

$$f_0(\epsilon_i) = \frac{1}{e^{(\epsilon_i - \mu)/k_B T} - 1}, \tag{1.1}$$

which is now known as the *Bose-Einstein distribution*. Here, ϵ_i is the energy of the i^{th} state, k_B is Boltzmann's constant and T the temperature. The chemical potential μ enters the equation to conserve the number of particles.

If T is lowered, then μ must increase in order to keep the number of particles $N = \sum_i f_0(\epsilon_i)$ fixed. However, $\mu < \epsilon_0$ must also hold, otherwise negative densities would occur. Therefore, the occupation number of an arbitrary excited state ($i > 0$) cannot exceed $(e^{(\epsilon_i - \epsilon_0)/k_B T} - 1)^{-1}$, and this imposes an upper bound of the total number of particles that are in an excited state. When cooling the sytem below a critical temperature T_c, the N particles can no longer be accomodated in the excited states. Einstein postulated that the remaining particles must reside in the ground state of the system, leading to a macroscopic occupation of this state: the system exhibits Bose-Einstein condensation. In figure 1.1 an experimental realization of Bose Einstein condensation (BEC) can be seen.

At the critical temperature, several thermodynamic quantities show discontinuities and hence Bose-Einstein condensation is regarded as a phase transition [39], it is a whole new state of matter. Moreover, a Bose-Einstein condensate (BEC) is a unique system in which quantum effects manifest themselves at a macroscopic scale. When the atoms form a condensate, they all reside in the same quantum state and form a giant matter wave. Their collective

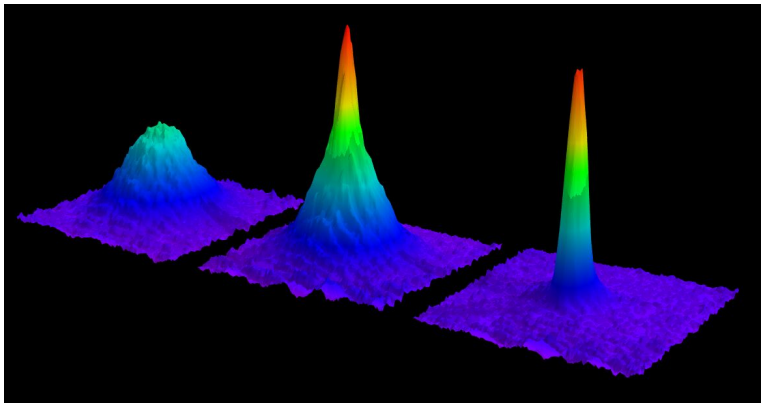

Figure 1.1.: *Absorption image of trapped atoms around the critical temperature. In the horizontal plane are two spatial dimensions, with the total absorption along the third dimension on the vertical axis. After switching off the trap the gas cloud can expand enough to take an absorption image. The leftmost picture shows an uncondensed cloud, with a temperature just above the transition point, which is at about $2\mu K$. The middle picture shows a cloud just below the transition point and a condensate appears as a sharp peak in the middle, surrounded by a thermal cloud of uncondensed atoms. The rightmost picture shows a cloud cooled far below the transition temperature and nearly all atoms have condensed into the ground state, leaving a sharp peak. All pictures are about 1 mm across. Picture taken from [33].*

wavefunction can even be observed optically, providing a unique magnifying glass onto the quantum world. Finally, a BEC is also a system that is easily controlled by lasers and magnetic fields, providing a very attractive testing ground for researching fundamental physics.

1.2. Experimental realisation

Although initially predicted in 1924, it took more than 70 years before the first true experimental realization of Bose-Einstein condensation. The main difficulty faced by experimentators lies with the incredibly low temperatures needed to obtain Bose-Einstein condensation.

In a simplified quantum description atoms are represented by wave packets with a spatial extension given by the de Broglie wavelength

$$\lambda_B = \sqrt{\frac{2\pi\hbar^2}{mk_BT}}, \tag{1.2}$$

where m is the particle mass and h $(= 2\pi\hbar)$ is Planck's constant. For high temperatures, the de Broglie wavelength becomes very small and the particles can be regarded as classical point masses, whereas for low temperatures the particles behave much more like waves. When Bose-Einstein condensation occurs the particles' wavepackets overlap, or in other words, the de Broglie wavelength becomes equal to the mean atomic separation. Using n to denote the

density of the atoms, we thus obtain

$$\lambda_B = n^{-\frac{1}{3}}. \tag{1.3}$$

Using the definition of λ_B (1.2) in (1.3) we obtain a rough estimate for the transition temperature T_c at which BEC occurs,

$$T_c = \frac{2\pi\hbar^2 n^{\frac{2}{3}}}{mk_B}. \tag{1.4}$$

To satisfy criterion (1.3) and obtain BEC in a gas, the experimenter could try to either lower the temperature or increase the particle density. However, at low temperatures gases tend to liquify or solidify, and hence the gas actually needs to be very dilute instead. Typically, particle densities of $10^{13} - 10^{15} cm^{-3}$ are needed. At such low densities, three-body collisions are rare, and the rate at which atoms clump together and form liquids or solids is so slow that metastable states can be achieved with lifetimes of seconds or even minutes, long enough for experiments to be conducted.

However, the critical temperature at these densities becomes of the order of μK, or even nK above absolute zero temperature. To cool a gas so far down is no simple task, and when BEC was finally achieved by the group of Cornell and Wieman in 1995 [4] and by the group of Ketterle shortly afterwards [27], they were rewarded with the 1997 Nobel Prize in physics for their efforts. These first realisations of a BEC were achieved using a combination of laser cooling and evaporative cooling.

Laser cooling is a technique where a laser is slightly detuned below an electronic transition of the atoms to be cooled. When an atom moves towards the laser, the frequency of the laser experienced by the atom changes due to the Doppler effect, and when the natural linewidth of the laser overlaps with the transition the atom will absorb a photon. This photon is then re-emitted shortly afterwards, in a random direction and due to the conservation of momentum the atom will see a net decrease in its velocity in the direction of the laser. The detuning ensures that only atoms with a velocity component towards the laser are selected, and by setting up lasers along all three cartesian axes, a net cooling of the gas can be achieved. Using this technique, atoms can only be cooled down to the so-called recoil temperature, which is the temperature associated with the velocity of an atom initially at rest that has emitted a single photon.

The next and final step in cooling the trapped gas is evaporative cooling. In this technique, the atoms with the highest energies are removed from the trap. The remaining atoms then rethermalize to a lower temperature. By repeating this process, the ultra-low temperatures necessary for BEC can be achieved.

For a more extensive treatment of various cooling schemes, see [92].

1.3. Superfluidity and vortices

Superfluidity is a state of matter in which it behaves as liquid having zero viscosity, that is, it can flow at low velocities without dissipating energy. A Bose-Einstein condensate is in such a state, which makes it an interesting subject to study. Superfluids are also found in

superconducting metals where the electrons form a superfluid, or in liquid Helium. In fact, in the case of superconductivity the fermionic electrons form pairs (Cooper pairs) that can be regarded as bosons, and as such they can undergo Bose-Einstein condensation [7, 75].

There are a number of phenomena that are observed for superfluids which are all intimately connected to the zero viscosity, see for example [119], and in fact the occurrence of one or more of these phenomena is often taken as a definition of superfluidity. One of the most interesting of these phenomena is the response of a superfluid to rotation.

When an ordinary liquid is placed in a rotating container, it will (after a short period of time) co-rotate with the container. Its velocity field $\mathbf{v}$ at position $\mathbf{r}$ will assume the simple form

$$\mathbf{v} = \mathbf{\Omega} \times \mathbf{r} = \Omega r \hat{e}_\theta,$$

where $\mathbf{\Omega}$ is the rotation vector of the container, and $\hat{e}_\theta$ the unit vector tangential to the rotation. The rotation $\nabla \times \mathbf{v}$ of the fluid will be uniform, since

$$\nabla \times \mathbf{v} = \nabla \times (\mathbf{\Omega} \times \mathbf{r}) = 2\mathbf{\Omega}$$

everywhere in the fluid. However, as we will see (section 1.6), a superfluid is irrotational: $\nabla \times \mathbf{v} = 0$ has to hold. It cannot simply rotate as the classical fluid would, but it will form vortices instead. Vortices have a singular velocity field of the form

$$\mathbf{v} = \frac{\hbar}{m}\frac{s}{r}\hat{e}_\theta,$$

where m is the mass of the atoms and s is the vortex winding number, which is an integer, making the velocity field quantized. To escape the singularity at $r = 0$ the fluid density must go to zero there. The irrotationality constraint is satisfied everywhere, except at $r = 0$:

$$\nabla \times \mathbf{v} = \frac{s\hbar}{m}\frac{\delta(r)}{r}\hat{e}_\theta,$$

such that the vortices store a single 'unit' of rotation in their cores. In rotating traps, superfluids form a regular lattice of $s = 1$ vortices, such that the spatial average rotation is equal to 2Ω and hence 'mimic' uniform rotation [107]. Such vortex lattices can, and have been, observed optically, see figure 1.2.

The peculiar response of a superfluid to rotation tells us a lot about the underlying fundamental physics. For instance, dipolar interactions between atoms influence the structure of the vortex lattice [71]. Additionally, quantized vortices or analogous structures are found in various other systems, such as liquid crystals, non-linear optical systems and superconducters [108]. The regime of very fast rotating BECs currently receives theoretical and experimental interest, since in this area exotic phenomena such as vortex melting and the bosonic quantum Hall effect can occur [57].

In chapter 4 we will have a closer look at vortex states in general, and investigate the effect of long range dipolar interactions on them.

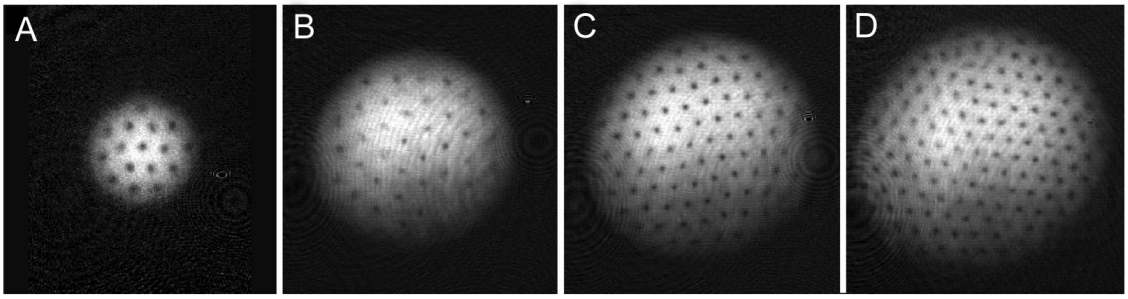

Figure 1.2.: *Experimentally observed vortex lattices in a BEC of Na-atoms, with approximately (A) 16, (B) 32, (C) 80, and (D) 130 vortices, crystallised in triangular lattices. Picture taken from [1].*

1.4. Gross-Pitaevskii equation

In this section we will derive an equation governing the dynamics of the BEC. At first, one could think that this is an easy task. The single particle eigenstates of the trapping potential can in principle be found, and since all particles condense in the ground state, a naive guess for the condensate wave function could be a simple product of the single particle wave functions in the eigenstates of the potential. However, in reality the particles *interact* and thus alter the eigenstates of the system. Finding the single particle eigenstates of an interacting system is a very difficult task. However, we are only interested in the ground state of this system, and since this state is macroscopically occupied this will allow us to make some approximations and derive a nonlinear Schrödinger equation describing the dynamics of this ground state.

In order to find this equation for the ground state, we first need to start with all eigenstates of the system of interacting particles, and we will make use of a special formalism called second quantisation.

1.4.1. Second Quantisation

Suppose we have a complete set of eigenstates $|K_i\rangle$ and eigenvalues K_i, $i = 0, 1, 2\ldots$, of some operator[1] $\hat{K}$, such that $\hat{K}\,|K_i\rangle = K_i\,|K_i\rangle$. For a many-body system we can then define the occupation-number-state

$$|n_0, n_1, n_2, \ldots\rangle$$

as the state with n_0 particles in the ground state $|K_0\rangle$, n_1 particles in the first excited state $|K_1\rangle$, and in general n_i particles in the i^{th} state $|K_i\rangle$. We can then define the creation and annihilation operators $\hat{a}_i^\dagger$ and $\hat{a}_i$ that create or destroy a particle in the i^{th} state, such that

$$\hat{a}_i^\dagger\,|n_0, n_1, \ldots, n_i - 1, \ldots\rangle = \sqrt{n_i - 1}\,|n_0, n_1, \ldots, n_i, \ldots\rangle \tag{1.5}$$

$$\hat{a}_i\,|n_0, n_1, \ldots, n_i, \ldots\rangle = \sqrt{n_i}\,|n_0, n_1, \ldots, n_i - 1, \ldots\rangle\,. \tag{1.6}$$

[1] Operators shall be marked with a hat '^'

For Bosons, these operators satisfy the following commutation relations

$$\begin{aligned} \hat{a}_i^\dagger \hat{a}_j^\dagger - \hat{a}_j^\dagger \hat{a}_i^\dagger &= 0 \\ \hat{a}_i \hat{a}_j - \hat{a}_j \hat{a}_i &= 0 \\ \hat{a}_i \hat{a}_j^\dagger - \hat{a}_j^\dagger \hat{a}_i &= \delta_{ij} \end{aligned} \tag{1.7}$$

A derivation of the proportionality constants on the right hand sides in equations (1.5) and (1.6), along with the commutation relations (1.7), can be found for instance in [91]. From these equations the number operator

$$\hat{N}_i = \hat{a}_i^\dagger \hat{a}_i \tag{1.8}$$

can be defined as the operator that counts the number of particles in the i^{th} state. Of course, we can repeat the above definition for a different set of eigenstates $|L_q\rangle$ and eigenvalues L_q, $q = 0, 1, 2, \ldots$, of some other operator $\hat{L}$. Denoting the associated creation and annihilation operators by $\hat{b}_q^\dagger, \hat{b}_q$, we can express the $\hat{a}_i^\dagger, \hat{a}_i$ operators as

$$\hat{a}_i^\dagger = \sum_q \hat{b}_q^\dagger \langle L_q | K_i \rangle \tag{1.9}$$

$$\hat{a}_i = \sum_q \hat{b}_q \langle L_q | K_i \rangle^*, \tag{1.10}$$

where the latter equality is simply the hermitian adjoint of the first. We can now construct operators that measure the value of dynamical variables of a many body system of identical particles, such as the kinetic energy. The additive one particle quantity K is measured by the operator

$$\hat{\mathcal{K}} = \sum_i K_i \hat{N}_i = \sum_i K_i \hat{a}_i^\dagger \hat{a}_i,$$

whereas a general two particle operator, such as interaction energy, can be constructed as

$$\begin{aligned} \hat{\mathcal{U}} = \frac{1}{2} \sum_{i \neq j} \hat{N}_i \hat{N}_j U_{ij} + \frac{1}{2} \sum_i \hat{N}_i (\hat{N}_i - 1) U_{ii} &= \frac{1}{2} \sum_{i,j} (\hat{N}_i \hat{N}_j - \hat{N}_i \delta_{ij}) U_{ij} \\ &= \frac{1}{2} \sum_{i,j} \hat{a}_i^\dagger \hat{a}_j^\dagger \hat{a}_j \hat{a}_i U_{ij}, \end{aligned}$$

where the real quantities $U_{ij} = U_{ji}$ denote the contribution of the interaction of a pair of particles in the i^{th} and j^{th} state. To obtain the last equality the commutation rules (1.7) are used. In a dilute gas only two-body interactions will be relevant, as three-body interactions and higher will be extremely rare. We therefore now have all the necessary ingredients to construct the Hamiltonian operator $\hat{\mathcal{H}} = \hat{\mathcal{K}} + \hat{\mathcal{U}}$ for a dilute gas of identical particles, by taking for the quantity $\hat{\mathcal{K}}$ the kinetic plus potential energy, and letting $\hat{\mathcal{U}}$ describe the interactions. Using equations (1.9) and (1.10) we write it in its most general form, such that

$$\hat{\mathcal{H}} = \sum_{m,n} \hat{b}_m^\dagger \hat{b}_n^\dagger \langle L_m | K | L_n \rangle + \frac{1}{2} \sum_{q,r,s,t} \hat{b}_q^\dagger \hat{b}_r^\dagger \hat{b}_s \hat{b}_t \langle qr | U | ts \rangle \tag{1.11}$$

with the two-particle matrix element

$$\langle qr | U | ts \rangle = \sum_{i,j} \langle L_q | K_i \rangle \langle K_i | L_t \rangle \langle L_r | K_j \rangle \langle K_j | L_s \rangle U_{ij}$$

which can be interpreted as the contribution of the interaction of two particles in the states $|L_t\rangle$ and $|L_s\rangle$, resulting in a pair of particles in the states $|L_q\rangle$ and $|L_r\rangle$ (respectively) after the interaction.

Instead of a discrete base, we can also use the eigenfunctions and eigenvalues of an operator with a continuous spectrum, such as the position operator. With the intention of passing on to the continuum limit, we first partition all space in finite cells, centered at position $\mathbf{r}$ with volume $\mathrm{d}V = dr \times dr \times dr$, where dr is some finite length. The one-particle state where the particle is in cell $\mathbf{r}$ is denoted simply by $|\mathbf{r}\rangle$. Clearly,

$$\langle \mathbf{r} | \mathbf{r}' \rangle = \delta_{rr'}. \tag{1.12}$$

The operators that create (annihilate) a particle in cell $\mathbf{r}$ are denoted by $\hat{\psi}^\dagger(\mathbf{r})$ ($\hat{\psi}(\mathbf{r})$), for which the commutation rules (1.7) still hold, with $\mathbf{r}$ taking over the role of the discrete index i. Using equations (1.9) and (1.10) we can transform between the two bases, where the matrix element $\langle \mathbf{r} | K_i \rangle$ will appear in the process. In the continuum limit, this quantity can be identified with the Schrödinger wave function $\varphi_i(\mathbf{r})$ of the i^{th} single-particle state, such that

$$\hat{a}_i = \lim_{dr \to 0} \sum_{\mathbf{r}} \hat{\psi}(\mathbf{r}) \langle \mathbf{r} | K_i \rangle^* = \int \hat{\psi}(\mathbf{r}) \varphi_i(\mathbf{r}) \mathrm{d}^3 r \tag{1.13}$$

$$\hat{\psi}(\mathbf{r}) = \lim_{dr \to 0} \sum_{i} \hat{a}_i \langle \mathbf{r} | K_i \rangle = \sum_i \hat{a}_i \varphi_i(\mathbf{r}). \tag{1.14}$$

The relation (1.12) transforms into

$$\langle \mathbf{r} | \mathbf{r}' \rangle = \delta(\mathbf{r} - \mathbf{r}'),$$

and the particle creation and annihilation operators satisfy the commutation relations

$$\begin{aligned} \hat{\psi}(\mathbf{r}) \hat{\psi}(\mathbf{r}') - \hat{\psi}(\mathbf{r}') \hat{\psi}(\mathbf{r}) &= 0 \\ \hat{\psi}^\dagger(\mathbf{r}) \hat{\psi}^\dagger(\mathbf{r}') - \hat{\psi}^\dagger(\mathbf{r}') \hat{\psi}^\dagger(\mathbf{r}) &= 0 \\ \hat{\psi}(\mathbf{r}) \hat{\psi}^\dagger(\mathbf{r}') - \hat{\psi}^\dagger(\mathbf{r}') \hat{\psi}(\mathbf{r}) &= \delta(\mathbf{r} - \mathbf{r}'). \end{aligned} \tag{1.15}$$

Using the coordinate representation in equation (1.11) by taking $\hat{\psi}^\dagger(\mathbf{r}), \hat{\psi}(\mathbf{r})$ for the operators $\hat{b}_q^\dagger, \hat{b}_q$ and passing to the continuum limit we find for the Hamiltonian of our dilute many particle system

$$\hat{\mathcal{H}} = \iint \hat{\psi}^\dagger(\mathbf{r}')\langle \mathbf{r}'|K|\mathbf{r}''\rangle\hat{\psi}(\mathbf{r}'')\mathrm{d}^3\mathbf{r}'\mathrm{d}\mathbf{r}''$$
$$+\frac{1}{2}\iiiint \hat{\psi}^\dagger(\mathbf{r}')\hat{\psi}^\dagger(\mathbf{r}'')\hat{\psi}(\mathbf{r}''')\hat{\psi}(\mathbf{r}'''')\langle \mathbf{r}'\mathbf{r}''|U|\mathbf{r}''''\mathbf{r}'''\rangle\mathrm{d}^3\mathbf{r}'\mathrm{d}\mathbf{r}''\mathrm{d}\mathbf{r}'''\mathrm{d}\mathbf{r}'''' \tag{1.16}$$

The operator K that measures the single particle kinetic- and potential energy is a local operator, such that its matrix elements can be written as[2]

$$\langle \mathbf{r}'|K|\mathbf{r}''\rangle = \left(-\frac{\hbar^2}{2m}(\nabla')^2 + V(\mathbf{r}')\right)\delta(\mathbf{r}'-\mathbf{r}''),$$

where $V(\mathbf{r}')$ is the external trapping potential. Similarly, the interaction energy between particles can also be taken to be local,

$$\langle \mathbf{r}'\mathbf{r}''|U|\mathbf{r}''''\mathbf{r}'''\rangle = U(\mathbf{r}',\mathbf{r}'')\delta(\mathbf{r}'-\mathbf{r}'''')\delta(\mathbf{r}''-\mathbf{r}'''). \tag{1.17}$$

Note that the locality here applies to each particle individually, the interaction only depends on the positions of the particles, and the interaction potential is diagonal in the coordinates of the individual particles. Nonlocal interactions are not diagonal and involve particle displacements[3].

The formalism developed in this section is called second quantisation. In the next subsection we will use it to derive an equation governing the dynamics of the BEC.

1.4.2. The BEC wave function

In this section the single particle eigenstates associated with the creation and annihilation operators $\hat{a}_i^\dagger$ and $\hat{a}_i$ are taken to be those of an interacting system. We do not know yet what these states are, in fact finding one of them (the ground state) is the objective of this section. Nevertheless, they can still be treated as if they are known[4], and we will expect to find a self consistent equation for them.

BEC occurs when one of the single-particle states becomes macroscopically occupied, usually this is the ground state. Let the number of particles occupying the ground state of the interacting system be denoted by N_0, which is of the order of magnitude of the total number of particles $N \gg 1$. The expectation value of the number operator $\hat{a}_i^\dagger\hat{a}_i$ is given by $\langle \hat{a}_i^\dagger\hat{a}_i\rangle = n_i$. We therefore have for the ground state that $\langle \hat{a}_0^\dagger\hat{a}_0\rangle = N_0 = \mathcal{O}(N)$, whereas for the other states

[2] The matrix elements of an operator $H_0(\hat{r},\hat{p})$, composed of position- and momentum operators $\hat{r},\hat{p}$ in the coordinate representation, are diagonal and of the form $\langle \mathbf{r}'|H_0(\hat{r},\hat{p})|\mathbf{r}''\rangle = H_0(\mathbf{r}', \frac{\hbar}{\mathrm{i}}\nabla')\delta(\mathbf{r}'-\mathbf{r}'')$, see for instance [91], ch. 14, sec. 7.

[3] A situation where such a nonlocal interaction occurs could be a system where two particles form a pair with a finite lifetime during the interaction, and as a pair they experience a different external potential than the individual particles would (for example due to a changed dipole moment). After the pair breaks up, the particles re-appear at different places than at the start of the interaction. The intermediate pair state is treated as a 'black box' and the interaction potential becomes nonlocal, it displaces the particles and the interaction potential is not diagonal.

[4] For the interested reader, reference [109], chapter 2, has a proper definition of these eigenstates, but such a definition is not necessary here.

$\langle \hat{a}_i^\dagger \hat{a}_i \rangle = \mathcal{O}(1)$. However, for all single particle states i the commutator $[\hat{a}_i^\dagger, \hat{a}_i] = 1$, so for the ground state

$$\langle \hat{a}_0^\dagger \hat{a}_0 \rangle = N_0 \simeq N_0 + 1 = \langle \hat{a}_0 \hat{a}_0^\dagger \rangle.$$

This means that up to $\mathcal{O}(N_0^{-1})$ we can neglect the noncommutativity of $\hat{a}_0^\dagger$ and $\hat{a}_0$. The operators $\hat{a}_0^\dagger, \hat{a}_0$ can then be replaced by the (complex) number $\sqrt{N_0}$, an approximation first made by Bogoliubov in 1947 [12]. Physically, this substitution says that the effect of removing or adding a single particle to the condensate should not affect the macroscopic properties of the entire system. Separating the ground state component of the field operator in equation (1.14) from the other states,

$$\hat{\psi}(\mathbf{r}) = \varphi_0(\mathbf{r})\hat{a}_0 + \sum_{i \neq 0} \varphi_i(\mathbf{r})\hat{a}_i$$

and inserting the Bogoliubov approximation $\hat{a}_0 \to \sqrt{N_0}$ we can write

$$\hat{\psi}(\mathbf{r}) = \Psi_0(\mathbf{r}) + \delta\hat{\Psi} \tag{1.18}$$

where we have defined $\Psi_0(\mathbf{r}) = \varphi_0(\mathbf{r})\sqrt{N_0}$ as the condensate wave function, and the noncondensate term $\delta\hat{\Psi} = \sum_{i \neq 0} \varphi_i(\mathbf{r})\hat{a}_i$.

In the case of a dilute gas in the limit of zero temperature, we can neglect the non-condensate term and approximate the operator $\hat{\psi}(\mathbf{r})$ by the complex valued field $\Psi_0(\mathbf{r})$. The condensate can then be viewed as a single matter-wave, as opposed to a microscopic description of particles. This is analogous to the case of electrodynamics, where the microscopic photon picture is abandoned in favour of a classical field picture of electric and magnetic fields.

In order to find the dynamics of the condensate then, we need to look at the time evolution of the field operator $\hat{\psi}(\mathbf{r})$. Given the Hamiltonian operator of (1.16), the time evolution of $\hat{\psi}(\mathbf{r})$ is given by the Heisenberg equation[5]

$$\mathrm{i}\hbar \frac{\partial \hat{\psi}(\mathbf{r})}{\partial t} = \left[\hat{\psi}(\mathbf{r}), \hat{\mathcal{H}}\right],$$

which, after using the commutation relations (1.15), results in

$$\mathrm{i}\hbar \frac{\partial \hat{\psi}(\mathbf{r})}{\partial t} = \mathcal{H}_0 \hat{\psi}(\mathbf{r}) + \int \hat{\psi}^\dagger(\mathbf{r}') U(\mathbf{r}, \mathbf{r}') \hat{\psi}(\mathbf{r}') \mathrm{d}^3\mathbf{r}' \hat{\psi}(\mathbf{r}), \tag{1.19}$$

with

$$\mathcal{H}_0 = -\frac{\hbar^2}{2m}\nabla^2 + V(\mathbf{r}).$$

Until now the two-particle interaction potential U has been left unspecified. Typically, $U(\mathbf{r}, \mathbf{r}') = U(\mathbf{r} - \mathbf{r}')$ is a complicated function of the distance between the two interacting atoms, and in fact it is usually not known precisely while small errors in its representation

[5] See for instance [91], Ch. 15, sec. 7.

can have large consequences [111]. Moreover, the true potential would support bound states which would lead to a solid ground state. Indeed, the Bose-Einstein condensate is in a metastable state. While in this state the BEC is a dilute gas (see Sec. 1.2), in which the average interatomic distances are much larger than the range of the interaction potential. When considering an interaction event, we are only interested in how the atoms emerge from the interaction. Therefore, the true potential is replaced with an *effective* interaction potential which posesses the same scattering properties as the original potential. In practice, a zero-range contact potential of the form

$$U(\mathbf{r}-\mathbf{r}') = g\delta(\mathbf{r}-\mathbf{r}') \tag{1.20}$$

is used. The interaction strength is characterised by the parameter

$$g = \frac{4\pi\hbar^2 a}{m}, \tag{1.21}$$

where a is the so-called *s-wave scattering length*. The sign of a determines whether the interactions are repulsive $(+)$ or attractrive $(-)$. In this work we will assume $g > 0$, unless explicitly stated otherwise. When expanding the incoming and outgoing particles in a scattering event in Legendre polynomials labeled by some index l, it turns out that for ultracold gases only the lowest energy $l = 0$ wave is relevant. Historically, this wave is called the s-wave, similar to the labeling of the electron shells of an atom. For this reason, the contact interactions are often referred to as *s-wave interactions*. The $l = 0$ wave is spherically symmetric, and the only effect of the scattering process is a phase shift between incoming and outgoing waves, the magnitude of this shift is exactly a. The contact potential (1.20) has exactly this scattering property, and as stated before, the detailed dynamics within the interaction potential range are not important. A more detailed account of the partial wave expansion in Legendre polynomials can for instance be found in [91, 22], and this theory applied to BEC's in particular and the derivation of the effective potential (1.20) can be found in [109, 107].

Inserting the contact potential (1.20) in the equation of motion for the field operator (1.19) and applying the Bogoliubov approximation $\hat{\psi}(\mathbf{r}) \to \Psi_0(\mathbf{r})$ (1.18) we finally arrive at the celebrated Gross-Pitaevskii equation

$$i\hbar\frac{\partial\Psi(\mathbf{r},t)}{\partial t} = \left[-\frac{\hbar^2}{2m}\nabla^2 + V(\mathbf{r}) + g|\Psi(\mathbf{r},t)|^2\right]\Psi(\mathbf{r},t), \tag{1.22}$$

describing the time evolution of the *condensate wave function*. This equation was independently derived by E.P. Gross and L.P. Pitaevskii [49, 110]. It has the intuitively clear form of a nonlinear Schrödinger equation, with an additional potential proportional to the local atomic density. The Gross Pitaevskii equation is used to describe macroscopic behavior of the BEC, at length scales larger than the interatomic separation distance. Its validity depends on the ground state being macroscopically occupied, which is necessary for making the Bogoliubov approximation, and the interatomic distances being much larger than the interaction range such that a contact potential can be employed.

Next, we will look at stationary solutions. By writing

$$\Psi(\mathbf{r},t) = \psi(\mathbf{r})\mathrm{e}^{-\mathrm{i}\mu t/\hbar} \tag{1.23}$$

we obtain the time independent Gross Pitaevskii equation

$$\left[-\frac{\hbar^2}{2m}\nabla^2 + V(r) + g|\psi(r)|^2\right]\psi(r) = \mu\psi(r) \tag{1.24}$$

for the stationary solution $\psi(\mathbf{r})$, where μ is the chemical potential. Often, this equation is also simply referred to as the Gross-Pitaevskii equation.

Alternatively, the Gross-Pitaevskii equation may be obtained by variational minimization of the condensate energy[6]

$$E[\psi] = \int \left[\frac{1}{2}\frac{\hbar^2}{2m}|\nabla\psi(\mathbf{r})|^2 + V(\mathbf{r})|\psi(\mathbf{r})|^2 + \frac{1}{2}g|\psi(\mathbf{r})|^4\right] d^3\mathbf{r}. \tag{1.25}$$

Variation is performed with respect to the complex conjugate of the wave function ψ^*, with a Lagrange multiplier μ to add the constraint that the number of particles N is conserved [107]. It can be shown that for $g > 0$ there is a unique ψ_0 for which $E[\psi_0]$ has a minimum, and that ψ_0 is at least once continuously differentiable and satisfies the time-independent Gross-Pitaevskii equation (1.24) in the sense of distributions [79]. Moreover, in the same reference it is shown that when the external potential $V \in \mathcal{C}^\infty$, then also $\psi_0 \in \mathcal{C}^\infty$, which will always be the case in this work.

The time-independent Gross-Pitaevskii is a second order semilinear differential equation, where semilinear means that it is linear in the highest order derivatives, but contains non-linear terms in the unknown itself. The equation admits generally complex solutions of the form

$$\psi(\mathbf{r}) = \sqrt{n(\mathbf{r})}\mathrm{e}^{\mathrm{i}\varphi(\mathbf{r})},$$

where the amplitude $\sqrt{n}$ and phase φ are both real. Gradients of the phase field $\varphi(\mathbf{r})$ are associated with stationary currents of the system, namely when we evaluate the probability current $\mathbf{j}$ [21], we find

$$\mathbf{j} = \frac{\hbar}{2m\mathrm{i}}\left(\Psi^*\nabla\Psi - \Psi\nabla\Psi^*\right) = n\mathbf{v}, \tag{1.26}$$

where we have written

$$\mathbf{v} = \frac{\hbar}{m}\nabla\varphi.$$

This result should be compared with the particle current of a classical velocity field, which is also exactly of the form $\mathbf{j} = n\mathbf{v}$. Clearly, when φ does not depend on position, there are no currents. Put the other way around, when there are no currents in the system, the wave function $\psi(\mathbf{r})$ satisfying the Gross-Pitaevskii equation (1.24) can be taken to be real. The

[6] Note that the condensate energy is not recovered when 'sandwiching' the Gross-Pitaevskii operator $\hat{H}_{GP}$ (the part between square brackets in eq. (1.22)) with the condensate wavefunction: $E \neq \int \Psi^* \hat{H}_{GP}\Psi$. This is due to the interactions in the system, and the fact that the 'wavefunction' Ψ is not a wavefunction in the strict sense. The mean field $\Psi(\mathbf{r})$ is *not* the many body wavefunction of the system, see for instance [109], p. 42, for a further discussion on this subject. Still, in this work we will out of convenience refer to $\Psi(\mathbf{r})$ simply as the 'wavefunction of the condensate'.

case that the phase φ is a nonzero constant can be viewed as a translation in time in equation (1.23).

As a final note in this section, it should be mentioned that non-linear Schrödinger equations also occur in various other physical systems. Notable examples occur in nonlinear optics [127], the description of water waves [139] and the assembly of RNA viruses [130], although these systems typically do not contain external, spatially varying, potential terms.

1.4.3. The healing length

There exists a particular length scale in Bose-Einstein condensates which we shall encounter in various places in this work. As such, it deserves its own special subsection in this introduction. This length scale is the *healing length*, defined as

$$\xi = \frac{\hbar}{\sqrt{mn_0 g}}, \tag{1.27}$$

where n_0 is a typical density of the system. Clearly, the healing length becomes smaller when the density of the system becomes higher. The healing length is the length scale over which a condensate, subjected to a local perturbation, returns to its 'normal' background density. For instance, consider a uniform BEC with a hard wall placed at $x = 0$, such that for $x \leq 0$ the potential is infinite and the condensate density must be zero. For $x > 0$, the potential is zero and the condensate wave function $\psi(\mathbf{r})$ must satisy the Gross-Pitaevskii equation

$$-\frac{\hbar^2}{2m}\frac{\mathrm{d}^2\psi}{\mathrm{d}x^2} + g|\psi|^2\psi = \mu\psi, \tag{1.28}$$

where the chemical potential is equal to $\mu = g|\psi_0|^2$ [107], with $|\psi_0|^2 = n_0^2$ the condensate density far away from the wall. In this situation we expect there to be no stationary currents in the lowest energy state, and we can take ψ to be real-valued. Equation (1.28) then turns into

$$\frac{\hbar^2}{2m}\frac{\mathrm{d}^2\psi}{\mathrm{d}x^2} = -g(n_0 - \psi^2)\psi,$$

with boundary conditions: $\psi(0) = 0, \psi(\infty) = \sqrt{n_0}$. This can be analytically solved yielding [107]

$$\psi(x) = \sqrt{n_0}\tanh\left(\frac{x}{\xi}\right)$$

with ξ the healing length, defined in equation (1.27). Here, ψ rises from 0 to $3/4\sqrt{n_0}$ in approximately one healing length, illustrating its role as the length scale at which the condensate responds to local perturbations.

1.5. BEC in a harmonic trap, and the Thomas-Fermi approximation

In this work we will be concerned with BEC's of atoms with a large magnetic dipole moment in a harmonic trap. In this section we will first investigate the simpler system without dipolar interactions obscuring some of the basic physics. In the next section we will introduce the dipolar interactions and explore their consequences compared to the nondipolar case.

The harmonic trapping potential V is specified as

$$V(\mathbf{r}) = \frac{1}{2}m\left[\omega_x^2 x^2 + \omega_y^2 y^2 + \omega_z^2 z^2\right], \tag{1.29}$$

where the frequencies $\omega_x, \omega_y, \omega_z$ characterizes the mean trapping strength in the xy-plane. In both theoretical and experimental work the harmonic trap is the most commonly used potential.

For large condensates in such a trap with many particles, the kinetic energy term (∇^2) in the time independent Gross-Pitaevskii equation (1.24) becomes small with respect to the interaction term $g|\Psi|^2$, see Appendix A.1. In appropriately scaled units, the Gross-Pitaevskii equation becomes of the form

$$-\frac{1}{2}\epsilon^2\nabla^2\psi(\mathbf{r}) + \left[V(\mathbf{r}) - 1 + |\psi^2|\right]\psi(\mathbf{r}) = 0, \tag{1.30}$$

with $\epsilon \ll 1$ a small parameter. The famous *Thomas-Fermi approximation* then consists of neglecting the kinetic energy term [107], turning the time independent Gross-Pitaevskii equation into

$$|\psi(\mathbf{r})|^2 = \frac{\mu - V(\mathbf{r})}{g}. \tag{1.31}$$

The condensate density $|\psi|^2$ assumes a parabolic density profile, or more generally its shape is an inverted potential V. In this notation also the role of μ controlling the number of particles becomes immediately clear. This density profile is sketched in figure 1.3. In the same figure an ideal condensate density without interactions is depicted, having a gaussian profile. Both densities represent the same number of atoms, enabling us to see the influence of the interactions.

The gaussian density profile (no interactions) has a peak in the centre of the condensate, as the potential is the lowest there. The spread of the wave function is solely caused by the kinetic energy of the particles, and tails off when going further away from the centre of the trap. The parabolic density profile (with repulsive interactions) also has a peak in the centre, however it is much flatter than the gaussian density. The mean repulsive particle interactions are proportional to the density, and in the centre of the condensate the interactions are highest. Hence, the particles tend to get pushed away more from the centre, resulting in a flatter profile and a lower peak density.

As a final note, it is not *a priori* clear that in the Gross-Pitaevskii equation (1.30) the ϵ^2 term can be neglected. For instance, the ordinary Schrödinger equation for states with

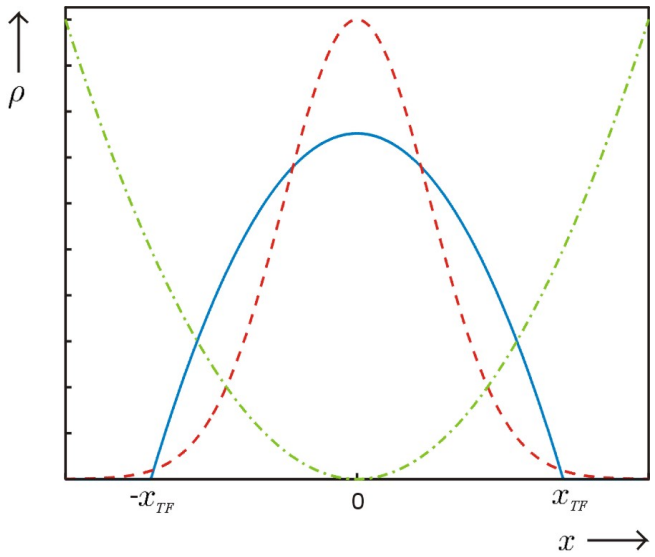

Figure 1.3.: *Shape of the density (arbitrary units) of a BEC in a harmonic trap potential (schematically indicated in green, dash-dotted). The solid blue line represents the density when repulsive interactions are present, the dashed red line the case without interactions. The repulsive ($g > 0$)interactions push the particles away from the highest density in the center of the trap, resulting in a less spiked density. The densities are both normalized to represent the same number of particles.*

a high energy can be brought in exactly the same form, only without the $|\psi|^2$ term, and solutions of this equation are known to be highly oscillatory. In this case, balance between the ϵ^2 term and the term between square brackets can only be achieved when the solution turns highly oscillatory. In the case of the Gross-Pitaevskii equation, the nonlinear $|\psi|^2$ term allows the term between square brackets individually to become small, canceling the need for highly oscillatory terms. In Appendix A.2 this scenario is explored further, and by constructing a consistent asymptotic approximation the legitimacy of initially neglecting the ϵ^2 term is confirmed. It is found that in the bulk of the condensate, the density profile is indeed parabolic, whereas far away from the center of the trap the density is Gaussian. These two regions are connected by a boundary layer of thickness proportional to $\epsilon^{2/3}$. Interestingly, inside this boundary layer the condensate wave function has to satisfy the Painlevé II equation, a canonical nonlinear differential equation defining a new class of transcendental functions. This equation is discussed in further detail in Appendix A.3.

1.6. Hydrodynamic equations

Starting from the Gross-Pitaevskii equation (1.22), which describes the time evolution of the complex-valued wavefunction Ψ, we will proceed to derive an equivalent set of equations that describes the phase and amplitude dynamics of Ψseparately. To obtain this result, we subsitute

$$\Psi = f e^{i\varphi}, \tag{1.32}$$

for the wave function of the condensate, where f and φ are strictly real, such that

$$\frac{\partial \Psi}{\partial t} = \left(\frac{\partial f}{\partial t} + i f \frac{\partial \varphi}{\partial t} \right) e^{i\varphi},$$

and

$$\nabla^2 \Psi = \left[\nabla^2 f - f(\nabla\varphi)^2 + i(2\nabla f \cdot \nabla\varphi + f\nabla^2\varphi) \right] e^{i\varphi}.$$

Substituting this in the Gross-Pitaevskii equation (1.22), and dividing by $e^{i\varphi}$, gives

$$-\hbar f \frac{\partial \varphi}{\partial t} + i\hbar \frac{\partial f}{\partial t} = -\frac{\hbar^2}{2m} \left(\nabla^2 f - f(\nabla\varphi)^2 \right) + V(\mathbf{r})\, f + g\, f^3 - i\frac{\hbar^2}{2m} \left(\nabla f \cdot \nabla\varphi + \frac{1}{2} f \nabla^2 \varphi \right). \tag{1.33}$$

Upon noting that $V(\mathbf{r}), f$ and φ are all real quantities, we can split equation (1.33) into two equations for the real and imaginary parts, resulting in

$$\hbar \frac{\partial \nabla\varphi}{\partial t} = -\nabla \left(-\frac{\hbar^2}{2m} \left[\frac{1}{f} \nabla^2 f + (\nabla\varphi)^2 \right] + V(\mathbf{r}) + g\, f^2 \right) \tag{1.34}$$

for the real part, where we have taken the gradient of the entire expression, and

$$2\hbar f \frac{\partial f}{\partial t} = \hbar \frac{\partial f^2}{\partial t} = -\frac{\hbar^2}{2m} \left(2f \nabla f \cdot \nabla\varphi + f^2 \nabla^2 \varphi \right) \tag{1.35}$$

for the imaginary part, which we have multiplied by $2f$. The result of taking the gradient and the multiplication by $2f$ is that we can cleverly rewrite these two equations as

$$\frac{\partial n}{\partial t} = -\nabla \cdot (n\mathbf{v}), \tag{1.36}$$

and

$$m \frac{\partial \mathbf{v}}{\partial t} = -\nabla \left(\frac{1}{2} m \mathbf{v} \cdot \mathbf{v} + V(\mathbf{r}) + gn - \frac{\hbar^2}{2m} \frac{\nabla^2 \sqrt{n}}{\sqrt{n}} \right) \tag{1.37}$$

where we have interpreted f^2 as the particle density of the condensate n, and

$$\mathbf{v} = \frac{\hbar}{m} \nabla\varphi \tag{1.38}$$

as the velocity $\mathbf{v}$ of the condensate[7]. The equations (1.36) and (1.37) are commonly known as the *superfluid hydrodynamic equations* [107], since they closely resemble the equation of continuity and the equation of motion from standard fluid dynamics.

[7] See also equation (1.26), where a similar result was derived for stationary states. Here, the interpretation of the gradient of the phase turns out to hold also for the more general, time dependent situation.

The Thomas-Fermi approximation outlined in the previous section can also be extended to the time dependent case, see Appendix A.4. In the hydrodynamic equations then, the last term on the right hand side of equation (1.37), the so-called quantum pressure, is neglected for large condensates.

Unless the velocity potential $\frac{\hbar}{m}\varphi$ is singular, the velocity field $\mathbf{v}$ must be irrotational, as

$$\nabla \times \mathbf{v} = \frac{\hbar}{m}\nabla \times \nabla\varphi = 0. \tag{1.39}$$

Experimentally, this irrotationality manifests itself as a certain resistance of the superfluid to rotation. This is one of the hallmarks of a superfluid [62, 119]. When placed in a rotating bucket, the superfluid cannot co-rotate as a solid body with the bucket, as a classic fluid would. The only way the superfluid can rotate is by forming a phase singularity: a vortex, to be discussed in chapter 4.

1.7. Dipolar Interactions

In the previous sections the atoms only interacted through the isotropic, short range s-wave interactions. As simple as these interactions might seem, they already give rise to a very rich field of physics[8].

However, in this work we will be concerned with systems in which the particles have more complicated interactions, namely dipole-dipole interactions. In particular, we shall consider dipoles that are aligned along an external field, and we shall take the alignment axis to be the z-axis. The dipolar two-body interaction potential is well known and given by [63]

$$U_{dd}(\mathbf{r}) = \frac{C_{dd}}{4\pi}\frac{1-3\cos^2\theta}{r^3}, \tag{1.40}$$

for two dipoles separated by a vector $\mathbf{r}$, with $r = |\mathbf{r}|$, and θ the angle $\mathbf{r}$ makes with respect to the z-axis (illustrated in figure 1.4(a)). The interaction strength is characterised by the coupling constant C_{dd}, whose value is dependent on the type of dipoles. For electrical dipoles induced by a static electric field $\underline{E} = \hat{z}E$, the coupling constant $C_{dd} = E^2\alpha^2/\epsilon_0$ [135, 88], with α the static electric polarizability. Electric dipoles, such as polar molecules, have an interaction strength dependent on the external field and are therefore tunable in strength. Alternatively, if the atoms have permanent magnetic dipoles, d_m, one has $C_{dd} = \mu_0 d_m^2$ [45]. Currently, the only experimentally available condensed dipolar gas consists of Chromium atoms, which have an anomalously large permanent magnetic dipole moment [47]. In principle for such permanent magnetic dipoles we have that $C_{dd} > 0$, however there exists an experimental trick to tune the value of C_{dd} not only in size, but also the sign can be reversed [43].

The interaction energy (1.40) is anisotropic and long-range, in sharp contrast to the s-wave interactions. We shall first discuss the anisotropy. For $C_{dd} > 0$, two dipoles are repulsive when they are side-by-side, but they attract each other when they are aligned end-to-end (see figure 1.4(b)). In a trapped dipolar BEC it is therefore energetically more favourable for the

[8] See, for instance, reference [11] for a review of current research on ultracold quantum gases.

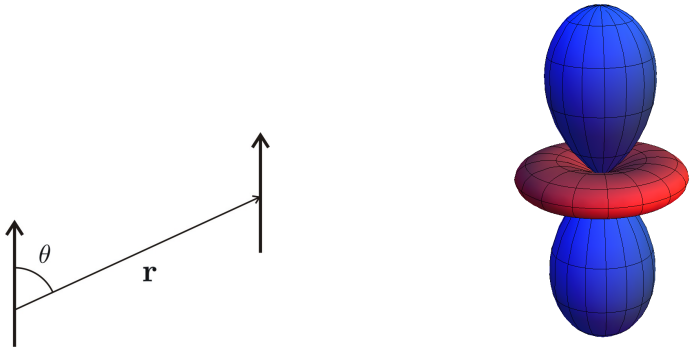

Figure 1.4.: *Left: schematic overview of the relevant variables for the dipolar interaction potential U_{dd}. Right: Equipotential surfaces for the anisotropic dipolar potential with $C_{dd} > 0$, where points on the blue surface have the same potential as those on the red surface, but with opposite sign (blue is negative and attractive, red is positive and repulsive). For $C_{dd} < 0$ the colors of the surfaces have swapped.*

dipoles to be aligned. Consequentially, the effect of the dipolar interactions is theoretically expected to elongate the condensate along the z-axis [136, 35], and indeed this has been observed experimentally in the Chromium BEC [125]. When the dipolar interactions are reversed ($C_{dd} < 0$), the situation is reversed and the effect of the dipolar interactions will be to make the condensate more oblate (pancake like). In chapter 2 we will theoretically investigate the shape of the dipolar BEC in more detail.

Another aspect of the anisotropy of the dipolar interactions is the possibility of a collapse of the condensate. When the dipolar interactions are strong enough, the attractive part can overcome any repulsive forces in the system (s-wave or kinetic) and cause the condensate to collapse. Indeed, such collapses and stabilisation thereof are observed in the Chromium BEC [69], and can lead to rich dynamics [104, 73, 78].

To discuss the long-range nature of the dipolar interactions we first need to define what exactly is meant by the term 'long-range'. Typically, interaction potentials are of the form $r^{-\alpha}$, where $\alpha \geq 0$. Now consider a single particle situated at $r = 0$ in a spherical volume with a radius R, and a uniform density ρ of some material which interacts with the particle through a $r^{-\alpha}$ potential. If we want to calculate the potential energy of the particle, we can perform the integral

$$\int \frac{\rho}{r^\alpha} \mathrm{d}V = \int_\epsilon^R 2\pi r^2 \frac{\rho}{r^\alpha} dr \propto \begin{cases} r^{3-\alpha}\big|_\epsilon^R, & (\alpha \neq 3) \\ \log R, & (\alpha = 3) \end{cases}$$

where we have omitted a small volume in the vicinity of the particle to avoid singularities. Physically, such an excluded volume is in practice almost always justified due to effects such as the Pauli exclusion principle and other short range forces that are neglected in the current description. When $\alpha > 3$, the above integral converges and hence if we want to calculate the energy of such a particle in an infinite uniform medium, it suffices to only include particles within some finite distance R: the interaction has a finite range. Clearly, when $\alpha \leq 3$ such a

range cannot be defined as the integral diverges for $R \to \infty$, and the interactions are said to be long-range. In general, an interaction of the form $r^{-\alpha}$ is termed long-range when $\alpha < d$, where d is the dimension of the system. The dipolar interactions have $\alpha = 3$ and are therefore a border-case.

One of the most important consequences of long-range interactions is that energy is no longer additive. Consider a box, with sides of length L and a volume $V = L^3$, filled with a continuous density ρ of particles interacting through some potential U, and with a total interaction energy E. Next, we divide the system in two separate volumes V_1 and V_2, such that there are two separate subsystems with energies E_1 and E_2. To calculate the energy of the system, we first define the quantity

$$E_{ij} = \int_{V_i} \rho(\mathbf{r}) \int_{V_j} \rho(\mathbf{r}') U(\mathbf{r} - \mathbf{r}') \mathrm{d}^3\mathbf{r}' \mathrm{d}^3 r,$$

with $i, j = 1, 2$, which is the energy associated with the interaction of subsystem i with subsystem j. We then have for the energy of the entire system that

$$E = E_{11} + E_{12} + E_{21} + E_{22}, \tag{1.41}$$

and for the two subsystems

$$E_1 = E_{11}, \qquad E_2 = E_{22}.$$

Clearly, $E \neq E_1 + E_2$ where the difference is equal to the interaction energies of one subsystem with the other, $E_{12} + E_{21}$. When the interactions have a finite range R, then the only significant contribution to E_{12} and E_{21} comes from the particles near the interface between the two systems. Therefore, the error made in approximating $E = E_1 + E_2$ is proportional to the surface area of the interface and is of order $\mathcal{O}(RL^2)$, whereas the total energy is proportional to the *volume* of the system and is of order $\mathcal{O}(L^3)$. In the thermodynamic limit, where the number of particles and system volume go to infinity such that $R \ll L$, the energy E of the system is approximately equal to $E_1 + E_2$. However, when the interactions are *long-range*, no such range R exists and the energy is not additive[9].

The non-additivity of the energy has important statistical mechanical consequences. For instance, it is possible that there is an inequivalence of ensembles, where the phase diagrams of the canonical and microcanonical ensemble are different [26, 48, 13]. Another consequence of non-additivity is the possibility of *negative specific heat*, where a system heats up as it loses energy [26, 54, 82].

Another property of long-range interactions is that all particles of a system contribute to the field acting on the particles, giving rise to a self consistent description of the dynamics, which are typically chaotic as well. Such dynamics are predicted to result in formation of localised density structures through instabilities [26, 48].

In the most recent decade, BEC theory and experiments have reached impressive quality and are becoming more and more attractive as a model system for various physical systems.

[9] Note that this does not necessarily mean that the energy is not extensive, it can still be possible that the energy is proportional to the number of constituents while keeping the intensive variables constant[26].

Long range interactions on the other hand provide a rich theoretical laboratory for statistical physics, and therefore Bose-Einstein condensates with dipolar interactions could become a key system to investigate them in. Already, several of the peculiar effects of long-range interactions have been found theoretically in dipolar BECs, such as new quantum phase transitions [6, 71], and the formation of localized structures near instabilities [104, 73, 78].

1.8. Dipolar Potential

Equation (1.40) of the previous section is the interaction energy of two classical dipoles. As in the case of the s-wave contact interactions, one might expect that an effective potential is needed to efficiently describe the interaction between two atoms. Surprisingly enough, the bare dipole-dipole interaction potential (1.40) works very well. For dipole moments of the order of one Bohr magneton and away from shape resonances it can be used directly [136], a result confirmed by a thorough calculation [30, 31], although this suggested a renormalization of the coupling constant C_{dd} [138].

The pseudo-interaction potential U of equation (1.20) may therefore be amended as follows to include the dipole-dipole interactions:

$$U(\mathbf{r}-\mathbf{r}') = g\delta(\mathbf{r}-\mathbf{r}') + U_{dd}(\mathbf{r}-\mathbf{r}'),$$

where $\mathbf{r}-\mathbf{r}'$ again denotes the separation vector of the two interacting atoms, and $U_{dd}(\mathbf{r}-\mathbf{r}')$ is the bare dipole-dipole interaction specified in equation (1.40). Substituting this result again in equation (1.19), and making the Bogoliubov approximation, the Gross-Pitaevskii equation becomes

$$i\hbar\frac{\partial\Psi(\mathbf{r},t)}{\partial t} = \left[-\frac{\hbar^2}{2m}\nabla^2 + V(\mathbf{r}) + g|\Psi(\mathbf{r},t)|^2 + \Phi_{dd}[n](\mathbf{r})\right]\Psi(\mathbf{r},t), \tag{1.42}$$

where

$$\Phi_{dd}[n](\mathbf{r}) = \int U_{dd}(\mathbf{r}-\mathbf{r}')n(\mathbf{r}')\mathrm{d}^3\mathbf{r}', \tag{1.43}$$

with $n = |\Psi(\mathbf{r},t)|^2$ the density of the condensate. Clearly, the potential Φ_{dd} is nonlocal since its value at a certain point $\mathbf{r}$ depends on the shape and density of the entire condensate, reflecting the long-range nature of the dipole-dipole interactions.

Since the short range, isotropic s-wave interactions are still present in the condensate, it makes sense to define the dipolar interaction strength relative to the s-wave interactions through the parameter [43]

$$\epsilon_{dd} = \frac{C_{dd}}{3g}.$$

The factor 3 is chosen such that a homogeneous dipolar gas with $g > 0$ and $C_{dd} > 0$ becomes susceptible to collapse exactly when $\epsilon_{dd} = 1$. For systems $\epsilon_{dd} > 1$ we can therefore say that the dipolar interactions dominate the s-wave interactions. For $C_{dd} < 0$ the critical value

is $\epsilon_{dd} = -\frac{1}{2}$. These critical values can be understood when one calculates the Bogoliubov excitation spectrum of the homogeneous gas [45]

$$E_B^2 = \left(\frac{p^2}{2m}\right)^2 + 2gn\left\{1 + \epsilon_{dd}\left(3\cos^2\theta - 1\right)\right\}\frac{p^2}{2m}.$$

Here, E_B is the energy associated with a plane wave perturbation (phonon) of the gas, with momentum p and θ is the angle between the wavevector of the phonon and the z-axis (the polarization axis of the dipoles). Excitations of the homogenous gas with momentum p then evolve in time as exp. Clearly, E_B is always real valued for $-\frac{1}{2} \leq \epsilon_{dd} \leq 1$, signifying that all excitations are stable. Outside this range, the energy can become complex and given the exponential time evolution the excitations grow in amplitude signifying an instability of the gas. It should be noted however, that in trapped gases such collapses can be stabilised by choosing the trap geometry such that the dipoles are predominantly repulsive.

The ^{52}Cr isotope used in the Chromium experiments typically has $\epsilon_{dd} \simeq 0.16$ [47], which is a relatively low value. However, through the use of Feshbach resonances [37, 38] the s-wave interaction strength can be tuned to arbitrary values and hence ϵ_{dd} can be varied arbitrarily also [69].

1.8.1. Electrostatic analogy

Using a clever trick, the dipolar potential can be rewritten in terms of an electrostatic potential. We start by writing down the interaction energy of two general dipoles $\mathbf{p}_1$, $\mathbf{p}_2$ [63]

$$U_{12}(\mathbf{r}) = \mu_0 \frac{\mathbf{p}_1 \cdot \mathbf{p}_2 - 3(\hat{r} \cdot \mathbf{p}_1)(\hat{r} \cdot \mathbf{p}_2)}{r^3},$$

where $\mathbf{r} = r\hat{r}$ is the vector separating the two dipoles and μ_0 is the permeability of free space. The dipolar interaction energy for aligned dipoles U_{dd} is regained by setting $\mathbf{p}_1 = \mathbf{p}_2 = d_m\hat{p}$, where $\hat{p}$ is a unit vector in the direction of alignment and d_m is the magnitude of the dipole moment. The dipolar interactions strength $C_{dd} = \mu_0 d_m^2$, such that we get

$$\begin{aligned} U_{dd}(\mathbf{r}) &= C_{dd}\sum_{i,j=1}^{3}\frac{\hat{p}_i\hat{p}_j\delta_{ij} - 3(\hat{r}_i\hat{p}_i)(\hat{r}_j\hat{p}_j)}{4\pi r^3} \\ &= C_{dd}\sum_{i,j=1}^{3}\hat{p}_i\left(\frac{\delta_{ij} - 3\hat{r}_i\hat{r}_j}{4\pi r^3}\right)\hat{p}_j \\ &= C_{dd}\hat{p}^T\mathbf{D}(\mathbf{r})\hat{p}, \end{aligned} \tag{1.44}$$

where we have defined the rank 2 tensor

$$[\mathbf{D}(\mathbf{r})]_{ij} = \left(\frac{\delta_{ij} - 3\hat{r}_i\hat{r}_j}{4\pi r^3}\right).$$

In a book by Craig and Thirunamachandran [25], it is carefully derived that $\mathbf{D}$ can be rewritten as

$$[\mathbf{D}(\mathbf{r})]_{ij} = -\nabla_i\nabla_j\frac{1}{4\pi r} - \frac{1}{3}\delta_{ij}\delta(\mathbf{r}).$$

Substituting this result back in (1.44), we can write the dipolar potential as

$$\Phi_{dd}[n](\mathbf{r}) = -C_{dd}\hat{p}_i\hat{p}_j\left(\nabla_i\nabla_j\phi[n](\mathbf{r}) + \frac{\delta_{ij}}{3}n(\mathbf{r})\right), \tag{1.45}$$

with

$$\phi[n](\mathbf{r}) = \frac{1}{4\pi}\int\frac{n(\mathbf{r}')}{|\mathbf{r}-\mathbf{r}'|}d^3\mathbf{r}'. \tag{1.46}$$

Apart from the prefactor, ϕ is exactly the electrostatic potential due to a 'charge' distribution n, or alternatively, the gravitational potential due to a 'mass' distribution[10] n. These potentials have been widely studied in the respective fields of electrostatics and astrophysics, and allows us to use the vast body of knowledge from these fields in calculating the dipolar potential. Once the 'electrostatic / gravitational' potential is known, the dipolar potential is easily calculated using equation (1.45). Indeed, in chapters 2 and 3 we exploit this analogy by using results from $19th$ century astrophysics to calculate the dipolar potential explicitly.

In this work in particular, the alignment axis of the dipoles is taken to be the z-axis, such that $\hat{p} = \hat{z}$, and we can simplify equation (1.45) to

$$\Phi_{dd}[n](\mathbf{r}) = -C_{dd}\left(\frac{\partial^2}{\partial z^2}\phi[n](\mathbf{r}) + \frac{n(\mathbf{r})}{3}\right). \tag{1.47}$$

The above equation also shows that the dipolar interaction potential can be decomposed into a local term proportional to the density n, and a long range part which is calculated using the electrostatic potential.

1.8.2. Linearity of the Dipolar potential

The dipolar potential Φ_{dd} has the important property that it is a linear functional of the density:

$$\Phi_{dd}[n_a + n_b](\mathbf{r}) = \Phi_{dd}[n_a](\mathbf{r}) + \Phi_{dd}[n_b](\mathbf{r}).$$

This means that given some complicated density distribution $n = n_a + n_b$, where n_a, n_b are density distributions of a simpler form, the calculation of the dipolar potential can be split into the calculation of the dipolar potential of the separate densities n_a, n_b and added together afterwards. For instance, in the case of a vortex in a uniform background density, the density can be split into the uniform background, and some negative 'density' distribution of the vortex core. Alternatively, the negative densities can be thought of as ordinary density distributions of dipoles of the opposite sign. Figure 1.5 illustrates this procedure for the vortex density. Throughout this work we shall frequently exploit the linearity of the dipolar potential to simplify calculations.

1.9. Outline and readers' guide

In this chapter we have given a short introduction into the field of Bose-Einstein condensation and some of the theoretical concepts that are needed in this project. The remainder of this report is now structured as follows.

[10] n is a number density, not a mass density, hence the quotation marks.

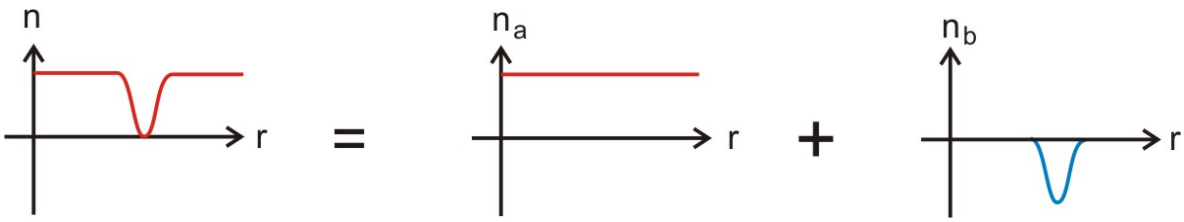

Figure 1.5.: *Schematic decomposition of a density with a vortex, n, into a uniform background density n_a and a negative vortex core density n_b. Since the dipolar potential is a linear functional of the density the potential of the vortex core n_b can be calculated separately from that of the background density, significantly simplifying the problem.*

Chapters 2 and 3 are the manuscripts of two papers, that are to be submitted to the journal Physical Review A. Therefore, these chapters are more or less self-contained and are geared towards a more specialist audience. Both chapters exclusively treat condensates in the Thomas-Fermi approximation. Chapter 2 details the stationary states of a trapped, dipolar BEC, and calculates the elementary excitation frequencies, with applications to possible collapses of the condensate. Chapter 3 investigates the stationary states of a dipolar BEC in a *rotating* harmonic trap, and maps out dynamical instabilities that can lead to vortex lattice formation.

The remaining chapters 4 and 5 are preliminary calculations investigating phenomena beyond the Thomas-Fermi approximation. Chapter 4 takes a closer look at vortices, and in particular at the effects of dipolar interactions on the structure of a single vortex core, and the dipolar interaction energy of two separate vortex cores. Chapter 5 investigates the response of a uniform condensate to an immersed impurity atom. These latter two chapters are not as thoroughly completed research projects as the previous two chapters, but can serve as a solid basis for further studies of the respective subjects.

As this turned out to be a fairly bulky report, there follows a rough readers' guide, geared towards different types of audiences that might want to focus on different parts of the report upon first reading.

For the general physicist audience: the calculations of chapter 5 are fairly dense, therefore these readers might want to skip through sections 5.2 and 5.3 of this chapter. Most of the remaining calculation details of the other chapters are conveniently moved to the appendices, their omittance should not interfere with the continuity of the main text.

The mathematically inclined reader might want to skip through chapters 2 and 3 upon first reading, and start immediately with chapter 4 and 5. Furthermore, he or she will find many of the calculations' details in the appendices, including those pertaining to the first two chapters.

A bird's eye overview of the mathematical aspects of this research would be as follows.

- Chapter 1, and appendix A: Scaling and perturbation analysis in relation to the Thomas-Fermi approximation. Also, in the perturbation analysis we will encounter the Painlevé II equation, which is highlighted in a dedicated section in appendix A.
- Chapter 2, and Appendices C to F: Determination of stability by energy analysis and

linearisation of hydrodynamic equations, involving calculation of dipole potential of heterogenous ellipsoids with polynomial densities.

- Chapter 3, and appendices E, F, and H: Similar linearisation of hydrodynamic equations, and perturbation analysis to determine the location of a bifurcation point in the phase diagram of stationary states in the rotating trap.
- Chapter 4, and appendices I to K: Numerical calculation of the ground state of a dipolar BEC containing a vortex in the center, involving Fourier and Hankel transforms for dealing with the dipolar potential, minimization of a nonlinear functional through the steepest descent method, and some scaling for making the equations suited for numerical calculations.
- Chapter 5: Integral asymptotics for large values of parameters appearing in exponential terms of the integrand, and appearing in the argument of a Bessel function. Some perturbation analysis.

2. Excitation frequencies: applications to collapse and rotating systems

The results presented in this chapter are obtained in collaboration with N. G. Parker, S. J. J. M. F. Kokkelmans, A. M. Martin and D. H. J. O'Dell. The manuscript as presented here will be submitted to the journal Physical Review A.

In this paper, we analyse the low-lying excitation frequencies and the static solutions of trapped Bose-Einstein condensates with dipolar atomic interactions. Working in the Thomas-Fermi limit we present a general and versatile methodology for deriving the static solutions and their excitation frequencies. We map out in detail the static solutions and the excitation modes in the experimentally relevant parameter spaces. In particular we show that the collapse of the condensate is consistently mediated by an anisotropic quadrupolar collective mode.

2.1. Introduction

Since the realization of dilute atomic Bose-Einstein condensates (BECs) in 1995 [4, 27, 28], there has been a surge of research interest in these quantum degenerate gases [107]. While they are typically dominated by s-wave atomic interactions, recent condensates have been formed with additional dipolar atomic interactions [47, 131, 8]. In contrast to short-range and isotropic s-wave interactions, dipolar interactions are long-range and anisotropic, and this introduces rich new phenomena. For example, experiments have revealed strong anisotropic effects such as the dipole-dependent expansion of the condensate [125, 72], d-wave collapse and explosion [73], and the enhanced stability to collapse in flattened geometries [69].

For particles with a dipole moment, separated by $\mathbf{r}$, the interaction potential can be represented by a pseudo-potential of the form [136, 64],

$$U(\mathbf{r}) = g\delta(\mathbf{r}) + \frac{C_{\rm dd}}{4\pi}\,\hat{\rm e}_i\hat{\rm e}_j\frac{(\delta_{ij} - 3\hat{r}_i\hat{r}_j)}{r^3}. \tag{2.1}$$

Here $g = 4\pi\hbar^2 a_{\rm s}/m$ characterises the s-wave interactions, where $a_{\rm s}$ is the s-wave scattering length and m is the atomic mass, and $C_{\rm dd}$ parameterises the strength of the dipolar interactions. An important quantity is the ratio of these coupling strengths, defined as [43],

$$\epsilon_{dd} = C_{\rm dd}/3g. \tag{2.2}$$

To date, dipolar condensates have been formed with magnetic dipolar interactions, characterised by $C_{\rm dd} = \mu_0 d^2$, where d is the magnetic dipole moment and μ_0 is the permeability of free space. [47, 131, 8]. While s-wave interactions still dominate at zero bias field (e.g., $\epsilon_{dd} \approx 0.16$ in the ^{52}Cr BEC experiments [47]), g can be tuned from positive to negative

and even to zero [69] by means of a Feshbach resonance [37, 38]. Furthermore, for magnetic dipoles the sign and amplitude of the effective value of $C_{\rm dd}$ can be tuned using fastly rotating magnetic fields [43]. Note that electric dipoles offer similar control over the coupling strength and ultra-cold gases featuring electric dipoles are now close to reaching degeneracy [32, 70, 99, 117]. As such one can realistically explore a huge parameter space of interactions.

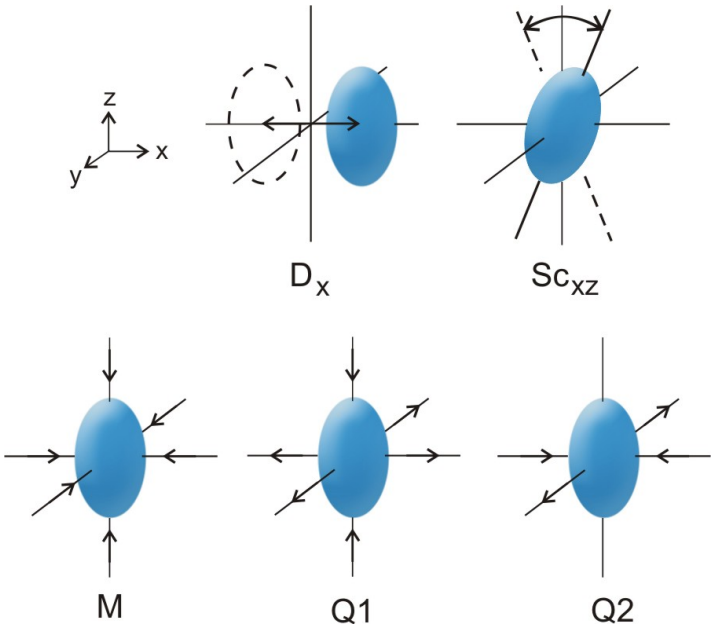

Figure 2.1.: Schematic illustration of the basic collective modes under consideration: the dipole mode D (shown here in the x-direction D_x), scissors mode Sc (shown here in $x-z$ plane Sc_{xz}), the monopole mode M and the quadrupole modes Q_1 and Q_2. These modes are discussed in more detail in Section 2.3.

The ground state solutions of a trapped dipolar BEC have been theoretically established for the limited regime of $g \geq 0$ and $C_{dd} > 0$ [45, 118, 136, 44, 97, 35, 113] and the dipolar interactions have been shown to have profound effect. For example, if the dipoles are aligned in the z-direction, then a condensate that is elongated along z will be dominated by attractive end-to-end dipoles and in extreme cases can be unstable to collapse. Conversely a condensate that is flattened along z will be dominated by repulsive side-by-side dipoles and this can suppress collapse. In the limit $\epsilon_{dd} \to \infty$ density wave structures have also been predicted [114]. Away from such structures and for sufficiently repulsive interactions [103], the Thomas-Fermi approximation can be employed to neglect the kinetic energy of ground state solutions. Under the usual harmonic trapping, the condensate density profile then approximates an inverted parabola [97], and this provides a versatile tool for examining condensate solutions and dynamics [109].

The collective excitations of trapped BECs are also of great importance [109]. The most basic excitations are the dipole (centre-of-mass), monopole (breathing), quadrupole and scissors modes, illustrated schematically in Fig. 2.1. Their characterization offers important opportunities to measure interaction effects, test theoretical models, and even detect weak forces [52, 96]. Specifically, the scissors mode provides an important test for the condensate superfluidity [50, 86, 24], while the quadrupole mode plays a key role in the onset of vortex nucleation

in rotating condensates [112, 123, 84, 102, 129, 60], see also chapter 3 of this report. While the collective modes of a dipolar BEC have been studied previously [137, 44, 97, 113, 42], key issues remain at large, for example, the regimes of $C_{\rm dd} < 0$ and $g < 0$, and the behaviour of the scissors modes. This provides the motivation for the current work.

In this paper we present a general and accessible methodology for determining the static solutions and excitation frequencies of trapped dipolar BECs in the Thomas-Fermi limit. We explore the static solutions and the low-lying collective excitations throughout a large and experimentally relevant parameter space, including positive and negative dipolar couplings $C_{\rm dd}$, positive and negative s-wave interactions g, and cylindrically and non-cylindrically symmetric systems. Moreover, our approach enables us to identify the modes responsible for collapse of the condensate.

Section 2.2 is devoted to the static solutions of the system. Beginning with the underlying Gross-Pitaevskii theory for the condensate mean-field, we make the Thomas-Fermi approximation and outline the methodology for deriving the TF static solutions. We then use it to map out the static solutions with cylindrical symmetry, for both repulsive and attractive s-wave interactions, and then present an example case of the static solutions in a non-cylindrically-symmetry geometry. We compare to recent experimental observations where possible.

In Section 2.3 we present our methodology for deriving the excitation frequencies of a dipolar BEC. This is based on the approach of Sinha and Castin [123] whereby one considers perturbations around the static solutions (derived in Section 2.2) and employs linearized equations of motion for these perturbations. At the heart of our approach is the calculation of the dipolar potential of a heterogeneous ellipsoid BEC, performed by employing results from astrophysics [34, 36, 76] and detailed in Appendix B.

In Section 2.4 we apply this method to calculate the frequencies of the important low-lying modes of the system, namely the monopole, dipole, quadrupole and scissors modes, for a cylindrically-symmetric condensate. We show how these frequencies vary with the key parameters of the system, ϵ_{dd} and trap ratio γ, and give physical explanations for our observations. In Section 2.5 we extend our analysis to non-cylindrically-symmetric BECs. Although the parameter space of such systems is very large, we present pertinent examples. An important feature of non-cylindrically-symmetric systems is that they support a family of scissors modes which can be employed as a test for superfluidity. As such, in Section 2.6, we focus on these scissors modes and show how they vary with key parameters. Finally, in Section 2.7, we summarise our findings.

2.2. Static solutions

2.2.1. Methodology of obtaining static solutions

At zero temperature the condensate is well-described by a mean-field order parameter, or 'wavefunction', $\psi(\mathbf{r}, t)$. This defines an atomic density distribution via $n(\mathbf{r}, t) = |\psi(\mathbf{r}, t)|^2$. Static solutions, denoted by $\tilde{\psi}(\mathbf{r})$, satisfy the time-independent Gross-Pitaevskii equation (GPE) given by [109],

$$\left[-\frac{\hbar^2}{2m}\nabla^2 + V(\mathbf{r}) + \Phi_{dd}(\mathbf{r}) + g\left|\tilde{\psi}(\mathbf{r})\right|^2\right]\tilde{\psi}(\mathbf{r}) = \mu\tilde{\psi}(\mathbf{r}). \tag{2.3}$$

where μ is the chemical potential of the system. The external potential $V(\mathbf{r})$ is typically harmonic with the general form,

$$V(\mathbf{r}) = \frac{1}{2}m\omega_\perp^2\left[(1-\epsilon)x^2 + (1+\epsilon)y^2 + \gamma^2 z^2\right]. \tag{2.4}$$

Here $\omega_\perp$ is the average trap frequency in the $x-y$ plane and the trap aspect ratio $\gamma = \omega_z/\omega_\perp$ defines the trapping in the axial (z) direction. The trap ellipticity in the $x-y$ plane ϵ defines the transverse trap frequencies via $\omega_x = \sqrt{1-\epsilon}\omega_\perp$ and $\omega_y = \sqrt{1+\epsilon}\omega_\perp$. Note that when $\epsilon = 0$ the trap is cylindrically symmetric.

The Φ_{dd}-term in Eq. (2.3) is the mean-field potential arising from the dipolar interactions. For dipoles aligned along the z-direction, it can be expressed as [25, 35]

$$\Phi_{dd}(\mathbf{r}) = -C_{dd}\left(\frac{\partial^2}{\partial z^2}\phi(\mathbf{r}) + \frac{1}{3}n(\mathbf{r})\right), \tag{2.5}$$

where $\phi(\mathbf{r})$ is a 'fictitious' electrostatic potential given by,

$$\phi(\mathbf{r}) = \frac{1}{4\pi}\int \frac{n(\mathbf{r})}{|\mathbf{r}-\mathbf{r}'|}\mathrm{d}^3\mathbf{r}'. \tag{2.6}$$

Note that this satisfies Poisson's equation $\nabla^2\phi = -n$.

We assume the Thomas-Fermi approximation, where the zero-point kinetic energy of the atoms in the trap is taken to be negligible in comparison to the potential and interactions effects. Note that the criteria for the Thomas-Fermi approximation to hold in a dipolar BEC has recently been outlined in [103]. Dropping the relevant ∇^2-term in Eq. (2.3) leads to

$$V(\mathbf{r}) + \Phi_{dd}(\mathbf{r}) + gn(\mathbf{r}) = \mu. \tag{2.7}$$

For an s-wave BEC under harmonic trapping, the density profile is known to be an inverted parabola [109] with the general form,

$$n(\mathbf{r}) = n_0\left(1 - \frac{x^2}{R_x^2} - \frac{y^2}{R_y^2} - \frac{z^2}{R_z^2}\right) \quad \text{for } n(\mathbf{r}) \geq 0 \tag{2.8}$$

where $n_0 = 15N/(8\pi R_x R_y R_z)$ is the central density. In order to obtain the dipolar potential arising from this density distribution, one must find the corresponding electrostatic potential of Eq. (2.6). Refs. [97, 35] follow this procedure, and arrive at the remarkable conclusion that the dipolar potential Φ_{dd} is also parabolic. In section 2.3 and Appendix B we point out that this result can be extended using 19th century astrophysics [34, 36, 76] to arbitrary polynomial densities yielding polynomial dipolar potentials of the same degree. For the parabolic density profile at hand, the internal dipolar potential is given by [35, 129]

$$\begin{aligned}\Phi_{dd}(\mathbf{r}) = &-g\epsilon_{dd}n(\mathbf{r}) + \frac{3g\epsilon_{dd}n_0\kappa_x\kappa_y}{2} \\ &\times\left[\beta_{001} - \left(\beta_{101}x^2 + \beta_{011}y^2 + 3\beta_{002}z^2\right)R_z^{-2}\right]\end{aligned} \tag{2.9}$$

where $\kappa_x = R_x/R_z$ and $\kappa_y = R_y/R_z$ are the aspect ratios of the condensate, and

$$\beta_{ijk} = \int_0^\infty \frac{\mathrm{d}s}{(\kappa_x^2+s)^{i+\frac{1}{2}}(\kappa_y^2+s)^{j+\frac{1}{2}}(1+s)^{k+\frac{1}{2}}}, \tag{2.10}$$

where i, j, k are integers. Then, for the density profile of Eq. (2.8), Eq. (2.7) becomes

$$\begin{aligned}\mu &= 3g\epsilon_{dd}\frac{n_0\kappa_x\kappa_y}{2R_z^2}\left[R_z^2\beta_{001} - \beta_{101}x^2 - \beta_{011}y^2 - 3\beta_{002}z^2\right] \\ &+ V(\mathbf{r}) + \frac{gn_0}{R_z^2}\left(R_z^2 - \frac{x^2}{\kappa_x^2} - \frac{y^2}{\kappa_y^2} - z^2\right). \end{aligned} \tag{2.11}$$

Inspection of the coefficients of x^2, y^2 and z^2 leads to three self-consistency relations, given by

$$\kappa_x^2 = \frac{\omega_z^2}{\omega_x^2}\frac{1+\epsilon_{dd}\left(\frac{3}{2}\kappa_x^3\kappa_y\beta_{101}-1\right)}{1-\epsilon_{dd}\left(1-\frac{9\kappa_x\kappa_y}{2}\beta_{002}\right)}, \tag{2.12}$$

$$\kappa_y^2 = \frac{\omega_z^2}{\omega_y^2}\frac{1+\epsilon_{dd}\left(\frac{3}{2}\kappa_y^3\kappa_x\beta_{011}-1\right)}{1-\epsilon_{dd}\left(1-\frac{9\kappa_x\kappa_y}{2}\beta_{002}\right)}, \tag{2.13}$$

$$R_z^2 = \frac{2gn_0}{m\omega_z^2}\left[1-\epsilon_{dd}\left(1-\frac{9\kappa_x\kappa_y}{2}\beta_{002}\right)\right]. \tag{2.14}$$

Solving Eqs. (2.12)-(2.14) reveals the static solutions of the system.

The parabolic density profile (2.8) defines an energy landscape

$$\begin{aligned}E &= \frac{15N^2g}{28\pi\kappa_x\kappa_yR_z^3}\left[(1-\epsilon_{dd})\right. \\ &+ \left.\frac{3}{8}\kappa_x\kappa_y\epsilon_{dd}\left(7\beta_{001}-3\beta_{002}-\kappa_x^2\beta_{101}-\kappa_y^2\beta_{011}\right)\right] \\ &+ \frac{N}{14}mR_z^2\left(\kappa_x^2\omega_x^2+\kappa_y^2\omega_y^2+\gamma^2\right). \end{aligned} \tag{2.15}$$

Static solutions correspond to stationary points in the energy landscape. If the stationary point is a local minimum in the energy landscape, it corresponds to a physically stable solution. However, if the stationary point is a maximum or a saddle point, the corresponding solution will be dynamically unstable. The nature of the stationary point can be determined by performing a second derivative test (see Appendix D) on Eq. (2.15) with respect to the parameters κ_x, κ_y, and R_z. This leads to 6 lengthy equations, which are included in Appendix C. Note that this only determines whether the stationary point is a local minimum *within this class of parabolic density profiles*. Although higher order (beyond quadrupole) modes can become unstable in certain regimes, as a criterion of stability we will use the local minima of (2.15). This assumption is supported by the recent experiments by Koch et al [69], where for $\epsilon_{dd} > 1$ and $\epsilon_{dd} < -0.5$ ($g > 0$) the dipolar BEC is stable over significant time-scales.

Note that for a cylindrically-symmetric trap $\epsilon = 0$, the condensate profile is also cylindrically-symmetric with aspect ratio $\kappa_x = \kappa_y =: \kappa$. The integrals β_{ijk} of Eq. (2.10) then evaluate to [46],

$$\beta_{ijk} = 2\frac{{}_2F_1\left(k+\frac{1}{2},1;i+j+k+\frac{3}{2};1-\kappa^2\right)}{(1+2i+2j+2k)\kappa^{2(i+j)}}, \tag{2.16}$$

where ${}_2F_1$ denotes the Gauss hypergeometric function [2].

2.2.2. Cylindrically-symmetric static solutions for $g > 0$

We have obtained the static solutions for a cylindrically-symmetric BEC by solving Eqs. (2.12) to (2.14) numerically. The solutions behave differently depending on whether the s-wave interactions are repulsive or attractive. We begin by considering the $g > 0$ case. The ensuing static solutions, characterised by their aspect ratio κ, are presented in Fig. 2.2 as a function of ϵ_{dd} with each line representing a different trap ratio γ. While the Thomas-Fermi solutions in the regime $\epsilon_{dd} > 0$ have been dicussed previously [97, 35], the regime of $\epsilon_{dd} < 0$ has not been studied. Note that when we fix $g > 0$, the regime $\epsilon_{dd} < 0$ corresponds to $C_{\rm dd} < 0$ where the dipolar interaction behaves counter-intuitively, repelling along z and attracting in the transverse direction. This can be achieved by rapid rotation about the z-axis of the field aligning the dipoles [43].

First consider the range $-1/2 < \epsilon_{dd} < 1$ (white region in Fig. (2.2)) for which stable solutions exist for all trap ratios (outside of this range the existence of stable static solutions depends on γ). We can understand this by considering the limiting case of a homogeneous dipolar condensate. The energy of a plane wave perturbation (phonon) with momentum p is given by the Bogoliubov spectrum [45],

$$E_{\rm B}^2 = \left(\frac{p^2}{2m}\right)^2 + 2gn\left\{1 + \varepsilon_{\rm dd}\left(3\cos^2\theta - 1\right)\right\}\frac{p^2}{2m}, \tag{2.17}$$

where θ is the angle between the momentum of the phonon and the polarization direction. The perturbation evolves as $\sim \exp(iE_{\rm B}t/\hbar)$ and so when $E_{\rm B}^2 < 0$ the perturbations grow exponentially, signifying a dynamical instability. Stability requires that $E_{\rm B}^2 > 0$ which, for $g > 0$, corresponds to the requirement that $[1 + (3\cos^2\theta - 1)\epsilon_{dd}] \geq 0$ in Eq. (2.17). This leads to the stability condition $-1/2 < \epsilon_{dd} < 1$ and thus explains the robustness of solutions therein. For trapped condensates, variations of ϵ_{dd} induce a modification of the condensate aspect ratio κ. Note that for $\epsilon_{dd} = 0$, $\kappa = \gamma$. For $\epsilon_{dd} > 0$, the dipolar interaction is attractive along z and repulsive perpendicular to it. Hence, as ϵ_{dd} is increased the condensate elongates along z, i.e., κ decreases. Conversely, for $\epsilon_{dd} < 0$, the effective dipolar interaction is repulsive along z and attractive transversely. Hence as $|\epsilon_{dd}|$ increases the system flattens and κ increases. This effect can be likened to magnetostriction. One should also note that for $-1/2 < \epsilon_{dd} < 1$ the energy landscape of the system (2.15) has only one stationary point, namely the global energy minimum corresponding to the solution itself. This further indicates the robustness of solutions within this range.

Outside of the regime $-1/2 < \epsilon_{dd} < 1$ the *global* energy minimum of the system is a collapsed state where at least one of the radii has zero width. However, the presence of trapping can support a *local* energy minimum corresponding to a metastable solution (light grey region in Fig. (2.2)). Such an energy landscape features an additional stationary point, which is a saddle point connecting the metastable solution to the collapsed state and is indicated by the dark grey region in Fig. (2.2). The occurence of these metastable solutions depends sensitively on ϵ_{dd} and γ. Consider $\epsilon_{dd} > 1$, for which there is a susceptibility to collapse towards an infinitely narrow line of end-to-end dipoles ($R_x \to 0$). If the trap is sufficiently flattened this collapse mechanism is suppressed and metastable condensate solutions persist even as $\epsilon_{dd} \to \infty$ [118, 136, 35]. This critical trap ratio is $\gamma_{\rm crit}^+ > 5.17$ [136, 35]. If $\gamma < \gamma_{\rm crit}^+$ then at some critical value of ϵ_{dd} the local energy minimum disappears and no stable solutions exist. Now consider $\epsilon_{dd} < -0.5$ for which the system is susceptible to collapse into an infinitely

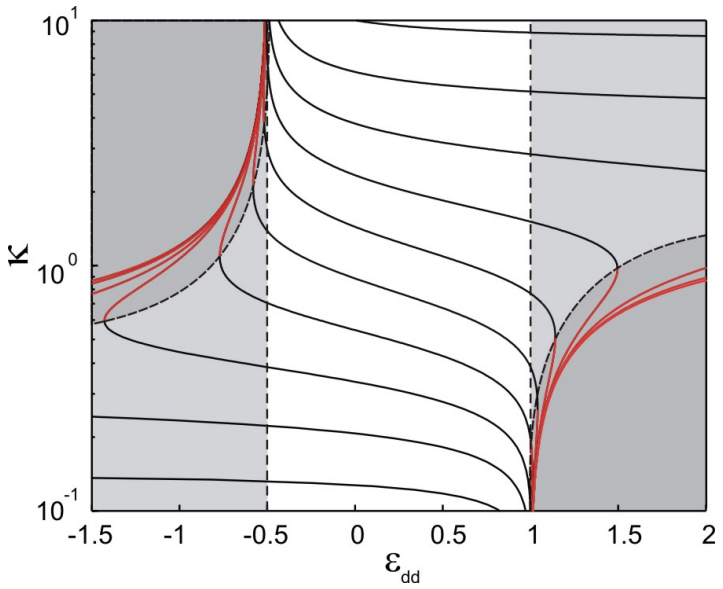

Figure 2.2.: Aspect ratio κ of the $g > 0$ cylindrically-symmmetric static solutions as a function of ϵ_{dd} according to Eqs. (2.12)-(2.14). Note that $\epsilon_{dd} < 0$ corresponds to $C_{dd} < 0$. The solid lines indicate the static solutions for specific trap ratios γ which are equally spaced on a logarithmic scale in the range $\gamma = [0.1, 10]$, with black/red lines correspond to minimum/saddle points in the energy landscape. The parameter space of global, metastable and unstable solutions is denoted by white, light grey and dark grey regions, respectively.

thin pancake of side-by-side dipoles ($R_z \to 0$). If the trap is sufficiently elongated with $\gamma < \gamma_{\rm crit}^- = 0.19$ collapse is suppressed even in the limit $\epsilon_{dd} \to -\infty$. However, if $\gamma > \gamma_{\rm crit}^-$ then for sufficiently large and negative ϵ_{dd} the metastable solution disappears and the system is unstable to collapse.

In a recent experiment Lahaye *et al.* [73] measured the aspect ratio of the dipolar condensate over the range $0 \lesssim \epsilon_{dd} \lesssim 1$ using a Feshbach resonance to tune g, and found very good agreement with the TF predictions. Similarly, Koch *et al.* [69] observed the threshold for collapse in a $\gamma = 1$ system to be $\epsilon_{dd} \approx 1.1$, in excellent agreement with the TF prediction of $\epsilon_{dd} = 1.06$. Using various trap ratios, it was also found that collapse became suppressed in flattened geometries and the critical trap ratio was observed to exist in the range $\gamma_{\rm crit}^+ \approx 5 - 10$, which is in qualitative agreement with the TF predictions.

2.2.3. Cylindrically-symmetric static solutions for $g < 0$

We now consider the case of attractive s-wave interactions $g < 0$. This is experimentally relevant since a dipolar BEC with $g < 0$ was recently generated [69]. The static solutions are presented in Fig. (2.3). Be aware that since $g < 0$, $\epsilon_{dd} < 0$ ($\epsilon_{dd} > 0$) now correspond to $C_{\rm dd} > 0$ ($C_{\rm dd} < 0$). The diagram differs greatly from the $g > 0$ case and in particular no solutions exist in the range $-1/2 < \epsilon_{dd} < 1$. For $\epsilon_{dd} > 0$ solutions only exist for elongated geometries ($\gamma < \gamma_{\rm crit}^- = 0.19$) while for $\epsilon_{dd} < 0$ solutions only exist for flattened geometries ($\gamma > \gamma_{\rm crit}^+ = 5.17$). Furthermore, the attractive s-wave interactions always cause the global

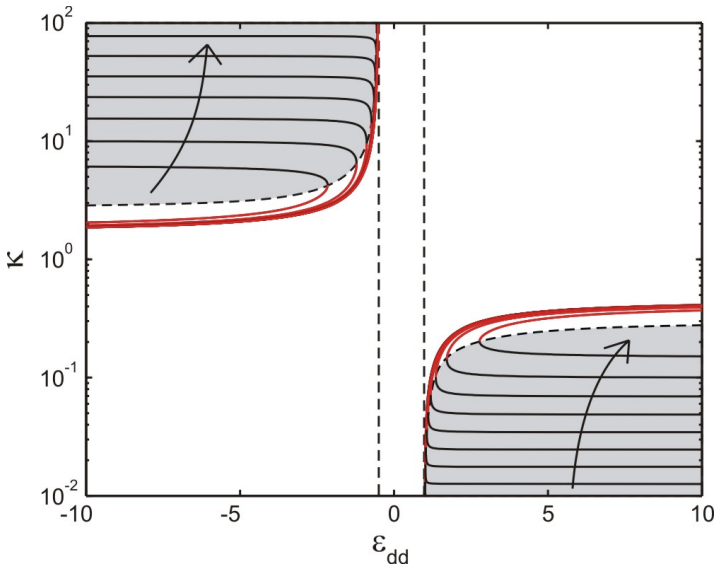

Figure 2.3.: Aspect ratio κ of the $g < 0$ cylindrically-symmetric static solutions as a function of ϵ_{dd}. Note that the regime of $\epsilon_{dd} > 0$ corresponds to $C_{dd} < 0$. The lines denote static solutions for specific trap ratios γ, equally spaced on a logarithmic scale in the ranges $\gamma = [0.010, \gamma^{-}_{\rm crit}]$ (lower right set of curves) and $\gamma = [\gamma^{+}_{\rm crit}, 150]$. Arrows indicate direction of increasing γ. The light grey region and black lines correspond to minimum points, while the red lines correspond to saddle points in the energy landscape.

minimum to be a collapsed state. This means that static solutions are only ever metastable (light grey region in Fig. (2.3)), while the system also supports saddle-shapped static points (red curves). Again, valuable insight can be gained from considering the Bogoliubov spectrum (2.17), this time with $g < 0$. Firstly, for the purely s-wave case we observe the well-known result [109] that a homogeneous attractive BEC is always unstable to collapse. With dipolar interactions the uniform system is stable to axial perturbations ($\theta = 0$) for $\epsilon_{dd} < -1/2$ and to radial perturbations ($\theta = \pi/2$) for $\epsilon_{dd} > 1$. This is exactly the opposite of the $g > 0$ case and clearly indicates the lack of solutions for $-1/2 < \epsilon_{dd} < 1$. Of course, $\epsilon_{dd} < -1/2$ and $\epsilon_{dd} > 1$ cannot be simultaneously satisfied and so a uniform dipolar system with $g < 0$ is always unstable. However, as discussed in the previous section, when the system is trapped the net dipolar interactions depend on the condensate shape and become repulsive in elongated systems for $\epsilon_{dd} > 0$ (for which $C_{\rm dd} < 0$) and flattened systems for $\epsilon_{dd} < 0$ (for which $C_{\rm dd} < 0$). In these cases the net repulsive dipolar interactions can stabilise against the attractive s-wave interactions, and leads to the regions of static solutions observed in Fig. (2.3).

Although our model predicts that no solutions exist for $-1/2 < \epsilon_{dd} < 1$, it is well-known that stable condensates with purely attractive s-wave interactions can exist. Zero-point motion of the atoms (ignored in the TF model), induced by the trapping potential, stabilises the condensate up to a critical number of atoms or interaction magnitude [109]. One can expect, therefore, that for finite number of atoms the presence of zero-point motion enhances the stability of the condensate beyond the TF solutions.

Koch *et al.* [69] produced a dipolar condensate with $g < 0$ and reported the onset of collapse

for $\epsilon_{dd} \gtrsim -7$. For their trap $\gamma = 10$ the TF static solutions disappear for $\epsilon_{dd} > -1.5$. The inclusion of zero-point motion cannot explain this discrepancy between theory and experiment since the use of a gaussian ansatz (which includes zero-point motion) leads to an almost identical prediction [69]. One possibility is that the dominant dipolar interactions may lead to significant deviations of the density profile from a single-peaked inverted parabola/gaussian profile, for example, Ronen *et al.* [114] have observed bi-concave density structures, albeit in the different regime of $\epsilon_{dd} \to \infty$.

Having indicated how the static solutions behave for attractive *s*-wave interactions $g < 0$, for the remainder of the paper we will generally focus on the more common case of repulsive *s*-wave interactions.

2.2.4. Non-cylindrically-symmetric static solutions

We now consider the more general case of a non-cylindrically-symmetric system for which the trap ellipticity ϵ is finite and κ_x and κ_y typically differ. Note that we perform our analysis of non-cylindrically-symmetric static solutions for repulsive *s*-wave interactions $g > 0$. In Fig. 2.4 we show how κ_x and κ_y vary as a function of ϵ_{dd} in a non-cylindrically-symmetric trap. Different values of trap ratio are considered and generic qualitative features exist. The splitting of κ_x and κ_y is evident, with κ_x shifting upwards and κ_y shifting downwards in comparison to the cylindrically-symmetric solutions. Furthermore, the branches become less stable to collapse. For example, for $\gamma = 0.18 < \gamma_{\rm crit}^{-}$, in the cylindrically-symmetric system there exist stable solutions for $\epsilon_{dd} \to -\infty$, but in the anisotropic case, stationary solutions only exist up to $\epsilon_{dd} \simeq 11$.

2.3. Calculation of the excitation spectrum

Now that we have demonstrated the prediction of the static solutions, we wish to proceed to determining their excitation spectrum. One method of approaching this is the variational approach [105, 136, 137, 44], where a gaussian ansatz for the BEC is employed to derive equation of motions for the gaussian widths. A similar approach has been employed in the Thomas-Fermi limit, where an equation of motion for the Thomas-Fermi widths has led to predictions of the collective modes [97, 42]. A more exact approach is obtained by solving the full Bogoliubov spectrum of the system [113] or by solving the full time-dependent GPE under a suitable peturbation [136, 137, 44].

In our approach we extend the methodology of Sinha and Castin [123], where linearized equations of motion are derived for small perturbations about the mean-field stationary solution. In comparison to the mean-field approaches described above, this method has the key advantage that it is trivially extended to arbitrary modes of excitation and unstable modes/dynamical instability. For example, extension of the variational approach to higher-order modes (e.g., to consider the scissors modes of an *s*-wave BEC [3]) requires that this is "built-in" to the variational ansatz itself. We outline our approach below.

The dynamics of the condensate wavefunction $\psi(\mathbf{r}, t)$ is described by the time dependent

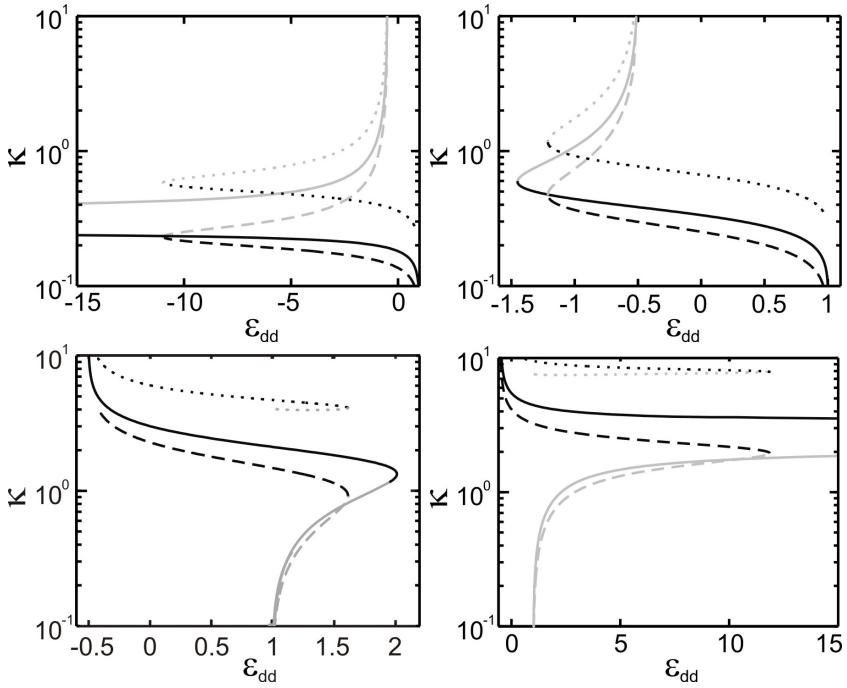

Figure 2.4.: Stable static solutions, characterised by the aspect ratios κ_x (dashed lines) and κ_y (dotted lines), in a non-cylindrically-symmetric trap with ellipticity $\epsilon = 0.75$ and (a) $\gamma = 0.18$, (b) $\gamma = 0.333$, (c) $\gamma = 3$ and (d) $\gamma = 5.5$. Stable (unstable) static solutions are indicates by black (grey) lines. The corresponding static solutions for $\epsilon = 0$ are indicated by solid lines.

Gross-Pitaevskii equation,

$$i\hbar\frac{\partial\psi}{\partial t} = \left[-\frac{\hbar^2}{2m}\nabla^2 + V + \Phi_{dd} + g\left|\psi\right|^2\right]\psi, \tag{2.18}$$

where, for convenience, we have dropped the arguments $\mathbf{r}$ and t. By expressing ψ in terms of its density n and phase φ as,

$$\psi = \sqrt{n}\mathrm{e}^{\mathrm{i}\varphi},$$

one obtains from Eq. (2.18) the well-known hydrodynamic equations,

$$\frac{\partial n}{\partial t} = -\frac{\hbar}{m}\nabla\cdot(n\nabla\varphi) \tag{2.19}$$

$$\hbar\frac{\partial\varphi}{\partial t} = -\frac{\hbar^2}{2m}|\nabla\varphi|^2 - V - gn - \Phi_{dd}. \tag{2.20}$$

For the latter case we have dropped the term $(\hbar^2/2m\sqrt{n})\nabla^2\sqrt{n}$ arising from density gradients - this is synonymous with making the TF approximation [109]. Note that static solutions satisfy the equilibrium conditions $\partial n/\partial t = 0$ and $\partial\varphi/\partial t = -\mu/\hbar$.

We now consider small perturbations of the density and phase, δn and $\delta\varphi$, to static solutions, and linearize the hydrodynamic equations (2.19, 2.20). The dynamics of the perturbations

are then described as (see Appendix E)

$$\frac{\partial}{\partial t}\begin{bmatrix}\delta\varphi\\ \delta n\end{bmatrix} = \mathcal{L}\begin{bmatrix}\delta\varphi\\ \delta n\end{bmatrix}, \tag{2.21}$$

where

$$\mathcal{L} = -\begin{bmatrix}0 & g(1+\epsilon_{dd}K)/m\\ \nabla\cdot n_0\nabla & 0\end{bmatrix}, \tag{2.22}$$

and the operator K is defined as

$$(K\delta n)(\mathbf{r}) = -3\frac{\partial^2}{\partial z^2}\int\frac{\delta n(\mathbf{r}')\mathrm{d}^3\mathbf{r}'}{4\pi|\mathbf{r}-\mathbf{r}'|} - \delta n(\mathbf{r}). \tag{2.23}$$

The integral in the above expression is carried out over the domain where the unperturbed density of Eq. (2.8) satisfies $n > 0$, that is, the general ellipsoidal domain with radii R_x, R_y, R_z. Extending the integration domain to the region where $n + \delta n > 0$ would only add $\mathcal{O}(\delta n^2)$ effects, since it is exactly in this extended domain that $n = \mathcal{O}(\delta n)$, whereas the size of the extension is also proportional to δn (see Appendix F). Clearly, to first order in δn, the quantity $\epsilon_{dd}K\delta n$ is the dipolar potential associated with the density distribtution δn. To obtain the global shape excitations of the BEC one has to find the eigenfunctions $\delta n, \delta\varphi$ and eigenvalues λ of operator $\mathcal{L}$ of Eq. (2.22). For such eigenfunctions equation (2.21) trivially yields an exponential time evolution of the form $\sim \exp(\lambda t)$. When the associated eigenvalue λ is imaginary, the eigenfunction corresponds to a time-dependent oscillation of the BEC. However, when λ posesses a positive real part, the eigenfunction represents an unstable excitation which grows exponentially. Such dynamical instabilities are an important consideration, for example in rotating condensates where they initiate vortex lattice formation [123, 102]. However, in the current study we will focus on stable excitations of non-rotating systems.

To find such eigenfunctions and eigenvalues we consider a polynomial ansatz for the perturbations in the coordinates x, y, and z, of a total degree ν [123], that is,

$$\delta n = \sum_{p,q,r} a_{pqr}x^p y^q z^r, \qquad \delta\varphi = \sum_{p,q,r} b_{pqr}x^p y^q z^r,$$

where

$$\nu = \max_{\substack{a_{pqr}\neq 0\\ b_{pqr}\neq 0}}\{p+q+r\}$$

All operators in Eq. (2.22), acting on such polynomials of degree ν, result again in polynomials of the same order. For the operator K this property might not be obvious, but using the results of Appendix B we can evaluate the integral in the first term in Eq. (2.23) exactly, yielding a polynomial of which the coefficients are given in terms of the integrals β_{ijk} defined in Eq. (2.10). The degree of this polynomial is $\nu+2$, and taking the derivative with respect to z twice lowers the degree by 2 again. Thus, operator (2.22) can be rewritten as a matrix mapping between scalar vectors of polynomial coefficients. Numerically finding the eigenvalues and eigenvectors of such a system is a simple task, which computational packages can typically perform.

We present only the lowest-lying shape oscillations corresponding to polynomial phase and density perturbations of degree $\nu = 1$ and $\nu = 2$. These form the monopole, dipole,

quadrupole and scissors modes. These excitations are illustrated schematically in Fig. 2.1 and described below. Note that a, b, c and d are real positive coefficients.

- **Dipole modes D_x, D_y and D_z**: A centre-of-mass motion along each trap axis[1]. The D_x mode, for instance, is characterised by $\delta n = \pm ax$.
- **Monopole mode M**: An in-phase oscillation of all radii with the form $\delta n = \pm a \pm (bx^2 + cy^2 + dz^2)$.
- **Quadrupole modes Q_1^{xy}, Q_1^{xz} and Q_1^{yz}**: The Q_1 modes feature two radii oscillating in-phase with each other (denoted in superscripts) and out-of-phase with the remaining radius. For example, the Q_1^{xy} mode is characterised by $\delta n = \pm a \pm (bx^2 + cy^2 - dz^2)$.
- **Quadrupole mode Q_2**: This 2D mode is supported only in a plane where the trapping has circular symmetry. For example, in the transverse plane of a cylindrically-symmetric system the transverse radii oscillates out-of-phase with each other, with no motion in z, according to $\delta n = \pm a(x \pm iy)^2$.
- **Scissors modes Sc_{xy}, Sc_{yz} and Sc_{xz}**: Shape preserving rotation of the BEC over a small angle in the xy, xz and yz plane, respectively. The Sc_{xy} mode is characterised by $\delta n = \pm axy$. Note that a scissors mode in a given plane requires that the condensate asymmetry in that plane is non-zero otherwise no cross-terms exist. Furthermore, the amplitude of the cross-terms should remain smaller than the condensate/trap asymmetry otherwise the scissors mode turns into a quadrupole mode [50].

Note that, in order to confirm the dynamical stability of the solution, one must also check that positive eigenvalues do not exist. We have performed this throughout this paper and consistently observe that when $\mathrm{Im}(\lambda) \neq 0$ that $\mathrm{Re}(\lambda) = 0$ and that when $\mathrm{Im}(\lambda) = 0$ that $\mathrm{Re}(\lambda) \neq 0$. It is also possible to determine excitation frequencies of higher order excitations of the BEC by including higher order monomial terms. Such modes, for example, play an important role in the dynamical instability of rotating systems [123, 129].

2.4. Excitations in a cylindrically-symmetric system

In this section we present the oscillation frequencies of the lowest lying stable excitations of a dipolar condensate in a cylindrically-symmetric trap. Through specific examples we indicate how they behave with the key experimental parameters, namely the dipolar interaction strength ϵ_{dd} and trap ratio γ. Note that we will discuss the scissors modes in more detail in Section 2.6. Here we will just point out that two scissors modes exist, corresponding to Sc_{xz} and Sc_{yz}, while the Sc_{xy} mode is non-existant due to the cylindrical symmetry of the system.

2.4.1. Variation with dipole interactions ϵ_{dd} for $g > 0$

In Fig. 2.5 we show how the collective mode frequencies vary with the dipolar interactions for the case of $g > 0$. Although it would be most relevant experimentally to present these

[1] For rotating systems the sloshing directions will differ from the trap axes, but these systems are not considered in this chapter.

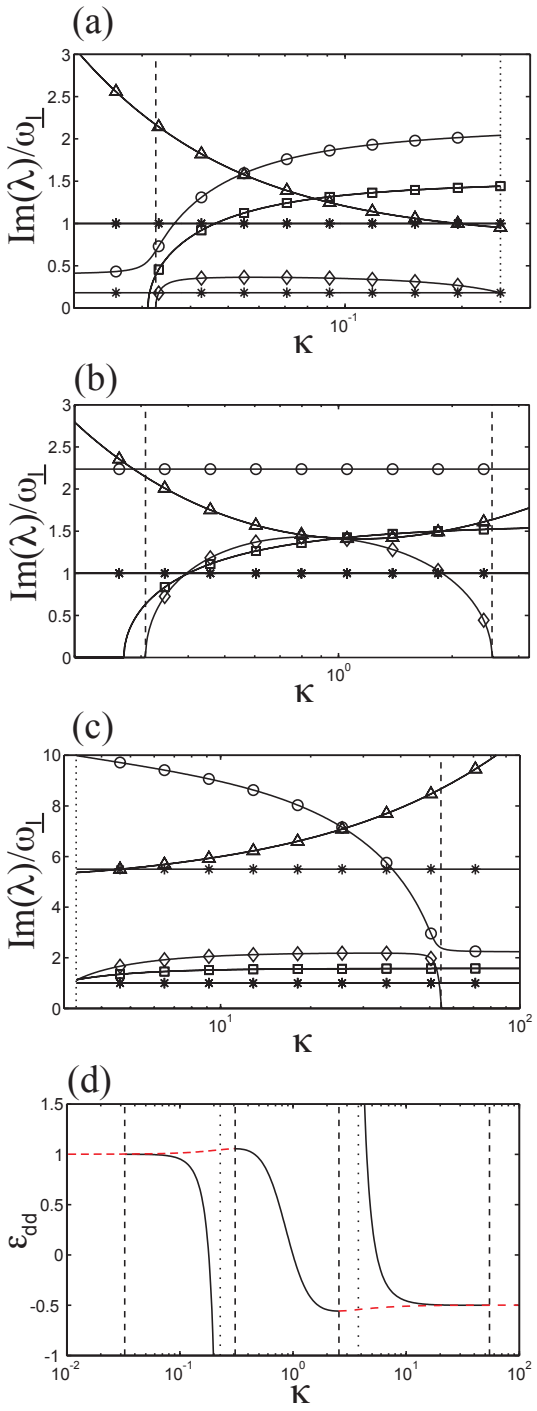

Figure 2.5.: Excitation frequencies as a function of condensate aspect ratio κ for a cylindrically-symmetric trap with aspect ratio (a) $\gamma = 0.18$, (b) $\gamma = 1$ and (c) $\gamma = 5.5$. Shown are the results for the modes M (circles), D (stars), Q_1 (diamonds), Q_2 (squares) and Sc (triangles). (d) Static solutions κ for $\gamma = 0.18$, 1 and 5.5.

frequencies as a function of ϵ_{dd}, this is problematic since two static solutions (metastable local minima and unstable saddle points) can exist for a given value of ϵ_{dd}. Moreover, in the critical region of collapse at the turning point from stable to unstable the excitation frequencies vary rapidly as a function of ϵ_{dd}, but not of κ. In order to clearly view the frequencies we have therefore employed the condensate aspect ratio κ as the variable. Note that the corresponding plot of frequencies, but as a function of ϵ_{dd}, can be found in Appendix G if desired.

We consider three values of trap ratio γ, which fall into three distinct regimes: (1) $\gamma < \gamma^{-}_{\rm crit}$, (2) $\gamma^{-}_{\rm crit} < \gamma < \gamma^{+}_{\rm crit}$ and (3) $\gamma^{+}_{\rm crit} < \gamma$. Recall that $\gamma^{+}_{\rm crit}(\gamma^{-}_{\rm crit})$ is the critical value above (below) which there exist stable solutions for $\epsilon_{dd} \to +\infty(-\infty)$, see also Fig. 2.2. In each case the aspect ratio of the *stable* solutions exists over a finite range $\kappa = [\kappa^{-}, \kappa^{+}]$. We will now discuss each regime in turn.

a) $\gamma < \gamma^{-}_{\rm crit}$

In Fig. 2.5(a) we present the excitation frequencies for $\gamma = 0.18$ as a function of κ. The corresponding static solutions are presented in Fig. 2.5(d) and confirm that the *stable* static solutions (black lines) exist over a range of $\kappa = [\kappa^{-}, \kappa^{+}]$, with $\kappa^{-} \approx 0.03$ and $\kappa^{+} \approx 0.25$ indicated by vertical lines (dashed and dotted, respectively). For $\kappa > \kappa^{+}$, no static solutions exist and so the excitation frequencies terminate at this point (dotted vertical line in Fig. 2.5(a) and (d)). For $\kappa < \kappa^{-}$, the static solution is no longer a local energy minimum but rather a saddle point/maximum that is unstable to collapse (transition marked with dashed, vertical line in Fig. 2.5(a) and (d)). Although this solution is not stable we can still determine its excitation spectrum. Crucially, this will reveal which modes are responsible for collapse and which remain stable throughout.

Three dipole modes (stars) exist. Dipole modes, in general, are decoupled from the internal dynamics of the condensate [109] and are determined by the trap frequencies ω_x, ω_y, and ω_z. For the cylindrically symmetric case, $\omega_x = \omega_y = \omega_\perp$, and hence only two distinct dipole modes are visible. For $\kappa < \kappa^{-}$ the dipole frequencies remain constant, indicating the dynamical stability of this mode.

In general, the remaining modes vary with the dipolar interactions. Perhaps the key mode here is the quadrupole Q_1 mode (diamonds). At the point of collapse the Q_1 frequency decreases to zero. This is connected to the dynamical instability of this mode since $\mathrm{Re}(\lambda) > 0$ for $\kappa < \kappa^{-}$. The physical interpretation of this is that the Q_1 mode, which is inherently anisotropic, mediates the anisotropic collapse of the condensate into an infinitely narrow cigar-shaped BEC. In the energy landscape picture, this occurs because the barrier between the local energy minimum and the collapsed $R_{x,y} = 0$ state disappears for $\kappa < \kappa^{-}$. Note that the link between collapse and the decrease of the quadrupole mode frequency to zero has been made in Ref. [44]. The Q_2 quadrupole mode (squares) decreases to zero, and becomes dynamically unstable, after the onset of collapse, i.e., in the back-bending region of the static solutions in Fig. 2.5(d). The monopole M mode (circles) remains stable for $\kappa < \kappa^{-}$ and increases with κ above this point.

b) $\gamma_{\rm crit}^- < \gamma < \gamma_{\rm crit}^+$

In Fig. 2.5(b) we present the excitation frequencies for $\gamma = 1$ as a function of ϵ_{dd}. Since $\gamma_{\rm crit}^- < \gamma < \gamma_{\rm crit}^+$, the solutions exist over a finite range of ϵ_{dd}. In terms of κ, collapse occurs at both limits of its range, i.e., for $\kappa < \kappa^-$ and $\kappa > \kappa^+$, where $\kappa^- \approx 0.3$ and $\kappa^+ \approx 2.5$ (dashed vertical lines in Fig. 2.5(b) and (d)).

Since the trap is spherically-symmetric, the dipole modes (stars) all have identical frequency, i.e. $\omega_\perp$. The Q_1 quadrupole frequency (diamonds) decreases to zero at both points of collapse, κ^- and κ^+. In the former case, this corresponds to the anisotropic collapse into an infinitely narrow BEC, while in the latter case, collapse occurs into an infinitely flattened BEC. In the low κ regime, the Q_2 quadrupole mode (squares) becomes unstable just past the point of collapse, but shows no instability in the opposite limit for $\kappa > \kappa^+$.

It is particularly interesting to note that the monopole modes (circles) shows no dependence on κ and therefore the dipolar interactions. This is specific to the case of $\gamma = 1$. By examining the form of the perturbations and solving the TF equations of motion [97] under a suitable perturbation, we find that the aspect ratio remains fixed throughout a monopole mode oscillation. Since the dipolar interactions are proportional to the trap aspect ratio κ and not the absolute value of the radii [97], the monopole mode then becomes independent of the dipolar interactions.

c) $\gamma > \gamma_{\rm crit}^+$

In Fig. 2.5(c) we plot the excitation frequencies for $\gamma = 5.5$. For $\kappa < \kappa^-$, no static solutions exist, and for $\kappa > \kappa^+$, no *stable* solutions exist. Here $\kappa^- \approx 3.3$ and $\kappa^+ \approx 54$ (dotted and dashed vertical lines, respectively, in Fig. 2.5(c) and (d)).

Again, the dipoles modes are constant, while the remaining modes vary with dipolar interactions. Apart from the quadrupole Q_1 mode, all modes are stable past the point of collapse, including the Q_2 quadrupole mode. The Q_1 mode decreases to zero at the point when the condensate collapses to an infinitely flattened pancake BEC, which is again consistent with this mode mediating the anisotropic collapse.

2.4.2. Variation with dipole interactions ϵ_{dd} for $g < 0$

We now consider the analogous case but with $g < 0$. As shown in Section 2.2.3 stable solutions only exist for $\gamma > \gamma_{\rm crit}^+ = 5.17$ and $\gamma < \gamma_{\rm crit}^- = 0.19$, with no stable solutions existing in the range $\gamma_{\rm crit}^- < \gamma < \gamma_{\rm crit}^+$. Hence we will only consider the two regimes of (1) $\gamma < \gamma_{\rm crit}^-$ and (2) $\gamma > \gamma_{\rm crit}^+$.

a) $\gamma < \gamma_{\rm crit}^-$

In Fig. 2.6(a) we present the excitation frequencies in a highly elongated trap $\gamma = 0.18$. Stable static solutions exist only for $\kappa^- < \kappa < \kappa^+$ where $\kappa^- \approx 0.25$ and $\kappa^+ \approx 0.29$. In this regime we find that all collective frequencies are purely imaginary and finite, and therefore stable. At the critical point for collapse $\kappa \approx 0.29$ the Q_1 mode frequency becomes zero and simultaneously becomes purely real, signifying its dynamical instability. This shows that,

as in the $g > 0$, the Q_1 mode mediates collapse and therefore that collapse proceeds in a highly anisotropic manner due to the anisotropic character of the dipolar interactions. The remaining modes do not become dynamically unstable past the critical point, and only vary weakly with κ throughout. Note that this latter fact indicates that the frequencies mainly depend on the condensate shape, and thus only 'indirectly' on the dipolar interactions rather than 'directly'. It should also be remarked that higher order modes with polynomial degree $\nu > 2$ also become unstable within the range $\kappa^- < \kappa < \kappa^+$ where no stable parabolic solutions lie, further re-iterating the *meta*stability of the $g < 0$ states and confirming the predictions made from the Bogoliubov spectrum (2.17).

b) $\gamma > \gamma^+_{\rm crit}$

Figure 2.6(b) shows the mode frequencies in a highly flattened trap $\gamma = 5.5$, for which stable static solutions exist only in the regime $\kappa^- < \kappa < \kappa^+$ where $\kappa^- \approx 2.7$ and $\kappa^+ \approx 3.3$. Similarly, at the point of collapse $\kappa \approx 2.7$ the Q_1 mode has zero frequency and is dynamically unstable. Well below the critical point the Q_2 mode frequency also becomes zero and dynamically unstable.

2.4.3. Variation with trap ratio γ

Having illustrated in the previous section how the excitation frequencies behave for $g < 0$, from now on we will limit ourselves to the case of $g > 0$. In Fig. 2.7 we plot the excitation frequencies as a function of γ for various values of ϵ_{dd}. A common feature is that the dipole frequencies scale with their corresponding trap frequencies, such that $\omega_{D_x} = \omega_{D_y} = \omega_\perp$ and $\omega_{D_z} = \gamma\omega_\perp$. We now consider the three regimes of zero, negative and positive ϵ_{dd}.

a) $\epsilon_{dd} = 0$

For $\epsilon_{dd} = 0$ stable solutions exist for all γ and the corresponding mode frequencies are plotted in Fig. 2.7(a). Our results agree with previous studies where the mode frequencies are derived analytically (see, e.g., [107] and [109]). The Q_2 quadrupole mode has fixed frequency $\omega_{Q_2} = \sqrt{2}\omega_\perp$. The scissors mode frequency corresponds to $\omega_{Sc_{xz}} = \omega_{Sc_{yz}} = \sqrt{1+\gamma^2}\omega_\perp$, and the remaining modes obey the equation [109],

$$\omega^2 = \omega_\perp^2 \left(2 + \frac{3}{2}\lambda^2 \pm \frac{1}{2}\sqrt{16 - 16\lambda^2 + 9\lambda^4}\right), \tag{2.24}$$

where the "+" and "-" solutions correspond to ω_M and ω_{Q_1}, respectively.

b) $\epsilon_{dd} < 0$

For $\epsilon_{dd} = -0.75$ (Fig. 2.7(b)) stable solutions, and collective modes, exist up to a critical trap ratio $\gamma^{\rm max} \approx 0.56$. Beyond that the attractive nature of side-by-side dipoles (recall $C_{dd} < 0$) makes the system unstable to collapse.

For all of the modes, excluding the Q_1 quadrupole mode, we see the same qualitative behaviour as for the non-dipolar case (grey lines) with the modes extending right up to the point of

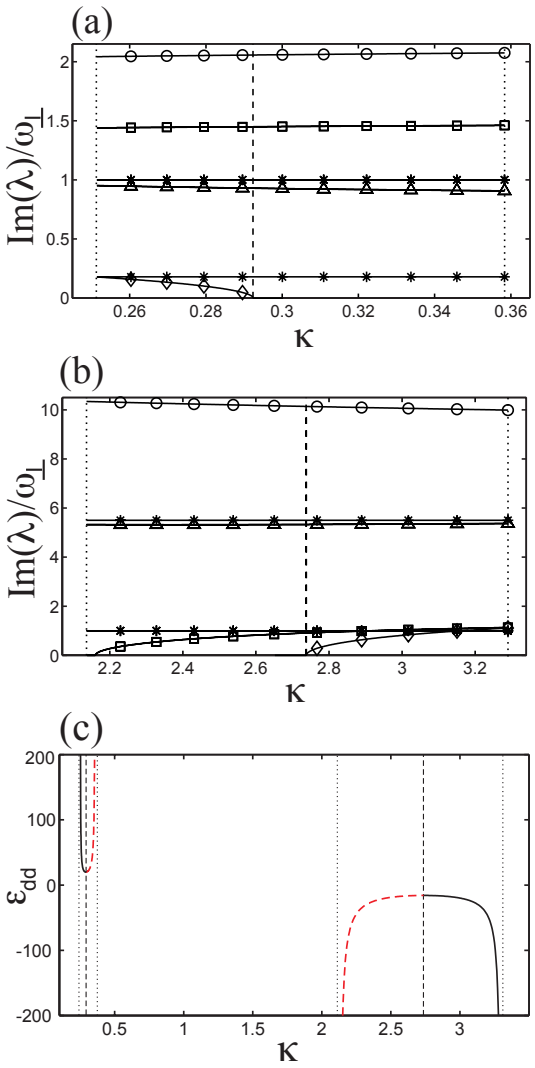

Figure 2.6.: Excitation frequencies as a function of condensate aspect ratio κ for a $g < 0$ cylindrically-symmetric trap with aspect ratio (a) $\gamma = 0.18$ and (b) $\gamma = 5.5$, with corresponding static solutions shown in figure (c). Included are the results for the modes M (circles), D (stars), Q_1 (diamonds), Q_2 (squares) and Sc (triangles). Dashed vertical lines indicate the critical point at which the stable static solutions turn into unstable ones, dotted vertical lines indicate endpoints of branches where static solutions cease to exist.

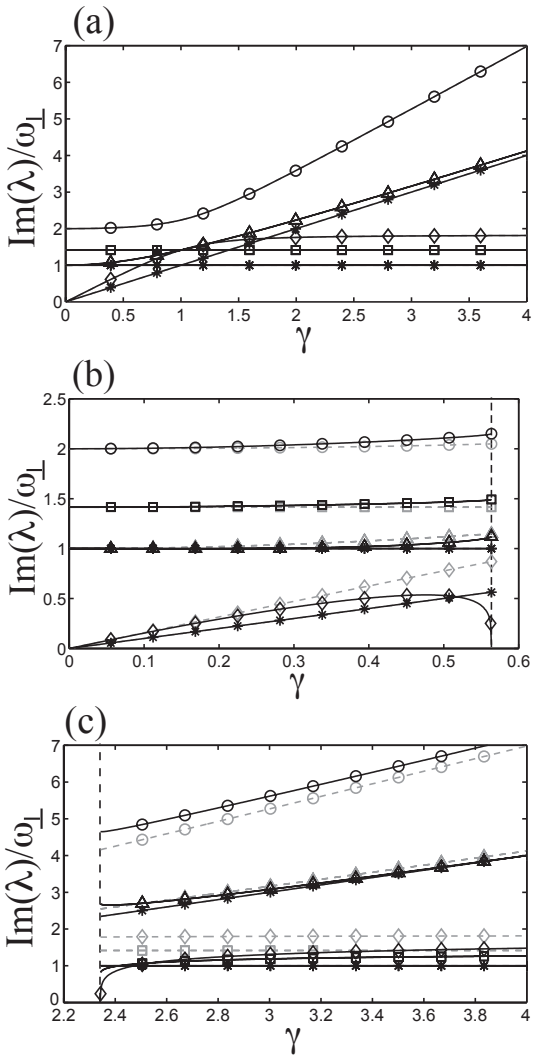

Figure 2.7.: Excitation frequencies in a cylindrically-symmetric trap as a function of the trap aspect ratio γ for (a) $\epsilon_{dd} = 0$, (b) $\epsilon_{dd} = -0.75$ and (c) $\epsilon_{dd} = 1.5$. Shown are the results for the modes M (circles), D (stars), Q_1 (diamonds), Q_2 (squares) and Sc (triangles). In figures (b) and (c) the frequencies for $\epsilon_{dd} = 0$ are included as dashed, gray lines.

collapse with no qualitative distinction from the non-dipolar case. The Q_1 quadrupole mode initially increases with γ, like the non-dipolar case, but as it approaches the point of collapse, it rapidly decreases towards zero. Above $\gamma^{\max}$, the Q_1 mode is dynamically unstable.

c) $\epsilon_{dd} > 0$

For $\epsilon_{dd} = 1.5$ (Fig. 2.7(a)) stable solutions exist only above a lower critical trap ratio $\gamma^{\min} \approx 2.3$. For $\gamma < \gamma^{\min}$ the attraction of the end-to-end dipoles becomes dominant and induces collapse. Indeed, we find that the Q_1 mode has zero frequency and is dynamically unstable for $\gamma < \gamma^{\min}$. Above this, the Q_1 and Q_2 frequencies increases towards the limiting values of the non-dipolar frequencies of $1.82\omega_\perp$ and $\sqrt{2}\omega_\perp$. The remaining modes behave qualitatively like the non-dipolar modes for $\gamma > \gamma^{\min}$.

2.5. Non-cylindrically-symmetric systems and relevance to rotating-trap systems

In this section we will apply our approach to the most general case of non-cylindrically-symmetric systems. An important scenario where this occurs is when condensates are rotated in elliptical harmonic traps. This has provided a robust method of generating vortices and vortex lattices in the condensate (see Ref. [66] for a review). The trap ellipticity makes the trap non-cylindrically-symmetric. While this is typically small (of the order of a few percent), the rotation tends to accentuate the ellipticity experienced by the condensate. Indeed one can derive effective harmonic trap frequencies for the condensate which show that the effective ellipticity can be orders of magnitude greater than the static ellipticity [112, 123, 129].

The rotating elliptical condensates support collective modes and these are of crucial importance in the formation of vortex lattices. By analysing the Thomas-Fermi condensate solutions in the rotating frame, it has been shown that the rotating Q_2 quadrupole mode can become highly unstable and lead to the breakdown of the vortex-free condensate [123, 129] (see also chapter 3 of this report). This prediction has been in excellent agreement with both experiments [84] and numerical simulations [102, 60]. Although we will not specifically consider rotation, our methodology can be easily extended to this scenario [129].

As in Section 2.2.4, we consider finite trap ellipticity ϵ in the $x - y$ plane. In Fig. 2.8 we present the mode frequencies as a function of ellipticity ϵ for three different examples. There are some important generic differences to the cylindrical case. Due to the complete anisotropy of the trapping potential the dipole mode frequencies (stars) all differ, and are equal to the corresponding trap frequencies $\omega_x = \sqrt{1-\varepsilon}\omega_\perp$, $\omega_y = \sqrt{1+\varepsilon}\omega_\perp$ and $\omega_z = \gamma\omega_\perp$. The monopole mode is present (circles) and its frequency increases with ϵ. The Q_2 mode is no longer present due to the breakdown of cylindrical symmetry. Instead we find a new Q_1 mode appearing (upper diamonds) which corresponds to the Q_1^{yz} mode for $\epsilon_{dd} > 0$ and the Q_1^{xz} mode for $\epsilon_{dd} \leq 0$. The usual quadrupole mode Q_1^{xy} is also present. The reader is reminded that the superscript in the Q_1 mode notation refers to the *in-phase* radii, the remaining radius oscillates out of phases with the other two. Although there are actually three permutations of Q_1, only two appear for any given value of ϵ_{dd} since linear combinations of these and the monopole mode can form the remaining Q_1 mode.

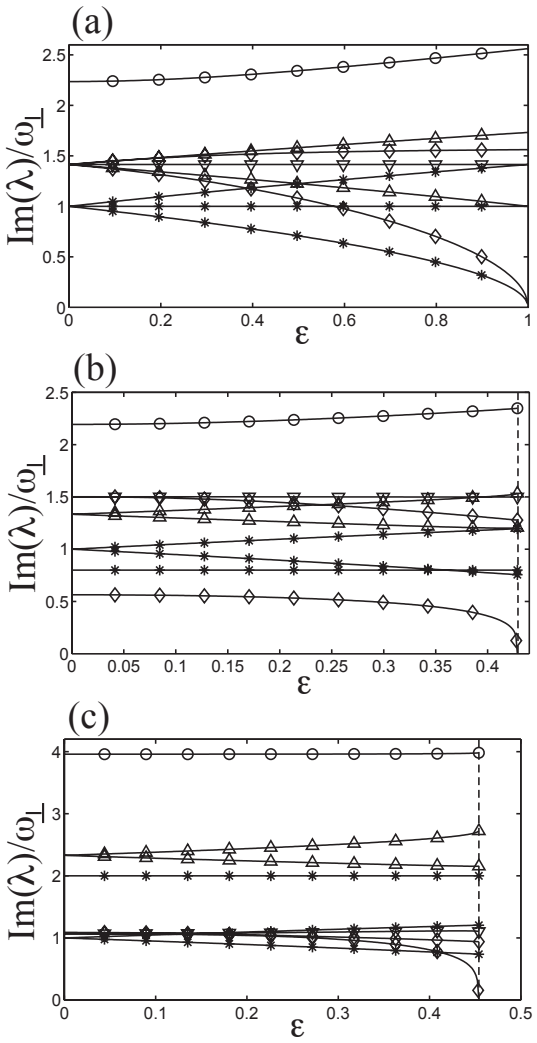

Figure 2.8.: Excitation frequencies in a non-cylindrically-symmetric trap as a function of the trap ellipticity in the $x-y$ plane ε for the cases of (a) $\epsilon_{dd}=0$ and $\gamma=1$, (b) $\epsilon_{dd}=-0.6$ and $\gamma=0.8$ and (c) $\epsilon_{dd}=1.25$ and $\gamma=2$. Shown are the modes D (stars), M (circles), Q_1 (diamonds), Sc_{xy} (triangles pointing down), Sc_{yz} (triangles pointing up, upper branch) and Sc_{xz} (triangles pointing up, lower branch).

We will now consider the specific features for the cases presented in Fig. 2.8. For $\epsilon_{dd} = 0$ and $\gamma = 1$ (Fig. 2.8(a)), the solutions are stable right up to $\epsilon = 1$. At this limit the x-direction becomes untrapped and this causes the system to become unstable with respect to the dipole D_x mode, as well the Q_1^{xy} mode which can now expand freely along the x-axis. For $\epsilon_{dd} = -0.6$ and $\gamma = 0.8$ (Fig. 2.8(b)) the solutions become unstable to collapse for $\epsilon \approx 0.425$. Only the lower Q_1^{xy} mode becomes dynamically unstable at this point, indicating that it is the mode responsible for collapse, which is towards a pancake shaped system. For $\epsilon_{dd} = 1.25$ (Fig. 2.8(c)) the solutions become unstable to collapse for $\epsilon \approx 0.45$. We again observe that the same Q_1 mode mediates the collapse, only this time the collapse is towards a cigar shaped system. The other modes remain stable.

2.6. Scissors modes

In this section we will discuss the scissors modes of the TF dipolar BEC. Note that a detailed account of the scissors mode can be found in [50]. The scissors mode of a trapped atomic cloud (thermal or BEC) is excited by suddenly rotating the anisotropic trapping potential over a small angle. Consequently, the atomic cloud will experience a restoring force exerted by the trap, and provided the angle of rotation is small, it will exhibit a shape preserving oscillation around the new equilibrium position. The exact response of the atomic cloud to the torque of the rotated trapping potential depends strongly on the moment of inertia of the cloud. Since a superfluid is restricted to irrotational flow, it will have a significantly different moment of inertia compared to a thermal cloud. In particular, when the trap anisotropy vanishes the moment of inertia of a superfluid also vanishes, whereas in a thermal cloud this is not the case. The superfluid scissors mode frequency will consequently approach a finite value, whereas for a thermal cloud it will vanish as the trap anisotropy approaches zero. A measurement of the scissors frequency therefore constitutes a direct test for superfluidity [50, 109], as has been verified experimentally for non-dipolar BECs [86, 24]. While the superfluid nature can also be verified by the creation of quantized vortices, this is not possible in highly-elongated systems.

The superfluidity of dipolar BECs has not been experimentally confirmed. As we have seen the dipolar BEC can become dominated by the attractive component of the dipolar interaction (e.g. for highly-elongated $\epsilon_{dd} > 0$ condensates or highly-flattened $\epsilon_{dd} < 0$ condensates) and, as for attractive s-wave condensates, may 'fragment' into multiple condensates [94], destroying the superfluidity of the system. Such superfluidity can be tested directly using the scissors modes.

In the following, we will consider the scissors mode to be excited by rotating both the trapping potential as well as the external aligning field of the dipoles simultaneously. Three scissors modes now appear due to the three distinct permutations of this mode, namely Sc_{xy} (triangles pointing down), Sc_{yz} (triangles pointing up, upper branch) and Sc_{xz} (triangles pointing up, lower branch). Clearly, from Fig. 2.8, the oscillation frequencies of the scissors modes are affected by the dipolar interactions. The effect of the dipolar interactions is two-fold. Firstly, since the dipolar interactions change the aspect ratio of the condensate, both the moment of inertia of the condensate and the torque from the trapping potential acting on it will be altered, which consequently will alter the oscillation frequency. Secondly, for the Sc_{xz}, Sc_{yz} modes there is an additional force present which is related to the relative position of the dipoles. This effect is easiest understood when considering a cigar shaped condensate. When

such a condensate is rotated with respect to the aligning field, the dipoles are on average slightly more side-by-side than in the equilibrium situation. As a result, there will be a dipolar restoring force trying to re-align the dipoles, which in turn is expected to affect the scissors mode frequencies. For a pancake shaped condensate the effect is opposite. Finally, note that this effect is absent for the Sc_{xy} mode.

2.7. Conclusions

We have presented a general and accessible methodology for determining the static solutions and excitation frequencies of trapped dipolar BECs in the Thomas-Fermi limit. We explore the static solutions and the low-lying collective excitations throughout a large and experimentally relevant parameter space, including positive and negative dipolar couplings $C_{\rm dd}$, positive and negative s-wave interactions g, and cylindrically and non-cylindrically symmetric systems. Moreover, our approach enables us to identify the modes responsible for collapse of the condensate. Special attention is being paid to the physics of the scissors mode, which can be used as a direct test of superfluidity.

2.8. acknowledgments

We acknowledge support from The Netherlands Organisation for Scientific Research (NWO) (R. M. W. van Bijnen and S. J. J. M. F. Kokkelmans), Canadian Commonwealth fellowship program (N. G. Parker), Australian Research Council (A. M. Martin) and Natural Sciences and Engineering Research Council of Canada (D. H. J. O'Dell). The authors also wish to thank T. Hortons for vital stimulation.

3. Exact solutions and stability of rotating dipolar Bose-Einstein condensates in the Thomas-Fermi limit

The results presented in this chapter are obtained in collaboration with A. J. Dow, D. H. J. O'Dell, N. G. Parker and A. M. Martin. The manuscript as presented here has been submitted to the journal Physical Review A, whereas a short synopsis of this work has already been published in the journal *Physical Review Letters* [129], and a slightly longer account in the journal *Laser Physics* [89], as an invited conference proceeding.

In this current paper, we present a theoretical analysis of dilute gas Bose-Einstein condensates with dipolar atomic interactions under rotation in elliptical traps. Working in the Thomas-Fermi limit, we employ the classical hydrodynamic equations to first derive the rotating condensate solutions and then consider their response to perturbations. We thereby map out the regimes of stability and instability for rotating dipolar Bose-Einstein condensates and in the latter case, discuss the possibility of vortex lattice formation. We employ our results to propose several routes to induce vortex lattice formation in a dipolar condensate.

3.1. Introduction

The achievement of Bose-Einstein condensation of ^{52}Cr atoms [47, 72, 69] has resulted in atomic Bose-Einstein condensates (BEC) with large dipole-dipole interactions. These long-range and anisotropic interactions introduce rich and complex physical effects, as well as novel opportunities to control BECs. A key example is how these interactions modify the static solutions of a trapped BEC. For a prolate (elongated) dipolar gas, with the dipoles polarised along its long axis, the net dipolar interaction is attractive, whereas for an oblate (flattened) configuration with the dipoles aligned along the short axis, the net dipolar interaction is repulsive. As a result, in comparison to a purely s-wave BEC, a dipolar BEC elongates along the direction of an applied polarizing field [118, 136]. When atomic interactions dominate over zero-point kinetic effects (formally defined as when the number of atoms tends towards infinity) the Thomas-Fermi (TF) approximation can be applied and the Gross-Pitaevskii equation for the condensate reduces to the equations of superfluid hydrodynamics at $T = 0$ [107, 109]. The TF approximation can also be applied to dipolar BECs: in a harmonic trap the exact solution for the density profile takes the familiar form of an inverted parabola [97, 35, 103].

Condensates are superfluids and so rotation can only occur through curl-free motion, e.g. via vortices with quantized circulation [107, 109]. Individual vortices [134, 98, 133] and vortex lattices [23, 140, 71] in dipolar condensates have already been studied theoretically. However, a key question that remains is how to make such states in the first place? Above a critical

rotation frequency Ω_v, the ground state contains a vortex lattice, and one experimentally successful method for achieving such a state is to use a rotating elliptical trap [85, 58]. For this scenario the hydrodynamic equations can be used to study the instability of the non-vortex state under rotation [112, 123]. The connection between this instability and the formation of a vortex lattice has been confirmed both by experiment [85, 58] and numerical simulations [80, 102]. In this paper we extend the TF approximation for rotating trapped condensates to include dipolar interactions [129, 89]. Specifically, starting from the hydrodynamic equations of motion we obtain the stationary solutions for a condensate in a rotating elliptical trap and find when they become dynamically unstable to perturbations. This enables us to predict the regimes of stable and unstable motion of a rotating dipolar condensate. While for a non-dipolar BEC (in the TF limit) the transition between stable and unstable motion is dependent only on the rotation frequency and trap ellipticity [112, 123], we show that for a dipolar BEC it is additionally dependent on the strength of the dipolar interactions and the geometry of the trap. For a dipolar BEC the critical rotation frequency at which vortices become favorable Ω_v is sensitive to the trap geometry and dipolar interactions [98], and so one cannot simply assume that instability will lead to a vortex lattice. Using a simple prediction for this frequency, we indicate the regimes in which one can expect vortex lattice formation. Experimentally accessible routes to generate instability and vortex lattices in dipolar condensates are discussed in detail.

This paper is structured as follows. In Section 3.2 we introduce the mean-field theory and the TF approximation for dipolar BECs, in Section 3.3 we derive the hydrodynamic equations for a trapped dipolar BEC in the rotating frame, and in Section 3.4 we obtain the corresponding stationary states and discuss their behaviour. In Section 3.5 we show how to obtain the dynamical stability of these states to perturbations, and in Section 3.6 we employ the results of the previous sections to discuss possible pathways to induce instability in the motion of the BEC and discuss the possibility that such instability leads to the formation of a vortex lattice. Finally in Section 3.6.2 we conclude our findings and suggest directions for future work.

3.2. Mean-field theory of a dipolar BEC

We consider a BEC with long-range dipolar atomic interactions, with the dipoles aligned in the z direction. The mean-field order parameter for the condensate $\psi \equiv \psi(\underline{r}, t)$ satisfies the Gross-Pitaevskii Equation (GPE) which is given by [45, 118, 135]

$$i\hbar\frac{\partial\psi}{\partial t} = \left[-\frac{\hbar^2}{2m}\nabla^2 + V(\underline{r}, t) + \Phi_{dd}(\underline{r}, t) + g\left|\psi\right|^2\right]\psi, \tag{3.1}$$

where m is the atomic mass and $V(\underline{r}, t)$ is the external confining potential. BECs typically feature s-wave atomic interactions which gives rise to a local cubic nonlinearity with coefficient $g = 4\pi\hbar^2 a/m$, where a is the s-wave scattering length. Note that a, and therefore g, can be experimentally tuned between positive values (repulsive interactions) and negative values (attractive interactions) by means of a Feshbach resonance [72, 69]. The dipolar interactions

lead to a non-local mean-field potential $\Phi_{dd}(\underline{r},t)$ which is given by [136]

$$\Phi_{dd}(\underline{r},t) = \int d^3r\ U_{dd}\left(\underline{r}-\underline{r}'\right)\rho\left(\underline{r}',t\right), \tag{3.2}$$

where $\rho(\underline{r},t) = |\psi(\underline{r},t)|^2$ is the condensate density and

$$U_{dd}(\underline{r}) = \frac{C_{dd}}{4\pi}\frac{1-3\cos^2\theta}{|\underline{r}|^3} \tag{3.3}$$

is the interaction potential of two dipoles separated by a vector $\underline{r}$, where θ is the angle between $\underline{r}$ and the polarization direction, which we take to be the z-axis. The dipolar BECs to date have featured permanent magnetic dipoles. Then, assuming the dipoles to have moment d_m and be aligned in an external magnetic field $\underline{B} = \hat{k}B$, the dipolar coupling is $C_{dd} = \mu_0 d_m^2$ [45], where μ_0 is the permeability of free space. Alternatively, for dipoles induced by a static electric field $\underline{E} = \hat{k}E$, the coupling constant $C_{dd} = E^2\alpha^2/\epsilon_0$ [135, 88], where α is the static polarizability and ϵ_0 is the permittivity of free space. In both cases, the sign and magnitude of C_{dd} can be tuned through the application of a fast-rotating external field [43].

We will specify the interaction strengths through the parameter $\varepsilon_{dd} = C_{dd}/3g$ which is the ratio of the dipolar interactions to the s-wave interactions [43]. We take the s-wave interactions to be repulsive, $g > 0$, and so where we discuss negative values of ε_{dd}, this corresponds to $C_{dd} < 0$. We will also limit our analysis to the regime of $-0.5 < \varepsilon_{dd} < 1$, where the Thomas-Fermi approach predicts that non-rotating stationary solutions are robustly stable [97].

We are concerned with a BEC confined by an elliptical harmonic trapping potential of the form

$$V(\underline{r}) = \frac{1}{2}m\omega_\perp^2\left[(1-\epsilon)x^2 + (1+\epsilon)y^2 + \gamma^2 z^2\right]. \tag{3.4}$$

In the $x-y$ plane the trap has mean trap frequency $\omega_\perp$ and ellipticity ϵ. The trap strength in the axial direction, and indeed the geometry of the trap itself, is specified by the trap ratio $\gamma = \omega_z/\omega_\perp$. When $\gamma \gg 1$ the BEC shape will typically be oblate (pancake-like) while for $\gamma \ll 1$ it will typically be prolate (cigar-like).

The time-dependent GPE (3.1) can be reduced to its time-independent form by making the substituation $\psi(\underline{r},t) = \sqrt{\rho(\underline{r})}\exp(i\mu t/\hbar)$, where μ is the chemical potential of the system. Assuming the TF approximation, where the kinetic energy of static solutions is taken to be negligible (in comparison to the potential and interaction energies) [103], the time-independent form of the GPE reduces to

$$V(\underline{r}) + \Phi_{dd}(\underline{r}) + g\rho(\underline{r}) = \mu, \tag{3.5}$$

where μ is the chemical potential of the condensate. For ease of calculation the dipolar potential $\Phi_{dd}(\underline{r})$ can be expressed as

$$\Phi_{dd}(\underline{r}) = -3g\varepsilon_{dd}\left(\frac{\partial^2}{\partial z^2}\phi(\underline{r}) + \frac{1}{3}\rho(\underline{r})\right), \tag{3.6}$$

where $\phi(\underline{r})$ is a fictitious 'electrostatic' potential defined by [97, 35]

$$\phi(\underline{r}) = \frac{1}{4\pi}\int\frac{d^3r'\rho(\underline{r}')}{|\underline{r}-\underline{r}'|}. \tag{3.7}$$

This effectively reduces the problem of calculating the dipolar potential (2) to the calculation of an electrostatic potential of the form (7), for which a much larger theoretical body of literature exists. Exact solutions of Eq. (5) for $\rho(\underline{r})$, $\phi(\underline{r})$ and hence $\Phi_{dd}(\underline{r})$ can be obtained for any general parabolic trap, as proven in Appendix A of Ref. [35]. In particular, the solutions of $\rho(\underline{r})$ take the form

$$\rho(\underline{r}) = \rho_0 \left(1 - \frac{x^2}{R_x^2} - \frac{y^2}{R_y^2} - \frac{z^2}{R_z^2}\right) \quad \text{for } \rho(\underline{r}) \geq 0 \tag{3.8}$$

where $\rho_0 = 15N/(8\pi R_x R_y R_z)$ is the central density. Remarkably, this is the general inverted parabola density profile familiar from the TF limit of non-dipolar BECs. An important distinction, however, is that for the dipolar BEC the aspect ratio of the parabolic solution differs from the trap aspect ratio.

3.3. Hydrodynamic Equations in the Rotating Frame

Having introduced the TF model of a dipolar BEC we now extend this to include rotation and derive hydrodynamic equations for the rotating system. We consider the rotation to act about the z-axis, described by the rotation vector $\underline{\Omega}$ where $\Omega = |\underline{\Omega}|$ is the rotation frequency and the effective Hamiltonian is given by

$$H_{\text{eff}} = H_0 - \underline{\Omega} \cdot \hat{L}, \tag{3.9}$$

where H_0 is the Hamiltonian in absence of the rotation and $\hat{L} = -i\hbar(\underline{r} \times \nabla)$ is the quantum mechanical angular momentum operator. Using this result with the Hamiltonian H_0 from Eq. (3.1) we obtain [75, 119]

$$\begin{aligned} i\hbar\frac{\partial\Psi(\underline{r},t)}{\partial t} &= \left[-\frac{\hbar^2}{2m}\nabla^2 + V(\underline{r}) + \Phi_{dd}(\underline{r},t) + g|\Psi(\underline{r},t)|^2\right. \\ &- \left.\Omega\frac{\hbar}{i}\left(x\frac{\partial}{\partial y} - y\frac{\partial}{\partial x}\right)\right]\Psi(\underline{r},t). \end{aligned} \tag{3.10}$$

Note that all space coordinates $\underline{r}$ are those of the rotating frame and the time independent trapping potential $V(\underline{r})$, given by Eq. (3.4), is stationary in this frame. Momentum coordinates, however, are expressed in the laboratory frame [75, 119, 74].

We can express the condensate mean field in terms of a density $\rho(\underline{r},t)$ and phase $S(\underline{r},t)$ as $\psi(\underline{r},t) = \sqrt{\rho(\underline{r},t)}\exp[iS(\underline{r},t)]$, and define the condensate velocity to be $\underline{v} = (\hbar/m)\nabla S$. Substuting into the time-dependent GPE (3.10) and equating imaginary and real terms leads to the following equations of motion

$$\frac{\partial\rho}{\partial t} = -\nabla\cdot[\rho\,(\underline{v} - \underline{\Omega}\times\underline{r})] \tag{3.11}$$

$$\begin{aligned} m\frac{\partial\underline{v}}{\partial t} &= -\nabla\left(\frac{1}{2}m\underline{v}\cdot\underline{v} + V(\underline{r}) + \Phi_{dd}(\underline{r})\right. \\ &\left. + g\rho - m\underline{v}\cdot[\underline{\Omega}\times\underline{r}]\right) \end{aligned} \tag{3.12}$$

In the absence of dipolar interactions ($\Phi_{dd} = 0$) Eqs. (3.11) and (3.12) are commonly known as the superfluid hydrodynamic equations [107] since they resemble the equation of continuity

and the equation of motion from standard fluid dynamics. Here we have extended them to include dipolar interactions.

Note that the definition of condensate velocity leads to the relation

$$\nabla \times \underline{v} = \frac{\hbar}{m} \nabla \times \nabla S = 0, \tag{3.13}$$

which immediately reveals that the condensate is irrotational. The exceptional case is when the velocity potential $(\hbar/m)S$ is singular, which arises when a quantized vortex occurs the system.

3.4. Stationary Solution of the Hydrodynamic Equations

We now search for stationary solutions of the hydrodynamic Eqs. (3.11) and (3.12). These states satisfy the equilibrium conditions

$$\frac{\partial \rho}{\partial t} = 0, \qquad \frac{\partial \underline{v}}{\partial t} = 0. \tag{3.14}$$

Following the approach of Recati et al. [112] we assume the velocity field ansatz

$$\underline{v} = \alpha \nabla (xy). \tag{3.15}$$

Here α is a velocity field amplitude that will provide us with a key parameter to parameterise our rotating solutions. Note that this is the velocity field in the laboratory frame expressed in the coordinates of the rotating frame, and also that it satisfies the irrotationality condition (3.13). Combining Eqs. (3.12) and (3.15) we obtain the relation

$$\mu = \frac{m}{2} \left(\tilde{\omega}_x^2 x^2 + \tilde{\omega}_y^2 y^2 + \omega_z^2 z^2 \right) + g\rho(\underline{r}) + \Phi_{dd}(\underline{r}), \tag{3.16}$$

where the *effective* trap frequencies $\tilde{\omega}_x$ and $\tilde{\omega}_y$ are given by,

$$\tilde{\omega}_x^2 = \omega_\perp^2 (1 - \epsilon) + \alpha^2 - 2\alpha\Omega \tag{3.17}$$

$$\tilde{\omega}_y^2 = \omega_\perp^2 (1 + \epsilon) + \alpha^2 + 2\alpha\Omega. \tag{3.18}$$

The dipolar potential inside an inverted parabola density profile (3.8) has been found in Refs. [35, 129] to be

$$\frac{\Phi_{dd}}{3g\varepsilon_{dd}} = \frac{\rho_0 \kappa_x \kappa_y}{2} \left[\beta_{001} - \frac{x^2 \beta_{101} + y^2 \beta_{011} + 3z^2 \beta_{002}}{R_z^2} \right] - \frac{\rho}{3} \tag{3.19}$$

where we have defined the condensate aspect ratios $\kappa_x = R_x/R_z$ and $\kappa_y = R_y/R_z$, and where the coefficients β_{ijk} are given by

$$\beta_{ijk} = \int_0^\infty \frac{ds}{\left(\kappa_x^2 + s\right)^{i+\frac{1}{2}} \left(\kappa_y^2 + s\right)^{j+\frac{1}{2}} \left(1 + s\right)^{k+\frac{1}{2}}}, \tag{3.20}$$

where i, j and k are integers. Note that for the cylindrically symmetric case, where $\kappa_x = \kappa_y = \kappa$, the integrals β_{ijk} evaluate to [46]

$$\beta_{ijk} = 2\frac{{}_2F_1\left(k+\frac{1}{2},1;i+j+k+\frac{3}{2};1-\kappa^2\right)}{(1+2i+2j+2k)\,\kappa^{2(i+j)}} \tag{3.21}$$

where ${}_2F_1$ denotes the Gauss hypergeometric function [2]. Thus we can rearrange Eq. (3.16) to obtain an expression for the density profile

$$\begin{aligned}\rho &= \frac{\mu - \frac{m}{2}\left(\tilde{\omega}_x^2x^2+\tilde{\omega}_y^2y^2+\omega_z^2z^2\right)}{g\left(1-\varepsilon_{dd}\right)} \\ &+ \frac{3g\varepsilon_{dd}\frac{n_0\kappa_x\kappa_y}{2R_z^2}\left[x^2\beta_{101}+y^2\beta_{011}+3z^2\beta_{002}-R_z^2\beta_{001}\right]}{g\left(1-\varepsilon_{dd}\right)}.\end{aligned} \tag{3.22}$$

Comparing the x^2, y^2 and z^2 terms in Eq. (3.8) and Eq. (3.22) we find three self-consistency relations that define the size and shape of the condensate:

$$\kappa_x^2 = \left(\frac{\omega_z}{\tilde{\omega}_x}\right)^2\frac{1+\varepsilon_{dd}\left(\frac{3}{2}\kappa_x^3\kappa_y\beta_{101}-1\right)}{\zeta}, \tag{3.23}$$

$$\kappa_y^2 = \left(\frac{\omega_z}{\tilde{\omega}_y}\right)^2\frac{1+\varepsilon_{dd}\left(\frac{3}{2}\kappa_y^3\kappa_x\beta_{011}-1\right)}{\zeta}, \tag{3.24}$$

$$R_z^2 = \frac{2g\rho_0}{m\omega_z^2}\zeta, \tag{3.25}$$

where $\zeta = 1-\varepsilon_{dd}\left[1-\frac{9\kappa_x\kappa_y}{2}\beta_{002}\right]$. Furthemore, by inserting Eq. (3.22) into Eq. (3.11) we find that stationary solutions satisfy the condition

$$\begin{aligned}0 &= (\alpha+\Omega)\left(\tilde{\omega}_x^2-\frac{3}{2}\varepsilon_{dd}\frac{\omega_\perp^2\kappa_x\kappa_y\gamma^2}{\zeta}\beta_{101}\right) \\ &+ (\alpha-\Omega)\left(\tilde{\omega}_y^2-\frac{3}{2}\varepsilon_{dd}\frac{\omega_\perp^2\kappa_x\kappa_y\gamma^2}{\zeta}\beta_{011}\right).\end{aligned} \tag{3.26}$$

We can now solve Eq. (3.26) to give the velocity field amplitude α for a given ε_{dd}, Ω and trap geometry. In the limit $\varepsilon_{dd} = 0$ this amplitude is independent of the s-wave interaction strength g and the trap ratio γ. However, in the presence of dipolar interactions the velocity field amplitude becomes dependent on both g and γ. For fixed ε_{dd} and trap geometry, Eq. (3.26) leads to branches of α as a function of rotation frequency Ω. These branches are significantly different between elliptical and non-elliptical traps, and so we will consider each case in turn. Note that we restrict our analysis to the range $\Omega < 1$: for $\Omega \sim 1$ the static solutions can disappear, with the condensate becoming unstable to a centre-of-mass instability [112].

3.4.1. Cylindrically symmetric traps: $\epsilon = 0$

We first consider the case of a trap with no ellipticity $\epsilon = 0$. In Fig. 3.1(a) we plot the solutions of Eq. (3.26) as a function of rotation frequency Ω for a spherically-symmetric trap

$\gamma = 1$ and for various values of ε_{dd}. Before dicussing the specific cases, let us first point out that for each ε_{dd} the solutions have the same qualitative structure. Up to some critical rotation frequency, only one solution exists, corresponding to $\alpha = 0$. At this critical point the solution bifurcates, giving two additional solutions for $\alpha > 0$ and $\alpha < 0$ on top of the original $\alpha = 0$ solution. We term this critical frequency the bifurcation frequency Ω_b.

For $\varepsilon_{dd} = 0$ we regain the results of Refs. [112, 123] with a bifurcation point at $\Omega_b = \omega_\perp/\sqrt{2}$ and, for $\Omega > \Omega_b$, non-zero solutions given by $\alpha = \pm\sqrt{2\Omega^2 - \omega_\perp^2}/\omega_\perp$ [112]. The physical significance of the bifurcation frequency has been established for the non-dipolar case and is related to the fact that the system becomes energetically unstable to quadrupole modes for $\Omega \geq \omega_\perp/\sqrt{2}$. In the TF limit, a general surface excitation with angular momentum $\hbar l = \hbar q_l R$, where R is the TF radius and q_l is the quantized wave number, obeys the classical dispersion relation $\omega_l^2 = (q_l/m)\nabla_R V$ involving the local harmonic potential $V = m\omega_\perp^2 R^2/2$ evaluated at R [109]. Consequently, for the non-rotating and non-dipolar BEC $\omega_l = \sqrt{l}\omega_\perp$. Meanwhile, inclusion of the rotational term in the Hamiltonian (3.9) shifts the mode frequency by $-l\Omega$. Then, in the rotating frame, the frequency of the $l = 2$ quadrupole surface excitation becomes $\omega_2(\Omega) = \sqrt{2}\omega_\perp - 2\Omega$ [109]. The bifurcation frequency thus coincides with the vanishing of the energy of the quadrupolar mode in the rotating frame, and the two additional solutions arise from excitation of the quadrupole mode for $\Omega \geq \omega_\perp/\sqrt{2}$.

For the non-dipolar BEC it is noteworthy that Ω_b does not depend on the interactions. This feature arises because the mode frequencies ω_l themselves are independent of g. However, in the case of long-range dipolar interactions the potential Φ_{dd} of Eq. (3.6) gives non-local contributions, breaking the simple dependence of the force $-\nabla V$ upon R [97]. Thus we expect the resonant condition for exciting the quadrupolar mode, i.e. $\Omega_b = \omega_l/l$ (with $l = 2$), to change with ε_{dd}. In Fig. 3.1(a) we see that this is the case: as dipole interactions are introduced, our solutions change and the bifurcation point, Ω_b, moves to lower (higher) frequencies for $\varepsilon_{dd} > 0$ ($\varepsilon_{dd} < 0$). Note that the parabolic solution still satisfies the hydrodynamic equations providing $-0.5 < \varepsilon_{dd} < 1$. Outside of this range the parabolic solution may still exist but it is no longer guaranteed to be stable against perturbations.

Density profiles for $\alpha = 0$ have zero ellipticity in the $x - y$ plane. By contrast, the $|\alpha| > 0$ solutions have an elliptical density profile, even though the trap itself has zero ellipticity. This remarkable feature arises due to a spontaneous breaking of the axial rotational symmetry at the bifurcation point. For $\alpha > 0$ the condensate is elongated in x while for $\alpha < 0$ it is elongated in y, as illustrated in the insets in Fig. 3.1(a). In the absence of dipolar interactions the $|\alpha| > 0$ solutions can be intepreted solely in terms of the effective trapping frequencies $\tilde{\omega}_x$ and $\tilde{\omega}_y$ given by Eqs. (3.17) and (3.18). The introduction of dipolar interactions considerably complicates this picture, since they also modify the shape of the solutions. Notably, for $\varepsilon_{dd} > 0$ the dipolar interactions make the BEC more prolate, i.e., reduce κ_x and κ_y, while for $\varepsilon_{dd} < 0$ they make the BEC more oblate, i.e., increase κ_x and κ_y.

In Fig. 3.1(a) we see that as the dipole interactions are increased the bifurcation point Ω_b moves to lower frequencies. The bifurcation point can be calculated analytically as follows. First, we note that for $\alpha = 0$ the condensate is cylindrically symmetric and $\kappa_x = \kappa_y = \kappa$. The aspect ratio κ is found from [97, 35]

$$\left[\left(\frac{\gamma^2}{2} + 1\right)\frac{f(\kappa)}{1-\kappa^2} - 1\right] + \frac{(\varepsilon_{dd} - 1)\left(\kappa^2 - \gamma^2\right)}{3\kappa^2\varepsilon_{dd}} = 0 \tag{3.27}$$

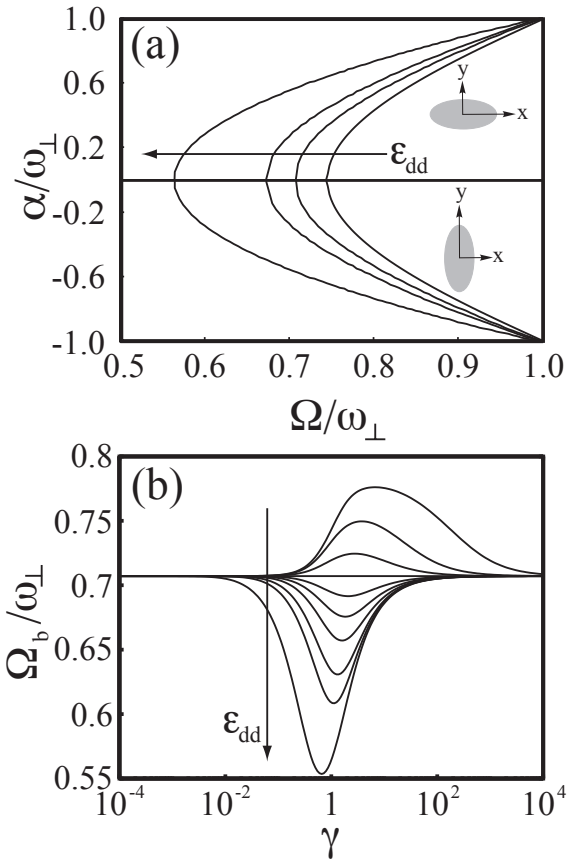

Figure 3.1.: (a) Irrotational velocity field amplitude α of the static condensate solutions as a function of the trap rotation frequency Ω in a spherically-symmetric trap ($\gamma = 1$ and $\epsilon = 0$). Various values of ε_{dd} are presented: $\varepsilon_{dd} = -0.5$, 0, 0.5 and 1.0. Insets illustrate the geometry of the condensate in the $x - y$ plane. (b) The bifurcation frequency Ω_b (the point at which the solutions of α in (a) bifurcate) according to Eq. (3.29) versus trap ratio γ. Plotted are the results for $\varepsilon_{dd} = -0.49$, -0.4, -0.2, 0, 0.2, 0.4, 0.6, 0.8, 0.9 and 0.99. In (a) and (b) ε_{dd} increases in the direction of the arrow.

where

$$f(\kappa) = \frac{2 + \kappa^2 \left[4 - 3\beta_{000}\right]}{2\left(1 - \kappa^2\right)}. \tag{3.28}$$

where $\beta_{000} = (1/\sqrt{1-\kappa^2}) \ln[(1+\sqrt{1-\kappa^2})/(1-\sqrt{1-\kappa^2})]$ for the prolate case ($\kappa < 1$), and $\beta_{000} = (2/\sqrt{\kappa^2-1}) \arctan[\sqrt{\kappa^2-1}]$ for the oblate case ($\kappa > 1$). For small $\alpha \to 0_+$, we can calculate the first order corrections to κ_x and κ_y with respect to κ from Eqs. (3.23,3.24). We can then insert these values in Eq. (3.26) and solve for Ω, noting that in the limit $\alpha \to 0$ we have $\Omega \to \Omega_b$. Thus, we find (see Appendix H)

$$\frac{\Omega_b}{\omega_\perp} = \sqrt{\frac{1}{2} + \frac{3}{4}\kappa^2 \varepsilon_{dd} \gamma^2 \frac{\kappa^2 \beta_{201} - \beta_{101}}{1 - \varepsilon_{dd}\left(1 - \frac{9}{2}\kappa^2 \beta_{002}\right)}}. \tag{3.29}$$

In Fig. 3.1(b) we plot Ω_b [Eq. (3.29)] as a function of γ for various values of ε_{dd}. For $\varepsilon_{dd} = 0$ we find that the bifurcation point remains unaltered at $\Omega_b = \omega_x/\sqrt{2}$ as $\gamma = \omega_z/\omega_x$ is changed [112, 123]. As ε_{dd} is increased the value of γ for which Ω_b is a minimum changes from a trap shape which is oblate ($\gamma > 1$) to prolate ($\gamma < 1$). Note that for $\varepsilon = 0.99$ the minimum bifurcation frequency occurs at $\Omega_b \approx 0.55$, which is over a 20% deviation from the non-dipolar value. For more extreme values of ε_{dd} we can expect Ω_b to deviate even further, although the validity of the inverted parabola TF solution does not necessary hold. For a fixed γ we also find that as ε_{dd} increases the bifurcation frequency decreases monotonically.

3.4.2. Elliptical traps: $\epsilon > 0$

Consider now the effect of finite trap anisotropies ($\epsilon > 0$). Rotating elliptical traps have been created experimentally with laser and magnetic fields [85, 58]. Following the experiment of Madison *et al.* [85] we will employ a very weak trap ellipticity of $\epsilon = 0.025$. In Fig. 3.2(a) we have plotted the solutions to Eq. (3.26) for various values of ε_{dd} in a spherical trap $\gamma = 1$. As predicted for non-dipolar interactions [112, 123] the solutions become heavily modified for $\epsilon > 0$. There exists an upper branch of $\alpha > 0$ solutions which exists over the whole range of Ω, and a lower branch of $\alpha < 0$ solutions which back-bends and is double-valued. We term the frequency at which the lower branch back-bends to be the back-bending frequency Ω_b. The bifurcation frequency in non-elliptical traps can be regarded as the limiting case of the back-bending frequency, with the differing nonclamenture employed to emphasise the different structure of the solutions at this point. However, for convenience we will employ the same parameter for both, Ω_b. No $\alpha = 0$ solution exists (for any non-zero Ω). In the absence of dipolar interactions the effect of increasing the trap ellipticity is to *increase* the back-bending frequency Ω_b. Turning on the dipolar interactions, as in the case of $\epsilon = 0$, *reduces* Ω_b for $\varepsilon_{dd} > 0$, and *increases* Ω_b for $\varepsilon_{dd} < 0$. This is more clearly seen in Fig. 3.2(b) where Ω_b is plotted versus ε_{dd} for various values of the trap ratio γ. Also, as in the $\epsilon = 0$ case, increasing ε_{dd} decreases both κ_x and κ_y, i.e. the BEC becomes more prolate.

3.5. Dynamical Stability of Stationary Solutions

Although the solutions derived above are static solutions they are not necessarily stable, and so in this section we predict their dynamical stability. Consider small perturbations in the

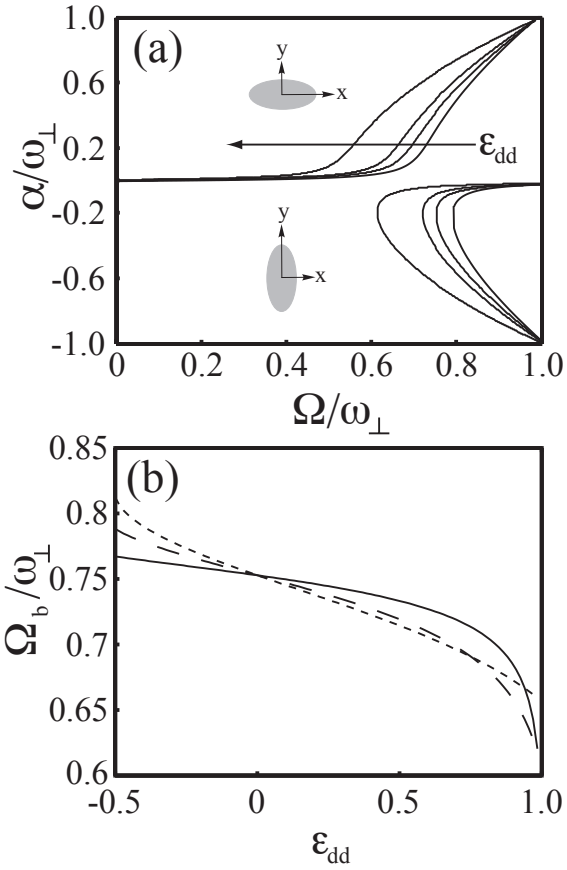

Figure 3.2.: (a) Irrotational velocity field amplitude, α, as a function of the trap rotation frequency, Ω, for a trap ratio $\gamma = 1$ and ellipticity $\epsilon = 0.025$. Various values of ε_{dd} are presented, $\varepsilon_{dd} = -0.49$, 0, 0.5 and 0.99, with ε_{dd} increasing in the direction of the arrow. Insets illustrate the geometry of the condensate in the $x-y$ plane. (b) Backbending point Ω_b versus ε_{dd} for $\epsilon = 0.025$ and $\gamma = 0.5$ (solid curve), 1.0 (long dashed curve) and 2.0 (short dashed curve).

BEC density and phase of the form $\rho = \rho_0 + \delta\rho$ and $S = S_0 + \delta S$. Then, by linearizing the hydrodynamic equations Eqs. (3.11, 3.12), the dynamics of such perturbations can be described as (see Appendices E and F)

$$\frac{\partial}{\partial t}\begin{bmatrix} \delta S \\ \delta\rho \end{bmatrix} = -\begin{bmatrix} \underline{v}_c \cdot \nabla & g\left(1+\varepsilon_{dd}K\right)/m \\ \nabla\cdot\rho_0\nabla & \left[(\nabla\cdot\underline{v}) + \underline{v}_c\cdot\nabla\right] \end{bmatrix}\begin{bmatrix} \delta S \\ \delta\rho \end{bmatrix} \tag{3.30}$$

where $\underline{v}_c = \underline{v} - \underline{\Omega}\times\underline{r}$ and the integral operator K is defined as

$$(K\delta\rho)(\underline{r}) = -3\frac{\partial^2}{\partial z^2}\int \frac{\delta\rho(\underline{r}')\ d\underline{r}'}{4\pi\left|\underline{r}-\underline{r}'\right|} - \delta\rho(\underline{r}). \tag{3.31}$$

The integral in the above expression is carried out over the domain where $\rho_0 > 0$, that is, the general ellipsoidal domain with radii R_x, R_y, R_z of the unperturbed condensate. Extending the integration domain to the region where $\rho_0 + \delta\rho > 0$ adds higher order effects since it is exactly in this domain that $\rho_0 = \mathcal{O}(\delta\rho)$. To investigate the stability of the BEC, we look for eigenfunctions and eigenvalues of the operator (3.30): dynamical instability arises when one or more eigenvalues, λ, possess a positive real part. Note that the imaginary eigenvalues of Eq. (3.30) relate to stable collective modes of the system [111], e.g. sloshing and breathing, and have been analysed elsewhere for dipolar BECs (See Chapter 2 of this report). In order to find such eigenfunctions we follow Refs. [129, 123] and consider a polynomial ansatz for the perturbations in the coordinates x, y and z, of total degree N. All operators in (3.30), acting on polynomials of order N, result in polynomials of (at most) the same order, including the operator K. This latter fact was known to 19th century astrophysicists who calculated the gravitational potential of a heterogeneous ellipsoid with polynomial density [36, 34]. The integral appearing in Eq. (3.31) is exactly equivalent to such a potential. A more recent paper by Levin and Muratov summarises these results and presents a more manageable expression for the resulting potential [76]. Hence, using these results the operator K can be evaluated for a general polynomial density perturbation $\delta\rho = x^p y^q z^r$, with p, q and r being non-negative integers. Therefore, the perturbation evolution operator (3.30) can be rewritten as a scalar matrix operator, acting on vectors of polynomial coefficients, for which finding eigenvectors and eigenvalues is a trivial computational task.

Using the above approach we determine the real positive eigenvalues of Eq. (3.30) and thereby predict the regions of dynamical instability of the static solutions. We focus on the case of an elliptical trap since this is the experimentally relevant case. In the $\alpha < 0$ half-plane, the static solutions nearest the $\alpha = 0$ axis never become dynamically unstable, except for a small region $\Omega \simeq \omega_\perp$, due to a centre-of-mass instability of the condensate [115]. The other lower branch solutions are always dynamically unstable and therefore expected to be irrelevant to experiment. As such we only consider dynamical instability for the upper branch solutions, with $\alpha > 0$. In Fig. 3.3(a) we plot the maximum positive real eigenvalues of the upper branch solutions as a function of Ω. It is clear that dynamical instability occurs over a range of rotation frequencies. The lower bound of this region, which we define as Ω_i, is the key parameter (the upper bound is largely insensitive to ε_{dd}). As ε_{dd} is increased Ω_i decreases and, accordingly, the unstable range of Ω widens.

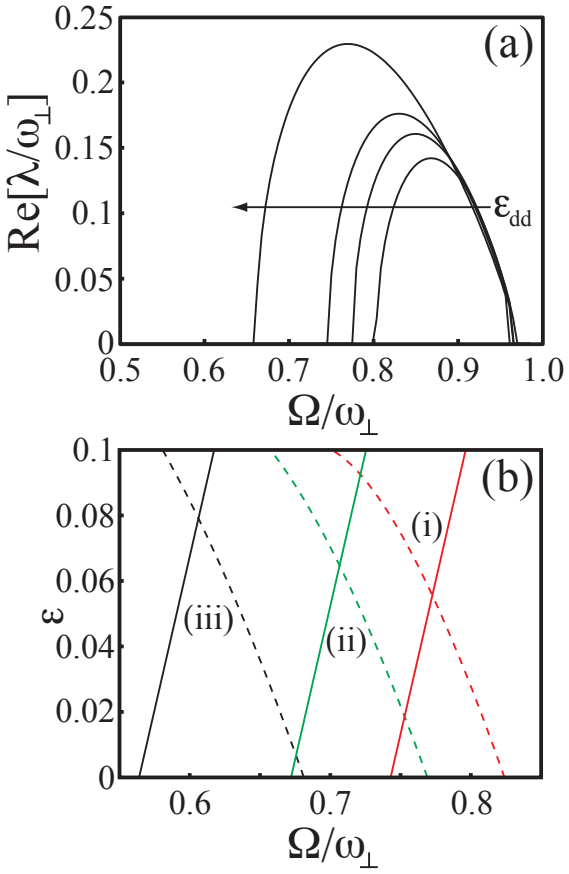

Figure 3.3.: (a) The maximum positive real eigenvalues of Eq. (3.30) (solid curves) for the upper-branch solutions of α as a function of Ω. We assume $\epsilon = 0.025$, $\gamma = 1$ and $N = 3$, and present various dipolar strengths $\varepsilon_{dd} = -0.49$, 0, 0.5 and 0.99, with ε_{dd} increasing in the direction of the arrow. (b) Phase diagram of ϵ versus Ω_b (solid curves) and Ω_i (dashed curves) for $\gamma = 1$ and (i) $\varepsilon_{dd} = -0.49$, (ii) 0.5 and (iii) 0.99.

3.6. Routes to instability and vortex lattice formation

3.6.1. Procedures to induce instability

For a non-dipolar BEC the static solutions and their stability in the rotating frame depend only on rotation frequency Ω and trap ellipticity ϵ. Adiabatic changes in ϵ and Ω can be employed to evolve the condensate through the static solutions and reach a point of instability. Indeed, this has been realized both experimentally [85, 58] and numerically [80, 102], with excellent agreement to the hydrodynamic predictions. For the case of a dipolar BEC we have shown in Sections 3.4 and 3.5 that the static solutions and their instability depend additionally on the trap ratio γ and the interaction parameter ε_{dd}. Since all of these parameters can be experimentally tuned in time, one can realistically consider each parameter as a distinct route to traverse the parameter space of solutions and induce instability in the system. Below we describe each such route, beginning with the established routes in which (i) Ω and (ii) ϵ are varied, and then novel routes based on adiabatic changes in (iii) ε_{dd} and (iv) γ. In each case it is crucial to consider the behaviour of the points of instability, namely the back-bending point Ω_b and the onset of dynamical instability of the upper branch Ω_i.

i) Adiabatic introduction of Ω: The relevant parameter space of ϵ and Ω is presented in Fig. 3.3(b), with the instability frequencies $\Omega_b(\epsilon)$ (solid curves) and $\Omega_i(\epsilon)$ (dashed curves) indicated. We imagine a BEC confined to a non-rotating trap with finite ellipticity ϵ. The trap rotation frequency Ω is then increased adiabatically such that the BEC follows the upper branch solution, such as those shown in Fig. 3.2(a). The BEC traces out a horizontal path in Fig. 3.3(b) until it reaches $\Omega_i(\epsilon)$. Here the stationary solution becomes dynamically unstable or, more precisely, the local energy minimum of the stationary state turns into a saddle point. Figure 3.3(b) shows that as ε_{dd} is increased, $\Omega_i(\epsilon)$ is decreased and as such instabilities in the stationary solutions will occur at lower rotation frequencies.

ii) Adiabatic introduction of ϵ: Here we begin with a cylindrically symmetric ($\epsilon = 0$) trap, rotating at a fixed frequency Ω. The trap ellipticity ϵ is then increased adiabatically and in the phase diagram of Fig. 3.3(b) the BEC traces out a vertical path starting at $\epsilon = 0$. The ensuing dynamics depend on the trap rotation speed relative to $\Omega_b(\epsilon = 0)$:

(a) For $\Omega < \Omega_b(\epsilon = 0)$ the condensate follows the upper branch of the static solutions which moves progressively to larger α. For $\Omega < \Omega_i(\epsilon)$ the BEC remains stable but as ϵ is increased further the condensate eventually becomes dynamically unstable. Figure 3.3(b) shows that as ε_{dd} is increased $\Omega_i(\epsilon)$ is decreased and as such the dynamical instability of the stationary solutions occurs at a lower trap ellipticities.

(b) For $\Omega > \Omega_b(\epsilon = 0)$ the condensate accesses the lower branch solutions nearest the $\alpha = 0$ axis. These solutions are always dynamically stable and the criteria for instability is instead determined by whether the solution exists. As ϵ is increased the back-bending frequency $\Omega_b(\epsilon)$ increases. Therefore, when ϵ exceeds some critical value the lower branch solutions disappear for the chosen value of rotation frequency Ω. This occurs when $\Omega < \Omega_b(\epsilon)$. Figure 3.3(b) shows that as ε_{dd} is increased $\Omega_b(\epsilon)$ is decreased and as such instabilities in the system will occur at a higher trap ellipticity. At this point the condensate no longer represents a stable solution.

iii) Adiabatic change of ε_{dd}: The relevant parameter space of ε_{dd} and Ω is shown in Fig. 3.4(a) for several different trap ratios. We assume an initial BEC in a trap with finite

ellipticity $\epsilon = 0.025$ and rotation frequency Ω. This initial state can be achieved, for example, by increasing ϵ from zero at fixed Ω. Then, by changing ε_{dd} adiabatically an instability can be induced in two ways:

(a) For $\Omega < \Omega_b(\varepsilon_{dd})$ the condensate follows the upper branch solutions. Thus for $\Omega < \Omega_i(\varepsilon_{dd})$ the motion remains stable. However, for $\Omega > \Omega_i(\varepsilon_{dd})$ the upper branch becomes unstable. In Fig. 3.4(a) $\Omega_i(\varepsilon_{dd})$ (dashed curves) is plotted for different trap ratios. As can be seen, the upper branch becomes more stable as ε_{dd} is decreased.

(b) For $\Omega > \Omega_b(\varepsilon_{dd})$ the condensate follows the lower branch solutions nearest the $\alpha = 0$ axis. These solutions are always stable and hence an instability can only be induced when this solution no longer exists, i.e. $\Omega < \Omega_b(\varepsilon_{dd})$. Figure 3.4(a) shows $\Omega_b(\varepsilon_{dd})$ (solid curves) for various trap aspect ratios. As can be seen the back-bending frequency Ω_b decreases as ε_{dd} is increased. Thus if ε_{dd} is increased the system will remain stable. However if ε_{dd} is decreased then the motion will become unstable when $\Omega = \Omega_b(\varepsilon_{dd})$.

iv) Adiabatic change of γ: Figure 3.4(b) shows the parameter space of γ and Ω. Consider, again, an initial stable condensate with finite trap rotation frequency Ω and ellipticity $\epsilon = 0.025$. Then through adiabatic changes in γ the condensate can traverse the parameter space and, depending on the initial conditions, the instability can arise in two ways:

(a) For $\Omega < \Omega_b(\gamma)$ the condensate exists on the upper branch. It is then relevant to consider the onset of dynamical instability $\Omega_i(\gamma)$ (dashed curves in Fig. 3.4(b)). Providing $\Omega < \Omega_i(\gamma)$ the solution remains dynamically stable. However, once $\Omega > \Omega_i(\gamma)$ the upper branch solutions becomes unstable.

(b) For $\Omega > \Omega_b(\gamma)$ the condensate exists on the lower branch nearest the $\alpha = 0$ axis. These solutions are always dynamically stable and instability can only occur when the motion of the back-bending point causes the solution to disappear. This occurs when $\Omega < \Omega_b(\gamma)$, with $\Omega_b(\gamma)$ shown in Fig. 3.4(b) by solid curves for various dipolar interaction strengths.

3.6.2. Is the final state of the system a vortex lattice?

Having revealed the points at which a rotating dipolar condensate becomes unstable we will now address the question of whether this instability leads to a vortex lattice. First, let us review the situation for a non-dipolar BEC. The presence of vortices in the system becomes energetically favourable when the rotation frequency exceeds a critical frequency Ω_v. Working in the TF limit, with the background density taking the parabolic form (3.8), Ω_v can be approximated as [81]

$$\Omega_v = \frac{5}{2}\frac{\hbar}{mR^2}\ln\frac{0.67R}{\xi_s} \tag{3.32}$$

Here the condensate is assumed to be circularly symmetric with radius R, and $\xi_s = \hbar/\sqrt{2m\rho_0 g}$ is the healing length that characterises the size of the vortex core. For typical condensate parameters $\Omega_v \sim 0.4\omega_\perp$. It is observed experimentally, however, that vortex lattice formation occurs at considerably higher frequencies, typically $\Omega \sim 0.7\omega_\perp$. This difference arises because above Ω_v the vortex-free solutions remain remarkably stable. It is only once a hydrodynamic instability occurs (which occurs in the locality of $\Omega \approx 0.7\omega_\perp$) that the condensate has a mechanism to deviate from the vortex-free solution and relax into a vortex lattice. Another way of visualising this is as follows. Above Ω_v the vortex-free condensate resides in some local energy minimum, while the global minimum represents a vortex or vortex lattice state. Since

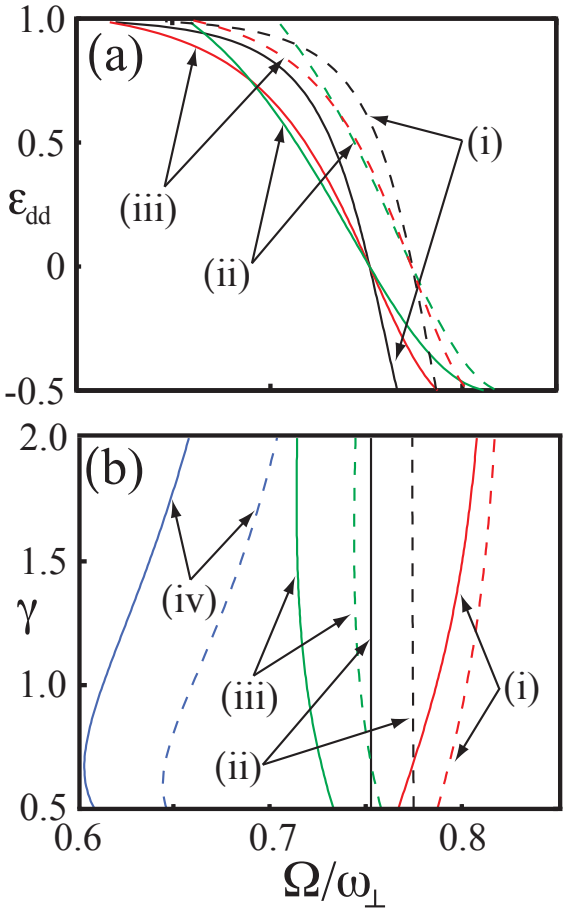

Figure 3.4.: (a) Phase diagram of ε_{dd} versus Ω_b (solid curves) and Ω_i (dashed curves) for $\epsilon = 0.025$ and (i) $\gamma = 0.5$, (ii) 1 and (iii) 2. (b) Phase diagram of γ versus Ω_b (solid curves) and Ω_i (dashed curves) for $\epsilon = 0.025$ and (i) $\varepsilon_{dd} = -0.49$, (ii) 0, (iii) 0.5 and (iv) 0.99.

the vortex is a topological defect, there typically exists a considerable energy barrier for a vortex to enter the system. However, the hydrodynamic instabilities offer a route to navigate the BEC out of the vortex-free local energy minimum towards the vortex lattice state.

Note that vortex lattice formation occurs via non-trivial dynamics. The initial hydrodynamic instability in the vortex-free state that we have discussed in this paper is only the first step [102]. For example, if the condensate is on the upper branch of hydrodynamic solutions (e.g. under adiabatic introduction of Ω) and undergoes a dynamical instability, this leads to the exponential growth of surface ripples in the condensate [102, 85]. Alternatively, if the condensate is on the lower branch and the static solutions disappear (e.g. following the introduction of ϵ) the condensate undergoes large and dramatic shape oscillations. In both cases the destabilisation of the vortex-free condensate leads to the nucleation of vortices into the system. A transient turbulent state of vortices and density perturbations then forms, which subsequently relaxes into a vortex lattice configuration [102, 100].

In the presence of dipolar interactions, however, the critical frequency for a vortex depends crucially on the trap geometry γ and the strength of the dipolar interactions ε_{dd}. Following reference [98] we will make a simple and approximated extension of Eq. (3.32) to a dipolar BEC. We will consider a circularly-symmetric dipolar condensate with radius $R = R_x = R_y$ that satisfies Eqs. (3.25), and insert this into Eq. (3.32) for the condensate radius. This method still assumes that the size of the vortex is characterised by the s-wave healing length ξ_s. Although one does expect the dipolar interactions to modify the vortex size, it should be noted that Eq. (3.32) only has logarithmic accuracy and is relatively insensitive to the choice of vortex lengthscale. The dominant effect of the dipolar interactions in Eq. (3.32) comes from the radial size and is accounted for. Note also that this expression is for a circularly symmetric system while we are largely concerned with elliptical traps. However we will employ a very weak ellipticity $\epsilon = 0.025$ for which we expect the correction to the critical frequency to be correspondingly small.

As an example, we take the parameter space of rotation frequency Ω and dipolar interactions ε_{dd}. We first consider the behavior in an oblate trap with $\gamma = 10$. In Fig. 3.5(a) we plot the instability frequencies Ω_i and Ω_b for this system as a function of the dipolar interactions ε_{dd}. Depending on the specifics of how this parameter space is traversed, either by adiabatic changes in Ω (vertical path) or ε_{dd} (horizontal path), the condensate will become unstable when it reaches one of the instability lines (short and long dashed lines). These points of instability decrease weakly with dipolar interactions and have the approximate value $\Omega_i \approx \Omega_b \approx 0.75\omega_\perp$. On the same plot we present the critical rotation frequency Ω_v according to Eq. (3.32). In order to calculate this we have assumed a BEC of 150,000 ^{52}Cr atoms confined within a trap with $\omega_\perp = 2\pi \times 200$Hz. In this oblate system we see that the dipolar interactions lead to a decrease in Ω_v, as noted in [98]. This dependence is very weak and throughout the range of ε_{dd} presented it maintains the approximate value $\Omega_v \approx 0.1\omega_\perp$. Importantly these results show that when the condensate becomes unstable a vortex/vortex lattice state is energetically favoured. As such, we expect that in an oblate dipolar BEC a vortex lattice will ultimately form when these instabilities are reached.

In Fig. 3.5(b), we make a similar plot but for a prolate trap with $\gamma = 0.1$. The instability frequencies show a somewhat similar behaviour to the oblate case. However, Ω_v is drastically different, increasing significantly with ε_{dd}. We find that this qualitative behaviour occurs consistently in prolate systems, as noted in [98]. This introduces two regimes depending on the

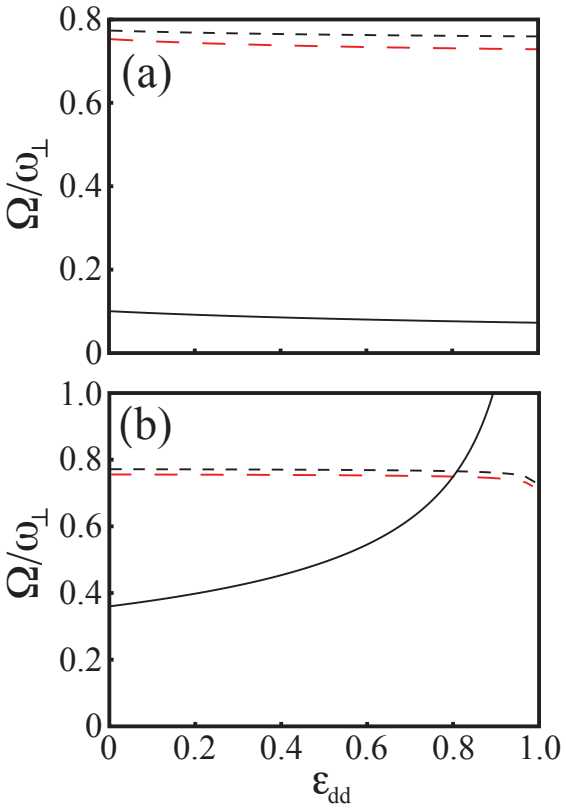

Figure 3.5.: The relation between the instability frequencies, Ω_b (long dashed red curve) and Ω_i (short dashed curve), and the critical rotation frequency for vorticity Ω_v (solid curve) for (a) an oblate trap $\gamma = 10$ and (b) a prolate trap $\gamma = 0.1$. The instability frequencies are based on a trap with ellipticity $\epsilon = 0.025$ while Ω_v is obtained from Eq. (3.32) under the assumption of a ^{52}Cr BEC with $150,000$ atoms and scattering length $a_s = 5.1$nm in a circularly symmetric trap with $\omega_\perp = 2\pi \times 200$Hz.

dipolar interactions. For $\varepsilon_{dd} \lesssim 0.8$, $\Omega_{i,b} > \Omega_v$, and so we expect a vortex/vortex lattice state to form following the instability. However, for $\varepsilon \gtrsim 0.8$ we find an intriguing new regime in which $\Omega_{i,b} < \Omega_v$. In other words, while the instability in the vortex-free parabolic density profile still occurs, a vortex state is not energetically favorable. The final state of the system is therefore not clear. Given that a prolate dipolar BEC is dominated by attractive interactions (since the dipoles lie predominantly in an attractive end-to-end configuration) one might expect similar behavior to the case of conventional BECs with attractive interactions ($g < 0$) where the formation of a vortex lattice can also be energetically unfavorable. Suggestions for final state of the condensate in this case include centre-of-mass motion and collective oscillations, such as quadrupole modes or higher angular momentum-carrying shape excitations [132, 93, 106]. However the nature of the true final state in this case is beyond the scope of this work and warrants further investigation.

3.7. Conclusions

By calculating the static hydrodynamic solutions of a rotating dipolar BEC and studying their stability, we have predicted the regimes of stable and unstable motion. In general we find that the bifurcation frequency Ω_b decreases with increasing dipolar interactions. In addition, the onset of dynamical instability in the upper branch solutions, Ω_i, decreases with increasing dipolar interactions. Furthermore these frequencies depend on the aspect ratio of the trap.

By utilising the novel features of dipolar condensates we detail several routes to traverse the parameter space of static solutions and reach a point of instability. This can be achieved through adiabatic changes in trap rotation frequency Ω, trap ellipticity ϵ, dipolar interactions ε_{dd} and trap aspect ratio γ, all of which are experimentally tunable quantities. While the former two methods have been employed for non-dipolar BECs, the latter two methods are unique to dipolar BECs. These instabilities are particularly important because they offer the possibility of forming a vortex lattice in a dipolar condensate. However, unlike for conventional BECs with repulsive interactions, the formation of a vortex lattice is not always favoured and depends sensitively on the shape of the system. For a prolate BEC with strong dipolar interactions there exists a regime in which the rotating system is unstable and yet it is energetically unfavourable to form a lattice. Other outcomes may then develop, such as a centre-of-mass motion of the system or collective modes with angular momentum. However, for oblate dipolar condensates, as well as prolate condensates with weak dipolar interactions, the presence of vortices is energetically favoured at the point of instability and we expect the instability to lead to the formation of a vortex lattice.

We acknowledge financial support from the Australian Research Council (AMM), the Canadian Commonwealth Scholarship Program (NGP) and the Natural Sciences and Engineering Research Council of Canada (DHJOD).

4. Vortices

4.1. Introduction

The fact that a superfluid is an irrotational potential flow leads to peculiar behaviour when it is subjected to a (uniformly) rotating potential. In the rotating frame, where thermal equilibrium is expected to take place, the energy of the system E_r is given by [74, 119, 75, 128]

$$E_r = E - \mathbf{\Omega} \cdot \mathbf{L},$$

where E and $\mathbf{L}$ are the energy and angular momentum of the system in the laboratory coordinate frame, and $\mathbf{\Omega}$ the rotation vector of the potential. Clearly, when the rotation speed Ω of the potential increases, it becomes favourable for the system to increase its angular momentum. However, due to the irrotationality constraint (1.39) the superfluid cannot simply co-rotate with the potential to accomodate angular momentum, and it must find other ways to do so.

One of the ways to store angular momentum in a superfluid is through the formation of vortices[1], already briefly discussed in section 1.3. In this chapter we will take a closer look at vortex states, and the effects of dipolar interactions on such systems.

Since the BEC wavefunction is single valued, the phase φ must satisfy the following condition along any closed loop:

$$\oint \nabla\varphi \cdot \mathrm{d}\mathbf{l} = 2\pi s,$$

with $s = 0, 1, 2, \ldots$. The superfluid velocity is proportional to the gradient of the phase according to equation (1.38), such that the *circulation* of the superfluid takes the form

$$\oint \mathbf{v} \cdot \mathrm{d}\mathbf{l} = 2\pi \frac{\hbar}{m} s, \tag{4.1}$$

which is quantized in units of h/m. Next we will consider a vortex in a uniform medium with background density n_0. In cylinder coordinates, the vortex is situated at $r = 0$ and extends along the z-axis. The flow pattern is purely azimuthal, and when we take a circle with radius r around the z-axis as a contour of integration, then from equation (4.1) it follows that the tangential superfluid velocity is given by

$$v = \frac{\hbar}{m} \frac{s}{r} \hat{\theta}, \tag{4.2}$$

[1] In chapter 3 we look at non-vorticial equilibrium configurations of the system in a rotating harmonic trap.

where $\hat{\theta}$ is the unit vector of the azimuthal angle θ. Compared with the velocity field associated with uniform rotation, $\mathbf{v} = \mathbf{\Omega} \times \mathbf{r}$, the superfluid behaves radically different. Although both flow patterns are azimuthal, the tangential velocity of the vortex flow decreases radially outward, and diverges for $r \to 0$, whereas in case of uniform rotation the tangential velocity increases when going radially outward and vanishes for $r \to 0$, as illustrated in figure 4.1. Since the parameter s is an integer, the vortex flow is quantised.

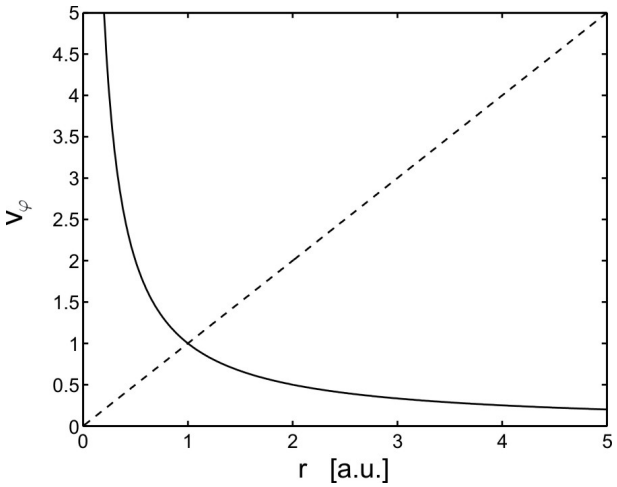

Figure 4.1.: *Velocity* $|\mathbf{v}|$ *of the vortex velocity field (solid line) compared with that of the uniform rotation velocity field (dashed line).*

The vortex flow pattern is irrotational everywhere, except for the core:

$$\nabla \times \mathbf{v} = 2\pi s \frac{\hbar}{m} \delta(x)\delta(y)\hat{z},$$

where x, y, z are the cartesian coordinates, and $\hat{z}$ the unit vector in the z-direction. At $r = 0$, the phase φ has a singularity and the velocities diverge, such that the condensate density must be equal to zero there. Furthermore, it can be shown that the density must be a function of the radial coordinate r only. First, due to translational symmetry the density cannot depend on the z-coordinate. Next, we note that the velocity potential of the vortex flow is harmonic, and $\nabla \cdot \mathbf{v} = 0$. The conservation of mass (in cylinder coordinates) then requires that

$$0 = \nabla \cdot (n\mathbf{v}) = \nabla n \cdot \mathbf{v} + n\nabla \cdot \mathbf{v} = \nabla n \cdot \mathbf{v} = \frac{\hbar}{mr^2} \frac{\partial n}{\partial \theta},$$

such that we conclude that the density can only be a function of the radial coordinate: $n = n(r)$. In the next section we will investigate the exact density profile of an otherwise uniform condensate containing a vortex.

The kinetic energy of a vortex flow pattern within a cylindrically symmetric vessel, with radius R_0 and filled with otherwise uniform background density n_0, is, per unit length along the z-axis, approximately given by [107]

$$U \simeq s^2 \pi n_0 \frac{\hbar^2}{m} \ln \frac{R_0}{\xi}, \tag{4.3}$$

where ξ is the healing length, and $R_0 \gg \xi$. For an infinite uniform system this energy diverges, hence the need to consider only a finite system with radius R_0. The main observation to be made from the energy expression (4.3) is that it is proportional to s^2. This suggests that multiple vortices with quantization $s = 1$ could be energetically more favourable than a single vortex with $s > 1$. To find out whether this is the case, one must also look at the interaction energy of two vortices.

Two vortices of circulation s_1 and s_2 separated by a distance R, in a cylindrical container with radius R_0 and with background uniform density n_0, have an interaction energy per unit length equal to [107]

$$U_{int}^{kin} = \frac{2\pi s_1 s_2 \hbar^2 n_0}{m} \ln \frac{R_0}{R},$$

where $R_0 \gg R$ and $R \gg \xi$. Clearly, the interaction energy is small compared to the energy associated with creating vortices in the first place, and hence we can draw the conclusion that the system will indeed form multiple $s = 1$ vortices in favour of multiply quantized $s > 1$ vortices with the same total rotation.

These $s = 1$ vortices arrange in a triangular lattice in such a way that the average rotation per unit area is equal to $\nabla \times \mathbf{v} = 2\Omega$, the rigid body rotation [107].

4.2. Vortex core structure without dipolar interactions

To find the condensate density associated with the vortex flow pattern (4.2), we write the condensate wave function as

$$\psi(\mathbf{r}) = \exp(\mathrm{i}s\theta)|\psi(\mathbf{r})|, \tag{4.4}$$

where θ is the azimuthal angle in cylinder coordinates, and where we have used the phase pattern $\varphi = s\theta$ corresponding to (4.2). This phase pattern is harmonic and therefore $\nabla \cdot \mathbf{v} = 0$. The conservation of mass requires that

$$0 = \nabla \cdot (|\psi(r)|^2 \mathbf{v}) = \nabla |\psi(r)|^2 \cdot \mathbf{v} + |\psi(r)|^2 \nabla \cdot \mathbf{v} = \nabla |\psi(r)|^2 \cdot \mathbf{v},$$

and for the purely azimuthal flow and translational symmetry in the z-direction we conclude that the density (and hence the amplitude of the wavefunction) can only be a function of the radial coordinate: $|\psi(\mathbf{r})| = |\psi(r)|$. Substituting this in the Gross-Pitaevskii equation (1.22), we get the following equation for the amplitude of the wave function $|\psi|$, in terms of the radial coordinate r,

$$-\frac{\hbar^2}{2m}\frac{1}{r}\frac{\mathrm{d}}{\mathrm{d}r}\left(r\frac{\mathrm{d}|\psi|}{\mathrm{d}r}\right) + \frac{\hbar^2 s^2}{2mr^2}|\psi| + g|\psi|^3 - \mu|\psi| = 0.$$

At $r \to \infty$, the condensate density returns to the background value n_0. We therefore scale the condensate wavefunction as

$$|\psi(r)| = \sqrt{n_0} f(\eta),$$

with the dimensionless length scale $\eta = r/\xi$, and ξ the healing length (1.27). For $\eta \to \infty$ then, we have that $f = 1$. Finally, after dividing by the energy[2] $n_0 g$, the Gross-Pitaevskii equation for the scaled wave function becomes

$$\frac{1}{\eta}\frac{\mathrm{d}}{\mathrm{d}\eta}\left(\eta\frac{\mathrm{d}f}{\mathrm{d}\eta}\right) + \left(1 - \frac{s^2}{\eta^2}\right) f - f^3 = 0, \tag{4.5}$$

with the boundary conditions that $f(\infty) = 1$ and $f(0) = 0$.

To investigate the behaviour of f at different distance scales from the origin, we substitute $\eta = Lx$, where L is some dimensionless length scale and x is a new dimensionless coordinate. Then, eq. (4.5) becomes

$$\frac{1}{L^2}\left(\frac{1}{x}\frac{\mathrm{d}f}{\mathrm{d}x} + \frac{\mathrm{d}^2 f}{\mathrm{d}x^2} - \frac{s^2}{x^2}\right) + f - f^3 = 0. \tag{4.6}$$

To investigate f close to the vortex core where $\eta \ll 1$, we put $L \ll 1$ such that $x = \mathcal{O}(1)$. Then, we immediately see that the $f - f^3$ term vanishes with respect to the L^{-2} term, and solving

$$\frac{1}{x}\frac{\mathrm{d}f}{\mathrm{d}x} + \frac{\mathrm{d}^2 f}{\mathrm{d}x^2} - \frac{s^2}{x^2} = 0$$

we find that $f = x^{\pm s}$. Since $f(0) = 0$ we take the positive root of s^2 and hence, in terms of η

$$f = a\eta^s, \tag{4.7}$$

close to the vortex core, for some constant a. In the other limit we already know the answer on physical grounds, namely $f \simeq 1$, and indeed we find when putting $L \gg 1$ that

$$f(1 - f^2) = 0,$$

and taking the positive root again we have $f = 1$ far away from the vortex core.

In the intermediate region, $L = \mathcal{O}(1)$ we would have to solve the full equation (4.5), which is analytically untractable. Therefore, to find the full solution for f we have to resort to numerics.

In order to do this, we first rewrite (4.5) as

$$\mathcal{L}[f] f = 0, \tag{4.8}$$

with the f-dependent operator

$$\mathcal{L}[f] = \frac{1}{\eta}\frac{\mathrm{d}}{\mathrm{d}\eta}\left(\eta\frac{\mathrm{d}}{\mathrm{d}\eta}\right) + \left(1 - \frac{s^2}{\eta^2}\right) - f^2.$$

[2]The scaling steps taken here are similar to those described in more detail in Appendix A.

We can discretise this operator by constructing a discretized version of f on a grid of N points, and discretising the differential operators using central differences, with Dirichlet boundary conditions: $f(0) = 0$, $f(x_N) = 1$. To solve the nonlinear equation (4.8) we then proceed as follows. First, we make an initial guess $f = f_0$. Then, we iteratively solve

$$\mathcal{L}[f_n]f_{n+1} = 0,$$

until convergence is reached. Figure 4.2 shows the radial wavefunction for various values of s, clearly displaying the asymptotic behaviour of equation (4.7). The vortex core size is typically of the order of the healing length.

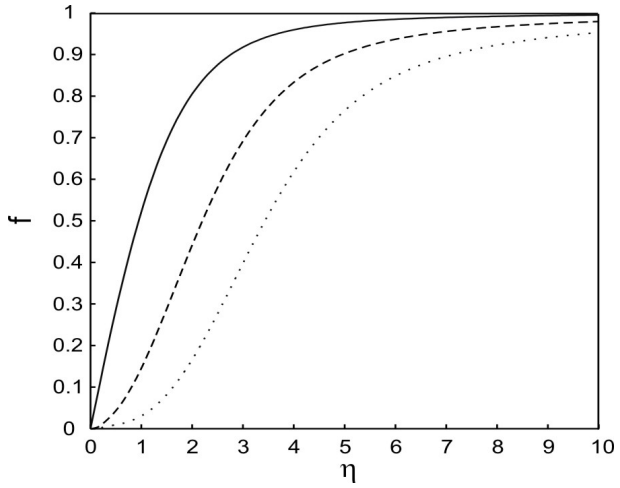

Figure 4.2.: *f as a function of η, for $s = 1, 2, 3$ (solid, dashed, and dotted line, respectively).*

4.3. Structure of a single vortex in a dipolar BEC

4.3.1. Introduction

In this section we will investigate the effects on the vortex state of turning on dipolar interactions. The long range, anisotropic nature of the dipolar interactions might affect the vortex core structure drastically. Early numerical work has already found a 'craterlike' vortex core structure [134], by solving the full Gross-Pitaevskii equation in 3D. The long range nature of the dipolar interactions could affect the vortex-vortex interaction, possibly leading to changes in the vortex lattice structure, an effect confirmed by some numerical studies [23, 71, 140].

Therefore, dipolar interactions can provide an easily controllable parameter to change vortex properties, which could lead to exciting new physics. Also, there exist other vorticial systems in which long range and/or anisotropic interactions play a role. For instance, in high-T_c superconductors the behaviour of magnetic fields can be modeled using vortices, and anisotropic interactions are thought to modify lattice structures thereof. Long range interactions in turn are used to model vortices in Helium. (refs from Pu)

Before we turn to investigating the vortex interactions and possible changes to the vortex lattice however, we must know the effect of dipolar interactions on the structure of the vortex core and the vortex core size.

In this section we will investigate the core structure of a vortex in a dipolar BEC in a harmonic trap, as opposed to the vortex line in a uniform system treated in the previous section. To minimize edge effects and approximate a uniform background density, we have to make the system very large, with a large number of atoms and a small healing length.

We start by explicitly specifying the vortex phase pattern as in equation (4.4),

$$\psi(\mathbf{r}) = f \exp(\mathrm{i}s\theta), \tag{4.9}$$

with f real valued, leading to a s^2/r^2 potential term in the time independent Gross-Pitaevskii equation for the wave function amplitude f:

$$\left(-\frac{\hbar^2}{2m}\nabla^2 + \frac{\hbar^2}{2m}\frac{s^2}{r^2} + \frac{1}{2}m\omega_\perp^2(r^2+\gamma^2 z^2) + gf^2 + \Phi_{dd}[f^2]\right) f = \mu f \tag{4.10}$$

Our main task in this section is solving the above equation for various values of the dipolar interaction strength, and observe the vortex core structure. For instance, we would like to know the vortex core volume A, which can be calculated as

$$A = \int (\rho_0 - \rho_v) dV,$$

where ρ_0 is the vortex-free density, and ρ_v is the density with a vortex present. Clearly, we need to work with a fixed chemical potential rather than a fixed number of particles when calculating ρ_0 and ρ_v, since otherwise A would be trivially equal to 0.

To isolate the effects of the dipolar interactions on the vortex core profile, the 'envelope' background density has to remain the same for calculations with different values of the dipolar interactions strength ϵ_{dd}. This can be done by adjusting the trapping frequencies and the chemical potential as a function of ϵ_{dd}. The details of this calculation and the scaling that is used can be found in Appendix K.

4.3.2. Numerical calculation

In this section we discuss the numerical solving of equation (4.10). First, recall (see section 1.4.2) that a solution of the time independent Gross-Pitaevskii equation corresponds to a stationary point of the energy of the BEC, where μ is a Lagrange-multiplier controlling the number of particles N. Here, we are interested in states with a fixed chemical potential, rather than fixed N. Therefore, instead of minimizing the internal energy of the system we want to minimize a different thermodynamic potential, namely the one associated with a fixed volume, fixed temperature ($T = 0$) and fixed chemical potential. This potential is obtained from a Legendre transform of the internal energy [17],

$$\Phi_G = E - TS - \mu N,$$

where S is the entropy of the system and N the number of particles. This potential is called the grand potential, or Landau potential, which has a minimum for the equilibrium state of the system [17]. The grand potential is a functional of the wavefunction f,

$$\Phi_G[f] = \int \left[\frac{1}{2}\frac{\hbar^2}{2m}(\nabla f)^2 + \frac{\hbar^2}{2m}\frac{s^2}{r^2}f^2 + V(\mathbf{r})f^2 + \frac{1}{2}gf^4 + \frac{1}{2}f^2\Phi_{dd}[f^2] - \mu f^2 \right] dV. \tag{4.11}$$

where we have used expression (1.25) for the internal energy. Indeed (see appendix J) minimization of the grand potential with respect to the wave function amplitude f leads to the time independent Gross-Pitaevskii equation (4.10). Such a minimization can be carried out in various ways, but here we use simple gradient descent, leading to the following nonlinear diffusion equation,

$$-\hbar\frac{\partial f}{\partial t} = \left(\frac{-\hbar^2}{2m}\nabla^2 + \frac{\hbar^2}{2m}\frac{s^2}{r^2} + V(\mathbf{r}) + g|\psi|^2 + \Phi_{dd}[f^2] - \mu \right) f, \tag{4.12}$$

which is propagated until convergence. Intuitively, from equation (4.12) it is apparent that if $\psi(t)$ converges to a stationary state for which $\frac{\partial \psi}{\partial t} = 0$, we have found a solution to equation (4.10). For the interested reader, Appendix J provides the exact details behind this scheme.

We will now proceed with tackling the numerical details associated with the time propagation of equation (4.12). Upon noting that the system is cylindrically symmetric it suffices to spatially discretise only the $r - z$ plane, where all other points of the system follow from rotating the wave function found in the $r - z$ plane.

The calculation of the dipolar potential of a given density distribution n can be efficiently carried out using Fourier transforms. Namely, the potential is of the form

$$\Phi_{dd}[n](\mathbf{r}) = \int U_{dd}(\mathbf{r} - \mathbf{r}')n(\mathbf{r}')\mathrm{d}^3\mathbf{r}',$$

which is a convolution of U_{dd} and n. It is well known that the Fourier transform of a convolution is simply a multiplication of the Fourier transforms of the two functions being convolved [15, 14]. To find the dipolar potential then, one simply has to calculate the Fourier transform of the density, multiply that with the (precalculated) Fourier transform of the dipolar interaction energy U_{dd}, and finally perform the inverse Fourier transform on this product to obtain the total dipolar potential. Using fast Fourier transforms (FFT) [15] this can be done very efficiently, and the cylinder symmetry of the system can be exploited to further reduce the computational cost by means of Hankel transforms [14]. Hankel transforms take advantage of the cylindrical symmetry of a system by integrating out the azimuthal component of the Fourier transform analytically, see appendix I for a further introduction to Hankel transforms. Analogous to FFT's, there also exist fast Hankel transforms [121]. In this work, we have used a Matlab implementation of the method described in [51], where the code is written by the same authors. This method requires a nonuniform grid spacing in the radial direction, increasing the complexity of the spatial discretisation of the Hamiltonian operator.

Finally, the long range nature of the dipolar interactions causes problems in discrete Fourier transforms. Representing the density of the condensate using only a finite number of Fourier waves produces periodic copies in space of the condensate when transforming back from the

Fourier representation. The dipolar potential will therefore also be influenced by these mirror images (infinitely many) of the condensate, unless the dipolar interactions are truncated to a finite range. Further details on numerically calculating the dipolar potential, Hankel transforms and truncation of dipolar interactions can be found in Appendix I.

Time propagation of equation (4.12) is performed by a simple Euler-forward scheme. Higher order schemes such as Crank-Nicholson were found to be inefficient due to the fact that the differential operator is dependent on the condensate density, and hence needs to be inverted at every time step, which is computationally demanding. For an ordinary diffusion equation, the time step Δt of the Euler-forward method is restricted by the grid size Δr, through the condition [90]

$$\frac{\Delta t}{\Delta r^2} \leq \frac{1}{2}, \tag{4.13}$$

where $\mathbf{r}$ and t are scaled such that the $\frac{\partial}{\partial t}$ and ∇^2 terms of the diffusion equation have the same prefactor. Loosely speaking, this condition requires that the time step is small enough such that information can propagate correctly accross the grid. Although equation (4.12) is not an ordinary linear diffusion equation, the above criterion gives a good first estimate of the maximum time step.

Even under this rather severe restriction, the Euler forward scheme performs consistently better in terms of speed than Crank-Nicholson. As a possible improvement for future research numerical schemes for time propagation should be considered. Bao et al. [5] investigate the Time-splitting Sine Spectral (TSSP) method and Euler backward (EB) numerical schemes and find that these schemes perform much better in terms of accuracy and speed. Additionally, Succi et al. [126] put forward the Synchronous Visscher (SV) scheme for handling the time propagation. TSSP and SV are explicit methods and relatively easy to program, however they carry a restriction on the time step in order to guarantee convergence. EB does not have such a restriction, being fully implicit, however this requires solving a linear system at each time step.

In this work we will keep the simple Euler forward time propagation, as we are not interested in the dynamics but merely the final state of the system. The particular time propagation scheme is therefore not important, as long as the scheme converges.

4.3.3. Results

Using the numerical scheme outlined in the previous section we can now find the ground state of the condensate with a vortex in the center. We will restrict our attention to a condensate with aspect ratio $\kappa = R_x/R_z = 10$, since flattened systems are primarily of experimental interest. For more elongated systems, vortices tend to become unstable [109, 107] and in the dipolar BEC a vortex core might not even form at all [98]. Furthermore, throughout this section we will maintain a ratio of healing length to condensate size of

$$\chi = \frac{\xi}{R_x} = 0.01,$$

such that approximately 100 healing lengths fit in the radial direction.

A typical vortex core for a condensate with $\epsilon_{dd} = 0.99$ is shown in figures 4.3 and 4.4. A distinct ripple can be seen surrounding the vortex core, in qualitative agreement with the

results found by [134]. For values of ϵ_{dd} ranging between $\epsilon_{dd} = 0$, and $\epsilon_{dd} \lesssim 1.2$, stable ground states have been found. For higher values of ϵ_{dd} the numerical scheme diverged and no stable ground states were found, indicative of a collapse due to the attractive part of the dipolar interactions becoming too large (see section 1.7). The transition between stable / unstable is not very clear, states that appear to converge can still start to diverge after propagating the scheme longer in time. In all cases of a non-converging state, the ripples started to grow indefinitely ultimately causing a collapse of the condensate. For $\epsilon_{dd} \leq 1$, the ground states appear stable and the numerical scheme converges. In our discussion we include values of ϵ_{dd} up to $\epsilon_{dd} = 1.2$, with the remark that the results for $\epsilon_{dd} > 1$ need further investigation with respect to their stability.

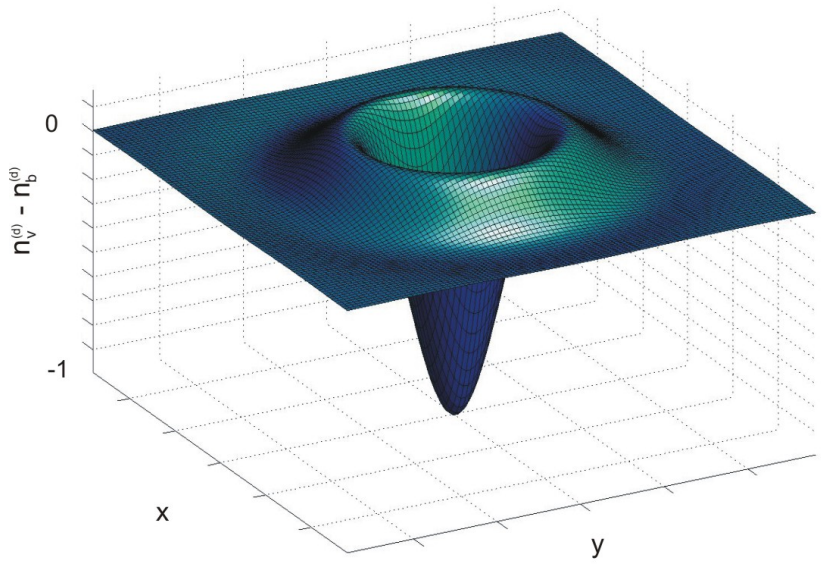

Figure 4.3.: *Typical vortex core density* $n_v^{(d)}$ *for* $\epsilon_{dd} = 0.99$*, with the background density* $n_b^{(d)}$ *subtracted, as a function of the radial coordinate* $r = \sqrt{x^2 + y^2}$ *(arbitrary units), in the center of the condensate at* $z = 0$*.*

The physical explanation behind the occurance of ripples might be as follows. For highly flattened systems and $\epsilon_{dd} > 0$, the dipoles are mainly side by side and hence experience repulsive interactions from each other. As outlined in section 1.8, the change in dipolar potential due to the vortex core can be treated as if there is a volume of dipoles of the opposite sign present. These negative dipoles attract the ordinary dipoles of the condensate, and hence it is energetically more favourable for the dipoles to be next to the vortex core. This effect can be considered analogous to screening behaviour of electrons screening out positive charges in plasmas [95, 87]. Similarly, the condensate dipoles are screening out the potential of the negative dipoles of the vortex core[3]. Figure 4.5 depicts this screening of the vortex core schematically, and the analogous case of ion screening in a plasma by electrons. Although the s-wave contact interactions are also repulsive, they do not lead to screening effects since

[3]In Chapter 5 we will take a closer look at screening / shielding effects of dipolar BECs in response to impurities.

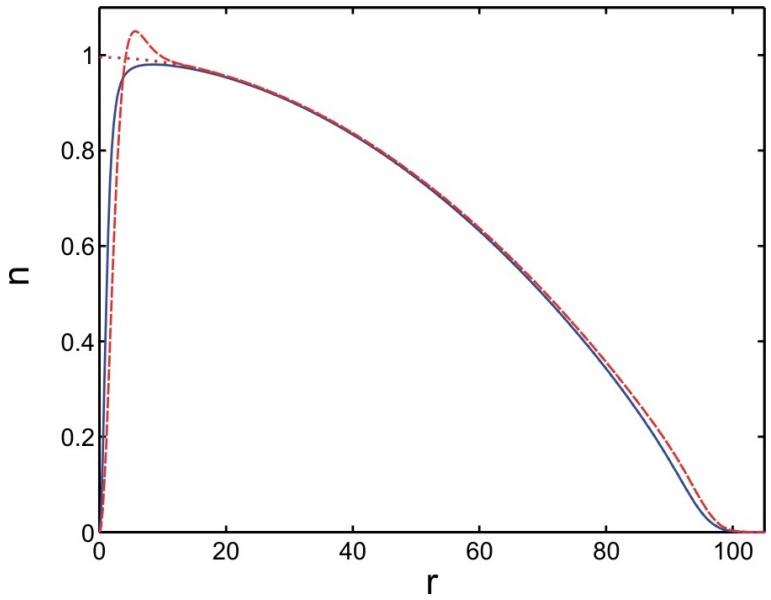

Figure 4.4.: *Vortex density profiles as a function of radial distance, in units of the healing length, plotted at $z = 0$ in the center of the condensate. Blue, solid line: $\epsilon_{dd} = 0$, red, dashed line: $\epsilon_{dd} = 0.99$. Red and blue dotted lines are the corresponding condensate densities without a vortex. Near $r = 0$ they are indisinguishable from each other, near the edge of the condensate ($r = 100$ healing lengths) they are indistinguishable from the corresponding vortex densities.*

they are zero-range interactions. That is, the contact interaction energy is not affected by the presence of the vortex core. In chapter 5 we will investigate screening behaviour of the dipolar BEC on a more fundamental level and calculate analytically the response of the condensate to an impurity.

As can be seen from figure 4.4b, the background densities change slightly near the edge of the condensate, when ϵ_{dd} is varied. Just as the occurance of ripples can be considered as 'screening' of the vortex core, this effect could be a screening of the condensate edge where there is equally well a large void which could make it energetically more favourable for the dipoles to be close to the condensate edge.

We define the following densities:

- $n_b^{(s)}$: Background density of a vortex-free condensate, with no dipolar interactions present (s-wave interactions only)
- $n_v^{(s)}$: Density of a vortex state, with no dipolar interactions present (s-wave interactions only)
- $n_b^{(d)}$: Background density of a vortex-free condensate, with dipolar interactions present
- $n_v^{(d)}$: Density of a vortex state, with dipolar interactions present.

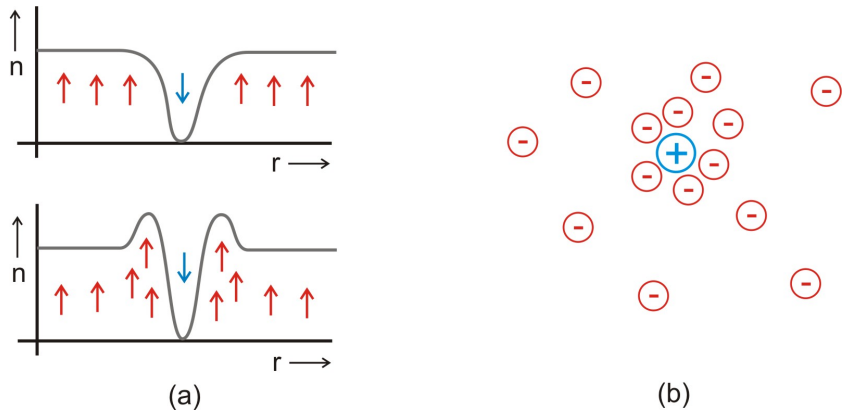

Figure 4.5.: *(a) Top figure: using the linearity of the dipolar potential, the potential of a vortex core can be treated as the dipolar potential due to a distribution of opposite dipoles, superimposed on the background density. Bottom figure: the condensate is attracted to this distribution of opposite dipoles and condensate dipoles pile up next to the vortex core, forming a ripple. (b) An analogous effect occurs in plasmas where free electrons are attracted towards ions and effectively screen out the coulomb potential of the ion.*

Figure 4.6 provides a more detailed look at the vortex core and the ripple size. In figure 4.6a, the vortex core profile is isolated by subtracting the background density profile $n_b^{(d)}$ of the vortex-free condensate from that of the vortex state $n_v^{(d)}$, where both densities are calculated at the same dipolar interaction strength ϵ_{dd}. There are two pronounced effects due to the dipolar interactions visible. First, the vortex core widens for increasing dipolar interactions. Widening of the vortex core adds more fictituous 'negative dipoles' and presumably lowers the energy that way[4]. Second, the density ripple surrounding the vortex core grows as ϵ_{dd} increases, which is assumed to be due to the screening effect.

To measure these two effects, we define the following quantities:

- **Vortex core density**: the density of the vortex state with the background density subtracted, for the case with only s-wave interactions present

$$n_{core}^{(s)} = n_v^{(s)} - n_b^{(s)},$$

and the case with dipolar interactions present

$$n_{core}^{(d)} = n_v^{(d)} - n_b^{(d)}.$$

Note that the vortex core density thus becomes mainly negative, indicating an absence of dipolar condensate.

[4]For attractive interactions the effect is expected to be opposite: vortex cores will become smaller or might not form at all, since creating a hole in the center of the condensate requires moving particles away from the center, an energetically favourable position, to the edge of the condensate [132, 98].

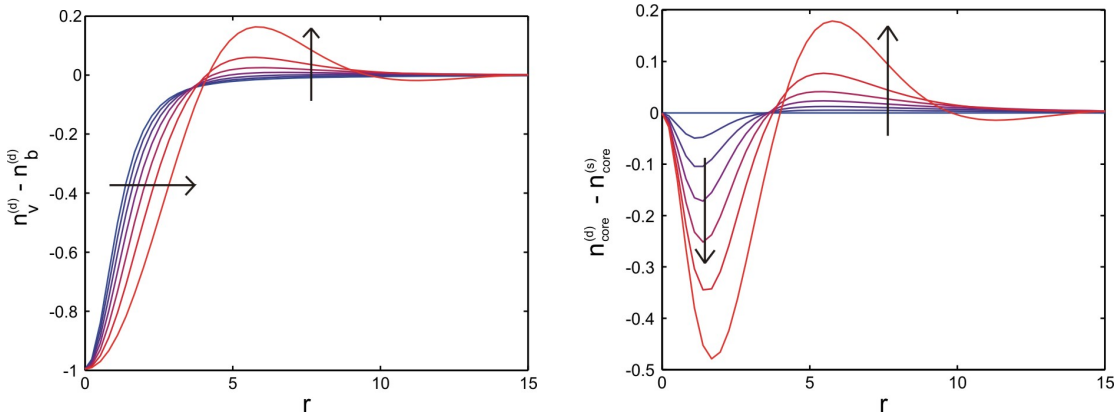

Figure 4.6.: *(a) Density difference of the vortex density $n_v^{(d)}$, and the corresponding non-vorticial density $n_b^{(d)}$, at $z = 0$ in the center of the condensate. The dipolar interaction strength ϵ_{dd} ranges from $\epsilon_{dd} = 0$ (blue curve) to $\epsilon_{dd} = 1.2$ (red curve), and the direction of increasing ϵ_{dd} (in steps of 0.2) is indicated with an arrow. (b) Relative densities of the dipolar vortex core compared to the non-dipolar vortex core $n_{core}^{(d)} - n_{core}^{(s)}$, at the center of the condensate $z = 0$. The widening of the vortex core is clearly visible near $r = 0$, with a surplus of condensate forming a ripple at about $r = 6$ healing lengths.*

- **Vortex core volume**: the total vortex core volume, defined as

$$V_{core}^{(s)} = \int n_{core}^{(s)}(\mathbf{r}) d^3\mathbf{r},$$

for the case with only s-wave interactions, and

$$V_{core}^{(d)} = \int n_{core}^{(d)}(\mathbf{r}) d^3\mathbf{r}$$

for the case with dipolar interactions present.

- **Ripple size and core widening**: Defining the auxiliary function

$$I_{\pm}[n](\mathbf{r}) = \begin{cases} n(\mathbf{r}) & \text{if} \quad \text{sgn}(n(\mathbf{r})) = \pm 1 \\ 0 & \text{if} \quad \text{sgn}(n(\mathbf{r})) = \mp 1 \end{cases},$$

we can calculate the total volume of the ripple as

$$V_{rip} = \int I_+[n_{core}^{(d)} - n_{core}^{(s)}](\mathbf{r}) d^3\mathbf{r},$$

and the widening of the vortex core due to the dipolar interactions as

$$V_{wid} = \int I_-[n_{core}^{(d)} - n_{core}^{(s)}](\mathbf{r}) d^3\mathbf{r}.$$

The volumes $V_{core}^{(d)}$, V_{rip}, and V_{wid} are plotted in figure 4.7. Due to the dipolar interactions, the total vortex core volume $V_{core}^{(d)}$ decreases to about 1/3 times the non-dipolar core volume at $\epsilon_{dd} = 1$. The ripple surrounding the vortex thus screens out the majority of the dipolar potential of the vortex core, but not all of it. The condensate is restricted in its variation by the kinetic energy term, which penalises rapid variations, and is prevented from raising the ripple even further to completely screen the vortex core.

We can also determine the vortex core radius, taken to be the point at which the radial density reaches 0.5 times the peak density. The core radius almost doubles from $R_{core} \simeq 1.2$ healing lengths for $\epsilon_{dd} = 0$, to $R_{core} \simeq 2$ healing lengths at $\epsilon_{dd} = 1.2$.

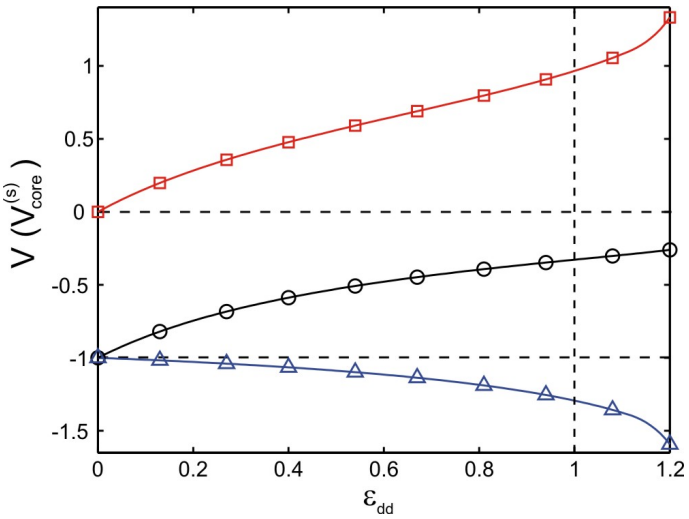

Figure 4.7.: *Volume of the dipolar vortex core $V_{core}^{(d)}$ (black, circles), widening of the vortex core V_{wid} (blue, triangles) and total volume of the ripple V_{rip} (red, squares). All volumes are plotted in units of the non-dipolar vortex core size $V_{core}^{(s)}$.*

To obtain a complete understanding of the effects of dipolar interactions, further studies are needed. Most notably, the condensate aspect ratio and healing length are not varied in the above calculations, but both quantities could have a significant effect on the core size and ripple size. Indeed, in chapters 2 and 3 we saw that the trap aspect ratio has a strong influence on the energetics and stationary states of a dipolar BEC. Furthermore, negative values of ϵ_{dd} are not considered yet, although vortices in systems with mainly attractive interactions could be an interesting research subject for further studies.

To counteract the instabilities observed for $\epsilon_{dd} > 1$, perhaps the system should be flattened further and κ must be taken much larger than the current value of 10. Also, the vortex state should become more stable when the system is put in rotation by adding a $-\mathbf{\Omega} \cdot \mathbf{L}$ potential term to the energy of the system[5]. Finally, recalling the discussion in section 4.3.2, different time stepping schemes, as proposed by references [5, 126], should be considered to exclude numerical causes for the divergences (as opposed to physical reasons), or perhaps completely different methods for minimizing the grand potential altogether, such as discussed in Appendix J.

[5] see the introduction of this chapter, and/or chapter 3.

In conclusion, the results of this numerical work give a global indication of the effect of dipolar interactions on the vortex core. Firstly, the vortex core is widened at the center. Secondly, a ripple around the vortex core forms that screens out part of the dipolar potential due to the vortex core. The total sum of these two effects however does not drastically affect the core volume, the core size stays within the same order of magnitude. The total core volume $V_{core}^{(d)}$ will be used in the next section to obtain an estimate of the effect of dipolar interactions on the vortex-vortex interaction. Further research and improvement of the numerics are needed to obtain a complete picture of the dipolar vortex core. On another note, similar calculations could be performed for solitons[6] Dark solitons have an interaction potential that decays exponentially [68], and as such dipolar interactions should have a more pronounced effect on the total interaction potential.

4.4. Dipolar interaction energy of 2 vortices

Consider the situation in fig. 4.8. We are going to determine the dipolar interaction potential between two vortices, oriented along the z-axis, and separated by a distance R in the xy-plane. In a local density approximation we can take the density n of the condensate to be uniform in the x and y directions, whereas for the z direction the density is nonhomogeneous.

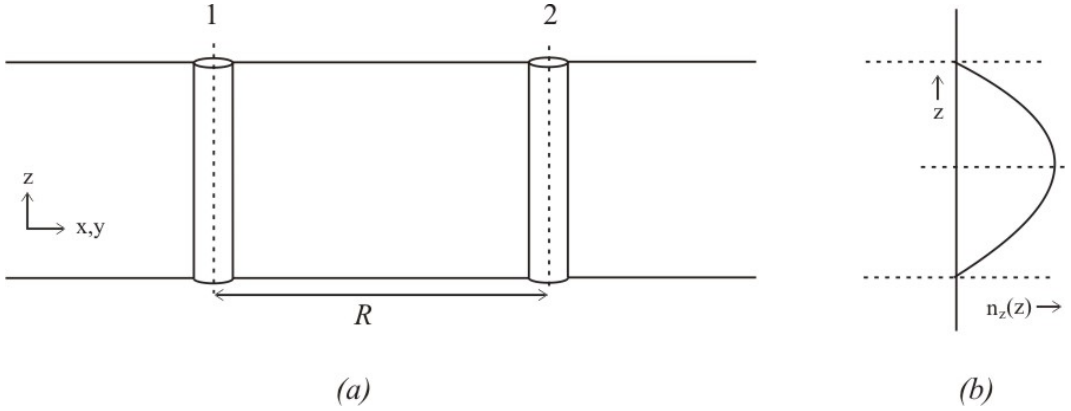

Figure 4.8.: *(a) Schematic drawing of two vortices oriented along the z-axis, separated a distance R in the x-y plane, located in a dipolar BEC with density dependent on z, but not x and y. When the vortex separation is much larger than their core sizes, they can be modeled as lines. (b) Schematic density distribution of the condensate as a function of z.*

For instance, when the condensate is strongly trapped in the z-direction (a very pancake shaped system) the axial density is given by

$$n(x, y, z) = n(z) = n_0 \exp(-z^2/R_z^2), \tag{4.14}$$

[6]Solitons are nondispersive wave structures, where the nonlinearity of the condensate counteracts the dispersion [107].

where R_z is a typical thickness of the pancake. On the other hand, when the condensate is less strongly trapped and the Thomas-Fermi approximation holds, the density is of the form

$$n(x,y,z) = n(z) = \begin{cases} n_0 \left(1 - \left(\frac{z}{R_z}\right)^2\right) & (|z| < R_z) \\ 0 & (|z| > R_z) \end{cases} \tag{4.15}$$

where the system is centered around $z = 0$ and (locally) of a thickness $2R_z$, and the density is zero outside this region. We can now model the two vortices as two cylinders filled with a negative density $n_v(x,y,z) = -n(z)$, superimposed on the condensate background density $n(z)$, such that the vortices are empty cylinders in the condensate. The dipolar potential due to a general density distribution n is

$$\Phi_{dd}[n](\mathbf{r}) = \int U_{dd}(\mathbf{r} - \mathbf{r}')n(\mathbf{r}')\mathrm{d}^3\mathbf{r}', \tag{4.16}$$

where the dipolar interaction energy of two dipoles separated by a vector $\mathbf{r}$ is

$$U_{dd}(\mathbf{r}) = \frac{C_{dd}}{4\pi}\frac{1 - 3\cos^2\theta}{r^3}, \tag{4.17}$$

with the coordinate $\mathbf{r}$ expressed in terms of $r = |\mathbf{r}|$ and the angle θ that it makes with the z-axis.

As explained in section 1.8.2, the dipolar potential $\Phi_{dd}[n]$ is a *linear* functional of the density n. Therefore, to study the effect of the dipolar interactions of the vortices we can then in fact look at the dipolar potential due to the two cylinders with negative density *alone*, and ignore the rest of the condensate. The contribution of the background density will not be dependent on the vortex separation R, although this is not generally true when the condensate density depends on x and y.

When the vortex core size d is much smaller than the vortex separation, we can model the cylinders as line densities. A line element $\mathrm{d}z$ of such a line carries a mass $\pi d^2 n(z)\mathrm{d}z$. Denoting the density of cylinder i by $n_v^{(i)}$, we get

$$n_v^{(i)}(x,y,z) = \pi d^2 n(z)\delta(x - x_i)\delta(y - y_i), \tag{4.18}$$

where x_i, y_i are the x and y coordinates of vortex i, such that the vortex separation is given by $R^2 = (x_1 - x_2)^2 + (y_1 - y_2)^2$.

We now need to know the energy U stored in the configuration of ('negative') dipole matter $n_v = n_v^{(1)} + n_v^{(2)}$, which can be calculated as

$$U = \frac{1}{2}\int n_v(\mathbf{r})\Phi_{dd}[n_v](\mathbf{r})\mathrm{d}^3\mathbf{r}. \tag{4.19}$$

The idea behind the above formula is, analogous to calculating the energy stored in a charge distribution [63], to move all the dipoles one-by-one to their final locations and sum the energy needed to do this. The factor of $\frac{1}{2}$ is there to compensate for double counting each dipole.

Inserting the vortex density (4.18) into the energy (4.19), we get

$$
\begin{aligned}
U &= \frac{1}{2}\int n_v(\mathbf{r})\Phi_{dd}[n_v](\mathbf{r})\mathrm{d}^3\mathbf{r} \\
&= \frac{1}{2}\int\int n_v(\mathbf{r})n_v(\mathbf{r}')U_{dd}(\mathbf{r}-\mathbf{r}')\mathrm{d}^3\mathbf{r}'\mathrm{d}^3\mathbf{r} \\
&= \frac{1}{2}(\pi d^2)^2\int\int \left(n(z)\delta(x-x_1)\delta(y-y_1)+n(z)\delta(x-x_2)\delta(y-y_2)\right)\otimes \\
&\qquad \left(n(z')\delta(x'-x_1)\delta(y'-y_1)+n(z')\delta(x'-x_2)\delta(y'-y_2)\right)U_{dd}(\mathbf{r}-\mathbf{r}')\mathrm{d}^3\mathbf{r}'\mathrm{d}^3\mathbf{r} \\
&=: \frac{1}{2}\sum_{i=1}^{2}\sum_{j=1}^{2}U_{ij},
\end{aligned}
$$

where we have defined

$$
\begin{aligned}
U_{ij} &= (\pi d^2)^2\int\int n(z')n(z)\delta(x-x_i)\delta(y-y_i)\delta(x'-x_j)\delta(y'-y_j)U_{dd}(\mathbf{r}-\mathbf{r}')\mathrm{d}^3\mathbf{r}'\mathrm{d}^3\mathbf{r} \\
&= (\pi d^2)^2\int\int n(z')n(z)U_{dd}(\mathbf{r}_i-\mathbf{r}'_j)\mathrm{d}z'\mathrm{d}z, \qquad (4.20)
\end{aligned}
$$

and $r_i = (x_i, y_i, z)$ is a coordinate on the i^{th} vortex line. Physically, we can interpret the U_{ii} terms as *self energies*, i.e. the energy associated with constructing a vortex line by itself. The cross terms $U_{ij}, j \neq i$ are the interaction energies, describing the energy associated with putting vortex line i in the potential set up by vortex line j. Therefore, the only terms that we are interested in are the cross terms $i \neq j$. In fact, the self energies tend to blow up to infinity for line charges. In future work, these self energies might need to be calculated as well and in this case we need to take the 3d structure of the vortex into account and abandon the line charge picture. Calculating the self energies might be an arduous task with complicated integrals, but conceptually not hard.

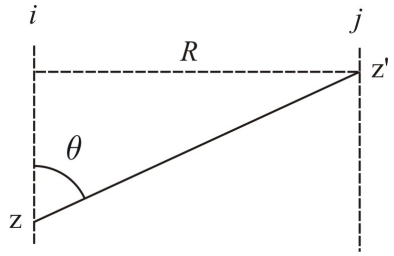

Figure 4.9.: *Overview of integration variables in calculation of U_{ij}.*

Continuing with the cross terms U_{ij} therefore, we need to express the dipolar interaction energy (4.17) occuring in Eq. (4.20) in terms of the coordinates z and z'. From fig. 4.9, we see that

$$\cos\theta = \frac{z'-z}{\sqrt{R^2+(z-z')^2}},$$

and

$$r^2 = R^2 + (z'-z)^2.$$

Then,

$$U_{12} = U_{21} = \frac{C_{dd}\pi d^4}{4}\int\int n(z)n(z')\frac{1-3\frac{(z'-z)^2}{R^2+(z'-z)^2}}{(R^2+(z-z')^2)^{\frac{3}{2}}}\mathrm{d}z\mathrm{d}z', \tag{4.21}$$

which we can rewrite as, using the substitution $\zeta = z/R_z$, $\tilde{n}(\zeta) = n(z)/n_0$,

$$U_{12} = \frac{C_{dd}\pi d^4 n_0^2}{4}\int\int \tilde{n}(\zeta)\tilde{n}(\zeta')\frac{1-3a^2\frac{(\zeta-\zeta')^2}{1+a^2(\zeta-\zeta')^2}}{R^3(1+a^2(\zeta-\zeta')^2)^{\frac{3}{2}}}R_z^2\mathrm{d}\zeta\mathrm{d}\zeta', \tag{4.22}$$

and where $a = R_z/R$. Some rearranging finally gives

$$U_{12} = \frac{C_{dd}\pi d^4 n_0^2 R_z^2}{4R^3}\int\int \tilde{n}(\zeta)\tilde{n}(\zeta')\left(\frac{3}{(1+a^2(\zeta-\zeta')^2)^{\frac{5}{2}}} - \frac{2}{(1+a^2(\zeta-\zeta')^2)^{\frac{3}{2}}}\right)\mathrm{d}\zeta\mathrm{d}\zeta'. \tag{4.23}$$

When the axial density profile is the Gaussian-density of Eq. (4.14), the integral in (4.23) cannot be evaluated analytically. However, since the Gaussian density occurs for a very tightly trapped condensate in the z-direction, we can assume that R_z is of the order of the healing length and therefore $R_z \ll R$. We can then expand expression (4.23) around $a = 0$ and integrate, yielding

$$\begin{aligned} U_{12} &= \frac{C_{dd}\pi d^4 n_0^2 R_z^2}{4R^3}\left[\pi - \frac{9}{2}(\pi-2)a^2 + \mathcal{O}(a^4)\right] \\ &= \frac{C_{dd}\pi^2 d^4 n_0^2 R_z^2}{4}\left[\frac{1}{R^3} - \frac{9}{2}(1-\frac{2}{\pi})\frac{R_z^2}{R^5} + \mathcal{O}(R^{-7})\right]. \end{aligned} \tag{4.24}$$

When the axial density profile is the Thomas-Fermi parabolic density of Eq. (4.15), expression (4.23) can be integrated exactly ([46], Eq. 2.272), yielding

$$U_{12} = \frac{2}{3}\frac{C_{dd}\pi d^4 n_0^2 R_z^2}{R^3}\frac{1}{a^6}\left(1-(1+7a^2)\sqrt{1+4a^2}+9a^2+6a^3\mathrm{arcsinh}2a\right), \tag{4.25}$$

When the vortex separation is much larger than the core length, $R \gg R_z$, we have that $a \ll 1$ and we can expand (4.25) around $a = 0$ and find

$$\begin{aligned} U_{12} &= \frac{2}{3}\frac{C_{dd}\pi d^4 n_0^2 R_z^2}{R^3}\left[2 - \frac{18}{5}a^2 + \mathcal{O}(a^4)\right] \\ &= \frac{4}{3}C_{dd}\pi d^4 n_0^2 R_z^2\left[\frac{1}{R^3} - \frac{9}{5}\frac{R_z^2}{R^5} + \mathcal{O}(R^{-7})\right]. \end{aligned} \tag{4.26}$$

On the other hand, when the vortex separation is small compared to the core length, $R \ll R_z$, the interaction energy behaves logarithmically in the separation distance R, as

$$U_{12} = \frac{4}{3} C_{dd} \pi^2 d^4 n_0^2 \left(\frac{-7 + 6\log 2 + 3\log \frac{R_z}{R}}{R_z} + \frac{9R}{2R_z^2} + \mathcal{O}(R^2) \right).$$

In conclusion, when the vortex separation $R \gg R_z$, the dipolar interaction potential behaves as R^{-3}, irrespective of the precise density distribution in the z-direction, with the intuitively clear interpretation that the vortices can be considered as two giant dipoles. When the vortices are closer together such that $R \ll R_z$, the dipolar interaction between them changes character to a weaker (at least at short ranges) logarithmic dependence.

4.4.1. Comparing with hydrodynamic interaction energy

We can now compare the dipolar interaction potential of two vortices with the 'normal' hydrodynamic interaction. Due to the kinetic energy, two vortices of circulation l_1 and l_2, in a cylindrical container filled with a homogeneous condensate with constant density $n = \frac{2}{3} n_0$, have an interaction energy per unit length equal to [107]

$$U_{int}^{kin} = \frac{4\pi s_1 s_2 \hbar^2 n_0}{3m} \ln \frac{R_0}{R},$$

where R_0 is a measure of the distance of the vortices from the boundary of the container. Note that a change in R_0 only offsets the interaction energy by a constant. Evidently, when the circulations s_1 and s_2 have opposite signs the two vortices attract. Moreover, this expression does not depend strongly on the exact vortex core profiles, the majority of the interaction energy is contributed from the flow fields far away from the core [107, 109]. Therefore, we can assume that the above expression also holds in good approximation for vortices in dipolar condensates.

We consider the case that $R_z \ll R$. We can then combine the asymptotic results (4.26) and (4.24), by writing the interaction energy per unit length as (to leading order)

$$U_{int}^{dd} = \frac{U_{12} + U_{21}}{2R_z} = g\epsilon_{dd} \pi d^4 n_0^2 R_z \frac{A}{R^3}, \tag{4.27}$$

where we have used that $C_{dd} = 3g\epsilon_{dd}$ and where $A = \frac{3}{4}\pi$ for the gaussian density (4.14) and $A = 4$ in the Thomas-Fermi limit (4.15). For a vortex of unit circulation, the vortex core size is comparable in size to the healing length ξ, that is

$$d = \xi = \frac{\hbar}{\sqrt{m n_0 g}}.$$

Inserting this in Eq. (4.27) we find for the total interaction energy per unit length between two vortices that

$$U_{int} = U_{int}^{kin} + U_{int}^{dd} = \frac{\pi \hbar^2 n_0}{m} \left(2 s_1 s_2 \ln \frac{R_0}{R} + \epsilon_{dd} R_z \xi^2 \frac{A}{R^3} \right).$$

When ϵ_{dd} and the quantity $s_1 s_2$ have the same sign, then the interaction between the vortices stays monotonically increasing or monotonically decreasing, and the interaction remains qualitatively the same. However, when $\epsilon_{dd} < 0$ and $s_1 s_2 > 0$ at short ranges the attractive

dipolar term dominates the interaction, whereas for long ranges the repulsive kinetic term is larger. Thus, in this case the vortices are repulsive at large separations, but as the distance is decreased past some critical point, their interaction changes sign and the vortices become attractive. In the other case, $\epsilon_{dd} > 0$ but $s_1 s_2 < 0$, the vortices are repulsive at short ranges, but attractive at long range. The interaction potential then features a potential well at the turning point.

This extremum in the interaction potential can be calculated by setting the derivative of the interaction equal to zero. When we express the length of the vortex core in terms of the healing length, $R_z = L\xi$, we find for the location of the extremum that

$$R = -\xi \left(\frac{3A\epsilon_{dd} L}{2 s_1 s_2} \right)^{\frac{1}{3}} .$$

Unless the product $\epsilon_{dd} L$ is very large, this distance is always of the order of a few healing lengths. For instance, setting $\epsilon_{dd} L = 10^k$, then the location of the extremum in the interaction is at $10^{k/3}$ healing lengths. In order for the approximations made in the above calculations to be valid, we must have that $R \gg \xi$, or $(\epsilon_{dd} L)^{1/3} \gg 1$.

4.4.2. Possible Experimental Scenarios

As shown in the previous section, the presence of dipolar interactions can lead to an extremum in the interaction potential between two vortices when the sign of the dipolar interaction strength ϵ_{dd} is opposite to the sign of the product of vortex quantization numbers $s_1 s_2$. This theoretical result is valid when the condition $(\epsilon_{dd} L)^{1/3} \gg 1$ is satisfied.

Experimentally, this extremum might manifest itself as follows. Firstly, when $s_1 s_2 < 0$ and $\epsilon_{dd} > 0$, it is possible that a vortex and antivortex form a bound pair when they get trapped in the interaction potential minimum. Secondly, in the case that $s_1 s_2 > 0$ and $\epsilon_{dd} < 0$, two vortices will experience a repulsion when they are brought close together, up to a certain point where the maximum in the interaction potential is passed. After this point, the vortices will instead attract and move towards each other. A possible consequence could be that the vortices then merge to form stable multiply quantized vortices, a novel feature in dilute gases. Indeed, there have been theoretical investigations with anharmonic (quartic) traps where a massive multiply quantized vortex is predicted to form in the center of the trap ([116], and references therein), but this scenario is different in that the multiply quantized vortices would not be restrained to the center of the trap and individual vortices still remain repulsive at long ranges. Lattices of such vortices could then form, possibly with mixed quantizations leading to interesting lattice structures. Or, when adding more vortices to a condensate (e.g. by increasing the trap rotation speed), a number of transitions might be observed where the vortices jump to higher quantization numbers. But before such scenarios are attempted both theoretically and experimentally, a closer investigation of the interaction potential at short ranges is required. For such calculations the 3d structure of the vortex core, and its self-energy[7] need to be taken into account. These require the (electrostatic / gravitational) potentials of hollow and solid cylinders, which are known analytically from the investigation of gravitional forces at short distances, see for example references [18] and [19]. Another

[7] See equation (4.20) and the discussion immediately below it.

possible avenue for theoretical research could be by means of numerical simulation, since the analytic expressions for cylinder potentials turn out to be very complicated.

5. Condensate response to an impurity

5.1. Introduction

In section 4.3.3 we saw that the condensate response to a vortex core bears some resemblance to screening effects in systems with long-range Coulomb interactions. For instance, when a very heavy positive ion is added to a plasma at the origin, it tends to attract negatively charged electrons and repel positively charged ions. Effectively, the ion gathers a shielding cloud that cancels its charge and this effect strongly dampens the electric field set up by the ion. More generally, in the presence of mobile charge carriers a particle's electrostatic potential falls off faster than it would in vacuum, and this effect is known as *Debye shielding* [95]. Similar effects occur in many physical systems, for example in semiconductors [67], electrolytes [77] and charged colloidal suspensions [77].

Suppose we have a uniform electron gas with density n, and we introduce a point charge q at the origin. Denoting the density response of the electrons by δn and the electrostatic potential of the density response plus point charge by $\delta\phi$, Poisson's equation for the electrostatic potential then becomes

$$-\nabla^2\delta\phi = \frac{1}{\epsilon_0}\left[q\delta(\mathbf{r}) - e\delta n\right],$$

where e is the electron charge and ϵ_0 the permittivity of free space [63]. It is often a reasonable assumption that the density response is proportional to the change in potential $\delta\phi$ [87]. Thus, setting $e\delta n = \epsilon_0 a^2\delta\phi$, for some a, we get

$$\left(\nabla^2 - a^2\right)\delta\phi = \frac{q}{\epsilon_0}\delta(\mathbf{r}),$$

which is solved by

$$\delta\phi = \frac{q}{4\pi\epsilon_0}\frac{\mathrm{e}^{-ar}}{r},$$

which is called the screened Coulomb potential [87]. Clearly, the shielding effect is not merely a change in amplitude of the potential, but it drastically alters the character of the Coulomb potential from long range to short range. Shielding is a universal effect and potentials of the above form occur in many systems [77].

To investigate whether dipolar Bose-Einstein condensates exhibit similar shielding effects, we consider a homogeneous condensate with an impurity added at the origin in this chapter, and calculate the resulting density response and dipolar potential.

5.2. Density response to an impurity

Consider a uniform gas with constant density n, with a small potential perturbation δV_{imp} added at constant chemical potential $\mu = ng(1-\epsilon_{dd})$, leading to a perturbation in the density

δn. The Gross-Pitaevskii equation for this system reads

$$\left(-\frac{1}{2}\frac{\hbar^2}{m}\nabla^2 + \delta V_{imp} + g(n+\delta n) + \Phi_{dd}[n+\delta n]\right)\sqrt{n+\delta n} = \mu\sqrt{n+\delta n}.$$

There is only one length scale in the non-dipolar problem, and this is the healing length (see Sec. 1.4.3)

$$\xi = \frac{\hbar}{\sqrt{mng}}.$$

Scaling all length scales by ξ, all energies by the energy ng and all densities by n results in the dimensionless equation

$$\left(-\frac{1}{2}\nabla^2 + \delta V'_{imp} + 1 + \delta n' + \epsilon_{dd}\Phi'_{dd}[1+\delta n]\right)\sqrt{1+\delta n'} = (1-\epsilon_{dd})\sqrt{1+\delta n'}, \tag{5.1}$$

where $\delta n' = \delta n/n$, $\delta V'_{imp} = \delta V_{imp}/ng$, and $\epsilon_{dd}\Phi'_{dd} = \Phi_{dd}/ng$. In the following we will drop the primes, under the assumption that we will be working in the above units.

We can rewrite (5.1) as

$$-\frac{1}{2}\frac{1}{\sqrt{1+\delta n}}\nabla^2\sqrt{1+\delta n} + \delta V_{imp} + \delta n + \epsilon_{dd}\Phi_{dd}[\delta n] = 0,$$

by dividing by the wave function $\sqrt{1+\delta n}$ and noting that $\Phi_{dd}[1] = 1$, where we have used equation (1.47) and the fact that the potential cannot depend on z because of translational symmetry, hence the second derivative term vanishes. Since the density response δn is assumed to be small, we can expand the first term on the left hand side by using that

$$\sqrt{1+\delta n} = 1 + \frac{1}{2}\delta n + \mathcal{O}(\delta n^2) \tag{5.2}$$

$$\frac{1}{\sqrt{1+\delta n}} = 1 - \frac{1}{2}\delta n + \mathcal{O}(\delta n^2) \tag{5.3}$$

such that we get the following integral-differential equation

$$0 = -\frac{1}{2}\left(1-\frac{1}{2}\delta n\right)\nabla^2\left(1+\frac{1}{2}\delta n\right) + \delta V_{imp} + \delta n + \epsilon_{dd}\Phi_{dd}[\delta n] \tag{5.4}$$

$$= -\frac{1}{2}\nabla^2\delta n + \delta V_{imp} + \delta n + \epsilon_{dd}\Phi_{dd}[\delta n]. \tag{5.5}$$

Since the dipolar potential has the form of a convolution, this equation becomes algebraic when we take the Fourier transform:

$$\left[\frac{1}{2}k^2 + 1 + \epsilon_{dd}\left(3\frac{k_z^2}{k^2} - 1\right)\right]\delta\tilde{n} + \delta\tilde{V}_{imp} = 0, \tag{5.6}$$

where we write $\tilde{f} = \mathcal{F}[f]$ to denote the Fourier transform of a certain quantity f. We will be using the Fourier convention defined in equations (I.1), (I.2), while writing $\mathbf{k} = 2\pi\boldsymbol{\nu}$ and $k_z = 2\pi\nu_z$ for ease of notation. We are looking for screening effects analogous to the electrostatic case detailed in the introduction, therefore as a potential perturbation δV_{imp} we take the potential (both dipolar and s-wave contact interactions) due to the addition of a quantity $\delta_{dd} > 0$ of foreign material at the origin, with some *fixed* density distribution δm.

This foreign material will generally have a different dipolar interaction coefficient C'_{dd}, which characterises the strength of the dipolar interaction of the impurity with the rest of the condensate. The impurity will also have a different s-wave scattering length a' and associated contact interaction strength g', such that the potential due to the impurity is equal to

$$\delta V_{imp}(\mathbf{r}) = \left(C^* \Phi_{dd}[\delta m](\mathbf{r}) + g^* \delta m(\mathbf{r})\right), \tag{5.7}$$

where $C^* = C'_{dd}/C_{dd}$ and $g^* = g'/g$. To simulate the effect of a single foreign particle being added at the origin, we take as an impurity density distribution

$$\delta m = \sqrt{\frac{\sqrt{\delta_{dd}}}{\pi^3}} \mathrm{e}^{-r^2/\sqrt{\delta_{dd}}}. \tag{5.8}$$

This density distribution is chosen exactly such that in the limit of $\delta_{dd} \to 0$ it becomes a delta distribution: $\delta m = \delta_{dd}\delta(\mathbf{r})$ [83]. For the density distribution (5.8) we have for all coordinates $\mathbf{r}$, including the origin, that $\delta m(\mathbf{r})$ exists and also $\delta m(\mathbf{r}) \leq \delta_{dd}^{1/4} \pi^{-3/2}$, such that perturbation theory can be correctly applied. In particular, the expansions (5.2), (5.3) are correct and equation (5.5) indeed describes the density response of the condensate to the impurity.

In the limit $\delta_{dd} \to 0$ we can now safely replace the density distribution by the delta distribution

$$\delta m = \delta_{dd}\delta(\mathbf{r}).$$

The Fourier transform of δV_{imp}, equation (5.7), with δm the delta density distribution, is equal to

$$\delta\tilde{V}_{imp} = \delta_{dd} C^* \left(3\epsilon_{dd}\frac{k_z^2}{k^2} + \frac{g^*}{C^*} - \epsilon_{dd}\right). \tag{5.9}$$

Using this potential perturbation in equation (5.6) we arrive at the following expression for the density response

$$\delta\tilde{n} = \frac{-\delta_{dd} C^* \left(3\epsilon_{dd}\frac{k_z^2}{k^2} + \frac{g^*}{C^*} - \epsilon_{dd}\right)}{\frac{1}{2}k^2 + 1 - \epsilon_{dd} + 3\epsilon_{dd}\frac{k_z^2}{k^2}} = \delta_{dd} C^* \left[\frac{\frac{1}{2}k^2 + \frac{1}{2}A}{\frac{1}{2}k^2 + 1 - \epsilon_{dd} + 3\epsilon_{dd}\frac{k_z^2}{k^2}} - 1\right], \tag{5.10}$$

where we have defined

$$A = 2\left(\frac{g^*}{C^*} - 1\right). \tag{5.11}$$

The dipolar potential in the medium is then the potential due to both the perturbation and the density response, and we can calculate it using (1.47)

$$\Phi_{dd}[\delta n + C^*\delta m] = -3\epsilon_{dd}\left(\frac{\partial^2}{\partial z^2}\phi[\delta n + C^*\delta m] + \frac{\delta n + C^*\delta m}{3}\right) \tag{5.12}$$

where the associated electrostatic potential

$$\phi[\delta n + C^*\delta m] = \frac{1}{4\pi}\int \frac{\delta n(\mathbf{r}') + C^*\delta m(\mathbf{r}')}{|\mathbf{r}-\mathbf{r}'|}\mathrm{d}^3\mathbf{r}'$$

can be calculated in Fourier space, using (5.10), to be

$$\tilde{\phi}[\delta n + C^*\delta m] = \delta_{dd}C^*\frac{k^2+A}{k^4+2(1-\epsilon_{dd})k^2+6\epsilon_{dd}k_z^2}. \tag{5.13}$$

In principle equation (5.12) together with (5.13) solves the problem, but of course we would like to know the dipolar potential in real space rather than momentum space, which is the topic of the next two sections.

We will only calculate the electrostatic potential $\phi[\delta n + C^*\delta m]$, as the density response δn, and thus the total dipolar potential, can be simply found from $\phi[\delta n + C^*\delta m]$ by noting that

$$-\nabla^2\phi[\delta n] = -\nabla^2\frac{1}{4\pi}\int\frac{\delta n(\mathbf{r}')}{|\mathbf{r}-\mathbf{r}'|}\mathrm{d}^3\mathbf{r}' = \int \delta n(\mathbf{r}')\delta(\mathbf{r}-\mathbf{r}')\mathrm{d}^3\mathbf{r}' = \delta n(\mathbf{r}), \tag{5.14}$$

such that $\delta n = -\nabla^2\phi[\delta n + C^*\delta m] - C^*\delta m$, and where we have used that $|\mathbf{r}-\mathbf{r}'|^{-1}$ is the Green's function of the Laplace operator in three dimensions [63, 65]:

$$\nabla^2\left(\frac{1}{|\mathbf{r}-\mathbf{r}'|}\right) = -4\pi\delta(\mathbf{r}-\mathbf{r}').$$

Once the density response and the electrostatic potential are known, the dipolar potential then simply follows through equation (1.47).

5.3. The screened electrostatic potential

To find the screened electrostatic potential in real space, we need to compute the Fourier transform in the z-direction of (5.13), followed by a Hankel transform (see Appendix I) in the r-plane. In other words, we have to calculate the quantity

$$\phi[\delta n + C^*\delta m] = \frac{\delta_{dd}C^*}{8\pi^3}I(r,z), \tag{5.15}$$

where

$$I(r,z) = \int_0^\infty\int_{-\infty}^\infty \frac{(k_r^2+k_z^2+A)\mathrm{e}^{\mathrm{i}k_z z}J_0(k_r r)k_r}{k_z^4+2(1+2\epsilon_{dd}+k_r^2)k_z^2+k_r^4+2(1-\epsilon_{dd})k_r^2}\mathrm{d}k_z\mathrm{d}k_r. \tag{5.16}$$

We can rewrite this as

$$I(r,z) = \int_0^\infty\int_{-\infty}^\infty \frac{(k_r^2+k_z^2+A)\mathrm{e}^{\mathrm{i}k_z z}J_0(k_r r)k_r}{(\gamma_+^2+k_z^2)(\gamma_-^2+k_z^2)}\mathrm{d}k_z\mathrm{d}k_r, \tag{5.17}$$

with

$$\gamma_{\pm}^2 = 1 + 2\epsilon_{dd} + k_r^2 \pm \sqrt{(1+2\epsilon_{dd})^2 + 6\epsilon_{dd}k_r^2}. \tag{5.18}$$

Note that $\gamma_{\pm}^2$ is real and positive for $0 \leq \epsilon_{dd} < 1$ and $k_r > 0$. For γ_+ this statement is trivial. For γ_- this can be seen by first noting that in the limit $k_r \to \infty$ we have that $\gamma_- > 0$. Also, $\gamma_- = 0$ for $k_r = 0$. It remains to verify that there are no positive real roots on the k_r-axis of the equation

$$1 + 2\epsilon_{dd} + k_r^2 = \sqrt{(1+2\epsilon_{dd})^2 + 6\epsilon_{dd}k_r^2}.$$

This equation is satisfied for

$$k_r = 0, \qquad k_r = \pm\sqrt{2(\epsilon_{dd} - 1)},$$

from which is follows that there are no positive real roots for $0 \leq \epsilon_{dd} < 1$. For negative ϵ_{dd} however, both $\gamma_{\pm}$ become complex, since the $\sqrt{(1+2\epsilon_{dd})^2 + 6\epsilon_{dd}k_r^2}$ term becomes imaginary for large k_r. The real part of γ_- is then equal to $1 + 2\epsilon_{dd} + k_r^2$, which is always nonzero and positive for $\epsilon_{dd} > -\frac{1}{2}$.

By noting that the real part of $I(r,z)$ is symmetric in k_z and the imaginary part anti-symmetric, we can replace the integral over k_z by a Fourier-cosine transform from 0 to $+\infty$ by writing

$$I(r,z) = 2\int_0^\infty \int_0^\infty \frac{(k_r^2 + k_z^2 + A)\cos(k_z z) J_0(k_r r)}{(\gamma_+^2 + k_z^2)(\gamma_-^2 + k_z^2)} \mathrm{d}k_z k_r \mathrm{d}k_r. \tag{5.19}$$

The inner integral is known, it can be found in [46], from formulas 3.728.1 and 3.728.3 which state that (respectively)

$$\int_0^\infty \frac{\cos(ax)\mathrm{d}x}{(\beta^2 + x^2)(\gamma^2 + x^2)} = \frac{\pi(\beta \mathrm{e}^{-a\gamma} - \gamma \mathrm{e}^{-a\beta})}{2\beta\gamma(\beta^2 - \gamma^2)} \tag{5.20}$$

and

$$\int_0^\infty \frac{x^2\cos(ax)\mathrm{d}x}{(\beta^2 + x^2)(\gamma^2 + x^2)} = \frac{\pi(\beta \mathrm{e}^{-a\beta} - \gamma \mathrm{e}^{-a\gamma})}{2(\beta^2 - \gamma^2)}, \tag{5.21}$$

subject to the conditions that $a > 0$, Re $\beta > 0$ and Re $\gamma > 0$. By setting $a = z$, $\beta = \gamma_+$, $\gamma = \gamma_-$, these conditions are satisfied by $\gamma_\pm$ for $-\frac{1}{2} < \epsilon_{dd} < 1$ as calculated above, and we thus find that

$$I(r,z) = 2\int_0^\infty \left[F_+(k_r)\mathrm{e}^{-z\gamma_+} - F_-(k_r)\mathrm{e}^{-z\gamma_-}\right] J_0(k_r r) k_r \mathrm{d}k_r, \tag{5.22}$$

where

$$F_\pm(k_r) = \frac{\pi(\gamma_\pm^2 - k_r^2 - A)}{2\gamma_\pm(\gamma_+^2 - \gamma_-^2)}. \tag{5.23}$$

It should be noted that the inner integral in equation (5.19) can only be evaluated for $k_r > 0$, so in principle there could be a problem when we want to evaluate the outer integral with the lower integration limit equal to 0. To be formally correct we should replace the lower limit by some small constant $\epsilon > 0$, and then take the limit of $\epsilon \to 0$ in the end. It is found however

that this procedure does not affect the final result in our case, and for notational simplicity we simply put $k_r = 0$ as the lower integration limit in the following sections.

The remaining integral (5.22) is very complicated and we have little hope for evaluating it exactly. Therefore, in the next two sections we will look at its asymptotic value in the limits that $z \to \infty$ and $r \to \infty$.

To investigate these limits, we will also be needing asymptotics of the products $k_r F_+$ and $k_r F_-$, so we will list those here. For $k_r \ll 1$, we have that

$$k_r F_-(k_r) = -\frac{A\pi}{4\sqrt{1+\epsilon_{dd}-2\epsilon_{dd}^2}} + \mathcal{O}(k_r^2) \tag{5.24}$$

$$k_r F_+(k_r) = \frac{\pi\,(2-A+4\epsilon_{dd})}{4\sqrt{2}\,(1+2\epsilon_{dd})^{\frac{3}{2}}} k_r + \mathcal{O}(k_r^3). \tag{5.25}$$

In the other limit that $k_r \to \infty$, we find that

$$\lim_{k_r\to\infty} F_\pm = \pm\frac{\pi}{4}, \tag{5.26}$$

and moreover

$$k_r(F_+ - F_-) - \frac{\pi}{2} \propto k_r^{-2}. \tag{5.27}$$

5.3.1. The limit case that $z \to \infty$, $r = 0$

In this section we will evaluate the asymptotic behaviour of the integral (5.22) for the case that $r = 0$ and $z \to \infty$. For this purpose we will use Laplace's method [9], which is a technique for finding the asymptotic behaviour of integrals of the form

$$I_L(z) = \int_a^b f(t)\mathrm{e}^{-z\phi(t)}\mathrm{d}t, \tag{5.28}$$

where a, b are real constants,$f(t)$ and $\phi(t)$ are real and continuous and $\phi(t)$ has a minimum at $c \in [a, b]$. The idea of this method is then as follows. Since the large parameter z appears in an exponential, the only contributions to the leading order behaviour are coming from a small interval centered around the minimum of $\phi(t)$, that is, we can approximate the integral (5.28) by

$$I_L(z) = \int_{c-\epsilon_-}^{c+\epsilon_+} f(t)\mathrm{e}^{-z\phi(t)}\mathrm{d}t,$$

where $\epsilon_\pm$ are arbitrary positive numbers with at most one of the two equal to zero and with the constraint that the integration interval is a subinterval of $[a, b]$. When the $\epsilon_\pm$ are chosen small enough, $f(t)$ and $\phi(t)$ can be approximated by their respective Taylor expansions around $t = c$. The remaining integrals are then, perhaps surprisingly, evaluated by extending the integration interval to infinity. Intuitively, this can be understood by the fact that contributions to the integral from outside the small region around the minimum of $\phi(t)$ are vanishing exponentially compared to those from within this region. Although the Taylor expansions are perhaps no longer valid outside this region, the error introduced this way is always vanishing for $z \to \infty$ due to the exponential term. A detailed discussion is given in [9].

For our particular case (5.22), we have in fact two exponential terms. But since $\gamma_+ > \gamma_-$, we only have to consider the term with γ_- in the exponent, as the other term will become exponentially small compared to this one for large z. Furthermore, γ_- has its minimum at $k_r = 0$, as shown in the discussion following equation (5.18). Expanding γ_- around $k_r = 0$ then, gives

$$\gamma_-(k_r) = 0 + \sqrt{\frac{1-\epsilon_{dd}}{1+2\epsilon_{dd}}}k_r + \mathcal{O}(k_r^2)(k_r \ll 1). \tag{5.29}$$

Using the above expansion, together with that of $k_r F_-$ given in equation (5.24), we can thus approximate the integral (5.22) as

$$\begin{aligned} I(r,z) &\simeq -\frac{A\pi}{4\sqrt{1+\epsilon_{dd}-2\epsilon_{dd}^2}}\int_0^{\epsilon}\exp\left(-z\sqrt{\frac{1-\epsilon_{dd}}{1+2\epsilon_{dd}}}k_r\right)\mathrm{d}k_r & (5.30)\\ &\simeq -\frac{A\pi}{4\sqrt{1+\epsilon_{dd}-2\epsilon_{dd}^2}}\int_0^{\infty}\exp\left(-z\sqrt{\frac{1-\epsilon_{dd}}{1+2\epsilon_{dd}}}k_r\right)\mathrm{d}k_r & (5.31)\\ &= -\frac{A\pi}{4(1-\epsilon_{dd})}\frac{1}{z} \qquad (z\to\infty), & (5.32)\end{aligned}$$

provided that $A \neq 0$. When $A = 0$ we get a z^{-3} potential instead. Since the above result ($A \neq 0$) specifies the electrostatic potential, this means that the dipolar potential effectively goes as z^{-3}. The dipole moment of the perturbation is therefore not screened out, due to the kinetic energy term restricting the response of the condensate.

5.3.2. The limit case that $z = 0$, $r \to \infty$

To investigate the other limit in which $z = 0$, $r \to \infty$, we start by defining

$$F_0(k_r) = (F_+ - F_-)k_r - \frac{\pi}{2},$$

such that $F_0(k_r) \to 0$ for $k_r \to \infty$, where we have used equation (5.26). At $k_r = 0$ we have

$$F_0(0) = \frac{A\pi}{4\sqrt{1+\epsilon_{dd}-2\epsilon_{dd}^2}} - \frac{\pi}{2}.$$

Using this definition, the integral (5.22) turns into

$$\begin{aligned} I(r,z) = I(r) &= 2\int_0^{\infty}F_0(k_r)J_0(k_r r)dk_r - \pi\int_0^{\infty}J_0(k_r r)dk_r & (5.33)\\ &= 2\int_0^{\infty}F_0(k_r)J_0(k_r r)dk_r - \frac{\pi}{r}. & (5.34)\end{aligned}$$

We are now left with the task of asymptotically evaluating the integral in (5.34), but now the large parameter shows up inside the Bessel function, rather than inside an exponential. There exist techniques to deal with highly oscillatory integrands, but these all apply to imaginary

exponential oscillations. We will therefore rewrite the Bessel function using the following integral representation ([2], eq. 9.1.23)

$$J_0(x) = \frac{2}{\pi}\int_0^\infty \sin(x\cosh t)\mathrm{d}t = \frac{2}{\pi}\mathrm{Im}\int_0^\infty \exp(\mathrm{i}x\cosh t)\mathrm{d}t. \tag{5.35}$$

Inserting this representation in (5.34) and changing the order of integration then provides us with an integral with a highly oscillatory imaginary exponential:

$$I(r) = \frac{4}{\pi}\mathrm{Im}\int_0^\infty\int_0^\infty F_0(k_r)\mathrm{e}^{\mathrm{i}k_r r\cosh t}\mathrm{d}k_r\mathrm{d}t - \frac{\pi}{r}.$$

We now proceed by integrating by parts, such that

$$I(r) = \frac{4}{\pi}\mathrm{Im}\int_0^\infty \Big[F_0(k_r)\frac{\mathrm{e}^{\mathrm{i}k_r r\cosh t}}{\mathrm{i}r\cosh t}\Big|_{k_r=0}^{k_r=\infty} - \frac{1}{\mathrm{i}r\cosh t}\int_0^\infty \frac{\mathrm{d}F_0}{\mathrm{d}k_r}\mathrm{e}^{\mathrm{i}k_r r\cosh t}\mathrm{d}k_r\Big]\mathrm{d}t - \frac{\pi}{r}. \tag{5.36}$$

The boundary term vanishes at $k_r = \infty$, since we have defined F_0 to do exactly that. At $k_r = 0$, the boundary term yields

$$\begin{aligned}\frac{4}{\pi}\mathrm{Im}\int_0^\infty F_0(k_r)\frac{\mathrm{e}^{\mathrm{i}k_r r\cosh t}}{\mathrm{i}r\cosh t}\Big|_{k_r=0}dt = F_0(0)\frac{4}{\pi}\int_0^\infty \frac{1}{r\cosh t}dt = 2F_0(0)\frac{1}{r}\\ = \frac{A\pi}{4\sqrt{1+\epsilon_{dd}-2\epsilon_{dd}^2}}\frac{1}{r} - \frac{\pi}{r}.\end{aligned} \tag{5.37}$$

When we substitute this back in equation (5.36), we see that the $\frac{\pi}{r}$ terms cancel, and we are left with the following expression for $I(r)$:

$$I(r) = \frac{-A\pi}{4\sqrt{1+\epsilon_{dd}-2\epsilon_{dd}^2}}\frac{1}{r} - \frac{4}{\pi}\mathrm{Im}\int_0^\infty \frac{1}{\mathrm{i}r\cosh t}\int_0^\infty \frac{\mathrm{d}F_0}{\mathrm{d}k_r}\mathrm{e}^{\mathrm{i}k_r r\cosh t}\mathrm{d}k_r\mathrm{d}t. \tag{5.38}$$

We will now exploit the rapid oscillating behaviour of the integrand of the remaining integral over k_r. Namely, this integral can be shown to vanish in the limit of $r\to\infty$ by virtue of a very general result called the Riemann-Lebesque lemma. This lemma states that

$$\int_a^b f(x)\mathrm{e}^{\mathrm{i}r\phi(x)}dx \to 0, \qquad (r\to\infty), \tag{5.39}$$

for real a, b and any $f(x)$ for which $\int_a^b |f(x)|\mathrm{d}x$ exists, and any continuously differentiable $\phi(x)$, provided that ϕ is not constant on any subinterval of $[a,b]$ [9]. The result can be understood intuitively by noting that in the limit of $r\to\infty$ the integrand will oscillate faster and faster, such that contributions from adjacent subintervals nearly cancel. In our case we have that $\phi(x)$ in equation (5.39) is linear in x, and the proof becomes very simple. Namely,

$$B(r) := \int_a^b f(x)\mathrm{e}^{\mathrm{i}ax r}dx = \int_a^b f\left(x'+\frac{\pi}{ar}\right)\mathrm{e}^{\mathrm{i}ax'r+\mathrm{i}\pi}dx' = -\int_a^b f\left(x'+\frac{\pi}{ar}\right)\mathrm{e}^{\mathrm{i}ax'r}dx',$$

where we have made the substitution $x = x' + \frac{\pi}{ar}$. We can then write

$$B(r) = \frac{1}{2}\int_a^b \left[f(x) - f\left(x + \frac{\pi}{ar}\right)\right] \mathrm{e}^{\mathrm{i}axr} dx,$$

but that means that

$$|B(r)| \leq \frac{1}{2}\int_a^b \left|f(x) - f\left(x + \frac{\pi}{ar}\right)\right| dx,$$

which tends to zero for $r \to \infty$.

Here, $\frac{\mathrm{d}F_0}{\mathrm{d}k_r}$ is absolutely integrable since F_0 is differentiable everywhere and vanishes rapidly enough at infinity (see equation (5.27)), and therefore all constraints for the Riemann-Lebesque lemma are met, such that we can conclude that the integral over k_r in (5.38) vanishes. It remains to show that integration over t over an infinite domain does not yield any significant contribution. Formally, when we say that the integral over k_r vanishes as $r \to \infty$, we have that for any $\epsilon > 0$, there exists an $R(t, \epsilon)$ such that

$$\forall r > R(t,\epsilon): \quad \left|\int_0^\infty \frac{\mathrm{d}F_0}{\mathrm{d}k_r} \mathrm{e}^{\mathrm{i}k_r r \cosh t} \mathrm{d}k_r\right| \leq \epsilon. \tag{5.40}$$

Next, we define $R^-(\epsilon, t)$ as the smallest $R(t, \epsilon)$ satisfying the above statement, and consequently we define

$$R^*(\epsilon) = \max_t \left\{R^-(t,\epsilon)\right\}.$$

Then, for any $\epsilon > 0$ then $\forall r > R^*(\epsilon)$ we have that

$$\int_0^\infty \frac{1}{\mathrm{i}r\cosh t}\int_0^\infty \frac{\mathrm{d}F_0}{\mathrm{d}k_r}\mathrm{e}^{\mathrm{i}k_r r\cosh t}\mathrm{d}k_r\mathrm{d}t \leq \int_0^\infty \frac{\epsilon}{\cosh t}dt = \frac{\epsilon\pi}{2}.$$

But that means that the entire integral of equation (5.38) vanishes, and in conclusion we finally arrive at the following asymptotic approximation for the integral $I(r, z)$:

$$I(r) \simeq \frac{-A\pi}{4\sqrt{1 + \epsilon_{dd} - 2\epsilon_{dd}^2}}\frac{1}{r}, \qquad (r \to \infty) \tag{5.41}$$

provided $A \neq 0$. As in the limit for $z \to \infty$ we find a similar inverse distance dependence, albeit with a different prefactor. When $A = 0$, we have to perform integration by parts twice[1] more to find a nonzero leading order term, which is of the order r^{-3}.

In this section, we have obtained an asymptotic approximation to the integral (5.16) by splitting off the part of the function $k_r(F_+ - F_-)$ which was not absolutely integrable on $[0, \infty)$, such that we could treat the remaining part using integration by parts and application of the Riemann-Lebesque lemma. Here, the non-absolutely-integrable part was a constant for which we could evaluate the inverse Hankel transform integral explicitly (second integral appearing in (5.33)). However, when the function $k_r(F_+ - F_-)$ would have been of the form

$$k_r(F_+ - F_-) \simeq \sum_{n=1}^{N} a_n k_r^n, \qquad (k_r \to \infty),$$

[1] After the first integration by parts, we are left with a real-valued boundary term, and upon taking the imaginary part this vanishes.

the inverse Hankel transform integrals

$$I_n = \int_0^\infty a_n k_r^{n+1} J_0(k_r r) dk_r$$

do not exist. Such cases could then be treated using generalised functions [83] in combination with the representation (5.35), or alternatively by using Mellin transforms as discussed in the book by Handelsman and Bleistein [10], section 6.3.

5.4. Conclusions

Combining the results from the previous paragraphs, we can now calculate the effective dipolar potential far away from the impurity. In terms of the integral $I(r, z)$ defined in equation (5.16), the effective dipolar potential is given by (using equations (5.12), (5.14))

$$\Phi_{dd}[\delta n + C^* \delta m] = -\frac{C^* \delta_{dd} \epsilon_{dd}}{8\pi^3} \left(2\frac{\partial^2}{\partial z^2} - \frac{1}{r}\frac{\partial}{\partial r}\left(r \frac{\partial}{\partial r} \right) \right) I(r, z).$$

For $r \to \infty$, and $z = 0$, we expect the second derivative of $I(r, z)$ to z to be vanishingly small[2], and similarly for $z \to \infty$ and $r = 0$ we expect the derivatives with respect to r to vanish. Then, we can insert the asymptotic expansions (5.32) and (5.41) in these limits, to find

$$\Phi_{dd}[\delta n + C^* \delta m] \simeq \frac{A C^* \epsilon_{dd} \delta_{dd}}{8(1 - \epsilon_{dd})\pi^2} \frac{1}{z^3} \qquad (z \to \infty, r = 0),$$

and

$$\Phi_{dd}[\delta n + C^* \delta m] \simeq -\frac{A C^* \epsilon_{dd} \delta_{dd}}{32\sqrt{1\epsilon_{dd} - 2\epsilon_{dd}^2}\pi^2} \frac{1}{r^3} \qquad (r \to \infty, z = 0).$$

Clearly, the $1/r^3$ dependency is left intact, and we cannot speak of a shielding effect in the same sense as in the introduction of this chapter, where we saw that in (e.g.) plasmas the shielding effect changes the nature of the effective potential from long range to short range. Presumably, the quantum pressure prevents the condensate from forming the density response needed for such complete screening, and the absence of screening in dipolar BECs is directly due to the quantum nature of the material.

Further calculations could focus on different physical situations, such as spherical holes in the density by a hard wall potential, which would require a non-perturbative approach. Furthermore, several other studies report density oscillations [134, 114, 133]. In keeping with the shielding picture, these could be the analog of Friedel oscillations in plasmas [95, 87], and as such warrant further investigation.

[2]This result has been checked analytically, but the equations are not presented here.

6. Conclusions

In this project we studied Bose-Einstein condensates with long-range dipolar interactions.

In chapter 2 we present a general and accessible methodology for determining the static solutions and excitation frequencies of trapped dipolar BECs in the Thomas-Fermi limit. We explore the static solutions and the low-lying collective excitations throughout a large and experimentally relevant parameter space, including positive and negative dipolar couplings $C_{\rm dd}$, positive and negative s-wave interactions g, and cylindrically and non-cylindrically symmetric systems. Moreover, our approach enables us to identify the modes responsible for collapse of the condensate. The superfluidity of dipolar BECs has not been experimentally confirmed. Therefore, special attention is being paid to the scissors mode, which can be used as a direct test of superfluidity.

In chapter 3 we studied dipolar BECs in rotating harmonic traps. Specifically, starting from the hydrodynamic equations of motion we obtain the stationary solutions for a condensate in a rotating elliptical trap and find when they become dynamically unstable to perturbations. This enables us to predict the regimes of stable and unstable motion of a rotating dipolar condensate. While for a non-dipolar BEC (in the TF limit) the transition between stable and unstable motion is dependent only on the rotation frequency and trap ellipticity, we show that for a dipolar BEC it is additionally dependent on the strength of the dipolar interactions and the geometry of the trap. For a dipolar BEC the critical rotation frequency at which vortices become favorable Ω_v is sensitive to the trap geometry and dipolar interactions, and so one cannot simply assume that instability will lead to a vortex lattice. Using a simple prediction for this frequency, we indicate the regimes in which one can expect vortex lattice formation. Experimentally accessible routes to generate instability and vortex lattices in dipolar condensates are discussed in detail.

Chapter 4 is concerned with vortices in dipolar BECs. Through numerical calculations the effect of dipolar interactions on the core structure of a single vortex is mapped out for $0 < \epsilon_{dd} < 1.2$. For increasing dipolar interaction strength we observe two distinct effects. Firstly, the core radius increases to nearly twice the non-dipolar core radius. Secondly, a surplus of condensate accumulates around the vortex core forming a 'ripple'. This ripple effect is remniscent of shielding effects in systems such as plasmas, with long range Coulomb interactions and where mobile charge carriers act to screen out the Coulomb potential of immersed impurities. Furthermore in this chapter we study the dipolar interaction potential between two vortices under the approximation that the vortex core size is small compared to the vortex separation R. Under this assumption we find that the interaction potential behaves as $1/R^3$ when R is large compared to the length of the vortex cores, whereas it changes character to a logarithmic potential when the vortex separation becomes small compared to the core length. The additional dipolar interaction potential, which is not present in 'ordinary' non-dipolar condensates, could lead to exciting new physics such as multiply quantised vortices or bound vortex pairs.

The 'shielding' effect observed in chapter 4 provided the motivation for the research in chapter 5. To find out whether universal shielding effects such as those found in plasmas also occur in dipolar BECs we studied the effective potential generated by an impurity atom of a foreign species immersed in a homogeneous dipolar BEC, with the impurity posessing a dipole moment and scattering length different from that of the condensate. Using integral asymptotics, we obtained the potential at long distances from the impurity and found that the effective potential was proportional to $1/r^3$, with r the distance from the immersed impurity. The long range nature of the impurity potential was thus not affected, and although some shielding occurs in dipolar BECs, these effects are not of the same type as those observed in plasmas.

Mathematical aspects of this research include:

- Chapter 1, and appendix A: Scaling and perturbation analysis in relation to the Thomas-Fermi approximation. Also, the Painlevé II equation occurring in the boundary layer of the condensate was highlighted in the appendix.
- Chapter 2, and Appendices C to F: Determination of stability by energy analysis and linearisation of hydrodynamic equations, involving calculation of dipole potential of heterogenous ellipsoids with polynomial densities.
- Chapter 3, and appendices E, F, and H: Similar linearisation of hydrodynamic equations, and perturbation analysis of the bifurcation point in the phase diagram of stationary states in the rotating trap.
- Chapter 4, and appendices I to K: Numerical calculation of the ground state of a dipolar BEC containing a vortex in the center, involving Fourier and Hankel transforms for dealing with the dipolar potential, minimization of a nonlinear functional through the steepest descent method, and some scaling for making the equations suited for numerical calculations.
- Chapter 5: Integral asymptotics for large values of parameters appearing in exponential terms of the integrand, and appearing in the argument of a Bessel function. Some perturbation analysis.

This work has resulted in two publications in peer-reviewed journals to this date: a short synopsis of chapter 3 has been published in the journal *Physical Review Letters* [129], and a slightly longer account of this same chapter has been published in the journal *Laser Physics* [89], as an invited conference proceeding. Additionally, there are two more publications in preparation consisting of the manuscripts of chapters 2 and 3, that are to be submitted to the journal Physical Review A (Atomic, Molecular, and Optical Physics). The work described in chapters 2 and 3 has also been presented in poster format at conferences in Banff (Canada)[1], Grenoble (France)[2], and Lunteren[3] and Veldhoven[4] (Netherlands). The remaining chapters 4 and 5 are preliminary calculations investigating phenomena beyond the Thomas-Fermi approximation, and could serve as a solid basis for further research on dipolar BECs, or for reseach on other quantum degenerate gases with long-range interactions.

[1] CIFAR Cold Atoms meeting
[2] Workshop BEC 2008: "Theory of Quantum Gases and Quantum Coherence"
[3] AMO conference
[4] Physics FOM Veldhoven meeting

7. Technology Assessment

Since the spectacular experimential confirmation of Bose-Einstein condensation in 1995, the field of ultracold atomic gases has attracted enormous theoretical and experimental attention. The atoms in a Bose-Einstein condensate (BEC) conspire to form a giant matter wave, which is so large that it can even be observed optically. This provides a unique magnifying glass onto the quantum world, and together with the great experimental control using lasers and external electromagnetic fields, Bose-Einstein condensates turn out to be particularly well-suited systems to perform fundamental quantum mechanical research. Moreover, due to their tunability, BECs are also good model systems for general condensed matter physics.

The aforementioned fundamental research is essential for progress in technology on the long term. Envisaged applications include, for instance, atom lasers and quantum computers. Atom lasers are the matter wave analog of optical lasers. Due to the short de Broglie wavelength compared to that of light, interferometers based on atom lasers are predicted to be orders of magnitude more sensitive than current interferometer technology. Such precision could for instance help detect changes in space-time, or local changes in gravitational potential. Quantum computers constitute a fundamentally new type of computer, which employs quantum mechanical phenomena such as entanglement and superposition in order to solve particular problems many times faster than ordinary computers could. Finally, a fundamental understanding of superfluidity could benefit research into high-temperature superconductivity.

The dipolar BECs studied in this work feature novel long-range, anisotropic interactions. In light of the Bose-Einstein condensate as a testing ground for condensed matter physics, this opens the door to investigate systems with long-range interactions. Similar to the contact interactions, the dipolar interaction strength is controllable using external electromagnetic fields. Moreover, an extra control parameter is added through the dependence of the interaction characteristics on the trap geometry. Finally, quantum computing schemes have been proposed based on dipolar systems [29].

Bibliography

[1] J. R. Abo-Shaeer, C. Raman, J. M. Vogels, and W. Ketterle. *Science*, 292:476, 2001.

[2] M. Abramowitz and I. Stegun, editors. *Handbook of Mathematical Functions*. Dover, New York, 1974.

[3] U. Al Khawaja and H. T. C. Stoof. Nonlinear coupling between scissors modes of a bose-einstein condensate. *Phys. Rev. A*, 65(1):013605, Dec 2001.

[4] M. H. Anderson, J. R. Ensher, M. R. Matthews, C. E. Wieman, and E. A. Cornell. *Science*, 269:198, 1995.

[5] W. Bao and Q. Du. Computing the ground state solution of bose-einstein condensates by a normalized gradient flow. *SIAM J. Sci. Comput.*, 25(5):1674–1697, 2004.

[6] M Baranov, L Dobrek, K Góral, L Santos, and M Lewenstein. Ultracold dipolar gases - a challenge for experiments and theory. *Physica Scripta*, T102:74–81, 2002.

[7] J. Bardeen, L. N. Cooper, and J. R. Schrieffer. Theory of superconductivity. *Phys. Rev.*, 108(5):1175–1204, Dec 1957.

[8] Q. Beaufils, R. Chicireanu, T. Zanon, B. Laburthe-Tolra, E. Maréchal, L. Vernac, J.-C. Keller, and O. Gorceix. All-optical production of chromium bose-einstein condensates. *Physical Review A (Atomic, Molecular, and Optical Physics)*, 77(6):061601, 2008.

[9] Carl M. Bender and Steven A. Orszag. *Advanced Mathematical Methods for Scientists and Engineers I - Asymptotic Methods and Perturbation Theory*. Springer, Berlin, 1999.

[10] N. Bleistein and R. A. Handelsman. *Asymptotic Expansions of Integrals*. Dover Publications, Inc., New York, 1975.

[11] Immanuel Bloch, Jean Dalibard, and Wilhelm Zwerger. Many-body physics with ultracold gases. *Reviews of Modern Physics*, 80(3):885, 2008.

[12] N. N. Bogoliubov. *J. Phys (USSR)*, 11:23, 1947.

[13] F. Bouchet and J. Barre. Classification of phase transitions and ensemble inequivalence situations in systems with long range interactions. *J. Stat. Phys.*, 118:1073–1105, 2005.

[14] Ron Bracewell. *The fourier transform and its applications*. McGraw-Hill, 1965.

[15] E. Oran Brigham. *The fast Fourier transform and its applications*. Prentice Hall International, London, 1988.

[16] Jr. C. H. Edwards. *Advanced Calculus of Several Variables*. Academic Press, Inc., New York, 1973.

[17] David Chandler, editor. *Introduction to Modern Statistical Mechanics*. Oxford University Press, New York, 1987.

[18] Y. T. Chen. The gravitational field inside a long hollow cylinder of finite length. *Proc. R. Soc. Lond. A*, 394:47–68, 1984.

[19] Y. T. Chen, A. H. Cook, and A. J. F. Metherell. The gravitational field inside a long hollow cylinder of finite length. *Proc. R. Soc. Lond. A*, 382:75–82, 1982.

[20] P. A. Clarkson. Asymptotics of the second painlevé equation. *(Preprint) IMSAS Technical Report UKC/IMS/08/004*, 2008.

[21] C. Cohen-Tannoudji, B. Diu, and F. Laloë. *Quantum Mechanics, Volume One*. John Wiley and Sons, New York, 1977.

[22] C. Cohen-Tannoudji, B. Diu, and F. Laloë. *Quantum Mechanics, Volume Two*. John Wiley and Sons, New York, 1977.

[23] N. R. Cooper, E. H. Rezayi, and S. H. Simon. Vortex lattices in rotating atomic bose gases with dipolar interactions. *Physical Review Letters*, 95(20):200402, 2005.

[24] Marco Cozzini, Sandro Stringari, Vincent Bretin, Peter Rosenbusch, and Jean Dalibard. Scissors mode of a rotating bose-einstein condensate. *Phys. Rev. A*, 67(2):021602, Feb 2003.

[25] D. P. Craig and T. Thirunamachandran. *Molecular Quantum Electrodynamics, An Introduction to Radiation-Molecule interactions*. Academic Press, London, 1984.

[26] T. Dauxois, S. Ruffo, E. Arimondo, and M. Wilkens, editors. *Dynamics and Thermodynamics of Systems with Long-Range Interactions*. Springer Verlag, Berlin, 2002.

[27] K. B. Davis, M. O. Mewes, M. R. Andrews, N. J. van Druten, D. S. Durfee, D. M. Kurn, and W. Ketterle. Bose-einstein condensation in a gas of sodium atoms. *Phys. Rev. Lett.*, 75(22):3969–3973, Nov 1995.

[28] K. B. Davis, M. O. Mewes, M. R. Andrews, N. J. van Druten, D. S. Durfee, D. M. Kurn, and W. Ketterle. Bose-einstein condensation in a gas of sodium atoms. *Phys. Rev. Lett.*, 75(22):3969–3973, Nov 1995.

[29] D. DeMille. Quantum computation with trapped polar molecules. *Phys. Rev. Lett.*, 88(6):067901, Jan 2002.

[30] Andrei Derevianko. Anisotropic pseudopotential for polarized dilute quantum gases. *Phys. Rev. A*, 67(3):033607, Mar 2003.

[31] Andrei Derevianko. Erratum: Anisotropic pseudopotential for polarized dilute quantum gases [phys. rev. a 67, 033607 (2003)]. *Physical Review A (Atomic, Molecular, and Optical Physics)*, 72(3):039901, 2005.

[32] J. Doyle, B. Friedrich, R. V. Krems, and F. Masnou-Seeuws. *Eur. Phys. J. D*, 31:149, 2004.

[33] D.S. Durfee and W. Ketterle. *Optics Express*, 2:299–213, 1998.

[34] F. W. Dyson. *Quart. J. Pure and Appl. Math*, 25:259, 1891.

[35] Claudia Eberlein, Stefano Giovanazzi, and Duncan H. J. O'Dell. Exact solution of the thomas-fermi equation for a trapped bose-einstein condensate with dipole-dipole interactions. *Phys. Rev. A*, 71:033618, 2005.

[36] N. M. Ferrers. *Quart. J. Pure and Appl. Math*, 14:1, 1877.

[37] H. Feshbach. *Ann. Phys. (N.Y.)*, 5:357, 1958.

[38] H. Feshbach. *Ann. Phys. (N.Y.)*, 19:287, 1962.

[39] A. L. Fetter and J. D. Walecka. *Quantum theory of many-particle systems*. McGraw-Hill, 1971.

[40] Paul C. Fife. Asymptotic states for equations of reaction and diffusion. *Bulletin of the American Mathematical Society*, 84(5):693–726, 1978.

[41] I. M. Gelfand and S. V. Fomin. *Calculus of Variations*. Dover Publications, Inc., New York, 1963.

[42] S. Giovanazzi, L. Santos, and T. Pfau. Collective oscillations of dipolar bose-einstein condensates and accurate comparison between contact and dipolar interactions. *Physical Review A (Atomic, Molecular, and Optical Physics)*, 75(1):015604, 2007.

[43] Stefano Giovanazzi, Axel Görlitz, and Tilman Pfau. Tuning the dipolar interaction in quantum gases. *Phys. Rev. Lett.*, 89(13):130401, Sep 2002.

[44] K. Góral and L. Santos. Ground state and elementary excitations of single and binary bose-einstein condensates of trapped dipolar gases. *Phys. Rev. A*, 66(2):023613, Aug 2002.

[45] Krzysztof Góral, Kazimierz Rzążewski, and Tilman Pfau. Bose-einstein condensation with magnetic dipole-dipole forces. *Phys. Rev. A*, 61(5):051601, Mar 2000.

[46] L. S. Gradshteyn and I. M. Ryzhik, editors. *Table of Integrals, Series, and Products*. Academic Press, San Diego, sixth edition, 2000.

[47] Axel Griesmaier, Jörg Werner, Sven Hensler, Jürgen Stuhler, and Tilman Pfau. Bose-einstein condensation of chromium. *Physical Review Letters*, 94(16):160401, 2005.

[48] D.H.E. Gross. Microcanonical thermodynamics and statistical fragmentation of dissipative systems. the topological structure of the n-body phase space. *Physics Reports*, 279:119–201, 1997.

[49] E. P. Gross. *J. Math Phys.*, 4:195, 1963.

[50] D. Guéry-Odelin and S. Stringari. Scissors mode and superfluidity of a trapped bose-einstein condensed gas. *Phys. Rev. Lett.*, 83(22):4452–4455, Nov 1999.

[51] M. Guizar-Sicairos and J. C. Gutierrez-Vega. Computation of quasi-discrete hankel transforms of integer order for propagating optical wave fields. *J. Opt. Soc. Am. A*, 21(1):53, 2004.

[52] D. M. Harber, J. M. Obrecht, J. M. McGuirk, and E. A. Cornell. Measurement of the casimir-polder force through center-of-mass oscillations of a bose-einstein condensate. *Physical Review A (Atomic, Molecular, and Optical Physics)*, 72(3):033610, 2005.

[53] S. P. Hastings and J. B. McLeod. A boundary value problem associated with the second painlev transcendent and the korteweg-de vries equation. *Archive for Rational Mechanics and Analysis*, 73(1):31–51, 1980.

[54] S.W. Hawking. Black hole explosions? *Nature*, 248:30, 1974.

[55] D. Henry. In W. E. Fitzgibbon and H. F. Walker, editors, *Nonlinear diffusion*, pages 122–128, New York, 1977. Pitman Publishing Ltd.

[56] D. Henry. *Geometric Theory of Semilinear Parabolic Equations*. Springer Verlag, Berlin, 1981.

[57] Tin-Lun Ho. Bose-einstein condensates with large number of vortices. *Phys. Rev. Lett.*, 87(6):060403, Jul 2001.

[58] E. Hodby, G. Hechenblaikner, S. A. Hopkins, O. M. Maragò, and C. J. Foot. Vortex nucleation in bose-einstein condensates in an oblate, purely magnetic potential. *Phys. Rev. Lett.*, 88(1):010405, Dec 2001.

[59] M. H. Holmes. *Introduction to perturbation methods*. Springer Verlag, Berlin, 1995.

[60] N. G. Parker I. Corro and A. M. Martin. *J. Phys. B*, 40:3615, 2007.

[61] E. L. Ince. *Ordinary Differential Equations*. Dover Publications, Inc., New York, 1956.

[62] M. Inguscio, S. Stringari, and C. E. Wieman, editors. *Chapter by A. Fetter in the book: Bose-Einstein condensation in atomic gases : course Varenna on Lake Como, 7-17 July 1998*. IOS Press, Amsterdam, 1999.

[63] J. D. Jackson. *Classical Electrodynamics*. John Wiley and Sons, Inc., New York, third edition, 1998.

[64] K. Kanjilal, John L. Bohn, and D. Blume. Pseudopotential treatment of two aligned dipoles under external harmonic confinement. *Physical Review A (Atomic, Molecular, and Optical Physics)*, 75(5):052705, 2007.

[65] R. P. Kanwal. *Generalized Functions - Theory and Applications*. Birkhauser, Boston, third edition, 2004.

[66] P.G. Kevrekidis, D.J. Frantzeskakis, and Ricardo R. Carretero-González, editors. *Emergent Nonlinear Phenomena in Bose-Einstein Condensates: Theory and Experiment*. Springer Verlag, Berlin, 2008.

[67] C. Kittel, editor. *Quantum Theory of Solids*. John Wiley and Sons, New York, second edition, 1987.

[68] Y. S. Kivshar and Wieslaw Królikowski. Lagrangian approach for dark solitons. *Optics Communications*, 114:353–362, 1995.

[69] T. Koch, T. Lahaye, J. Metz, B. Frohlich, A. Griesmaier, and T. Pfau. Stabilizing a purely dipolar quantum gas against collapse. *Nat. Phys.*, 4:218, 2008.

[70] T. Köhler, K. Góral, and P. S. Julienne. *Rev. Mod. Phys.*, 78:1311, 2006.

[71] S. Komineas and N. R. Cooper. Vortex lattices in bose-einstein condensates with dipolar interactions beyond the weak-interaction limit. *Physical Review A (Atomic, Molecular, and Optical Physics)*, 75(2):023623, 2007.

[72] T. Lahaye, T. Koch, B. Frohlich, M. Fattori, J. Metz, A. Griesmaier, S. Giovanazzi, and T. Pfau. Strong dipolar effects in a quantum ferrofluid. *Nature*, 448:672, 2007.

[73] T. Lahaye, J. Metz, B. Fröhlich, T. Koch, M. Meister, A. Griesmaier, T. Pfau, H. Saito, Y. Kawaguchi, and M. Ueda. d-wave collapse and explosion of a dipolar bose-einstein condensate. *Physical Review Letters*, 101(8):080401, 2008.

[74] L. D. Landau and E. M. Lifshitz. *Mechanics*. Pergamon Press, Oxford, second edition, 1969.

[75] A. J. Leggett. *Quantum Liquids: Bose-Condensation and Cooper Pairing in Condensed Matter Systems*. Oxford University Press, 2006.

[76] M. L. Levin and R. Z. Muratov. On the internal potential of heterogeneous ellipsoids. *Astrophys. J.*, 166:441–445, 1971.

[77] Yan Levin. Electrostatic correlations: from plasma to biology. *Re. Prog. Phys.*, 65:1577–1632, 2002.

[78] Maciej Lewenstein. Dancing the bose-nova with a twirl. *Physics*, 1:13, Aug 2008.

[79] Elliott H. Lieb, Robert Seiringer, and Jakob Yngvason. Bosons in a trap: A rigorous derivation of the gross-pitaevskii energy functional. *Phys. Rev. A*, 61(4):043602, Mar 2000.

[80] Emil Lundh, J.-P. Martikainen, and Kalle-Antti Suominen. Vortex nucleation in bose-einstein condensates in time-dependent traps. *Phys. Rev. A*, 67(6):063604, Jun 2003.

[81] Emil Lundh, C. J. Pethick, and H. Smith. Zero-temperature properties of a trapped bose-condensed gas: Beyond the thomas-fermi approximation. *Phys. Rev. A*, 55(3):2126–2131, Mar 1997.

[82] D. Lynden-Bell and R. M. Lynden-Bell. On the negative specific heat paradox. *Mont. Not. R. Astron. Soc.*, 181:405–419, November 1977.

[83] F.R.S. M. J. Lighthill. *Introduction to Fourier Analysis and Generalised Functions*. Cambridge University Press, London, 1958.

[84] K. W. Madison, F. Chevy, V. Bretin, and J. Dalibard. Stationary states of a rotating bose-einstein condensate: Routes to vortex nucleation. *Phys. Rev. Lett.*, 86(20):4443–4446, May 2001.

[85] K. W. Madison, F. Chevy, W. Wohlleben, and J. Dalibard. Vortex formation in a stirred bose-einstein condensate. *Phys. Rev. Lett.*, 84(5):806–809, Jan 2000.

[86] O. M. Maragò, S. A. Hopkins, J. Arlt, E. Hodby, G. Hechenblaikner, and C. J. Foot. Observation of the scissors mode and evidence for superfluidity of a trapped bose-einstein condensed gas. *Phys. Rev. Lett.*, 84(10):2056–2059, Mar 2000.

[87] N. H. March and M. Parrinello, editors. *Collective Effects in Solids and Liquids*. Adam Hilger LTD, Bristol, 1982.

[88] M. Marinescu and L. You. Controlling atom-atom interaction at ultralow temperatures by dc electric fields. *Phys. Rev. Lett.*, 81(21):4596–4599, Nov 1998.

[89] A. M. Martin, N. G. Parker, R. M. W. van Bijnen, A. Dow, and D. H. J. O'Dell. *Laser Physics*, 18:322, 2008.

[90] R. M. M. Mattheij, S. W. Rienstra, and J.H.M. ten Thije Boonkkamp. *Partial differential equations : modeling, analysis, computation*. SIAM, Philadelphia, 2005.

[91] E. Merzbacher. *Quantum Mechanics*. John Wiley and Sons, Inc., New York, 1970.

[92] H. J. Metcalf and P. van der Straten. *Laser Cooling and Trapping*. Springer-Verlag, New York, 1999.

[93] B. Mottelson. Yrast spectra of weakly interacting bose-einstein condensates. *Phys. Rev. Lett.*, 83(14):2695–2698, Oct 1999.

[94] Erich J. Mueller, Tin-Lun Ho, Masahito Ueda, and Gordon Baym. Fragmentation of bose-einstein condensates. *Physical Review A (Atomic, Molecular, and Optical Physics)*, 74(3):033612, 2006.

[95] D. R. Nicholson, editor. *Introduction to Plasma Theory*. John Wiley and Sons, New York, 1983.

[96] J. M. Obrecht, R. J. Wild, M. Antezza, L. P. Pitaevskii, S. Stringari, and E. A. Cornell. Measurement of the temperature dependence of the casimir-polder force. *Physical Review Letters*, 98(6):063201, 2007.

[97] Duncan H. J. O'Dell, Stefano Giovanazzi, and Claudia Eberlein. Exact hydrodynamics of a trapped dipolar bose-einstein condensate. *Phys. Rev. Lett.*, 92(25):250401, Jun 2004.

[98] D. H. J. O'Dell and C. Eberlein. Vortex in a trapped bose-einstein condensate with dipole-dipole interactions. *Physical Review A (Atomic, Molecular, and Optical Physics)*, 75(1):013604, 2007.

[99] C. Ospelkaus, S. Ospelkaus, L. Humbert, P. Ernst, K. Sengstock, and K. Bongs. Ultracold heteronuclear molecules in a 3d optical lattice. *Physical Review Letters*, 97(12):120402, 2006.

[100] N. G. Parker and C. S. Adams. Emergence and decay of turbulence in stirred atomic bose-einstein condensates. *Physical Review Letters*, 95(14):145301, 2005.

[101] N. G. Parker and C. S. Adams. *J. Phys. B*, 39:43, 2006.

[102] N. G. Parker, R. M. W. van Bijnen, and A. M. Martin. Instabilities leading to vortex lattice formation in rotating bose-einstein condensates. *Physical Review A (Atomic, Molecular, and Optical Physics)*, 73(6):061603, 2006.

[103] N.G. Parker and D.H.J. O'Dell. *arxiv:0807.5110*, 2008.

[104] N.G. Parker, C. Ticknor, A.M. Martin, and DH.J. O'Dell. Thomas-fermi collapse and shell formation in dipolar atomic bose-einstein condensates. *preprint*, 2008.

[105] Víctor M. Pérez-García, H. Michinel, J. I. Cirac, M. Lewenstein, and P. Zoller. Low energy excitations of a bose-einstein condensate: A time-dependent variational analysis. *Phys. Rev. Lett.*, 77(27):5320–5323, Dec 1996.

[106] C. J. Pethick and L. P. Pitaevskii. Criterion for bose-einstein condensation for particles in traps. *Phys. Rev. A*, 62(3):033609, Aug 2000.

[107] C.J. Pethick and H. Smith. *Bose-Einstein condensation in Dilute Gases*. Cambridge University Press, Cambridge, 2002.

[108] L. M. Pismen. *Vortices in nonlinear fields : from liquid crystals to superfluids, from non-equilibrium patterns to cosmic strings*. Clarendon Press, Oxford, 1999.

[109] L. Pitaevskii and S. Stringari. *Bose Einstein Condensation*. Clarendon Press, Oxford, 2003.

[110] L. P. Pitaevskii. *Sov. Phys. JETP*, 13:451, 1963.

[111] C. Westbrook R. Kaiser and F. David, editors. *Chapter by Y. Castin, in the book: Coherent Matter Waves, Lecture Notes of Les Houches Summer School*. Springer Verlag, berlin, 2001.

[112] A. Recati, F. Zambelli, and S. Stringari. Overcritical rotation of a trapped bose-einstein condensate. *Phys. Rev. Lett.*, 86(3):377–380, Jan 2001.

[113] Shai Ronen, Daniele C. E. Bortolotti, and John L. Bohn. Bogoliubov modes of a dipolar condensate in a cylindrical trap. *Physical Review A (Atomic, Molecular, and Optical Physics)*, 74(1):013623, 2006.

[114] Shai Ronen, Daniele C. E. Bortolotti, and John L. Bohn. Radial and angular rotons in trapped dipolar gases. *Physical Review Letters*, 98(3):030406, 2007.

[115] P. Rosenbusch, D. S. Petrov, S. Sinha, F. Chevy, V. Bretin, Y. Castin, G. Shlyapnikov, and J. Dalibard. Critical rotation of a harmonically trapped bose gas. *Phys. Rev. Lett.*, 88(25):250403, Jun 2002.

[116] Nicolas Rougerie. Transition to the giant vortex state for a bose-einstein condensate in a rotating anharmonic trap, 2008.

[117] Jeremy M. Sage, Sunil Sainis, Thomas Bergeman, and David DeMille. Optical production of ultracold polar molecules. *Physical Review Letters*, 94(20):203001, 2005.

[118] L. Santos, G. V. Shlyapnikov, P. Zoller, and M. Lewenstein. Bose-einstein condensation in trapped dipolar gases. *Phys. Rev. Lett.*, 85(9):1791–1794, Aug 2000.

[119] Craig M. Savage and Mukunda P. Das, editors. *Chapter by A.J. Leggett in the book: Bose-Einstein condensation : from atomic physics to quantum fluids : Canberra, Australia 17-28 January 2000.* World Scientific, Singapore, 2000.

[120] J. R. Shewchuk. An introduction to the conjugate gradient method without the agonizing pain. *(unpublished), online available at http://www.adt.unipd.it/corsi/CalcoloNumerico/painless-conjugate-gradient.pdf*, 1994.

[121] A. E. Siegman. Quasi fast hankel transform. *Optics Letters*, 1(1):13, 1977.

[122] L. Simon. Asymptotics for a class of non-linear evolution equations, with applications to geometric problems. *Annals of Mathematics*, 118:525–571, 1983.

[123] Subhasis Sinha and Yvan Castin. Dynamic instability of a rotating bose-einstein condensate. *Phys. Rev. Lett.*, 87(19):190402, Oct 2001.

[124] D. Spring. On the second derivative test for constrained local extrema. *The American Mathematical Monthly*, 92(9):631–643, 1985.

[125] J. Stuhler, A. Griesmaier, T. Koch, M. Fattori, T. Pfau, S. Giovanazzi, P. Pedri, and L. Santos. Observation of dipole-dipole interaction in a degenerate quantum gas. *Physical Review Letters*, 95(15):150406, 2005.

[126] Sauro Succi, Federico Toschi, Mario P. Tosi, and Patrizia Vignolo. Bose-einstein condensates and the numerical solution of the gross-pitaevskii equation. *Computing in Science and Engg.*, 7(6):48–57, 2005.

[127] C. Sulem and P. L. Sulem. *The Nonlinear Schrödinger Equation: Self-focusing and Wave Collapse*. Springer, Neww York, 1999.

[128] R. M. W. van Bijnen. Instabilities of a bose-einstein condensate in a rotating anisotropic harmonic trap. Technical Report CQT 2007 - 12, Eindhoven University of Technology, 2007.

[129] R. M. W. van Bijnen, D. H. J. O'Dell, N. G. Parker, and A. M. Martin. Dynamical instability of a rotating dipolar bose-einstein condensate. *Physical Review Letters*, 98(15):150401, 2007.

[130] Paul van der Schoot and Robijn Bruinsma. Electrostatics and the assembly of an rna virus. *Phys. Rev. E*, 71:061928, 2005.

[131] M. Vengalattore, S. R. Leslie, J. Guzman, and D. M. Stamper-Kurn. Spontaneously modulated spin textures in a dipolar spinor bose-einstein condensate. *Physical Review Letters*, 100(17):170403, 2008.

[132] N. K. Wilkin, J. M. F. Gunn, and R. A. Smith. Do attractive bosons condense? *Phys. Rev. Lett.*, 80(11):2265–2268, Mar 1998.

[133] Ryan M. Wilson, Shai Ronen, John L. Bohn, and Han Pu. Manifestations of the roton mode in dipolar bose-einstein condensates. *Physical Review Letters*, 100(24):245302, 2008.

[134] S. Yi and H. Pu. Vortex structures in dipolar condensates. *Physical Review A (Atomic, Molecular, and Optical Physics)*, 73(6):061602, 2006.

[135] S. Yi and L. You. Trapped atomic condensates with anisotropic interactions. *Phys. Rev. A*, 61(4):041604, Mar 2000.

[136] S. Yi and L. You. Trapped condensates of atoms with dipole interactions. *Phys. Rev. A*, 63(5):053607, Apr 2001.

[137] S. Yi and L. You. Probing dipolar effects with condensate shape oscillation. *Phys. Rev. A*, 66(1):013607, Jul 2002.

[138] S. Yi and L. You. Calibrating dipolar interaction in an atomic condensate. *Phys. Rev. Lett.*, 92(19):193201, May 2004.

[139] V. E. Zakharov. Stability of periodic waves of finite amplitude on the surface of a deep fluid. *Journal of Applied Mechanics and Technical Physics*, 9(2):190–194, 1968.

[140] Jian Zhang and Hui Zhai. Vortex lattices in planar bose-einstein condensates with dipolar interactions. *Physical Review Letters*, 95(20):200403, 2005.

A. Thomas-Fermi approximation

In this Appendix we discuss the Thomas-Fermi approximation of sections 1.5 and 1.6 in more detail.

In section A.1 we show explicitly that the kinetic energy term occurring in the time-*independent* Gross-Pitaevskii equation (1.24) acquires a small prefactor for large condensates. Then, in section A.2 we explore solutions for which the kinetic energy term is neglected, the so-called the Thomas-Fermi approximation [107, 109]. In the same section we also determine higher order corrections. In this process we encounter a boundary layer, in which the wavefunction has to satisfy a special nonlinear differential equation: the Painlevé equation, which is discussed in more detail in section A.3. Finally, in section A.4 we show that in the hydrodynamic equations of section 1.6 we can make a similar approximation of neglecting part of the kinetic energy.

A.1. Time-independent GPE

We consider the case where the external potential V is a cylindrically symmetric harmonic oscillator potential

$$V(\mathbf{r}) = \frac{1}{2}\omega_\perp^2(r_x^2 + r_y^2 + \gamma^2 r_z^2), \tag{A.1}$$

with the relative trapping strength in the z-direction characterised by the dimensionless constant γ.

We start by scaling the spatial coordinate $\mathbf{r}$ by a typical length scale ξ, such that

$$\mathbf{r} = \xi\mathbf{r}', \qquad \nabla = \xi^{-1}\nabla',$$

and our new coordinate $\mathbf{r}' = \mathcal{O}(1)$. The wavefunction is scaled via a typical density n_0 (usually taken to be the peak density in the center of the trap) and expressed in the new coordinates,

$$\psi(\mathbf{r}) = \sqrt{n_0}\psi'(\mathbf{r}'),$$

such that $\psi' \leq 1$. Inserting the above definitions in the time-independent Gross-Pitaevskii equation (1.24), and dividing by the energy $n_0 g$, we get the dimensionless equation

$$\frac{\mu}{n_0 g}\psi'(\mathbf{r}') = \left(-\frac{\hbar^2}{2mn_0 g\xi^2}\nabla'^2 + \frac{1}{2}\frac{m\omega_\perp^2}{n_0 g}\xi^2\left(x'^2 + y'^2 + \gamma^2 z'^2\right) + |\psi'|^2\right)\psi'(\mathbf{r}'). \tag{A.2}$$

The first two terms on the right hand side provide us with two length scales we can choose from to scale our units with,

$$\xi_1 = \sqrt{\frac{n_0 g}{m\omega_\perp^2}}, \qquad \xi_2 = \frac{\hbar}{\sqrt{m n_0 g}}.$$

The first of these, ξ_1, is the typical size of the BEC in the harmonic trap (A.1), which we shall call the oscillator length. For instance, when there are many particles in the trap (n_0 large), or when the interactions are strong (g large), the oscillator length becomes larger, signifying a large BEC. On the other hand, for strong traps ($m\omega_\perp^2$ large), the BEC is 'squeezed' and its physical size, the oscillator length, becomes smaller. The other length scale, ξ_2, is known as the healing- or coherence length [107]. It is the length scale at which the wave function of a uniform BEC returns to its bulk value when subjected to a localized perturbation. Typically, for higher densities the healing length becomes smaller. Thus, for large condensates $\xi_1 \gg \xi_2$. We therefore pick $\xi = \xi_1$, and obtain

$$\mu'\psi'(\mathbf{r}') = \left(-\frac{1}{2}\left(\frac{\xi_2}{\xi_1}\right)^2 \nabla'^2 + \frac{1}{2}\left(x'^2 + y'^2 + \gamma^2 z'^2\right) + |\psi'|^2 \right) \psi'(\mathbf{r}'), \tag{A.3}$$

where $\mu' = \frac{\mu}{n_0 g}$. The quantity

$$\left(\frac{\xi_2}{\xi_1}\right) = \frac{\hbar\omega}{n_0 g}$$

is the ratio of the single particle oscillator energy and the single particle interaction energy in the center of the trap. For large condensates, the peak density n_0 becomes very large, and $\frac{\xi_2}{\xi_1}$ becomes small. In the Thomas-Fermi approximation the $\left(\frac{\xi_2}{\xi_1}\right)^2$ term is neglected, in which case μ' becomes $\mathcal{O}(1)$ [107], otherwise the assumption $\psi' = \mathcal{O}(1)$ cannot hold.

A.2. Thomas-Fermi approximation and higher order corrections

Consider the rescaled time independent Gross-Pitaevskii equation (A.3). We want to find the wave function that satisfies this equation. Because of its non-linearity it is unfeasible to find an exact solution. Therefore, we will attempt to find an approximation using perturbation theory, using $\left(\frac{\xi_2}{\xi_1}\right) \ll 1$ as a small parameter. We will study this problem in 1D only, but the results are easily generalized to higher dimensions. Furthermore we assume that $\tilde{\psi}$ is real valued, corresponding to a state without stationary currents (as discussed in section 1.4.2).

We start by rescaling equation (A.3) slightly, such that in 1D it becomes

$$\left[-\epsilon^2 \frac{\partial^2}{\partial x^2} + x^2 - 1 + \tilde{\psi}^2 \right] \tilde{\psi} = 0, \tag{A.4}$$

where we have set $\tilde{\psi} = \psi'/\sqrt{\mu'}$, $x = x'/\sqrt{2\mu'}$, and $\epsilon = \left(\frac{\xi_2}{2\mu'\xi_1}\right) \ll 1$ is our small parameter. Assuming that $\tilde{\psi}$ varies with $x = \mathcal{O}(1)$ and not on any smaller length scale, we will try an asymptotic expansion of the form

$$\tilde{\psi} = \tilde{\psi}_0 + \epsilon^2 \tilde{\psi}_1 + \mathcal{O}(\epsilon^4). \tag{A.5}$$

Plugging this in gives

$$\left(x^2-1\right)\tilde{\psi}_0+\tilde{\psi}_0^3+\epsilon^2\left(-\frac{\partial^2}{\partial x^2}\tilde{\psi}_0+x^2\tilde{\psi}_1-\tilde{\psi}_1+3\tilde{\psi}_0^2\tilde{\psi}_1\right)+\mathcal{O}(\epsilon^4)=0. \tag{A.6}$$

Evaluating the leading order equation gives

$$\tilde{\psi}_0^3=-(x^2-1)\tilde{\psi}_0, \tag{A.7}$$

which is solved for non-trivial $\tilde{\psi}$ by

$$\tilde{\psi}(x)=\begin{cases}\pm\sqrt{1-x^2} & |x|\leq 1\\ \\ 0 & |x|>1\end{cases} \tag{A.8}$$

Notice that outside $|x|\leq 1$, we have no choice but set $\tilde{\psi}_0=0$ when $\tilde{\psi}$ is real. Inside $|x|\leq 1$ though $\tilde{\psi}_0=0$ is also a solution, but this would make our assumed scaling of $\tilde{\psi}$ invalid.

This solution is consistent with the assumption that $\tilde{\psi}''(x)=\mathcal{O}(1)$ in the interior of the domain $|x|<1$, but breaks down near the point $x=1$, where $\tilde{\psi}_0$ becomes $\mathcal{O}(\epsilon^2)$ and $\tilde{\psi}''(x)$ becomes large. Therefore, we will continue looking for a local approximation by introducing a boundary layer at $x=1$[1]. Before doing so, we will first continue with finding the $\mathcal{O}(\epsilon^2)$-correction to $\tilde{\psi}$ in the interior of the condensate. The $\mathcal{O}(\epsilon^2)$ equation reads

$$-\frac{\partial^2}{\partial x^2}\tilde{\psi}_0+\left(x^2-1+3\tilde{\psi}_0^2\right)\tilde{\psi}_1=0. \tag{A.9}$$

Plugging in the expression (A.8) for $\tilde{\psi}_0$, and solving the resulting equation for $\tilde{\psi}_1$ gives

$$\tilde{\psi}_1=-\frac{1}{2(1-x^2)^{\frac{5}{2}}}. \tag{A.10}$$

Note that this expression is negative, as one would expect since some of the condensate will reside outside the Thomas-Fermi radius $x=1$, so in order to keep the total number of atoms constant the density has to decrease inside the Thomas-Fermi radius. It is also interesting to note that $\tilde{\psi}_1$ has a singularity at $x=1$, which again shows that the expansion (A.6) fails near that point.

We will now proceed with the boundary layer at $x=1$, by introducing the boundary layer coordinate

$$\eta=\frac{x-1}{\epsilon^\alpha}, \tag{A.11}$$

for some $\alpha>0$, which determines the width of the boundary layer. Since $\tilde{\psi}$ might have a different order of magnitude in the boundary layer, we scale

[1] Of course, there is also a boundary layer at $x=-1$, but the wavefunction at $x<0$ simply follows from mirroring the situation at $x>0$.

$$\psi'(x) = \epsilon^{\beta}\tilde{\phi}(\eta), \tag{A.12}$$

where $\tilde{\phi} = \mathcal{O}(1)$. Plugging this in in equation (A.4) gives

$$-\epsilon^{2-2\alpha}\frac{\partial^2}{\partial\eta^2}\tilde{\phi} + \epsilon^{2\alpha}\eta^2\tilde{\phi} + 2\epsilon^{\alpha}\eta\tilde{\phi} + \epsilon^{2\beta}\tilde{\phi}^3 = 0 \tag{A.13}$$

Before we can find the proper value for α, we have to find which β determines the correct leading order behavior of $\tilde{\phi}$. In order to do this, note that for $-\eta \gg 1$,

$$\begin{aligned} \tilde{\psi}(x) &= \tilde{\psi}(\epsilon^{\alpha}\eta + 1) &&= \left(-\epsilon^{2\alpha}\eta^2 - 2\epsilon^{\alpha}\eta\right)^{\frac{1}{2}} \\ &\simeq \sqrt{2}\,\epsilon^{\alpha/2}\sqrt{-\eta} &&\simeq \epsilon^{\beta}\tilde{\phi}, \end{aligned} \tag{A.14}$$

from which we infer that $\beta = \alpha/2$. By substituting this result back in (A.13) we find

$$\begin{aligned} -\epsilon^{2-2\alpha}\tfrac{\partial^2}{\partial\eta^2}\tilde{\phi} \;+\; \epsilon^{2\alpha}\eta^2\;\tilde{\phi} \;+\; \epsilon^{\alpha}\left(2\;\eta\;\tilde{\phi} + \tilde{\phi}^3\right) \;&=\; 0, \\ \text{①} \qquad\qquad \text{②} \qquad\qquad \text{③} \end{aligned} \tag{A.15}$$

where we have numbered the different terms for clarity. Note that none of the terms can be individually zero and of leading order, since that would imply either a density $\tilde{\phi} = 0$, which would violate the assumption that $\tilde{\phi} = \mathcal{O}(1)$, or it would imply an imaginary or constant $\tilde{\phi}$, but both of which would cause the wave function ψ to be discontinuous at the edges of the boundary layer. It is also not possible that all three terms have the same order of magnitude, as can be easily seen by equating the powers of ϵ. Therefore, two of the terms have to have the same order of magnitude and balance each other, and the remaining term has to be of higher order. There are three possible scenarios:

1. Terms ① and ② balance, and term ③ is of higher order. This leads to $1 - \alpha = \alpha \Rightarrow \alpha = \frac{1}{2}$, but this violates the assumption that term ③ is of higher order.

2. Terms ② and ③ balance, and term ① is of higher order. This leads to $2\alpha = \alpha \Rightarrow \alpha = 0$, but then term ③ is no longer of higher order, and in fact there would be no boundary layer at all, so this case is also incorrect.

3. In the final case, terms ① and ③ balance, and term ② is of higher order. This leads to $2 - 2\alpha = \alpha \Rightarrow \alpha = \frac{2}{3}$, in which case term ② is indeed of higher order, and this is consistent with our assumptions.

Apparently, the third case is the *distinguished limit* [59] we are looking for, and therefore we set $\alpha = \frac{2}{3}$. The boundary layer width is therefore $\mathcal{O}(\epsilon^{\frac{2}{3}})$, whereas the condensate wavefunction is $\mathcal{O}(\epsilon^{\frac{1}{3}})$ in this region.

Alternatively, the thickness of the boundary layer could have been found by comparing the zeroth and first order solutions in the interior of the condensate. Where these become of

equal magnitude, the asymptotic expansion (A.5) is no longer valid and hence we must have entered the boundary layer. Setting $x = 1 - \epsilon^\alpha$, we find that

$$\sqrt{1-x^2} = \sqrt{2\epsilon^\alpha - \epsilon^{2\alpha}} \simeq \sqrt{2}\epsilon^{\alpha/2},$$

and

$$\frac{\epsilon^2}{(1-x^2)^{\frac{5}{2}}} = \epsilon^2(\epsilon^\alpha - \epsilon^{2\alpha})^{-\frac{5}{2}} \simeq \epsilon^{2-\frac{5}{2}\alpha}.$$

Equating these two orders of magnitude we get $\frac{1}{2}\alpha = 2 - \frac{5}{2}\alpha \Rightarrow \alpha = \frac{2}{3}$, which confirms our earlier analysis of the boundary layer thickness.

Continuing then with the perturbation analysis, we try an expansion of the form

$$\tilde{\phi} = \tilde{\phi}_0 + \epsilon^\gamma \tilde{\phi}_1 + \mathcal{O}(\epsilon^{2\gamma}), \tag{A.16}$$

where $\gamma > 0$ remains to be determined. Plugging this in in equation (A.15) gives us the following leading order equation for $\tilde{\phi}_0$

$$-\frac{\partial^2}{\partial\eta^2}\tilde{\phi}_0 + 2\eta\tilde{\phi}_0 + \tilde{\phi}_0^3 = 0. \tag{A.17}$$

The linear term in the coordinate η can be understood by noting that within the boundary layer, the external potential is approximately linear. When we use (A.17) in (A.15) we find

$$\epsilon^{\frac{2}{3}+\gamma}\left(-\frac{\partial^2}{\partial\eta^2}\tilde{\phi}_1 + 2\eta\ \tilde{\phi}_1 + 3\ \tilde{\phi}_0^2\ \tilde{\phi}_1\right) + \epsilon^{4/3}\ \eta^2\ \tilde{\phi}_0 + (\text{higher order terms}) = 0. \tag{A.18}$$

In order for the $\epsilon^{4/3}$-term to balance with any other term, we have to set $\gamma = \frac{2}{3}$. The $\mathcal{O}(\epsilon^{4/3})$ equation for $\tilde{\phi}_1$ becomes

$$-\frac{\partial^2}{\partial\eta^2}\tilde{\phi}_1 + 2\eta\ \tilde{\phi}_1 + 3\ \tilde{\phi}_0^2\ \tilde{\phi}_1 + \eta^2\ \tilde{\phi}_0 = 0. \tag{A.19}$$

We cannot solve equation (A.17) analytically, and are therefore also unable to solve (A.19). Interestingly though, the boundary equation is of a special form for which some asymptotic results are known. Section A.3 of this Appendix discusses some more details of the boundary layer equation (A.17). Here, we will check whether it at least allows a solution that matches asymptotically with the solution (A.8) in the interior of the condensate.

When we express the interior solution (A.8) in terms of the boundary layer coordinate η we found in equation (A.14) that

$$\tilde{\psi}(x) \simeq \sqrt{2}\epsilon^{2/3}\sqrt{-\eta}, \qquad \eta \to -\infty.$$

To see whether the solution to the boundary layer equation (A.17) matches to this solution, we try an asymptotic power series of the form

$$\tilde{\phi}_0(\eta) \simeq \sum_{i=0}^{N} a_i(-\eta)^{1/2-n} + \mathcal{O}((-\eta)^{-1/2-N}), \qquad (\eta \to \infty).$$

Substituting this expression in equation (A.17), and collecting like powers of η, we get

$$\begin{aligned} 0 &= 3(a_0^2 a_2 + a_1^2 a_0)(-\eta)^{-1/2} + 3a_0^2 a_1(-\eta)^{1/2} + (a_0^3 - 2a_0)(-\eta)^{3/2} \\ &+ \sum_{n=3}^{N} \left(-2a_n - a_n(3\frac{1}{2} - n)(2\frac{1}{2} - n) + \sum_{l=0}^{n} \sum_{m=0}^{n-l} a_l a_m a_{n-l-m} \right) (-\eta)^{3/2-n} \\ &+ \mathcal{O}((-\eta)^{1/2-N}). \end{aligned} \tag{A.20}$$

When we equate the coefficients appearing in front of the powers of $-\eta$ individually to zero, we quickly find that $a_{3k+1} = a_{3k+2} = 0$, $k = 0, 1, 2, \ldots$. For the remaining coefficients we find

$$a_0 = \sqrt{2}, \qquad a_3 = -\frac{1}{8\sqrt{2}}, \qquad a_6 = \frac{-73}{256\sqrt{2}}, \qquad \ldots$$

etcetera. Note that the n-th coefficient can be obtained from the first $n-1$ coefficients, so in principle any desired number of coefficients can be found. We can conclude that for $\eta \to -\infty$:

$$\tilde{\phi}_0 \simeq \sqrt{2}\sqrt{-\eta} - \frac{1}{8\sqrt{2}} \frac{1}{(-\eta)^{5/2}} + \mathcal{O}((-\eta)^{-7/2}), \tag{A.21}$$

which indeed matches with the interior solution (A.8).

In conclusion, we have found 3 distinct regions: first, the bulk of the condensate where we can neglect the quantum pressure and where we have found the known Thomas-Fermi parabolic density profile along with the first order correction. Second, the boundary layer where quantum pressure and interactions balance, and third the outer region where we can neglect the interactions and find a harmonic oscillator problem, which is in principle solvable and the solution exhibits a Gaussian behaviour. However, since we have no explicit solution in the boundary layer we have not been able to connect the different pieces into a single wave function. To do this, we must explore the special form of this equation in more detail in the next section.

A.3. Painlevé II boundary layer equation

The equation governing the behaviour of the wavefunction in the boundary layer (A.17), is of a special form. When we substitute $\phi_0 \to a\phi$, $x = \eta/b$, with $a = 2^{5/6}$ and $b = 2^{-1/3}$, we get precisely the *Painlevé II* equation:

$$-\phi''(x) + x\phi(x) + 2\phi(x)^3 + \alpha = 0, \tag{A.22}$$

with α an arbitrary constant, in our case $\alpha = 0$. The Painlevé equations are nonlinear ordinary differential equations, defining a new set of transcendental functions. Around the year 1900, Painlevé, Gambier and co-workers studied which second order, nonlinear, ordinary differential equations have no movable critical points. That is, out of the three types of singularity that a complex function may have - branch points, poles, and essential singularities[2] - the

[2]There also exist essential singularities that are branch points at the same time.

only movable singularities are poles. Movable singularities are singularities whose position is dependent on an integration constant, for example the ordinary differential equation

$$\frac{\mathrm{d}w}{\mathrm{d}z} + w^3 = 0,$$

has as a general solution

$$w(z) = \frac{1}{\sqrt{2(z - z_0)}},$$

with z_0 a constant of integration that determines a particular solution. Here, $w(z)$ has a branch point at $z = z_0$ and by picking different z_0's, the branch point can be moved. On the other hand, any N-th order linear ordinary differential equation

$$\sum_{n=0}^{N} a_n(z) \frac{\mathrm{d}^n w}{\mathrm{d}z^n} + f(z) = 0$$

can only have singularities that are not movable: their locations are determined by singularities of the coefficients $a_n(z)$ [61]. For instance, setting $a_0(z) = 1/(z-a)^2$, $a_2(z) = 1$, and $f(z) = 0$, the above differential equation is solved by $w(z) = c\exp(1/(z-a))$, which has an essential singularity at $z = a$, precisely where a_0 has a singularity. Furthermore, the location does not depend on the integration constant c and thus the singularity is not movable.

While for linear differential equations all singularities are thus not movable, for nonlinear ordinary differential equations singularities can both be movable and non-movable. The work of Painlevé and co-workers now consists of classifying *all* second order quasi-linear[3] differential equations that have no movable branch points and no movable essential singularities. They found 50 such equations, of which 44 could be either integrated in terms of previously known functions, or could be reduced to one of 6 new ordinary nonlinear differential equations, termed the Painlevé I-VI equations [61, 20]. These six equations define new, special functions called *Painlevé transcendentals*, much in the same fashion as, for instance, Bessel functions are defined by the Bessel equation.

In Bose-Einstein condensation in a harmonic trap, one of these Painlevé equations appears in the boundary layer equation (A.17), which happens to be the Painlevé II equation (A.22).

When $x \to \infty$, we must have that $\phi \to 0$. In this case, the ϕ^3 term becomes vanishingly small compared to the other terms, and we have

$$-\phi''(x) + x\phi(x) = 0.$$

This is precisely the Airy equation, whose solutions are the Airy functions $\mathrm{Ai}(x)$ and $\mathrm{Bi}(x)$. The Airy functions are oscillatory for $x < 0$, and have a turning point at $x = 0$ where they change their behaviour to $\sim \exp(\pm\frac{2}{3}x^{\frac{3}{2}})/x^{\frac{1}{4}}$ [2], where the + sign holds for the Bi function, and the minus sign for Ai. Clearly, the Bi can be discarded as it is incompatible with the boundary condition for $x \to \infty$.

[3] A quasi linear differential equation is linear in the highest order derivative, but contains nonlinear coefficients for lower order derivatives. This is to be contrasted with a semilinear differential equation, which only has nonlinearities in the zeroth order derivatives (the function itself) such as the Gross-Pitaevskii equation, and fully nonlinear differential equations in which the highest order derivatives have nonlinear coefficients.

In the other limit, $x \to -\infty$, the behaviour is more complicated. Rewriting the Painlevé equation to

$$-\phi''(x) + \left[x + 2\phi(x)^2\right]\phi(x) = 0,$$

we see from the term between square brackets that we can divide the left half plane $x < 0$ into 4 regions, as illustrated in figure A.1. First, in region (1), we have that $\phi > 0$ and $2\phi^2 + x > 0$, hence $\phi''(x) > 0$ and the solution ϕ is convex. In region (2), $\phi > 0$ and $2\phi^2 + x < 0$, so the solution is concave. Similarly, region (3) the solution will be convex again, and in region (4) it is concave. As a result, within the shaded region of figure A.1, the solution will generally become oscillatory, whereas outside the shaded region the solution will diverge to $\pm\infty$.

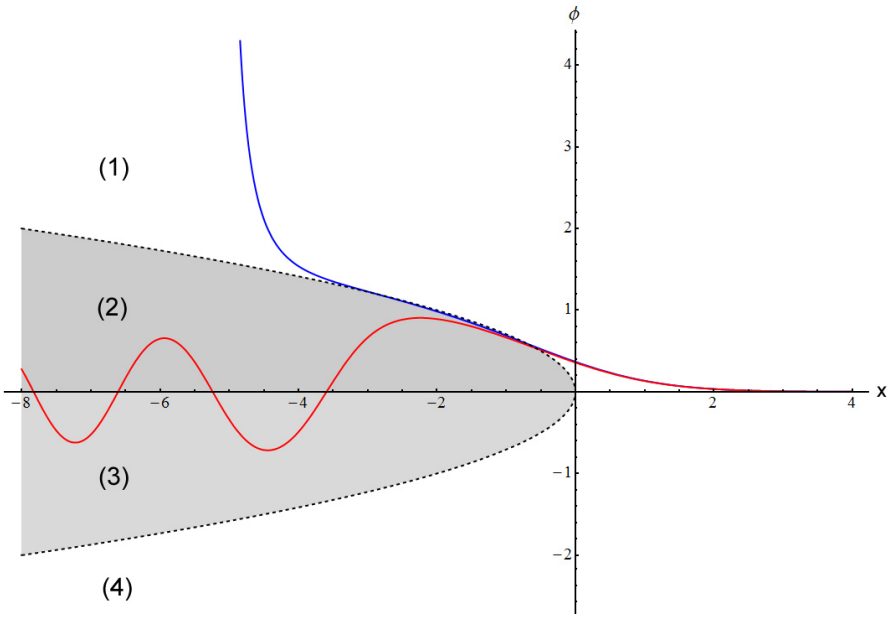

Figure A.1.: *Numerical solutions of the Painlevé II equation. Dotted line marks the* $\pm\sqrt{-\frac{1}{2}x}$ *line that divides the left half plane into a region (shaded) where the solution becomes oscillatory (red curve), and a region where the solutions diverge to a pole at some (movable)* $x = x_0$ *(blue curve).*

Hastings and McLeod [53] show that there exists a family of solutions $w_k(x)$, which is asymptotic to $k\mathrm{Ai}(x)$, for $x \to \infty$. They show that when $|k| < 1$, the solution is oscillatory and finite for $z \to -\infty$ (red curve in figure A.1), and for $|k| > 1$ it has a pole[4] and diverges at some $x = x_0$ (blue curve in figure A.1). When $k \downarrow 1$, the pole moves to ∞ and in the limit $|k| = 1$, we find $w_k(x) \sim \mathrm{sgn}(k)\sqrt{-\frac{1}{2}x}$. Similarly, when we approach $|k| = 1$ from below, the oscillations start further away from the origin, until in the limit $|k| \uparrow 1$, we recover the $w_k(x) \sim \mathrm{sgn}(k)\sqrt{-\frac{1}{2}x}$ solution again.

We can now look with renewed interest at the asymptotic solution in the boundary layer (A.21). When performing the rescaling $\phi_0 = a\phi$, $x = \eta/b$, with $a = 2^{5/6}$ and $b = 2^{-1/3}$ we see

[4]The exact dependence of the location of the pole on k is currently unknown [20].

that

$$\phi_0(\eta) = w_1(x) + \mathcal{O}((-x)^{-\frac{5}{2}}), \qquad x \to -\infty.$$

From the preceding we already knew that the solution to equation (A.17) was a member of the family of Painlevé transcendents, but now we know *which one*: it is w_1. Note that in the asymptotic expansion (A.21) all the higher order terms appeared to be negative, such that the solution stays just under the dashed line, and inside the shaded region of figure A.1, thus ensuring that it does not diverge at some finite $x = x_0$. Namely, as soon as the solution crosses the dashed line into region (1), it becomes convex and cannot remain close to the $\sqrt{-\frac{1}{2}x}$ solution, which is concave. Moreover, our solution can also not stay *on* the dashed $\sqrt{-\frac{1}{2}x}$ line, since this is not an exact solution of the Painlevé equation. Therefore, it has to remain under the dashed line which is consistent with what we found in the expansion (A.21). Finally, we now also know the behaviour of ϕ_0 in the other limit, $\eta \to \infty$, namely

$$\phi_0(\eta) = a\mathrm{Ai}(\eta/b), \qquad (\eta \to \infty),$$

allowing us to match the solution in the outer region where the behaviour is Gaussian, completing the perturbation analysis of the Thomas-Fermi density profile in one dimension.

A.4. Hydrodynamic equations

In this section we will outline the Thomas-Fermi approximation for the hydrodynamic equations

$$\frac{\partial n}{\partial t} = -\nabla \cdot \left(n(\mathbf{v} - \mathbf{\Omega} \times \mathbf{r})\right), \tag{A.23}$$

and

$$m\frac{\partial \mathbf{v}}{\partial t} = -\nabla\Big(\frac{1}{2}m\mathbf{v}\cdot\mathbf{v} + V(\mathbf{r}) + gn - \frac{\hbar^2}{2m}\frac{\nabla^2\sqrt{n}}{\sqrt{n}} + \Phi_{dd}[n] - m\mathbf{v}\cdot[\mathbf{\Omega}\cdot\mathbf{r}]\Big), \tag{A.24}$$

for a dipolar BEC in a rotating harmonic trap. For the nonrotating system, $\mathbf{\Omega} = \mathbf{0}$, and for the non-dipolar system we have that $\Phi_{dd}[n] = 0$.

Note that we cannot simply neglect the ∇^2 term of the time-dependent Gross-Pitaevskii equation (1.22) and then repeat the derivation of section 1.6 to obtain the new 'Thomas-Fermi hydrodynamic equations'. The reason is that the kinetic energy term consists not only of quantum pressure or zero point energy, which is associated with density gradients, but there are also contributions to the kinetic energy due to actual matter that is moving in a time dependent situation. Mathematically, these contributions follow from the ∇^2 operator acting on the phasefield of the condensate, which is associated with motion of the condensate through equation (1.38). Such kinetic energy contributions cannot be simply neglected, and therefore a careful re-derivation of the Thomas-Fermi approximation is warranted for the time dependent case.

First, we start by rescaling the length and time scales

$$\mathbf{r} = \xi_1 \mathbf{r}', \qquad t = t_0 t', \tag{A.25}$$

with ξ_1 a typical length scale, and t_0 a typical time scale and $\mathbf{r}', t'$ our new dimensionless coordinate and time variable. Similarly, we rescale the density and velocity using a typical density n_0 and typical velocity $v_0 = \frac{\hbar}{m\xi_2}$, with ξ_2 a second typical length scale, such that

$$n(\mathbf{r}, t) = n_0 n'(\mathbf{r}', t'), \qquad \mathbf{v}(\mathbf{r}, t) = v_0 \mathbf{v}'(\mathbf{r}', t') = \frac{\hbar}{m\xi_2}\mathbf{v}'(\mathbf{r}', t'), \tag{A.26}$$

and the dimensionless density and velocity satisfy $n', |\mathbf{v}'| = \mathcal{O}(1)$. The typical density n_0 is taken to be the peak density of the condensate, and for a harmonic trap this is the density attained in the centre of the condensate. Finally, we also rescale the rotation vector $\mathbf{\Omega}$ using a typical rotation frequency Ω_0,

$$\mathbf{\Omega} = \Omega_0 \widetilde{\mathbf{\Omega}}, \tag{A.27}$$

with the dimensionless rotation vector $\widetilde{\mathbf{\Omega}}$ satisfying $|\widetilde{\mathbf{\Omega}}| = \mathcal{O}(1)$.

Differentiation with respect to time becomes $\frac{\partial}{\partial t} = \frac{1}{t_0}\frac{\partial}{\partial t'}$ in terms of the new time variable t', and the gradient operator becomes $\nabla = \frac{1}{\xi_1}\nabla'$, where the prime denotes the coordinates upon which the ∇ operator acts.

Plugging these scaled variables back in the continuity equation (1.36), we obtain

$$\frac{n_0}{t_0}\frac{\partial n'}{\partial t'} = -n_0 \nabla' \cdot \left(n' \left(\frac{\hbar}{m\xi_2\xi_1}\mathbf{v}' - \Omega_0 \left[\widetilde{\mathbf{\Omega}} \times \mathbf{r}' \right] \right) \right). \tag{A.28}$$

When we restrict Ω_0 such that $\frac{\Omega_0}{\omega_\perp} = \mathcal{O}(1)$, we can use either frequency to scale our time with, we pick $\omega_\perp$. Therefore, we divide the entire equation by $n_0\omega_\perp$, and this suggests taking

$$t_0 = \omega_\perp^{-1}, \qquad \xi_1\xi_2 = \frac{\hbar}{\omega_\perp m}, \tag{A.29}$$

in order to scale all terms in equation (A.28) to be $\mathcal{O}(1)$. Continuing with the equation of motion, (1.37), plugging in the scaled variables and dividing by the energy $n_0 g$ gives

$$\begin{aligned} \frac{\hbar\omega_\perp}{\xi_2 n_0 g}\frac{\partial \mathbf{v}'}{\partial t'} = -\frac{1}{\xi_1}\nabla' \Big(& \frac{1}{2}\frac{\hbar^2}{m n_0 g \xi_2^2}\mathbf{v}' \cdot \mathbf{v}' + \frac{1}{2}\frac{m\omega_\perp^2\xi_1^2}{n_0 g}V'(\mathbf{r}') \\ & + \frac{\Phi_{dd}[n_0 n'](\xi_1 \mathbf{r})}{n_0 g} + n' - \frac{\hbar^2}{2m n_0 g \xi_1^2}\frac{1}{\sqrt{n'}}\nabla'^2\sqrt{n'} - \frac{\Omega_0\hbar\xi_1}{n_0 g \xi_2}\mathbf{v}' \cdot \left[\widetilde{\mathbf{\Omega}} \times \mathbf{r}' \right] \Big), \end{aligned} \tag{A.30}$$

where the dimensionless harmonic oscillator potential is given by

$$V'(\mathbf{r}') = \frac{1}{2}\left(x'^2 + y'^2 + \gamma^2 z'^2 \right). \tag{A.31}$$

The first term on the right-hand side between brackets suggests

$$\xi_2 = \frac{\hbar}{\sqrt{mn_0 g}}, \tag{A.32}$$

which we identify as the healing- or coherence length [107]. Inserting this in equation (A.29) gives

$$\xi_1 = \sqrt{\frac{n_0 g}{\omega_\perp^2 m}}. \tag{A.33}$$

Plugging in these length scales (A.32), (A.33), and the timescale $t_0 = \omega_\perp^{-1}$, equation (A.30) reduces to

$$\begin{aligned} \frac{\partial \mathbf{v}'}{\partial t'} = -\nabla' \big(&\frac{1}{2}\mathbf{v}' \cdot \mathbf{v}' + \frac{1}{2}V'(\mathbf{r}') + \epsilon_{dd}\Phi'_{dd}[n'](\mathbf{r}') \\ - + n' + \frac{1}{2}&\left(\frac{\xi_2}{\xi_1}\right)^2 \frac{1}{\sqrt{n'}}\nabla^2\sqrt{n'} - \frac{\Omega_0}{\omega_\perp}\mathbf{v}' \cdot \left[\widetilde{\mathbf{\Omega}} \times \mathbf{r}'\right]\big), \end{aligned} \tag{A.34}$$

with the dimensionless dipolar potential Φ'_{dd} defined as

$$\epsilon_{dd}\Phi'_{dd}[n'](\mathbf{r}') = \epsilon_{dd}\int U'_{dd}(\mathbf{r}' - \mathbf{r}'')n'(\mathbf{r}'')\mathrm{d}^3\mathbf{r}'' = \frac{\Phi_{dd}[n](\xi\mathbf{r})}{n_0 g}, \tag{A.35}$$

with the dimensionless interaction energy given by

$$U'_{dd}(\mathbf{r}' - \mathbf{r}'') = \frac{3}{4\pi}\frac{1 - 3\cos^2\theta}{|\mathbf{r}' - \mathbf{r}''|^3}. \tag{A.36}$$

Here, the quantity $\epsilon_{dd} = \frac{C_{dd}}{3g}$ arises naturally.
For large condensates ($n_0 \gg 1$), the quantity

$$\frac{\xi_2}{\xi_1} = \frac{\hbar\omega_\perp}{n_0 g} \tag{A.37}$$

becomes very small, and we neglect the $\mathcal{O}(\frac{\xi_2^2}{\xi_1^2})$ term in equation (A.34), the so-called quantum pressure term [107], which is due to density gradients. This is the same term that is neglected in Appendix A.1, and we assume that in the time-dependent case this is still possible[5]. Likewise, this approximation is called the *Thomas-Fermi approximation*. When making this approximation we have to keep in mind that this adds an extra restriction to the remaining dimensionless quantities, namely that $\gamma \gg \xi_2^2/\xi_1^2$ and $\Omega_0/\omega_\perp \gg \xi_2^2/\xi_1^2$. Otherwise the approximation of neglecting only the quantum pressure term is not valid.

After making the Thomas-Fermi approximation we are left with two equations describing the dynamics of the condensate, the equation of continuity

[5] Although an analytical proof is lacking, there are extensive numerical studies of time dependent states that confirm the accuracy of the Thomas-Fermi approximation, see for instance [100, 101, 102].

$$\frac{\partial n}{\partial t} = -\nabla \cdot (n(\mathbf{v} - [\mathbf{\Omega} \times \mathbf{r}])) \tag{A.38}$$

and the equation of motion

$$\frac{\partial \mathbf{v}}{\partial t} = -\nabla \left(\frac{1}{2}\mathbf{v} \cdot \mathbf{v} + V(\mathbf{r}) + n + \epsilon_{dd}\Phi_{dd}[n](\mathbf{r}) - \mathbf{v} \cdot [\mathbf{\Omega} \times \mathbf{r}] \right), \tag{A.39}$$

where we have dropped the primes and rescaled the rotation vector $\mathbf{\Omega} = \frac{\Omega_0}{\omega_\perp}\widetilde{\mathbf{\Omega}}$ one final time, since in practice $\Omega_0/\omega_\perp = \mathcal{O}(1)$. We therefore might as well absorb this ratio into $\mathbf{\Omega}$ to keep the notation a little cleaner. The potential V is the dimensionless harmonic oscillator of eq. (A.31).

B. Calculating the dipolar potential of a heterogenous ellipsoid BEC

The calculation of the potential of a heterogenous ellipsoid effecting a $1/r^2$ force law has attracted interest from various fields over the years. Such force laws are encountered in electrostatics, gravitational calculations, and now, through Eqs. (2.5) and (2.6) in the field of dipolar BECs.

Calculating the dipolar potential of a BEC in the Thomas-Fermi limit involves evaluating integrals of the form

$$\phi_{ijk} = \frac{1}{4\pi} \int \frac{x^i y^j z^k}{|\mathbf{r} - \mathbf{r}_0|} \mathrm{d}x\mathrm{d}y\mathrm{d}y, \tag{B.1}$$

where the domain of integration is a general ellipsoid with semi-axes R_x, R_y, R_z, the polynomial powers i, j, k are positive integers and the point $\mathbf{r}_0$ is an internal point of the ellipsoid. More specific, we need the second derivative with respect to z of ϕ_{ijk}, which is precisely the first term on the right hand side of Eq. (2.23). This problem has already been solved over a century ago, by the joint efforts of Green, Poisson, Cayley, Ferrers, Dyson and Routh, where the most crucial steps have been taken by Ferrers [36] and Dyson [34].

Through the efforts of Ferrers and Dyson, the triple integral of (B.1) is reduced to a finite number of single integrals, which moreover do not depend on $\mathbf{r}_0$. Specifically, for a general polynomial density $n = x^i y^j z^k$ of the ellipsoid, it is shown that the potential is of a polynomial form of degree $i + j + k + 2$. In the particular case of the dipolar potential the derivative of ϕ_{ijk} with respect to z is taken twice, such that the dipolar potential inside the BEC is again of the same degree as the density.

Although the works of Ferrers and Dyson in principle solve the problem, their results are not particularly suitable for numerical computation. A more recent paper by Levin and Muratov [76] expresses the integral ϕ_{ijk} in a more manageable form through the use of generalized depolarization factors

$$M_{lmn} = (2l-1)!!(2m-1)!!(2n-1)!! \frac{\kappa_x \kappa_y \beta_{lmn}}{2R_z^{2(l+m+n-1)}}, \tag{B.2}$$

where $m, l, n = 0, 1, 2 \ldots$, and β_{lmn} as defined in Eq. (2.10). Writing the polynomial coefficients i, j, k as

$$i = 2\lambda + \delta_\lambda, j = 2\mu + \delta_\mu, k = 2\nu + \delta_\nu,$$

with λ, μ, ν positive integers such that the $\delta_\mu, \delta_\nu, \delta_\lambda$ are either 0 or 1 for i, j, k even or odd (respectively), and setting

$$\sigma = \lambda + \mu + \nu + 1,$$

then, according to Levin and Muratov, the second derivative with respect to z of ϕ_{ijk} becomes

$$\frac{\partial^2}{\partial z^2}\phi_{ijk} = \frac{2R_x^i R_y^j R_z^k}{4^\sigma} i!j!k! \sum_{p=0}^{\sigma}\sum_{q=0}^{\sigma-p}\sum_{r=1}^{\sigma-p-q} \frac{S_{pqr}(2r+\delta_\nu)(2r+\delta_\nu-1)x_0^{2p+\delta_\lambda} y_0^{2q+\delta_\mu} z_0^{2r+\delta_\nu-2}}{(\sigma-p-q-r)!(2p\delta_\lambda+1)(2q\delta_\mu+1)(2r\delta_\nu+1)} \Gamma_{pqr}^{(i,j,k)}, \tag{B.3}$$

where

$$\Gamma_{pqr}^{(i,j,k)} =$$

$$\sum_{l=0}^{\lambda}\sum_{m=0}^{\mu}\sum_{n=0}^{\nu} \frac{S_{lmn} R_x^{2l+\delta_\lambda} R_y^{2m+\delta_\mu} R_z^{2n+\delta_\nu}}{(\lambda-l)!(\mu-m)!(\nu-n)!(2l\delta_\lambda+1)(2m\delta_\mu+1)(2n\delta_\nu+1)} M_{l+p+\delta_\lambda, m+q+\delta_\mu, n+r+\delta_\nu},$$

and

$$S_{lmn} = \frac{(-2)^{l+m+n}}{(2l)!(2m)!(2n)!}.$$

C. Energy derivatives

In this appendix we derive the derivatives of the energy of a parabolic condensate, given by equation (2.15), with respect to the condensate radius and aspect ratio. These are used in chapter 2 to determine the stability of the stationary states of the condensate, with respect to variations of the aspect ratio and radius. That is, we determine whether the stationary solution is stable *within the class of parabolic, cylindrically symmetric density profiles.*

C.1. Scaling the energy

Let $\tilde{\kappa} = \kappa_x = \kappa_y$ be the solution of the equations (2.12)-(2.14). Alternatively, $\tilde{\kappa}$ can be solved from the transcendental equation [35]

$$3\tilde{\kappa}^2\epsilon_{dd}\left[\left(\frac{\gamma^2}{2}+1\right)\frac{f(\tilde{\kappa})}{1-\tilde{\kappa}^2}-1\right]+(\epsilon_{dd}-1)(\tilde{\kappa}^2-\gamma^2)=0, \tag{C.1}$$

where

$$f(\tilde{\kappa}) = \beta_{001}(\tilde{\kappa}).$$

Then, the corresponding condensate radius $\tilde{R}_x$ is given by [35]:

$$\tilde{R}_x = \left[\frac{15N\tilde{\kappa}}{4\pi m\omega_x^2}\left\{1+\epsilon_{dd}\left(\frac{3}{2}\frac{\tilde{\kappa}^2 f(\tilde{\kappa})}{1-\tilde{\kappa}^2}-1\right)\right\}\right]^{\frac{1}{5}}.$$

The central density is then by

$$\tilde{n}_0 = \frac{15N\tilde{\kappa}}{8\pi\tilde{R}_x^3}.$$

The shape of a parabolic, cylindrically symmetric density profile is fully determined by the two parameters R_x, R_z, or equivalently, R_x and κ. The energy of a condensate with arbitrary κ, R_x is then given by

$$E_{tot} = \frac{N}{14}m\omega_x^2 R_x^2\left(2+\frac{\gamma^2}{\kappa^2}\right)+\frac{15}{28\pi}\frac{N^2 g\kappa}{R_x^3}[1-\epsilon_{dd}f(\kappa)].$$

The values $\tilde{\kappa}, \tilde{R}_x$ are determined by a specific choice of ϵ_{dd}, γ, our fixed 'experimental' parameters. Therefore, for a given ϵ_{dd}, γ we can use $\tilde{\kappa}, \tilde{R}_x$ to scale R_x, κ (the scaling will not change when deforming the condensate):

$$R_x = \tilde{R}_x R', \qquad \kappa = \tilde{\kappa}\kappa',$$

where κ', R' are our new dimensionless parameters. The solution $\tilde{\kappa}, \tilde{R}_x$, of which we are investigating the stability, lies (by definition) at $\kappa' = 1, R' = 1$. For a fixed ϵ_{dd}, γ, we can also define a typical energy $\tilde{n}_0 g$ to scale the total energy with

$$E' = \frac{E_{tot}}{N\tilde{n}_0 g} = \frac{1}{14}\frac{m\omega_x^2}{\tilde{n}_0 g}\tilde{R}_x^2 R'^2\left(2 + \frac{\gamma^2}{(\tilde{\kappa}\kappa')^2}\right) + \frac{2}{7}\frac{1}{\tilde{n}_0 g}\frac{15Ng\tilde{\kappa}\kappa'}{8\pi\tilde{R}_x^3 R'^3}\left(1 - \epsilon_{dd} f(\tilde{\kappa}\kappa')\right).$$

The quantity

$$\xi := \sqrt{\frac{\tilde{n}_0 g}{m\omega_x^2}},$$

appearing inversely squared in the first term of the rhs, is a length scale, whereas the quantity

$$n_0 := \frac{15Ng\tilde{\kappa}\kappa'}{8\pi\tilde{R}_x^3 R'^3}$$

is exactly the central density of a general parabolic condensate. The scaled energy then becomes

$$E' = \frac{1}{14}\left(\frac{\tilde{R}_x}{\xi}\right)^2 R'^2\left(2 + \frac{\gamma^2}{(\tilde{\kappa}\kappa')^2}\right) + \frac{2}{7}\frac{n_0}{\tilde{n}_0}[1 - \epsilon_{dd} f(\tilde{\kappa}\kappa')] \tag{C.2}$$

$$= \frac{1}{14}\left(\frac{\tilde{R}_x}{\xi}\right)^2 R'^2\left(2 + \frac{\gamma^2}{(\tilde{\kappa}\kappa')^2}\right) + \frac{2}{7}\frac{\kappa'}{R'^3}[1 - \epsilon_{dd} f(\tilde{\kappa}\kappa')]. \tag{C.3}$$

We can eliminate the length scale ξ by noting that

$$\begin{aligned}
\tilde{R}_x &= \left[2\frac{15Ng\tilde{\kappa}}{8\pi m\omega_x^2}\{1 + \epsilon_{dd}\left(\frac{3}{2}\frac{\tilde{\kappa}^2 f(\tilde{\kappa})}{1-\tilde{\kappa}^2} - 1\right)\}\right]^{\frac{1}{5}} = \left[2\frac{15Ng\tilde{\kappa}}{8\pi m\omega_x^2\tilde{R}_x^3}\tilde{R}_x^3\{1 + \epsilon_{dd}\left(\frac{3}{2}\frac{\tilde{\kappa}^2 f(\tilde{\kappa})}{1-\tilde{\kappa}^2} - 1\right)\}\right]^{\frac{1}{5}} \\
&= \left[2\frac{\tilde{n}_0 g}{m\omega_x^2}\tilde{R}_x^3\{1 + \epsilon_{dd}\left(\frac{3}{2}\frac{\tilde{\kappa}^2 f(\tilde{\kappa})}{1-\tilde{\kappa}^2} - 1\right)\}\right]^{\frac{1}{5}} = \left[2\xi^2\tilde{R}_x^3\{1 + \epsilon_{dd}\left(\frac{3}{2}\frac{\tilde{\kappa}^2 f(\tilde{\kappa})}{1-\tilde{\kappa}^2} - 1\right)\}\right]^{\frac{1}{5}} \\
&= \xi^{\frac{2}{5}}\tilde{R}_x^{\frac{3}{5}}\left[2\{1 + \epsilon_{dd}\left(\frac{3}{2}\frac{\tilde{\kappa}^2 f(\tilde{\kappa})}{1-\tilde{\kappa}^2} - 1\right)\}\right]^{\frac{1}{5}},
\end{aligned} \tag{C.4}$$

from which it follows that

$$\frac{\tilde{R}_x}{\xi} = \sqrt{2\left(1 + \epsilon_{dd}\left(\frac{3}{2}\frac{\tilde{\kappa}^2 f(\tilde{\kappa})}{1-\tilde{\kappa}^2} - 1\right)\right)},$$

which we can use to express the dimensionless energy E' of a general parabolic condensate in terms of $\tilde{\kappa}, \tilde{R}_x, \epsilon_{dd}$, and γ only:

$$E' = \frac{1}{7}\left(1 + \epsilon_{dd}\left(\frac{3}{2}\frac{\tilde{\kappa}^2 f(\tilde{\kappa})}{1-\tilde{\kappa}^2} - 1\right)\right) R'^2\left(2 + \frac{\gamma^2}{(\tilde{\kappa}\kappa')^2}\right) + \frac{2}{7}\frac{\kappa'}{R'^3}[1 - \epsilon_{dd} f(\tilde{\kappa}\kappa')], \tag{C.5}$$

in units of the energy $N\tilde{n}_0 g$, with the condensate radius in units of $\tilde{R}_x$ and the aspect ratio in units of $\tilde{\kappa}$.

C.2. Energy derivatives

To verify whether the solution $\tilde{\kappa}, \tilde{R}_x$ is a stable stationary point of the energy, we need to evaluate the energy E' from eq. (C.5) and its first and second derivatives, where the derivatives are taken with respect to κ' and R', since these parameters control the condensate shape deformation.

We have

$$\frac{\mathrm{d}E'}{\mathrm{d}R'} = \frac{1}{7}\left(\frac{\tilde{R}_x}{\xi}\right)^2 R'\left(2+\frac{\gamma^2}{(\tilde{\kappa}\kappa')^2}\right) + \frac{2}{7}\kappa'\frac{-3}{R'^4}[1-\epsilon_{dd}f(\tilde{\kappa}\kappa')], \tag{C.6}$$

$$\frac{\mathrm{d}^2E'}{\mathrm{d}R'^2} = \frac{1}{7}\left(\frac{\tilde{R}_x}{\xi}\right)^2 \left(2+\frac{\gamma^2}{(\tilde{\kappa}\kappa')^2}\right) + \frac{24}{7}\frac{\kappa'}{R'^5}[1-\epsilon_{dd}f(\tilde{\kappa}\kappa')], \tag{C.7}$$

$$\frac{\mathrm{d}E'}{\mathrm{d}\kappa'} = -\frac{1}{7}\left(\frac{\tilde{R}_x}{\xi}\right)^2 R'^2\frac{\gamma^2}{(\tilde{\kappa}\kappa')^3}\tilde{\kappa} + \frac{2}{7}\frac{1}{R'^3}[1-\epsilon_{dd}f(\tilde{\kappa}\kappa')] - \frac{2}{7}\frac{\kappa'}{R'^3}\epsilon_{dd}f'(\tilde{\kappa}\kappa')\tilde{\kappa}, \tag{C.8}$$

$$\frac{\mathrm{d}^2E'}{\mathrm{d}\kappa'^2} = \frac{3}{7}\left(\frac{\tilde{R}_x}{\xi}\right)^2 R'^2\frac{\gamma^2}{(\tilde{\kappa}\kappa')^4}\tilde{\kappa}^2 - \frac{4}{7R'^3}\epsilon_{dd}f'(\tilde{\kappa}\kappa')\tilde{\kappa} - \frac{2\kappa'}{7R'^3}\epsilon_{dd}f''(\tilde{\kappa}\kappa')\tilde{\kappa}^2 \tag{C.9}$$

$$\frac{\mathrm{d}^2E'}{\mathrm{d}R'\mathrm{d}\kappa'} = -\frac{2}{7}\left(\frac{\tilde{R}_x}{\xi}\right)^2 R'\frac{\gamma^2}{(\tilde{\kappa}\kappa')^3}\tilde{\kappa} - \frac{6}{7}\frac{1}{R'^4}[1-\epsilon_{dd}f(\tilde{\kappa}\kappa')] + \frac{6}{7}\frac{\kappa'}{R'^4}\epsilon_{dd}f'(\tilde{\kappa}\kappa')\tilde{\kappa}. \tag{C.10}$$

The first derivatives (C.6) and (C.8) are always equal to zero, when the transcendental equation (C.1) is satisfied (when equating them to zero, after some algebra (C.1) is regained).

To determine whether a given solution is an energy minimum, we need to evaluate the second derivatives (C.7), (C.9). If one of these is negative, we are dealing with a saddle point, or even a maximum. When they are both positive, we have to perform the *second partial derivative test* (see Appendix D). One has to evaluate the quantity

$$M = \frac{\mathrm{d}^2E'}{\mathrm{d}R'^2}\frac{\mathrm{d}^2E'}{\mathrm{d}\kappa'^2} - \left(\frac{\mathrm{d}^2E'}{\mathrm{d}R'\mathrm{d}\kappa'}\right)^2,$$

and when $M<0$ we can conclude that we are dealing with a saddle point after all.

For $\epsilon_{dd}>1$, we can conclude from (C.5) that there exists a cigar collapse. Namely, if we let κ' go to zero, but stop at a finite value such that $f(\tilde{\kappa}\kappa') > \epsilon_{dd}^{-1}$, and then take the limit $R'\to 0$, then $E'\to-\infty$. Since $f(\tilde{\kappa}\kappa')\leq 1$, this can only happen for $\epsilon_{dd}>1$. Thus, all solutions with $\epsilon_{dd}>1$ are at most a local minimum, they are metastable with respect to a cigar collapse (cf. [35]).

Finally, note that E' has a skewed asymptote for $\kappa'\to\infty$ (a pancake collapse), see figure. If this asymptote has a negative slope that would mean that the stationary point is (at most) a local minimum, and the condensate unstable to a pancake collapse. The slope of this asymptote is calculated from the limit

$$\lim_{\kappa'\to\infty}\frac{\mathrm{d}E'}{\mathrm{d}\kappa'} = 0+\frac{2}{7}\frac{1}{R'^3}(1+2\epsilon_{dd})-\frac{2}{7}\lim_{\kappa'\to\infty}\left[\frac{\kappa'}{R'^3}\epsilon_{dd}f'(\tilde{\kappa}\kappa')\tilde{\kappa}\right] \tag{C.11}$$

$$= \frac{2}{7}\frac{1}{R'^3}[1+2\epsilon_{dd}], \tag{C.12}$$

(the limit is evaluated using a symbolic manipulator such as Mathematica), which is smaller than zero when $\epsilon_{dd} < -\frac{1}{2}$. So the pancake collapse only seems to exist for $\epsilon_{dd} < -\frac{1}{2}$.

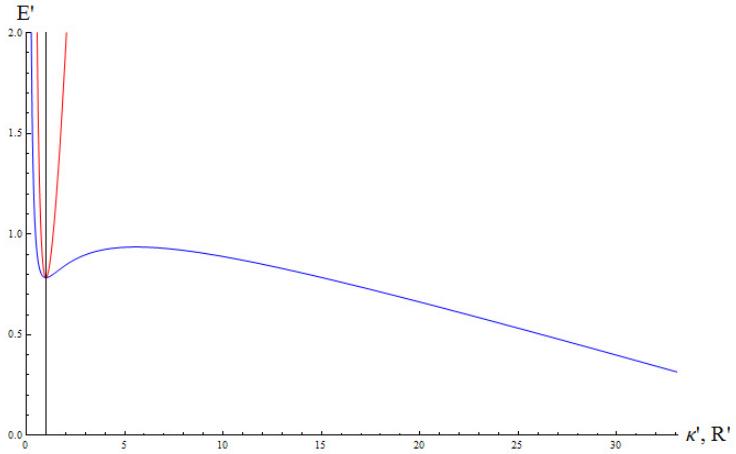

Figure C.1.: *Pancake collapse, the stationary solution at $\kappa' = 1, R' = 1$ is only a local minimum. (Blue curve is for varying κ', red for R')*

D. Second partial derivative test

Let $f : \mathbb{R}^n \to \mathbb{R}$, $f \in \mathcal{C}^3$, and let $\mathbf{a}$ be a critical point of f such that

$$\left.\frac{\partial f}{\partial x_i}\right|_{\mathbf{x}=\mathbf{a}} = 0, \qquad i = 1 \dots n.$$

To analyze whether the critical point $\mathbf{a}$ is a maximum, minimum, or a saddle point, consider the Taylor expansion of f around $\mathbf{a}$:

$$f(\mathbf{a}+\mathbf{h}) = f(\mathbf{a}) + \frac{1}{2}\sum_{i,j=1}^{n} \frac{\partial^2 f}{\partial x_i \partial x_j}(\mathbf{a}) h_i h_j + R_2(\mathbf{h}),$$

where $\lim_{\mathbf{h}\to\mathbf{0}} \frac{R_2(\mathbf{h})}{|\mathbf{h}|^2} = 0$, or in other words $R_2 = o(|\mathbf{h}|^2)$ [59]. Clearly, in order for $\mathbf{a}$ to be a minimum we must have that the quadratic form

$$q(\mathbf{h}) = \frac{1}{2}\sum_{i,j=1}^{n} \frac{\partial^2 f}{\partial x_i \partial x_j}(\mathbf{a}) h_i h_j \tag{D.1}$$

is strictly positive for all $\mathbf{h}$. In the opposite case, $q(\mathbf{h}) \leq 0, \forall \mathbf{h}$, we have that $\mathbf{a}$ is a maximum. When $q(\mathbf{h})$ attains both positive and negative values for various $\mathbf{h}$ then $\mathbf{a}$ is a saddle point [16]. When $q(\mathbf{h}) = 0$, then higher order derivatives of f need to be evaluated to determine the character of the critical point.

Rewriting (D.1) as

$$q(\mathbf{h}) = \mathbf{h}^T \mathbf{H} \mathbf{h}$$

where $\mathbf{H}$ is the *Hessian* matrix

$$\mathbf{H}(f) = \begin{bmatrix} \frac{\partial^2 f}{\partial x_1^2} & \frac{\partial^2 f}{\partial x_1 \partial x_2} & \cdots & \frac{\partial^2 f}{\partial x_1 \partial x_n} \\ \frac{\partial^2 f}{\partial x_2 \partial x_1} & \frac{\partial^2 f}{\partial x_2^2} & \cdots & \frac{\partial^2 f}{\partial x_2 \partial x_n} \\ \vdots & \vdots & \ddots & \vdots \\ \frac{\partial^2 f}{\partial x_n \partial x_1} & \frac{\partial^2 f}{\partial x_n \partial x_2} & \cdots & \frac{\partial^2 f}{\partial x_n^2} \end{bmatrix}, \tag{D.2}$$

such that in order to evaluate the character of the critical point $\mathbf{a}$, we need to determine whether $\mathbf{H}$ is positive definite, negative definite, or neither.

When f is real valued, $\mathbf{H}$ is also real valued and symmetric, and hence it is Hermitian. Then, there exists an orthogonal basis of eigenvectors of $\mathbf{H}$, and its eigenvalues are real. The matrix $\mathbf{H}$ is positive definite if all eigenvalues λ_i, $i = 1 \dots n$ of $\mathbf{H}$ satisfy $\lambda_i > 0$, it is negative definite

if $\lambda_i < 0$, and nondefinite if some are positive and some are negative. Correspondingly, $\mathbf{a}$ is a minimum, maximum or saddle point (respectively). In the remaining case where $\mathbf{H}$ is either positive or negative semi-definite ($\forall i : \lambda_i \leq 0$, or $\forall i : \lambda_i \geq 0$, with in both cases the equality attained for at least one i), the character of the critical point remains indeterminate.

An equivalent criterion is to examine the sequence of determinants Δ_k, $k = 1 \ldots n$ of the upper left $k \times k$ submatrices of $\mathbf{H}$. Then $\mathbf{H}$ is positive definite if $\Delta_k > 0$ and negative definite if $(-1)^k \Delta_k > 0$ for each k. The critical point $\mathbf{a}$ remains indeterminate if $\det \mathbf{H} = 0$, and it is a saddle point if neither of the above three conditions is satisfied.

A discussion of a second partial derivative test for constrained maximum-minimum problems can be found in refs. [16, 124].

E. Perturbation time evolution

In this Appendix we linearize the dimensionless hydrodynamic equations (A.38), in order to determine the time evolution of small perturbations to the density and phase. These results are used in chapters 2 and 3. In chapter 2, the trap rotation vector $\mathbf{\Omega} = \mathbf{0}$.

Starting with the dimensionless equation of continuity (A.38):

$$\frac{\partial n}{\partial t} = -\nabla \cdot (n(\mathbf{v} - [\mathbf{\Omega} \times \mathbf{r}])) \tag{E.1}$$

for the density, and (A.39)

$$\frac{\partial \varphi}{\partial t} = -\left(\frac{1}{2}\mathbf{v}\cdot\mathbf{v} + V(\mathbf{r}) + n + \epsilon_{dd}\Phi_{dd}[n](\mathbf{r}) - \mathbf{v}\cdot[\mathbf{\Omega}\times\mathbf{r}]\right), \tag{E.2}$$

where the latter equation is equivalent to (A.39) but where we have written it in terms of the condensate phase, rather than the velocity field. Beware the the dipolar potential Φ_{dd} in these equations is the *dimensionless* potential defined in definition (A.35), but with the prime omitted. The phase and velocity field are related to each other through equation (1.38). For these equations, we have a stationary solution of the form

$$\begin{aligned} \varphi &= \alpha\nabla(xy) + c =: \varphi_s \\ n = n_s &= 1 - \frac{x^2}{R_x^2} - \frac{y^2}{R_y^2} - \frac{z^2}{R_z^2}, \end{aligned} \tag{E.3}$$

for some R_x, R_y, R_z, to be determined from the self consistency relations, and c an arbitrary constant. Note that for the nonrotating case $\alpha = 0$

Next, let's consider the time evolution of slightly perturbed phase and density patterns. Writing the phase dependence of the time derivative of the density explicitly[1] as $\frac{\partial n}{\partial t} = \frac{\partial n}{\partial t}(\varphi)$ and the density dependence of the time derivative of the phase as $\frac{\partial \varphi}{\partial t} = \frac{\partial \varphi}{\partial t}(n)$ we get

$$\begin{aligned} \frac{\partial}{\partial t}[n_s + \delta n](\varphi_s + \delta\varphi) &= -\nabla\cdot[(n_s+\delta n)(\nabla\varphi_s + \nabla\delta\varphi - \Omega\times\mathbf{r})] \\ &= \frac{\partial n_s}{\partial t} - \nabla\cdot(\delta n(\nabla\varphi_s - \Omega\times\mathbf{r})) - \nabla\cdot(n_s\nabla\delta\varphi) + \mathcal{O}(\delta^2), \end{aligned} \tag{E.4}$$

and

$$\frac{\partial}{\partial t}[\varphi_s + \delta\varphi](n_s + \delta n) = -\Big(\frac{1}{2}(\nabla\varphi_s + \nabla\delta\varphi)^2 + V(\mathbf{r}) + n_s + \delta n$$

[1] We are actually working with the the vector valued function (n, φ), but this is slightly awkward on the notation. By writing the dependencies explicitly we can take time derivatives of a single component at a time.

$$+\epsilon_{dd}\Phi_{dd}[n+\delta n](\mathbf{r}) - (\nabla\varphi_s + \nabla\delta\varphi)\cdot(\Omega\times\mathbf{r})\Big) \tag{E.5}$$

$$= -\Big(\frac{1}{2}(\nabla\varphi)^2 + V(\mathbf{r}) + n_s + \epsilon_{dd}\Phi_{dd}[n_s](\mathbf{r}) - \nabla\varphi_s\cdot(\Omega\times\mathbf{r})$$

$$+\nabla\varphi_s\nabla\delta\varphi + \delta n + \epsilon_{dd}\Phi_{dd}[n_s+\delta n](\mathbf{r}) - \epsilon_{dd}\Phi_{dd}[n_s](\mathbf{r}) - \nabla\delta\varphi\cdot(\Omega\times\mathbf{r})\Big) + \mathcal{O}(\delta^2) \tag{E.6}$$

$$= \frac{\partial\varphi_s}{\partial t} - \delta n - \epsilon_{dd}\Phi_{dd}[n_s+\delta n](\mathbf{r}) + \epsilon_{dd}\Phi_{dd}[n_s](\mathbf{r}) - (\nabla\varphi_s\cdot\nabla\delta\varphi - (\Omega\times\mathbf{r})\cdot\nabla\delta\varphi) + \mathcal{O}(\delta^2). \tag{E.7}$$

To get from (E.5) to (E.6) $\epsilon_{dd}\Phi_{dd}[n](\mathbf{r})$ is added and subtracted once and some rearranging is done. To get from (E.6) to (E.7), note that the first line of (E.6) is exactly (E.2) for the stationary solutions n_s, φ_s.

Continuing with (E.7), note that n_s and φ_s are exactly such that $\frac{\partial n_s}{\partial t} = \frac{\partial\varphi_s}{\partial t} = 0$. Using this fact, and that $\nabla^2\varphi_s = 0$, we obtain the following system of equations

$$\frac{\partial}{\partial t}\begin{bmatrix}\delta n\\ \delta\varphi\end{bmatrix} = -\begin{bmatrix}(\nabla\varphi_s - \Omega\times\mathbf{r})\cdot\nabla & \nabla\cdot(n_s\nabla)\\ 1+\mathcal{K} & (\nabla\varphi_s - \Omega\times\mathbf{r})\cdot\nabla\end{bmatrix}\begin{bmatrix}\delta n\\ \delta\varphi\end{bmatrix} \tag{E.8}$$

describing the time evolution of small perturbations δn and $\delta\varphi$, neglecting $\mathcal{O}(\delta^2)$ terms. The operator $\mathcal{K}$ is defined as

$$(\mathcal{K}f)(\mathbf{r}) = \epsilon_{dd}\Phi_{dd}[n_s+\delta n](\mathbf{r}) - \epsilon_{dd}\Phi_{dd}[n_s](\mathbf{r}). \tag{E.9}$$

To first order in δ, we have that

$$(\mathcal{K}f)(\mathbf{r}) = \epsilon_{dd}\int U_{dd}(\mathbf{r}-\mathbf{r}')\delta n(\mathbf{r}')d^3\mathbf{r}', \tag{E.10}$$

where the domain of integration is the (ellipsoidal) domain of the unperturbed condensate density, see Appendix F. The reader is reminded again that the dipolar interaction energy in this expression is the dimensionless dipolar interaction energy defined in (A.36).

F. Integration domain

Related to the unperturbed condensate with density n specified in eq. (E.3), and the perturbed condensate with density $n + \delta n$, with δn, we define the following domains.

$$D = \{\mathbf{r} : n(\mathbf{r}) > 0\} \tag{F.1}$$
$$D^p = \{\mathbf{r} : (n + \delta n)(\mathbf{r}) > 0\} \tag{F.2}$$
$$P^+ = \{\mathbf{r} : \mathbf{r} \in D^p \wedge \mathbf{r} \notin D\} \tag{F.3}$$
$$P^- = \{\mathbf{r} : \mathbf{r} \notin D^p \wedge \mathbf{r} \in D\}, \tag{F.4}$$

such that

$$D^p = (D \cup P^+) \backslash P^-.$$

In words, D is the domain of the unperturbed condensate, D^p that of the perturbed condensate, P^+ is what is gained by perturbing the condensate, and P^- is what is lost. In the following we denote the amplitude of the density perturbation δn by a dimensionless constant δ. Then, for a small $\mathcal{O}(\delta)$ perturbation, we assume that the volumes of P^- and P^+ are also proportional to δ. This is at least true for a uniform perturbation: $\frac{4}{3}\pi(R+\delta)^3 - \frac{4}{3}\pi R^3 = \mathcal{O}(\delta)$, and for other simple forms of δn, such as linear and quadratic polynomials in the cartesian components of $\mathbf{r}$, this statement can be verified similarly.

Continuing then under this assumption,

$$\Phi_{dd}[n](\mathbf{r}) = \int_D U_{dd}(\mathbf{r} - \mathbf{r}')n(\mathbf{r}')d^3\mathbf{r}', \tag{F.5}$$

and

$$\Phi_{dd}[n + \delta n](\mathbf{r}) = \int_{D^p} U_{dd}(\mathbf{r} - \mathbf{r}')n(\mathbf{r}')d^3\mathbf{r}'$$
$$= \int_D U_{dd}(\mathbf{r} - \mathbf{r}')n(\mathbf{r}')d^3\mathbf{r}' + \int_{P^+} U_{dd}(\mathbf{r} - \mathbf{r}')n(\mathbf{r}')d^3\mathbf{r}' - \int_{P^-} U_{dd}(\mathbf{r} - \mathbf{r}')n(\mathbf{r}')d^3\mathbf{r}'$$
$$+ \int_D U_{dd}(\mathbf{r} - \mathbf{r}')\delta n(\mathbf{r}')d^3\mathbf{r}' + \mathcal{O}(\delta^2),$$

where the integrals of the density perturbation δn over P^+ and P^- are neglected, since these are $\mathcal{O}(\delta^2)$. Then, the quantity $\Phi_{dd}[n + \delta n] - \Phi_{dd}[n]$ as occurring in the calculation of the perturbation operator is

$$\Phi_{dd}[n+\delta n] - \Phi_{dd}[n] =$$
$$\int_D U_{dd}(\mathbf{r}-\mathbf{r}')\delta n(\mathbf{r}')d^3\mathbf{r}' + \int_{P^+} U_{dd}(\mathbf{r}-\mathbf{r}')n(\mathbf{r}')d^3\mathbf{r}' - \int_{P^-} U_{dd}(\mathbf{r}-\mathbf{r}')n(\mathbf{r}')d^3\mathbf{r}', \tag{F.6}$$

The last two terms are there, since we've assumed that $n = \mathcal{O}(1)$. However, exactly in the domains P^+, P^-, the unperturbed density n becomes also of $\mathcal{O}(\delta)$, since there n and δn are of equal magnitude. The last two terms then also become $\mathcal{O}(\delta^2)$, such tat the only relevant part of the integration domain to be included is the unperturbed domain D.

G. Excitation frequencies as a function of ϵ_{dd}

In Section 2.3 we considered the effect of the dipolar interactions on the mode frequencies and plotted this as a function of κ rather than ϵ_{dd} to remove the problem of the static solutions being double-valued. However, since ϵ_{dd} is a more obvious experimental parameter, we have plotted the corresponding frequency plots but as a function of ϵ_{dd} in Fig. G.1.

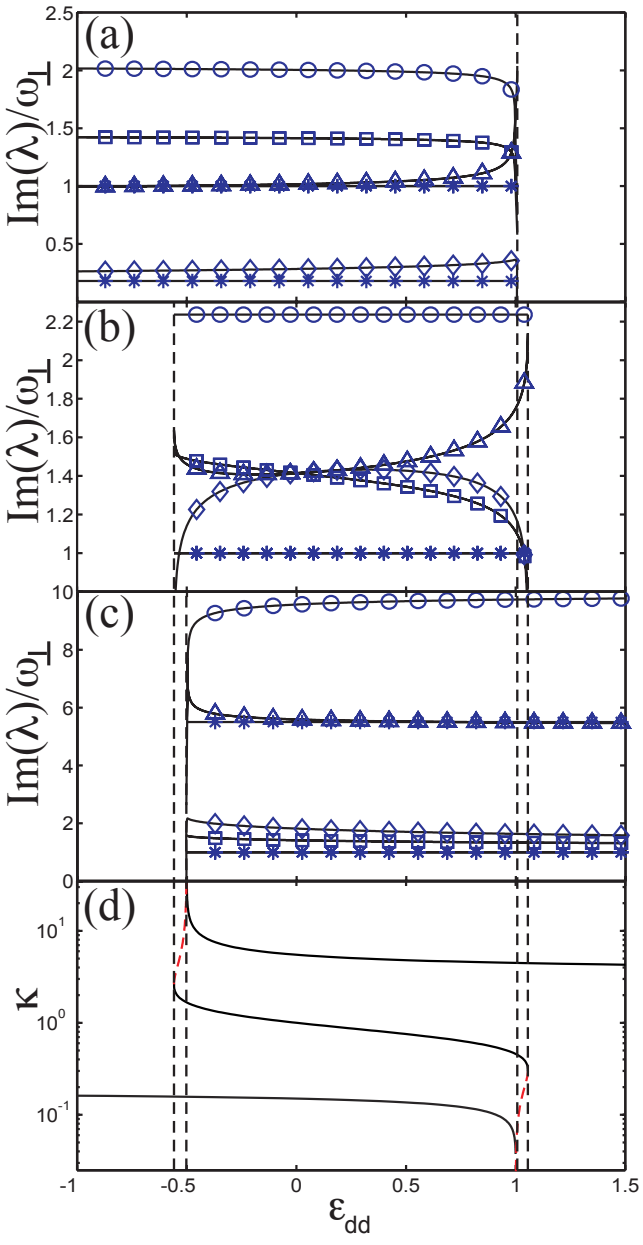

Figure G.1.: Excitation frequencies as a function of ϵ_{dd} for a cylindrically-symmetric trap with aspect ratio (a) $\gamma = 0.18$, (b) $\gamma = 1$ and (c) $\gamma = 5.5$. Shown are the results for the dipole (circles), quadrupole (squares) and scissors mode (triangles). (d) Static solutions κ for $\gamma = 0.18$, 1 and 5.5.

H. Bifurcation point calculation

In this Appendix we calculate the location of the bifurcation point of figure 3.1, as a function of the dipolar interactions strength ϵ_{dd}.

For $\alpha > 0$, eq. (3.26) has exactly one solution Ω. In the limit $\alpha \to 0$, this solution is the bifurcation point $\Omega \to \Omega_b$. So in order to find an expression for the bifurcation point, we set $0 < \alpha \ll 1$ and attempt to solve equation (3.26) for Ω. For $0 < \alpha \ll 1$, the effective trapping frequencies become

$$\widetilde{\omega}_x^2 = \omega_\perp^2 - 2\alpha\Omega + \mathcal{O}(\alpha^2),$$
$$\widetilde{\omega}_x^2 = \omega_\perp^2 + 2\alpha\Omega + \mathcal{O}(\alpha^2).$$

For nonzero α, the condensate aspect ratios κ_x, κ_y will also deviate from the cylindrically symmetric value κ found from eq. (3.27). Setting

$$\kappa_x = \kappa + \delta, \qquad \kappa_y = \kappa - \delta, \tag{H.1}$$

with $\delta \ll 1$, we can expand

$$\beta_{101} = \beta_{101} - 2\kappa\beta_{201}\delta + \mathcal{O}(\delta^2), \tag{H.2}$$
$$\beta_{011} = \beta_{101} + 2\kappa\beta_{201}\delta + \mathcal{O}(\delta^2), \tag{H.3}$$

with β_{ijk} defined in (3.20). Next, expanding

$$\left(\frac{\omega_z}{\widetilde{\omega}_x}\right)^2 = \gamma^2\left(1 + 2\frac{\Omega}{\omega_\perp^2}\alpha\right) + \mathcal{O}(\alpha^2),$$

and inserting the distorted aspect ratios of eq. (H.1), eq. (3.23) becomes (neglecting terms of order δ^2, α^2)

$$\kappa^2 + 2\kappa\delta = \gamma^2\left(1 + 2\frac{\Omega}{\omega_\perp^2}\alpha\right)\frac{1 - \epsilon_{dd} + \frac{3}{2}\epsilon_{dd}\kappa^4\beta_{101} + 3\epsilon_{dd}\kappa^3(\beta_{101} - \kappa^2\beta_{201})\delta}{\zeta} \tag{H.4}$$
$$= \gamma^2\left(1 + 2\frac{\Omega}{\omega_\perp^2}\alpha\right)\left(\frac{1 - \epsilon_{dd} + \frac{3}{2}\epsilon_{dd}\kappa^4\beta_{101}}{\zeta} + 3\epsilon_{dd}\kappa^3\frac{\beta_{101} - \kappa^2\beta_{201}}{\zeta}\delta\right) \tag{H.5}$$
$$= \left(1 + 2\frac{\Omega}{\omega_\perp^2}\alpha\right)\left(\kappa^2 + 2\kappa F(\beta_{101} - \kappa^2\beta_{201})\delta\right), \tag{H.6}$$

where in the last step we have used the zeroth order equation

H. Bifurcation point calculation

$$\kappa^2 = \gamma^2 \frac{1 - \epsilon_{dd} + \frac{3}{2}\epsilon_{dd}\kappa^4\beta_{101}}{\zeta},$$

and F is defined as

$$F := \frac{3}{2}\epsilon_{dd}\frac{\kappa^2\gamma^2}{\zeta}.$$

Eliminating κ^2 on both sides of (H.6), and dividing by 2κ we arrive at the first order equation

$$\delta = F(\beta_{101} - \kappa^2\beta_{201})\delta + \kappa\frac{\Omega}{\omega_\perp^2}\alpha + \mathcal{O}(\alpha\delta),$$

from which we find that

$$\begin{aligned}\delta &= \frac{\kappa}{1 - F(\beta_{101} - \kappa^2\beta_{201})}\frac{\Omega}{\omega_\perp^2}\alpha \\ &=: \Gamma\frac{\Omega}{\omega_\perp^2}\alpha.\end{aligned}$$

Thus, we have found the change in κ_x (and κ_y) to first order in α.

Next, we can insert this result in eq. (3.26) to find the bifurcation point. Using (H.2) and (H.3), we get

$$\begin{aligned}&(\alpha + \Omega)\left(\omega_\perp^2 - 2\alpha\Omega - F\left(\omega_\perp^2\beta_{101} - 2\kappa\beta_{201}\Gamma\Omega\alpha\right)\right) \\ &+(\alpha - \Omega)\left(\omega_\perp^2 + 2\alpha\Omega - F\left(\omega_\perp^2\beta_{101} + 2\kappa\beta_{201}\Gamma\Omega\alpha\right)\right) + \mathcal{O}(\alpha^2) = 0,\end{aligned}$$

leading to

$$2\alpha\left(\omega_\perp^2 - \omega_\perp^2 F\beta_{101} - 2\Omega^2 + 2\kappa\beta_{201}F\Gamma\Omega^2\right) + \mathcal{O}(\alpha^2) = 0,$$

such that

$$\frac{\Omega}{\omega_\perp} = \pm\sqrt{\frac{1}{2}\frac{1 - F\beta_{101}}{1 - \kappa\beta_{201}F\Gamma}} + \mathcal{O}(\alpha).$$

After some algebraic manipulations this can be written as

$$\frac{\Omega}{\omega_\perp} = \pm\sqrt{\frac{1}{2} + \frac{1}{2}F(\kappa^2\beta_{201} - \beta_{101})}.$$

I. Numerically calculating the dipolar potential

When performing numerical calculations, calculating the dipolar potential of a given density distribution n can be efficiently carried out using Fourier transforms. Namely, the potential is of the form

$$\Phi_{dd}[n](\mathbf{r}) = \int U_{dd}(\mathbf{r}-\mathbf{r}')n(\mathbf{r}')\mathrm{d}^3\mathbf{r}',$$

which is a convolution of U_{dd} and n. It is well known that the Fourier transform of a convolution is simply a multiplication of the Fourier transforms of the two functions being convolved [15, 14]. To find the dipolar potential then, one simply has to calculate the Fourier transform of the density, multiply that with the (precalculated) Fourier transform of the dipolar interaction energy U_{dd}, and finally perform the inverse Fourier transform on this product to obtain the total dipolar potential. Using fast Fourier transforms (FFT) [15] this can be done very efficiently.

In the next sections we will first derive the Fourier transform of U_{dd}, then have a closer look at the case where the density is cylindrically symmetric, and finally investigate possible problems with using Fourier transforms for long range interactions, and present solutions to these problems.

We will use the following convention for the forward Fourier transform $\mathcal{F}(\boldsymbol{\nu})$ of a function $f(\mathbf{r})$:

$$\mathcal{F}\left[f\right](\boldsymbol{\nu}) = \int f(\mathbf{r}')\mathrm{e}^{-2\pi\mathrm{i}\nu\cdot\mathbf{r}'}\mathrm{d}^3\mathbf{r}' \tag{I.1}$$

and for its inverse

$$f[\mathcal{F}](\mathbf{r}) = \int \mathcal{F}(\boldsymbol{\nu}')\mathrm{e}^{2\pi\mathrm{i}\nu'\cdot\mathbf{r}}\mathrm{d}^3\nu'. \tag{I.2}$$

I.0.1. Fourier transform of U_{dd}

Using that [25]

$$U_{dd}(\mathbf{r}) = \frac{C_d d}{4\pi}\frac{1-3\cos^2\theta}{r^3} = -C_{dd}\left(\frac{\partial^2}{\partial z^2}\left(\frac{1}{4\pi r}\right)+\frac{1}{3}\delta(\mathbf{r})\right),$$

we can split the problem of finding the Fourier transform of U_{dd} in two parts. The first part is the Fourier transform of $\frac{1}{3}\delta(\mathbf{r})$, which is simply a constant, $\frac{1}{3}$. The second part requires finding

the Fourier transform of $\frac{1}{r}$, and multiplying this by $4\pi^2\nu_z^2$ to perform the differentiation in $\boldsymbol{\nu}$-space. Using the well known result in potential theory that [63, 65]

$$\nabla^2\left(\frac{1}{r}\right) = -4\pi\delta(\mathbf{r}),$$

we proceed by replacing $\delta(\mathbf{r})$ by its Fourier transform

$$\nabla^2\left(\frac{1}{r}\right) = -4\pi\int \mathrm{e}^{-\mathrm{i}2\pi\boldsymbol{\nu}\cdot\mathbf{r}}\mathrm{d}^3\nu.$$

To find the Fourier transform of $1/r$ then, we would have to apply the inverse Laplace operator on the right hand side of this equation. Since the Laplace operator acts on the coordinate $\mathbf{r}$ and not on $\boldsymbol{\nu}$, the inverse operator only needs to be computed of the integrand, rather than the integral. Apparently,

$$-\nabla^2\frac{1}{(2\pi)^2\nu^2}\mathrm{e}^{-\mathrm{i}2\pi\boldsymbol{\nu}\cdot\mathbf{r}} = \mathrm{e}^{-\mathrm{i}2\pi\boldsymbol{\nu}\cdot\mathbf{r}},$$

such that the Fourier transform of $1/r$ is simply seen to be

$$\mathcal{F}\left[\frac{1}{r}\right](\boldsymbol{\nu}) = \frac{1}{\pi\nu^2}.$$

Putting the above results together, we find that the Fourier transform of U_{dd} is

$$\mathcal{F}\left[U_{dd}\right](\boldsymbol{\nu}) = \left(\frac{\nu_z}{\nu}\right)^2 - \frac{1}{3} = \cos^2\alpha - \frac{1}{3}, \tag{I.3}$$

where α is the angle $\boldsymbol{\nu}$ makes with respect to the ν_z axis.

I.0.2. Exploiting symmetry: Hankel transforms

When a function exhibits cylindrical symmetry, then so does its Fourier transform. This can be seen as follows. Let $f(x,y) = f(r)$ be a cylindrically symmetric function. Taking the Fourier transform

$$\begin{aligned}
\mathcal{F}\left[f\right](\nu) &= \int\int f(x,y)\mathrm{e}^{-\mathrm{i}2\pi(\nu_x x+\nu_y y)}\mathrm{d}x\mathrm{d}y && \text{(I.4)}\\
&= \int_0^\infty f(r)\int_0^{2\pi}\mathrm{e}^{-\mathrm{i}2\pi r(\cos\phi\nu_x+\sin\phi\nu_y)}\mathrm{d}\phi r\mathrm{d}r && \text{(I.5)}\\
&= \int_0^\infty f(r)\int_0^{2\pi}\mathrm{e}^{-\mathrm{i}2\pi r\sqrt{\nu_x^2+\nu_y^2}\sin(\phi+\arctan(-\nu_x/\nu_y))}\mathrm{d}\phi r\mathrm{d}r && \text{(I.6)}\\
&= 2\pi\int_0^\infty f(r)J_0(2\pi\nu_r r)r\mathrm{d}r, && \text{(I.7)}
\end{aligned}$$

where in the last step we have used the Bessel representation [2]

$$J_0(r) = \frac{1}{2\pi}\int_0^{2\pi}\mathrm{e}^{-\mathrm{i}r\cos\theta}\mathrm{d}\theta.$$

The (two dimensional) transform (I.7) is called a Hankel transform of zeroth order. Its inverse can be derived analogously and is given simply by

$$f[\mathcal{F}_H](r) = 2\pi \int_0^\infty \mathcal{F}_H(\nu_r) J_0(2\pi\nu_r r)\nu_r \mathrm{d}\nu_r.$$

In a numerical simulation of a cylindrically symmetric system the Fourier transform of the density can now be calculated using only two integrals rather than three: one Hankel transform for the radial part and a standard Fourier transform in the z-direction.

When a function f posesses more general symmetry in n dimensions, the transform is a Hankel transform of the n-th order [14]:

$$\mathcal{F}_H^n[f](\nu_r) = \frac{2\pi}{\nu_r^{\frac{1}{2}n-1}} \int_0^\infty f(r) J_{\frac{1}{2}n-1}(2\pi\nu_r r) r^{\frac{1}{2}n} \mathrm{d}r.$$

I.0.3. Long range interactions and discrete Fourier transforms

When employing the Fourier transforms on a computer, calculations will be done on discrete spatial grids and as a consequence we will also use discrete Fourier transforms rather than the continuous transform. However, to describe a spatially finite density distribution one would need infinitely many Fourier frequencies. When using only a finite set of frequencies this implicitly assumes that we are working with a 3D periodic lattice of condensates, all possessing long range interactions. Therefore, the periodic images of the condensate will also contribute to the potential felt by the actual 'original' condensate.

One way of correcting for this problem is to truncate the long range part of the dipolar interactions [113]. This can be done by multiplying U_{dd} by a block function[1], and using the Fourier transform of this truncated potential instead. This transform can be computed by using the convolution theorem in reverse: the Fourier transform of a product is a convolution of the two individual Fourier transforms. In the next paragraphs we will work out two useful cases.

Truncation in the z-direction. Suppose that we want to truncate the interactions at $|z| > Z$. The Fourier transform of the corresponding block function

$$\Delta_Z(\mathbf{r}) = \begin{cases} 1 & (Z \leq z \leq Z) \\ 0 & (|z| > Z). \end{cases}$$

is given by a 'sinc'-function

$$\mathcal{F}\left[\Delta_z(z)\right](\boldsymbol{\nu}) = \delta(\nu_x)\delta(\nu_y)\frac{\sin(2\pi Z\nu_z)}{\pi\nu_z}.$$

The Fourier transform of the truncated interactions is then found from convolving the above expression with (I.3):

[1] A block function is a function that is equal to 1 for some range of r or z, and 0 outside.

$$\begin{aligned}\frac{\mathcal{F}\left[\Delta_z(z)U_{dd}(\mathbf{r})\right](\boldsymbol{\nu})}{C_{dd}} &= \int\int\int\left(\cos^2\alpha' - \frac{1}{3}\right)\delta(\nu_x-\nu_x')\delta(\nu_y-\nu_y')\frac{\sin(2\pi Z(\nu_z-\nu_z')}{\pi(\nu_z-\nu_z')}\mathrm{d}^3\nu' \\ &= \int\left(\cos^2\alpha' - \frac{1}{3}\right)\frac{\sin(2\pi Z(\nu_z-\nu_z')}{\pi(\nu_z-\nu_z')}\mathrm{d}\nu_z' \\ &= \left[\cos^2\alpha - \frac{1}{3}\right] + \mathrm{e}^{-2\pi Z\nu_r}\left[\sin^2\alpha\cos(2\pi Z\nu_z) - \sin\alpha\cos\alpha\sin(2\pi Z\nu_z)\right] \\ &=: C_{dd}^{-1}F_Z(\nu_r,\nu_z), \end{aligned} \tag{I.8}$$

where ν_r is the distance to the ν_z axis.

Truncation on a cylinder. To find the truncation of the potential to a cylinder of height Z and radius R, we start from the z-truncated interaction energy (I.8), and multiply this with a cylindrical block function

$$\Delta_R(r,z) = \begin{cases} 1 & (0 \le r \le R) \\ 0 & (r > R). \end{cases}$$

Employing the convolution theorem again, the Fourier transform of the product of this block function with U_{dd} will be a convolution in ν-space. The Fourier transform of the cylindrically symmetric block function $\Delta_R(r)$ is calculated using a Hankel transform to be

$$\mathcal{F}\left[\Delta_R\right](\nu) = 2\pi\delta(\nu_z)\int_0^R J_0(2\pi\nu_r r)r\mathrm{d}r = \delta(\nu_z)R\frac{J_1(2\pi R\nu_r)}{\nu_r}.$$

Using furthermore that the distance between two points ν_r and ν_r' in polar coordinates is equal to

$$|\nu_r' - \nu_r| = \sqrt{\nu_r'^2 + \nu_r^2 - 2\nu_r'\nu_r\cos\theta},$$

the truncated potential becomes

$$\mathcal{F}\left[\Delta_R U_{dd}\right](\boldsymbol{\nu}) = C_{dd}\int_0^{2\pi}\int_0^{\infty} F_Z(\nu_r',\nu_z)R\frac{J_1(2\pi R\sqrt{\nu_r'^2+\nu_r^2-2\nu_r'\nu_r\cos\theta})}{\sqrt{\nu_r'^2+\nu_r^2-2\nu_r'\nu_r\cos\theta}}\nu_r'\mathrm{d}\nu_r'\mathrm{d}\theta,$$

with $F_Z(\nu_r,\nu_z)$ as defined in (I.8). Although the outcome of this integral is not known in an analytic form, the result is still useful for numerical calculations. The Fourier transform of the potential is only evaluated for a finite set of frequencies $\boldsymbol{\nu}$, which can be done numerically, and this is a calculation which only needs to be done once for a particular grid at the start of a simulation, any subsequent calculations on the same grid can then use the stored Fourier coefficients.

J. Minimization of grand potential

In this appendix we will discuss methods for finding the stationary points of the (nonlinear) energy and grand potential functionals for the (real valued) amplitude f of the vortex-state wave function. The internal energy is given by

$$E[f] = \int \left[\frac{1}{2} \frac{\hbar^2}{2m} (\nabla f)^2 + U(\mathbf{r}) f^2 + \frac{1}{2} g f^4 + \frac{1}{2} f^2 \Phi_{dd}[f^2] \right] d^3\mathbf{r}, \tag{J.1}$$

under the constraint that the number of particles is fixed, and where we have combined the external- and vortex potential by defining

$$U(\mathbf{r}) = \frac{\hbar^2}{2m} \frac{s^2}{r^2} + V(\mathbf{r}).$$

The grand potential is then given by

$$\Phi_G[f] = E[f] - \mu \int f^2 d^3\mathbf{r}, \tag{J.2}$$

where μ is a *fixed* parameter. Throughout this appendix we will be considering nontrivial f only, thus excluding pathological cases such as $f = 0$.

J.1. Variational minimization

First, we will confirm by variational analysis that stationary points of (J.1), (J.2) indeed satisfy the time independent Gross-Pitaevskii equation (4.10). To control the number of particles in variation of E we need to add a undetermined Lagrange multiplier $-\mu N$ and minimize $E - \mu N$, which is precisely equivalent to minimizing the grand potential. Hence we only need to consider the grand potential, for which the variational derivative with respect to a function v, or *Gateaux derivative*, is given by[1]

$$\begin{aligned}
d\Phi_G(f, v) &= \lim_{\epsilon \to 0} \frac{\Phi_G[f + \epsilon v] - \Phi_G[f]}{\epsilon} \\
&= \int \left[\frac{\hbar^2}{2m} \nabla f \nabla v + 2U(\mathbf{r}) f v + 2 g f^3 v + f v \Phi_{dd}[f^2](\mathbf{r}) + f^2 \Phi_{dd}[f v](\mathbf{r}) - 2\mu f v \right] d^3\mathbf{r} \\
&= \int \left[\frac{\hbar^2}{2m} \nabla f \nabla v + 2U(\mathbf{r}) f v + 2 g f^3 v + 2 f v \Phi_{dd}[f^2](\mathbf{r}) - 2\mu f v \right] d^3\mathbf{r} \\
&= \int \left[-\frac{\hbar^2}{2m} \nabla^2 f + 2U(\mathbf{r}) f + 2 g f^3 + 2 f \Phi_{dd}[f^2](\mathbf{r}) - 2\mu f \right] v \; d^3\mathbf{r}
\end{aligned} \tag{J.3}$$

[1] In physical literature this variational derivative is often denoted by $\delta\Phi_G[f]/\delta v$.

where in the second step we changed the order of integration of the last term:

$$\int f(\mathbf{r})^2 \Phi_{dd}[fv](\mathbf{r}) d^3\mathbf{r} = \int f(\mathbf{r})^2 \int f(\mathbf{r}') v(\mathbf{r}') U_{dd}(\mathbf{r}-\mathbf{r}') d^3\mathbf{r}' d^3\mathbf{r}$$
$$= \int\int f(\mathbf{r})^2 f(\mathbf{r}') v(\mathbf{r}') U_{dd}(\mathbf{r}-\mathbf{r}') d^3\mathbf{r} d^3\mathbf{r}' = \int f(\mathbf{r}') v(\mathbf{r}') \Phi_{dd}[f^2] d^3\mathbf{r}',$$

and in the third step we used integration by parts on the first term.

Clearly, if we require that the variational derivative (J.3) is zero for *any* function v, we must have that

$$-\frac{\hbar^2}{2m}\nabla^2 f + U(\mathbf{r}) f + g f^3 + f\Phi_{dd}[f^2](\mathbf{r}) - \mu f = 0,$$

which is precisely the time independent Gross-Pitaevskii equation (4.10).

J.2. Numerical minimization scheme

When numerically minimizing the grand potential, we start by discretising the space into a grid of M points $\mathbf{x}_i$, $i = 1, 2, \ldots M$. The condensate wave function f is represented by a finite vector $\mathbf{f}$ of values of the wavefunction on this grid, $f_i = f(\mathbf{x}_i)$. The finite grid represents a finite volume V, and in the following we always assume Dirichlet boundary conditions $f = 0$ at the edge of the volume.

The grand potential Φ_G can also be discretised, by discretising the gradients ∇ with (e.g.) centered differences, and the integral with appropriately weighted sums over the gridpoints. The dipolar potential is calculated using the methods described in Appendix I. Denoting the discretised grand potential by Φ_G^M, we thus have

$$\Phi_G[f] \doteq \Phi_G^M(\mathbf{f}),$$

and the problem is reduced to finding the discrete vector $\mathbf{f}$ that minimizes the function $\Phi_G^M : \mathbb{R}^M \to \mathbb{R}$. We minimize $\Phi_G^M(\mathbf{f})$ using the the *steepest descent* method.

This method is based on the fact that the M-dimensional gradient,

$$\nabla_M = \left(\frac{\partial}{\partial f_1}, \frac{\partial}{\partial f_2}, \ldots, \frac{\partial}{\partial f_M}\right),$$

acting on $\Phi_G^M(\mathbf{f})$ is a vector

$$\mathbf{a} = \nabla_M \Phi_G^M(\mathbf{f})$$

that points in the direction of the greatest increase of Φ_G^M. The negative gradient will therefore point in the direction of the greatest decrease. For sufficiently small $\lambda > 0$ we will then have that

$$\Phi_G^M(\mathbf{f}) - \lambda\mathbf{a} < \Phi_G^M(\mathbf{f}),$$

of course provided that $\mathbf{f}$ is not precisely a minimum of Φ_G^M.

Starting from an initial guess $\mathbf{f}_0$, the steepest descent method then consists of iterating the following assignment, until convergence is reached:

$$\mathbf{f}_{i+1} = \mathbf{f}_i - \lambda_i \nabla_M \Phi_G^M(\mathbf{f}_i).$$

At every step, we go downwards in the M-dimensional potential landscape, and this way we always end up in a (local) minimum, unless there exists an negative infinite well. This latter singularity would correspond to a dipolar-interactions-induced collapsed state. The parameter λ_i may be chosen constant, or it might be varied. In any case, it should be chosen small enough such that the scheme does not diverge.

In passing onto the continuum limit when $\lambda_i \to 0$, and $M \to \infty$, while keeping the volume of the system constant, the steepest descent scheme turns into the nonlinear diffusion equation

$$\hbar \frac{\partial f}{\partial t} = -\hat{H}(f), \tag{J.4}$$

with $\hat{H}$ the Gross-Pitaevskii operator

$$\hat{H}(f) = \left(-\frac{1}{2}\frac{\hbar^2}{2m}\nabla^2 + U(\mathbf{r}) + gf^2 + \Phi_{dd}[f^2](\mathbf{r}) - \mu \right) f. \tag{J.5}$$

The constant $\hbar$ is added, such that the iteration number can be interpreted as a *time* in the continuum limit. We can now conclude that the steepest descent scheme is precisely the Euler forward time propagation of the above diffusion equation, with time step λ_i. Using this knowledge, we can establish an upper bound for λ_i, from the stability requirement of the Euler forward scheme (4.13), as discussed in the main text.

Taking the scheme (J.4) as a starting point we can approach the problem from a different angle. We are given the task of propagating (J.4) in time and seek (numerical) methods to do so. Obviously, the earlier encountered Euler forward time propagation can be used, but there also exist more advanced numerical schemes. A few of such alternatives are discussed in the main text. For nonlinear diffusion problems several analytic results exist on the topic of existence and uniqueness of asymptotically stationary states (local minima of Φ_G^M). Fife [40] gives a good overview of several nonlinear diffusion equations encountered in physics and their asymptotic states, although these results are not applicable to the case of Bose-Einstein condensation. For the time evolution equation (J.4) without dipolar interactions present, Simon [122] provides conditions for existence of asymptotically stationary states, while Henry [55, 56] gives conditions under which there are only a finite number of possible asymptotic states of the system.

As an interesting side note, equation (J.4) is strongly reminiscient of *imaginary time propagation*. That is, the nonlinear diffusion equation is exactly the result if one makes the substitution $t \to \mathrm{i}\tau$ in the time dependent Gross-Pitaevskii equation (1.22). Imaginary time propagation[2] is a widely (ab)used trick in physics to obtain the ground state of a quantum system. When the operator $\hat{H}$ is Hermitian, as for instance in the ordinary Schrödinger

[2]Sometimes referred to as a Wick rotation of the time variable.

equation, it contains a complete set of orthogonal basis functions which are all damped exponentially when propagated in imaginary time, rather than the oscillatory behaviour exhibited in real time. Therefore, starting with any initial guess, excited states will damp out exponentially faster than the ground state and after some (imaginary) time, only the ground state wave function has a significant amplitude[3]. However, the Gross-Pitaevskii operator (J.5) is nonlinear and it cannot be assumed to posess a complete set of orthogonal eigenfunctions. Therefore, despite the fascinating resemblance, scheme (J.4) should not be confused with imaginary time propagation, even though this is often done in physical literatures.

As a final note, the steepest descent method is not the only possible choice for minimizing a nonlinear functional. Noteworthy alternatives include conjugate gradients [120], and the Rayleigh-Ritz method, which constructs a sequence of approximating functions f, by including more and more basis functions of some orthogonal, complete basis, and minimizing for the coefficients at each step [41].

[3]Note that even this state has a vanishing amplitude in imaginary time, and hence this scheme requires renormalization of the total wave function.

K. Scaling to maintain constant aspect ratio and radius

In this Appendix we discuss the parameters and scaling for the time-independent Gross-Pitaevskii equation for use in the numerical calculations of section 4.3.

K.1. Controlling the condensate peak density, radius and aspect ratio

From the results of chapter 2, we know that the solution of the cylindrically symmetric, time-independent Gross-Pitaevskii equation

$$\left(\frac{1}{2}m\omega_\perp^2(r^2+\gamma^2z^2)+g|\psi|^2+\Phi_{dd}[n]\right)\psi=\mu\psi,$$

in the Thomas-Fermi limit has a parabolic density profile. The goal of this appendix is to configure $\omega_\perp, \gamma$, and μ in such a way that this parabolic solution has a fixed peak density n_0, radius R_x and aspect ratio κ while the dipolar interaction strength ϵ_{dd} is being varied.

We start with the chemical potential μ. From comparing the constant term in equation (2.11), we have that (alternatively, see [35])

$$n_0=\frac{\mu}{1-\epsilon_{dd}f(\kappa)},$$

with

$$f(\kappa):=\beta_{001}(\kappa),$$

with β_{001} defined in equation (2.16).

Therefore, we must pick

$$\mu=n_0\left(1-\epsilon_{dd}f(\kappa)\right)$$

in order to keep n_0 fixed for varying ϵ_{dd}.

Continuing with the axial trapping strength γ, for given ϵ_{dd} and κ, the relative trapping strength γ is solved from equations (2.12 - 2.14), which can be alternatively rewritten as [35]

$$3\kappa^2\epsilon_{dd}\left[\left(\frac{\gamma^2}{2}+1\right)\frac{f(\kappa)}{1-\kappa^2}-1\right]+(\epsilon_{dd}-1)(\kappa^2-\gamma^2)=0,$$

such that

K. Scaling to maintain constant aspect ratio and radius

$$\gamma = \sqrt{\frac{\kappa^2\left(1-\kappa^2-\epsilon_{dd}(2\kappa^2+3f(\kappa)-2)\right)}{1-\kappa^2+\epsilon_{dd}\left(\left(1+\frac{3}{2}f(\kappa)\right)\kappa^2-1\right)}}.$$

Note that the above does not hold for $\kappa = 1$, in this particular case we have that

$$\epsilon_{dd} = \frac{5}{2}\frac{\gamma^2-1}{\gamma^2+2},$$

leading to

$$\gamma = \sqrt{\frac{2\epsilon_{dd}+\frac{5}{2}}{\frac{5}{2}-\epsilon_{dd}}}.$$

Finally, the Thomas-Fermi radius of the condensate R_x is given by [35]

$$\left[2\frac{15N\kappa}{8\pi}\frac{g}{m\omega_\perp^2}\left(1+\epsilon_{dd}\left(\frac{3}{2}\frac{\kappa^2 f(\kappa)}{1-\kappa^2}-1\right)\right)\right]^{\frac{1}{5}} \tag{K.1}$$

where the number of particles N in a general parabolic density profile with peak density n_0, radius R_x and aspect ratio κ is given by

$$N = \frac{8\pi R_x^3 n_0}{15\kappa}.$$

Combining this result with eq. (K.1) we get

$$R_x^5 = \frac{2gR_x^3 n_0}{m\omega_\perp^2}\left(1+\epsilon_{dd}\left(\frac{3}{2}\frac{\kappa^2 f(\kappa)}{1-\kappa^2}-1\right)\right),$$

such that in order to keep R_x fixed we must choose

$$\frac{1}{2}m\omega_\perp^2 = \frac{gn_0}{R_x^2}\left(1+\epsilon_{dd}\left(\frac{3}{2}\frac{\kappa^2 f(\kappa)}{1-\kappa^2}-1\right)\right) = \frac{gn_0}{R_x^2}\eta^2,$$

with

$$\eta^2 = \left(1+\epsilon_{dd}\left(\frac{3}{2}\frac{\kappa^2 f(\kappa)}{1-\kappa^2}-1\right)\right) \qquad (\kappa \neq 1), \tag{K.2}$$

and

$$\eta^2 = 1-\frac{2}{5}\epsilon_{dd} \qquad (\kappa = 1). \tag{K.3}$$

K.2. Scaling

In this section we scale the time-independent Gross-Pitaevskii equation (4.10) of section 4.3, such that it is suitable for numerical computation.

Inserting the results of the previous section in the time independent Gross-Pitaevskii equation, and adding a vortex phase pattern leads to the following equation for the real valued, radial wave function ψ:

$$\left(-\frac{\hbar^2}{2m}\nabla^2 + +\frac{\hbar^2}{2m}\frac{s^2}{r^2} + \frac{gn_0}{R_x^2}\eta(r^2+\gamma^2z^2) + g|\psi|^2 + \Phi_{dd}\right)\psi = n_0 g\left(1-\epsilon_{dd}f(\kappa)\right)\psi. \tag{K.4}$$

We scale the wave function as

$$\Psi(\mathbf{x}) = \sqrt{n_0}\psi'(\mathbf{r}') \tag{K.5}$$

with n_0 the peak density of the parabolic density in absence of a vortex core and in the Thomas-Fermi limit, and $\mathbf{r}'$ a scaled spatial coordinate using the Thomas-Fermi radius R_x such that $\mathbf{r} = R_x\mathbf{r}'$.

Substituting the above definitions in (K.4) and dividing by the energy $n_0 g$ we get the dimensionless equation

$$\left(-\frac{1}{2}\chi^2\nabla'^2 + \chi^2\frac{s^2}{r'^2} + \eta^2(r'^2+\gamma^2z'^2) + |\psi'|^2 + \epsilon_{dd}\Phi'_{dd}\right)\psi' = \mu\psi', \tag{K.6}$$

with

$$\epsilon_{dd}\Phi'_{dd} = \frac{\Phi_{dd}}{n_0 g},$$

and the dimensionless constant

$$\chi = \frac{\xi}{R_x},$$

which is the ratio of the healing length

$$\xi = \frac{\hbar}{\sqrt{mn_0 g}}$$

and the Thomas-Fermi radius R_x.

In the Thomas-Fermi limit, $\chi \ll 1$, and we expect the potential term due to the vortex phase pattern to be small, except for a small region of the order of the healing length around $r = 0$. We therefore expect that away from $r = 0$ and $r = R_x$, the solution of equation (K.6) still has a parabolic density profile with a dimensionless peak density and condensate radius both equal to 1, and an aspect ratio κ.